Improvement of Acoustic Emission Technology for Stress Corrosion Cracking

A thesis submitted for the degree of Doctor of Philosophy by:

Han Yang

Department of Mechanical and Aerospace Engineering

Brunel University London

London

United Kingdom

Acknowledgement

First and foremost, I would like to express my deep gratitude to my supervision team: academic supervisor, Dr Bin Wang for his invaluable supervision, patience and feedback throughout my study; industrial supervisor, Dr Stephen Grigg, for generously providing knowledge, expertise and insightful comments and suggestions at my research projects; mentor, Dr Yikun Wang, for her suggestions and support on my PhD study; previous industrial supervisor, Dr Ryan Marks for his dedicated guidance, encouragement, support at TWI Ltd. I could not have done this without them.

I also grateful to Dr Qing Lu for her guidance on corrosion and stress corrosion cracking. My sincere thanks go to Dr Channa Nageswaran, Ms Lu Zhao, Ms Dorothee Panggabean, Mr Simon Turner for their assistance and support in Non-destructive Testing. I would also like to take this opportunity to thank Mr Tyler London, Dr Longjie Wang and Dr Huan Wu for their support in numerical simulation. Special thanks go to Dr Linghao Zhou and Dr Jialin Tang for providing me with unconditional support and continuous encouragement throughout my years of study and through the process of this research. My appreciation also goes out to my colleagues at the Fatigue Lab, Corrosion Lab and MET Lab at TWI for their help in preparing and carrying out the tests described in this thesis. Additionally, this research would not have been possible without the generous support and funding from Lloyd's Register Foundation, Brunel University London and the National Structural Integrity Research Centre (NSIRC).

I am also grateful to my friends in TWI for their encouragement and moral support. I will never forget the happy time with them during lunch break. Thanks should also go to my housemate Dr Bo Li for the Friday hot pot dinner and his suggestions on my thesis write-up and job interview.

Finally, I would like to express my sincere gratitude to my family for their continuous love and support, which kept my motivation high during this process.

Declaration

The candidate confirms that the work submitted is his own and that appropriate credit has been given where reference has been made to the work of others.

This copy has been supplied on the understanding that it is copyright material and that no quotation from the thesis may be published without proper acknowledgement.

The right of Han Yang to be identified as the author of this work has been asserted by him in accordance with the Copyright, Designs and Patents Act 1988.

Some parts of the work have been published in the following article:

Yang, H., Wang, B., Grigg, S., Zhu, L., Liu, D., & Marks, R. (2022). Acoustic Emission Source Location Using Finite Element Generated Delta-T Mapping. *Sensors*, 22(7), 2493.

Yang, H., Wang, B., Liu, D., & Grigg, S. (2022). Investigation of delta-T mapping source location technique based on the arrival of A_0 modes. *In The 35th European conference on Acoustic Emission testing, EWGAE*.

List of tables

List of figures

Contents

Chapter 1 Introduction

This thesis investigates the advancement of Acoustic emission (AE) monitoring techniques and analysis methods that could be applied in the field of Structural Health Monitoring (SHM), with an emphasis on the use of advanced AE techniques to detect and locate damage and their application on the monitoring of corrosion and Stress corrosion cracking (SCC) in complex metallic structures. The work was divided into three main areas of research, which are an investigation into using FE (Finite Element) generated delta-T mapping to locate experimental AE signals on complex structures, source location of AE signals generated by corrosion and an experimental investigation into SCC damage locations on a metallic specimen.

1.1 Background

Corrosion damage is one of the most commonly seen and costly problems worldwide. According to a study conducted by Koch et al. [1], the estimated global cost of corrosion was 2.5 trillion dollars, or 3.4% of the global GDP in 2013. In addition to the huge economic loss, structural failures caused by corrosion damage can lead to serious individual safety and environmental consequences. For example, in April 1992, 215 people were killed and another 1500 people were injured due to the sewer explosion in Guadalajara, Mexico. The huge economic loss was estimated at 75 million dollars. The accident was due to the leakage of corroded gasoline into a nearby sewage main [2]. The sinking of the Erika (a tanker) on 12th of December, 1999 was another accident caused by corrosion. Around 19,000 tonnes of heavy oil were spilled, which resulted in devastating pollution to the maritime environment.

In this disaster, a large loss in revenue from tourism and fishing industries was felt by the local people [2].

Stress corrosion cracking (SCC) is one type of localised corrosion and has been a major cause of the premature failures of various structures and components in various industries, such as the oil, gas, and nuclear sectors [3,4]. The failure caused by SCC mechanisms, which adversely affects structural integrity, cannot be easily predicted and controlled. Without appropriate remedial measures, structural integrity is likely to be compromised with potential to cause catastrophic damage, leading to loss of lives and capital. In power and chemical plants, for instance, in order to eliminate unplanned shutdowns and reduce inspection and maintenance costs, there is a need for a proactive monitoring approach to assess the existing structural conditions for safe operation. As a method of monitoring structural performance and identifying damage at an early stage, Structural Health Monitoring (SHM) systems are gaining significant interest and have seen increased application. Recent industrial studies suggest that detecting damage at an early stage can reduce costs and increase the life expectancy of a structure [5]. Therefore, a practical and cost-efficient SHM method that can identify micro and macro defects at an early stage and continually assess the structural health is desirable to ensure that critical structural components can operate safely and efficiently throughout the expected service life.

To infuse continued confidence in the structural integrity, Non-Destructive Evaluation (NDE) inspections are performed periodically, which forms the basis of a SHM system. NDE techniques such as ultrasonic and X-ray methods have been proven to be very effective for detecting a considerable number of defects in materials and have been widely utilised in industry [6]. Despite its merits, there appears to be some possible negative consequences of periodic NDE-based inspections. In order to perform NDE, many components need to be removed from testing equipment and refitted thereafter, thus requiring a long period of time. Since for the in-service equipment, it is not feasible to remove components, the equipment cannot be used during NDE inspection periods, resulting in a loss in revenue. Moreover, areas of difficult access and complex geometry are particularly difficult to be examined by NDE techniques. Thus, a revision of the traditional SHM system is desirable, with a transition from lengthy periodic NDE inspection and maintenance to an autonomous SHM

system in which the structural integrity of the target equipment is continuously monitored in-service. The phenomenon of Acoustic Emission (AE), which is one type of NDE methods, lends itself well to such a system. AE is defined as the transient elastic energy released by a material when it experiences a change of deformation in its structure [7]. As a passive technique, AE only detects active defects.

1.2 Aim and objectives

AE techniques have been successfully applied in monitoring corrosion and SCC [8–13]. However, according to a systematic literature review carried out by the author, a relatively small proportion of the effort has been devoted to studies of source localisation of this damage in metallic structures, especially in complex metallic structures in engineering applications [14]. Thus, this research aims to improve the monitoring techniques and analysis methods required for the AE monitoring of corrosion and SCC. The key objectives of this study were:

- To better understand the advanced AE damage location technique, delta-T mapping, and to optimise this technique using FE method for the location of AE activity on specimens with complex geometries
- To carry out experimental investigations into identification of different source mechanisms during SCC
- To demonstrate a method of discrimination between AE signals arising from corrosion and SCC
- To verify that AE signals from SCC can be identified and located in metallic specimens with additional complexity
- To improve the ability of AE to detect and locate corrosion damage in complex structures

1.3 Research methodology

The FE method, which is a computer-based numerical technique, developed by engineers in the mid-1950s, is becoming increasingly popular because of fine discretization, efficient and reliable algorithms and fast computing systems. Moreover, the FE method allows for easy modelling of complex geometries of structures with anisotropic materials properties. Hence, the FE method as well as the experimental approach were used in this study to optimise delta-T mapping. To achieve the intended aim and objectives of this work on monitoring corrosion and SCC, experimental approaches were used.

1.4 Contribution to the knowledge

This thesis investigates the advancement of AE monitoring techniques and analysis methods that could be applied in the field of SHM, with an emphasis on the use of advanced AE techniques to detect and locate damage, and their application on the monitoring of corrosion and SCC in complex metallic structures. The key areas of contribution are highlighted below;

- A numerical delta-T mapping technique was developed by generating the training data using FE method. It was demonstrated that this technique decreased the time and man-power required for manually collecting and processing the training data whilst keeping a reasonable degree of source location accuracy.
- Based on the multiple methods which were developed and demonstrated for the detection of the A_0 mode arrival, the delta-T mapping technique was developed and applied to detect and locate corrosion damage in a complex structure.
- A thorough experimental investigation of AE monitoring of SCC was conducted, from which three stages of SCC damage development were identified. Real AE source identification was achieved in SCC tests with successful discriminations between corrosion and SCC damage.

1.5 Novelty statement

The novelty in this work is as follows;

- This is the first study in which FE method was used to collect data to train delta-T maps.
- Although AE monitoring of corrosion has been studied extensively, there is no work carried out on identification of first arriving mode when monitoring corrosion in a metallic specimen. This is the first study in which A_0 was identified to be the first arriving mode.
- Although time arrival estimation methods were well established for determining onset time of an AE signal with high signal-to-noise, no comprehensive work was dedicated to arrival time estimation of AE signals from corrosion, which are characterised by low signal-to-noise. Therefore, it is sensible to propose a novel method called window AIC method to accurately estimate arrival time of AE signals with low signal-to-noise.
- Because of the demonstration for the detection of the A_0 mode arrival, it is sensible to update delta-T mapping technique accordingly. The updated delta-T mapping technique is based on the A_0 mode arrival rather than the S_0 mode arrival. It was used to detect and locate the corrosion damage in a complex structure for the first time.
- A novel and thorough experimental investigation of AE monitoring of SCC was conducted, from which three stages of SCC damage development were identified.

1.6 Thesis organisation

This thesis is presented in seven chapters. Chapter One provides background information to the development of a SHM system for use on monitoring damage including corrosion and SCC. The potential for the use of AE techniques as a tool of SHM is discussed and the aim and objectives of this study have been declared.

Chapter Two covers literature reviews and theories relevant to this work. Theories of AE wave propagation, wave attenuation and source location are provided, along with the theory

of modal acoustic emission and wavelet transform. A comprehensive review on modelling AE with the FE method, monitoring corrosion and SCC with AE techniques are also included.

Within Chapter Three, full details of experimental equipment, procedures and techniques utilised throughout of this body of work are discussed.

Chapter Four covers an investigation into using FE generated delta-T mapping to locate experimental AE signals on a complex structure. A FE method for simulation of an artificial AE source is first investigated on a simple steel plate and validated by experimental results. This method is then applied on a more complex geometry plate to train a delta-T map for localization of experimental H-N sources. The results show that the FE generated delta-T map decreases the time and effort required for manually collecting and processing the training data, whilst keeping a reasonable degree of source location accuracy.

Chapter Five discusses source location of AE signals generated by corrosion. A novel arrival time estimation technique is presented to determine the arrival time of low signal-to-noise AE signals from corrosion. Furthermore, corrosion damage locations on a simple metallic plate are discussed. By identifying the correct arrival wave mode (i.e. A_0 mode), additional improvements to the technique presented in Chapter Four are discussed. The technique is then applied for the planar location of AE signals on a complex plate and results are presented.

Chapter Six includes the details of an experimental investigation into SCC damage locations on a metallic specimen. The reliability of AE technique to detect and identify different damage mechanisms (i.e. corrosion and SCC) are discussed. Additionally, based on AE signal parameters, clustering algorithms are used to identify and characterise signals from different source mechanisms.

Chapter Seven summarises the findings in this thesis and discusses the implications of these findings for future work.

1.7 Published outputs

Yang, H., Wang, B., Grigg, S., Zhu, L., Liu, D., & Marks, R. (2022). Acoustic Emission Source Location Using Finite Element Generated Delta-T Mapping. *Sensors*, 22(7), 2493.

Yang, H., Wang, B., Liu, D., & Grigg, S. (2022). Investigation of delta-T mapping source location technique based on the arrival of A_0 modes. *In The 35th European conference on Acoustic Emission testing, EWGAE.*

Chapter 2 Background Theory and Literature Review

This chapter presents relevant background information and theory on wave propagation, wave attenuation, modal analysis, wavelet transform analysis and AE source location techniques. A short history of AE is also included. Additionally, a structured literature review on Finite Element (FE) modelling of AE and monitoring corrosion and SCC with AE techniques is reported.

2.1 Acoustic emission

2.1.1 Introduction

AE is defined as the transient elastic energy released by a material when it experiences a change of deformation in its structure [7]. As a natural physical phenomenon, AE can be observed in wide-ranging materials, structures and processes. AE detected during the movement of a few dislocations in metals under stress is the smallest-scale [7]. The detection frequency range of AE is in the ultrasonic range, which is approximately from 10 kHz to 1 MHz [15]. However, it is suggested that the frequency of common AE signals lies between 100 kHz to 300 kHz [7]. Although there are differences in the set-up and hardware between AE systems, the process of obtaining AE data usually consists of the following six sequential steps [16] as illustrated in Figure 2.1.

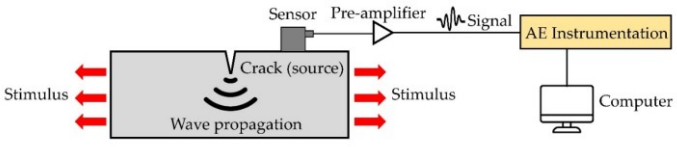

Figure 2.1– Principles of AE monitoring [16]

Firstly, the AE waves are generated at a source after the rapid release of elastic energy. Secondly, these waves cause surface displacements and arrive at the piezo-electric sensors which are mounted on the structure. Thirdly, the resulting tiny displacements of the surface are detected and converted into a small voltage by the sensors at various locations. Fourthly, this small voltage is amplified by a pre-amplifier to a strong and useable voltage. Fifthly, this strong voltage or the electrical signal is subsequently recorded and processed by the AE acquisition system. Finally, as the acquisition system is controlled and initialized by the system front-end run on an external computer, the acquisition data can be stored, displayed and analyzed in real time on the computer.

Many traditional Non-destructive Testing (NDT) methods, such as ultrasound and X-ray, are defined as active monitoring techniques because a known input source is required, while AE is classed as a passive technique. The thing which makes AE method different from traditional active NDT method is that the elastic waves which AE detects are generated from the structure itself during deformation. In other words, a known input source is not needed in AE technique. However, the requirement for AE testing is that the structure under investigation must be under loading to activate the AE source because the elastic waves will not be released from unstressed or non-active defects and therefore cannot be detected.

2.1.2 A short history of AE

Before the application of the AE technique was brought into the public eye in its present form by Kaiser in 1950 when he published his pioneering work of comprehensive study on AE as part of his PhD research [17], the phenomenon of AE has been observed for hundreds of years [18]. The ‘tin cry’ has been heard by tinsmiths since 1917. This ‘cry’ sound is generated due to plastic deformations of the materials as metals deform in twinning. Later, AE was firstly mentioned in material research by two French metallurgists Portevin and Le Chatelier [19]. They noted that audible noise was emitted from the specimen during a Luder’s line formation on the specimen. Subsequently, this phenomenon was also found in other metals. Later on, for a better understanding of fracture of the Earth’s Crust, a well-planned AE experiment was performed in 1933 [20]. In the experiment, the stress waves generated due to wood deformation were monitored by a phonograph pick-up with a steel needle [21].

In 1936, Forster and Scheil [22] successfully transformed the mechanical vibrations into electrical voltages in AE experiments by using purpose built instrumentation, which made it possible to monitor AE caused by martensitic transformations.

The year 1950 is often quoted as the beginning of AE history [7] because the first comprehensive investigation of AE phenomenon was published by Kaiser [17]. Tensile tests on metallic materials were performed with transducers, amplifiers and oscilloscopes employed to record AE. His most significant discovery is the observation of the 'Kaiser effect', which is a phenomenon defined as the absence of AE activity until previously applied stress on the specimen is exceeded. This effect has been widely and successfully applied to assess the stresses which structures have experienced in operation [23]. In 1961, the terminology of AE was firstly used in history by Schofield [24] after he re-examined Kaiser's work and published his pioneering work.

Until the mid-1950s, the frequency limit for AE monitoring is around 60 kHz, which is quite close to the generally established audio frequency range (20 Hz to 20 kHz). The presence of noise would reduce the AE signal and therefore the practical applications of AE techniques were greatly restricted. In 1964, the frequency limit of the AE sensor was substantially extended well above the audio range and up to 1 MHz by Dunegan et al. [25]. Due to this improvement, the applications of the AE technique grew rapidly in a variety of areas from basic materials research to NDT.

In 1940s, the geologists in Russia adopted the AE technique as a standard mining practice to identify impending mine collapse [26]. However, due to lack of information interchange between materials engineers and geologists, this technique was not used in the areas of SHM until Green et al. [27] published their work on testing rocket-motor casings with AE in 1964. After that, owing to relatively simplified instrumentation and inherent high sensitivity of AE techniques, AE applications went into the course of rapid development. Among these applications, crack growth monitoring is considered to be very essential. It has been found by Dunegan et al. [28] that AE waves produced in flawed steel pressure vessels are much earlier than those in unflawed steel pressure vessels. Hence, early stage crack propagation can be diagnosed and the failure stress can be predicted with acceptable error to avoid catastrophic failures of structures and economic losses.

Nowadays, AE techniques have application in almost all industries. Owing to the advances of modern computing with increasingly high processing speed and huge storage ability, acquisition and signal processing with high data sampling rates required for AE monitoring can be achieved. Full waveforms can also be captured throughout the AE tests and used to provide more useful information on AE wave propagation.

2.1.3 Hsu-Nielson source

Before starting an AE test, it is of vitally importance to check the sensitivity of a sensor after it has been mounted to a surface. The most commonly used method to do so is the pencil lead break (PLB) source, or the Hsu-Nielson (H-N) source, which is named due to the work conducted by Hsu and Breckenridge [29] and Nielsen [30]. The applicability of several AE sources were investigated by them in order to calibrate AE sensors. Their work showed that the H-N source is a practical and repeatable way for AE sensor calibration. According to its name, this type of source can be easily understood as the breaking of the lead of a mechanical pencil. The principle is that the force applied on the surface by a pencil lead tip results in a surface displacement, and after the pencil lead breaks, the rapid change of surface displacement and the release of the accumulated stress in the surface will lead to the generation of acoustic waves. The H-N source is a well-established and widely used artificial source of AE because of its repeatability and accessibility [31].

A typical 2H lead with a 0.3 mm or 0.5 mm diameter and a length of 2 mm to 3 mm is utilised in H-N sources. It is required that the lead is broken at a repeatable angle to reduce the risk of spurious signals. The guide ring ‘Nielson Shoe’ attached to the end of a pencil, as shown in Figure 2.2, can facilitate a repeatable angle.

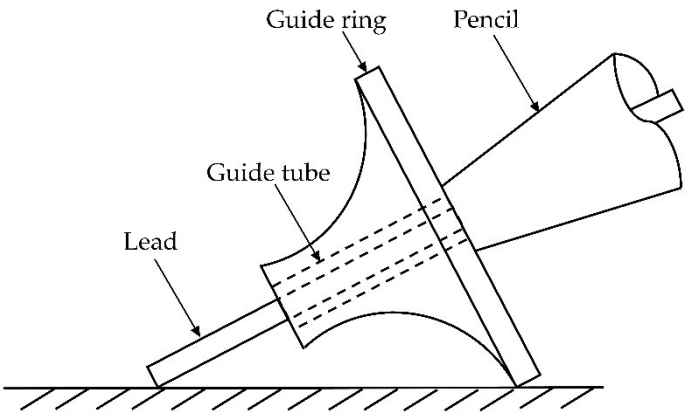

Figure 2.2–The Nielsen shoe on H-N source [29].

The standard procedures agreed by the European Working Group on Acoustic Emission (EWGAE) in October 1980 [32] for performing H-N sources consist of following steps;

1. Press the lead feed button continually until the lead protrudes.

2. Level the end of the lead with the end of the guide tube.

3. Press the lead feed button six times (This depends on the pencil) to protrude a 3 mm length lead.

4. Guide the pencil obliquely towards the surface of tested structure until the guide ring touches the surface.

5. Pivot the pencil on the contact point towards a steeper position until a lead break occurs.

When an H-N source is generated at a distance of 25mm from the central axis of properly mounted AE sensor, a hit of 98 to 100 dB amplitude will be picked up by the AE sensor and recorded by the acquisition system. Therefore, the AE sensor sensitivity after sensor mounting can be assessed by generating an H-N source close to the AE sensor. This method has been used in this research to verify the correct mounting of AE sensors. AE sensors will be removed and re-mounted if hits with amplitude below 98 dB are recorded during sensor sensitivity check.

2.1.4 Wave propagation mode

The wave propagation between an AE source and an AE sensor can alter the shape and size of an AE signal significantly. Therefore, it is important to have a good understanding of the wave propagation process. As some safety-critical equipment, e.g., pipes and pressure vessels can be regarded as a plate, the focus of this study is on classical plate wave propagation [33].

Wave propagation in a solid is a complicated problem. The detailed accounts of this problem can be found in the work of Rindorf [34] and Gorman and Prosser [35]. In an infinite solid medium, there are two possible types of elastic waves; longitudinal (pressure) and transverse (shear) waves. Longitudinal waves show localised compression and rarefaction and their particle motion is parallel to the direction of wave travel. In contrast, particles in transverse waves move at right angles to the propagation direction [36]. An example of the motion of longitudinal and transverse waves are shown in Figure 2.3.

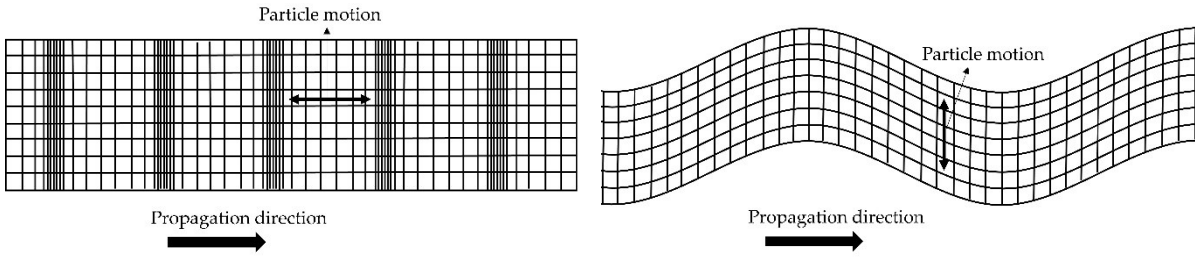

Figure 2.3– Two modes of bulk waves which exist in an infinite solid; (a) longitudinal wave and (b) transverse wave.

With the introduction of a surface, the combination of longitudinal and transverse waves give rise to Rayleigh waves, which travel along the surface of thick materials. The particle motion in Rayleigh waves is elliptical [37].

When two parallel surfaces are introduced in a medium, as in a plate, Lamb waves are formed as a combination of the longitudinal and transverse waves. There are two types of Lamb

waves, i.e., the symmetric and the anti-symmetric Lamb wave, which independently propagate along the surface. The characteristic equation for symmetric wave modes [38] is:

$$\frac{\tan(qh)}{\tan(ph)} = \frac{-4k^2pq}{(q^2-k^2)^2} \tag{2.1}$$

And for anti-symmetric wave modes:

$$\frac{\tan(qh)}{\tan(ph)} = \frac{-(q^2-k^2)^2}{4k^2pq} \tag{2.2}$$

in which:

$$p^2 = \left(\frac{\omega^2}{{c_L}^2} - k^2\right)$$
$$q^2 = \left(\frac{\omega^2}{{c_T}^2} - k^2\right) \tag{2.3}$$

k Wave number

ω Circular frequency

h Plate half-thickness

c_L Longitudinal wave velocity

c_T Transverse wave velocity

By calculating the solution of Equation (2.1) and (2.2), the precise form of particle motion in symmetric and anti-symmetric modes can be found. A family of waves, whose motion is symmetrical about the median plane of the plate was produced by Equation (2.1), while a family of waves whose motion is anti-symmetric about the median plane was produced by Equation (2.2) [39]. Among all the members in the two families of Lamb waves, two major Lamb wave modes are symmetrical zero-order (S_0, or extensional) and antisymmetric zero-order (A_0, or flexural) modes. It is possible for the higher order waves to develop with correct

geometric conditions. However higher order modes tend to have lower amplitude and carry considerably less energy than zero-order modes. Therefore, they are not widely used in AE monitoring [40].

A simplified graphic of propagation of S_0 and A_0 Lamb wave modes is shown in Figure 2.4. The movements of particles which are represented schematically by the ellipses are mainly parallel to the plate for S_0 mode and perpendicular to the plate for the A_0 mode [33].

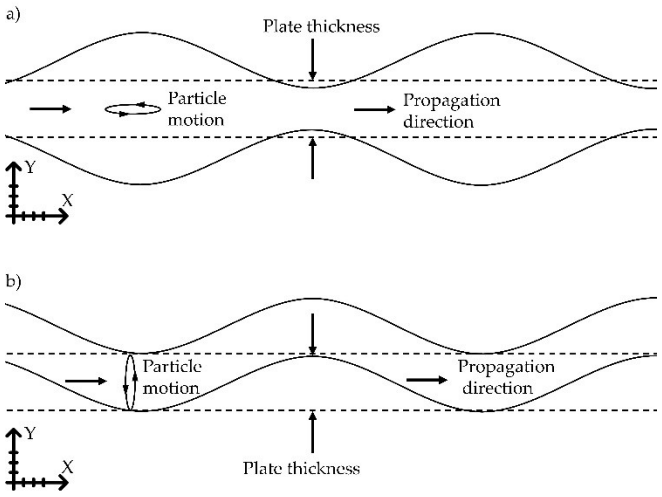

Figure 2.4– Propagation of S_0 (a) and A_0 (b) Lamb wave modes.

The behaviour of a Lamb wave is very complex because the velocities of the wave modes show a strong dependency on the frequency content and the plate thickness. For a specific geometry, the velocity of a wave is dependent on its frequency. This phenomenon is known as the dispersion [34]. With a known plate thickness, the relationship between the wave velocity and the frequency of each mode can be described by a set of curves known as the dispersion curves [41]. The dispersion linked with each wave mode can be observed in these curves.

In this study, the dispersion curves of Lamb waves in a thin plate were calculated, drawn and exported using a program called Vallen Dispersion[42]. The velocities of all the possible wave modes against their frequency content in a plate were calculated based on longitudinal and transversal velocities and the plate thickness. Figure 2.5 shows an example of calculated dispersion curves for steel (thickness=3 mm). In the diagram, each individual curve

represents the group velocity curve of a specific mode in a frequency range from 0 to 3 MHz (horizontally). As seen in the diagram, the propagation velocities of different frequency components of each mode vary, and there might be multiple Lamb wave modes at a given frequency component.

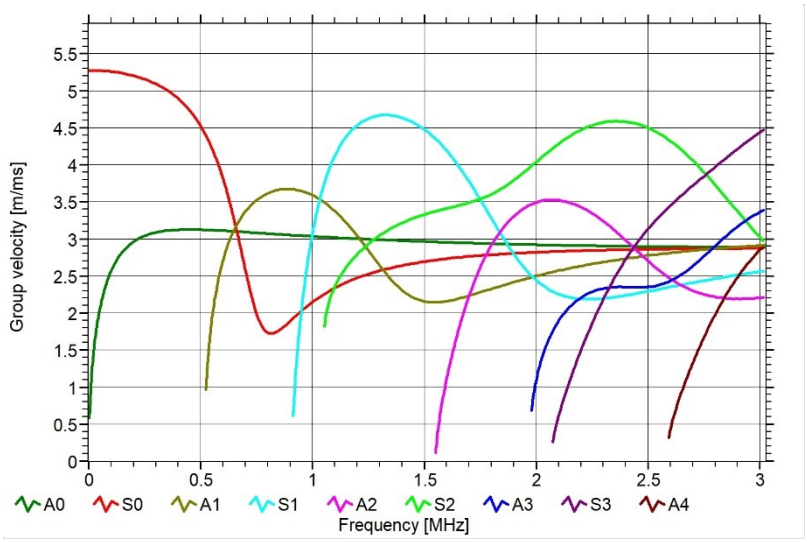

Figure 2.5– Dispersion curves for steel (thickness=3 mm) calculated by Vallen Dispersion

2.1.5 Wave attenuation

The loss of amplitude occurs when AE waves propagate within a medium. This phenomenon is a part of wave propagation and known as wave attenuation [43]. As the AE signals recorded from experiments are significantly influenced by the wave attenuation, it is necessary to have a good understanding of wave attenuation before processing and analysing AE signals.

According to Rindorf [34] and Pollock [44], four main factors contributing to wave attenuation are geometric spreading, energy absorption, wave dispersion and dissipation of acoustic energy into adjacent media. The details of these causes are given below.

Geometric spreading is a large contributor to wave attenuation and leads to a considerable amplitude decrease. When a wave is spreading out in all directions, the energy of the wave are redistributed over a larger and larger wave-front. This redistribution of energy at the wave-front results in a reduced amplitude of wave. For a bulk wave which exists in an

infinite solid, the amplitude of a signal decreases in inverse proportion to the distance of propagation. For wave propagation in two-dimensional plate-like structures, such as Lamb wave, the amplitude of a signal decreases in inverse proportion to the square root of the distance of propagation [43].

The energy absorption, which is the conversion of the elastic and kinetic wave energy to thermal energy through multiple material-dependant mechanisms, may affect the wave attenuation. The energy absorption has a much greater effect on the wave propagation in non-metallic materials such as composite than that in metals. This absorption mechanism usually depends on the frequency of a signal; a wave with higher frequencies experiences greater attenuation than that with lower frequencies.

Attenuation occurs due to dissipation of energy into surrounding media. Wherever a wave incident on a boundary between two different, some of energy crosses the boundary and is lost.

Attenuation may be affected by wave dispersion when Lamb waves propagate in a plate like structural component. As described in Section 2.1.4, the wave dispersion is the phenomena whereby the energy of a wave will spread out as the wave propagates, resulting a longer wave-front and a reduced peak amplitude. The rate of wave attenuation caused by dispersion are associated with the bandwidth of a signal and gradient of the dispersion curve.

2.1.6 AE modes

AE signals can be normally characterised as continuous or burst. The type of emission recorded is related to the source mechanism. A distinction between the two types was firstly given by Kaiser [17] in his pioneering work on AE.

2.1.6.1 Continuous emission

For continuous emission, waves are continually captured with no stop [45]. As shown in Figure 2.6, there are fluctuations in the amplitude of continuous waves, but no visually obvious features can be observed. Continuous emission is produced when mechanisms such as surface friction, fluid flow and machine vibrations occur and typically have the feature of

low energy. However, a very likely source of a continuous emission is the mechanical noise from the environment. The conditions of operating machines, such as bearings and gears, can be continually monitored for continuous emission, while the source location are very difficult to determine.

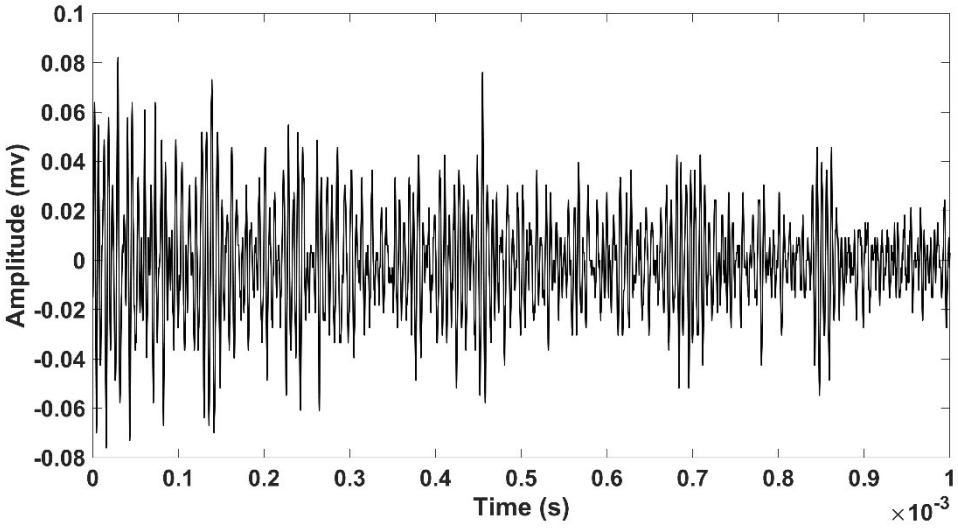

Figure 2.6– An example of a continuous emission recorded from a corrosion test

2.1.6.2 Burst emissions

Compared with a continuous emission, signal characteristics of an example of a burst emission, shown in Figure 2.7, are very different. A burst emission appear like damped oscillation with clear start and end points. They have definite peaks with notably larger amplitude than the background noise and hence they are less likely to be hidden within the noise level than a continuous emission. The duration of such burst signal is usually less than a few hundredths of a second. In general, the source of a burst emission are transient damage degradation processes, such as crack propagation and corrosion.

Burst type events are believed to be more suitable to be used in most techniques of AE [46]. Therefore, some commonly used parameter which are used to describe a burst type emission are addressed in the following Section 2.1.7.

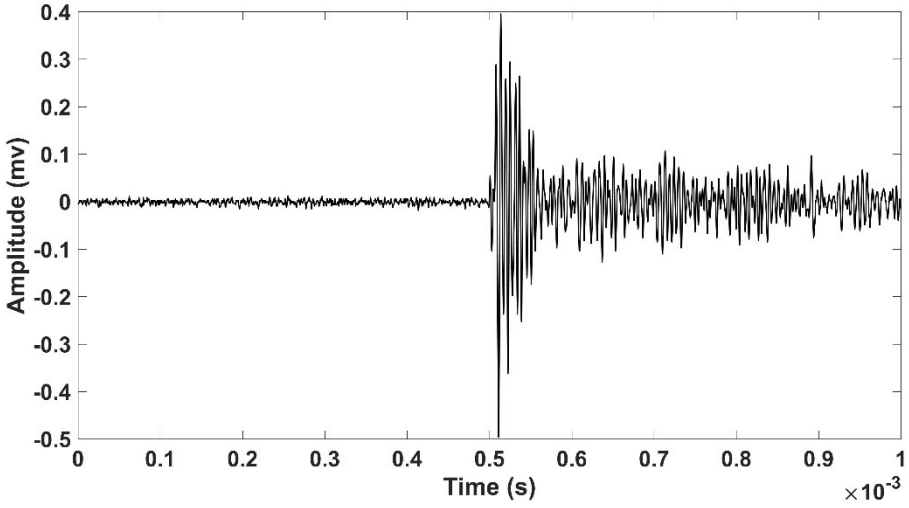

Figure 2.7– An example of a burst emission recorded from H-N sources

2.1.7 AE signal features

Amplitude, duration, rise time, Measured Area under the Rectified Signal Envelope (MARSE) energy, and threshold-crossing count are five major features extracted from a single typical burst AE wave [47].

Amplitude (A)

Amplitude is the maximum voltage in a waveform and is measured in decibels (dB).

Duration (D)

Duration refers to the time period between the first and last threshold crossings.

Rise time (R)

Rise time is the time interval between the rising edge of the first count and the signal peak.

MARSE energy (E)

MARSE is defined as the measure area under the envelope of the linear time voltage signal.

Threshold-crossing count (N)

Threshold-crossing count is defined as the number of times the signal rises and exceeds the threshold.

Besides above-mentioned parameters, there are some other useful parameters such as absolute energy and average signal level. Other parameters like average frequency (equals to counts divided by duration), initiation frequency and reverberation frequency [47] can be used to show the characterisation of the frequency of different parts of the single AE hit. The average frequency over the entire duration of an AE hit can be reflected by the value of the average frequency.

2.2 Modal acoustic emission

In conventional AE analysis, researchers mainly utilise simple signal measurement parameters such as amplitude, counts and energy, and largely ignore the application of plate wave theory to the analysis of AE signals. As a supplement to the conventional technique, the dispersive behaviour of Lamb wave propagation can be exploited to give rise to an enhanced understanding of the arrival of multiple symmetric and asymmetric Lamb wave modes, which is known as Modal Acoustic Emission (MAE) or plate wave AE.

The relationship between the S_0 and A_0 modes, which can be determined by performing MAE, has led to a method to determine the source orientation. In 1991, Gorman [36] performed H-N sources on both an aluminium and a composite plate and firstly demonstrated how to recognise two basic modes, i.e. S_0 and A_0 wave modes in AE signals. It was observed that the frequency contents and dispersion characteristics of the S_0 mode were significantly different from those of the A_0 mode. Further to this, a more in-depth study was undertaken by Gorman and Prosser [35]. Slots were machined into the aluminium plate at the respective angles and H-N sources were conducted at these slots to investigate the influence of the AE source orientation angle on amplitudes of S_0 and A_0 wave modes. A relationship was found to exist between amplitudes of both modes and orientation angles of AE sources based on the analytical results. Later, the amplitude of the S_0 and A_0 modes were further examined by

Carter [48]. H-N sources were performed in an 8mm steel I-beam. The ratio of the S_0 mode amplitude over the A_0 mode amplitude, or the Measured Amplitude Ratio (MAR) was calculate by Carter [48] using the Equation (2.4).

$$MAR\ \% = \text{Amplitude}\ (S_0)/\text{Amplitude}\ (A_0) * 100 \tag{2.4}$$

The results indicated that the H-N sources with different orientations in a steel I-beam can be discriminated by analysing the MAR of signals. Similarly, Pullin et al.[49] found that MAR of AE signals can be used to discriminate between H-N sources in plane and normal to the sensor face plane. Based on the analytical results of the MAR of signals recorded in a four point bending test indicated that the AE source in the test was out of plane to the sensor.

Another use of MAE is the determination of the source to sensor distance by finding temporal separation between S_0 and A_0 modes and their velocities as shown in Equation (2.5), which is called single sensor modal analysis (SSMA). An early application using this method can be found in [50] where a method of manual SSMA was utilised by Sachse and Sancar. As mentioned by Gorman [36] that the frequency contents and dispersion characteristics of the S_0 mode were significantly different from those of the A_0 mode, band-pass filtering techniques were used by Maji et al. [51], Dunegan [52] and Holford and Carter [53] to separate S_0 and A_0 modes, thus calculating the source to sensor distance using SSMA method. Later, SSMA method was examined on AE signals generated from a fatigue crack source by Pullin et al. [49]. Results showed that the estimation of a fatigue crack source to a sensor distance using SSMA was reasonably accurate.

$$D = \Delta t * (C_{S_0} * C_{A_0})/(C_{S_0} - C_{A_0}) \tag{2.5}$$

where:

D The source to sensor distance

Δt Arrival time differences between S_0 and A_0 modes

C_{S_0} Velocity of the S_0 mode

C_{A_0} Velocity of the A_0 mode

However, it should be noted that there are some limitations with the use of MAE. Since AE signals might be substantially affected by multiple wave propagation effects such as reflections, attenuation, mode conversions or dispersion, it can be very difficult to recognize two fundamental Lamb wave modes in AE signals, thus resulting in huge errors in estimation of the arrival time difference between S_0 and A_0 modes [54].

2.3 Wavelet transform

A wavelet transform is formulated on the same mathematical principles as the Fourier transform and displays time-frequency distributions of a signal. Unlike Fourier transform which only displays global frequency spectra over an entire signal without time information, a wavelet transform gives both local spectral details and temporal information [55].

The Continuous Wavelet Transform (CWT) is a linear transformation that decomposes signals through a set of dilated and translated parent wavelets by continuous convolution of the signal and shifting and scaling a parent wavelet. The CWT of function $f(t)$ can be written as:

$$WT(a,b) = \frac{1}{\sqrt{|a|}} \int_{-\infty}^{\infty} f(t)\psi^* \left(\frac{t-b}{a}\right) dt \tag{2.6}$$

where:

$\psi^*(t)$ The complex conjugation of the mother wavelet $\psi(t)$

a The scale of the mother wavelet

b The shift of the mother wavelet

The analysis function for CWT is defined as:

$$\psi_{a,b}(\mathrm{t}) = \frac{1}{\sqrt{|a|}}\psi(\frac{t-b}{a}) \tag{2.7}$$

$\psi_{a,b}(\mathrm{t})$ is generated by dilatations and translation of a mother wavelet $\psi(t)$. It is centered at b in time domain with a support width proportional to b. Requirement for the mother wavelet is to satisfy the following admissibility condition;

$$\int_{-\infty}^{\infty} \frac{|\hat{\psi}(\omega)|^2}{|\omega|} d\omega < \infty \tag{2.8}$$

The Gabor function was chosen as the mother wavelet in this study because a higher time and frequency resolution can be provided by Gabor function compared with any other wavelets [56]. This function is defined as:

$$\phi_g(t) = \frac{1}{\sqrt[4]{\pi}}\sqrt{\frac{\omega_0}{\gamma}}\exp[-\frac{(\omega_0/\gamma)^2}{2}t^2]\exp(i\omega_0 t) \tag{2.9}$$

The Fourier transform of Gabor function is defined as:

$$\hat{\phi}_g(\omega) = \frac{\sqrt{2\pi}}{\sqrt[4]{\pi}}\sqrt{\frac{\gamma}{\omega_0}}\exp[-\frac{(\gamma/\omega_0)^2}{2}(\omega-\omega_0)^2] \tag{2.10}$$

where:

ω_0 Positive constants

γ Positive constants

The 'AGU-Vallen Wavelet' software was employed to carry out all the wavelet transform analysis in this thesis. It is a freeware program developed by Vallen Systeme GmbH and Aoyama Gakuin University. Colour plots of the wavelet transform coefficient in time-frequency domain are produced by the software after the wavelet transform analysis. A typical two-dimensional wavelet transform diagram is given in Figure 2.8. Unlike a fast Fourier transform (FFT), the wavelet transform coefficients against time and frequency can

be viewed simultaneously in this diagram. The horizontal axis of the diagram is a measure of time and the vertical axis stands for the frequency range. The colour contour represents the wavelet transform coefficients of the signals with the highest coefficient region in red and smallest coefficient region in pink.

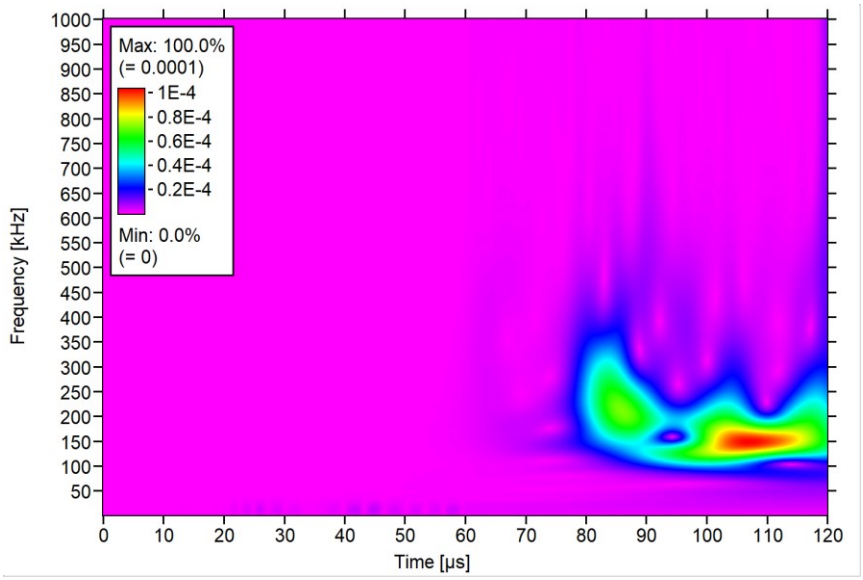

Figure 2.8– A typical two-dimensional wavelet transform diagram calculated by wavelet software

A wavelet coefficient plot shows the strength of the signal at a certain signal frequency. An example is presented in Figure 2.9, where the 150 kHz frequency is shown. The vertical axis of the plot stands for the wavelet coefficient value and the horizontal axis is the time domain of the signal.

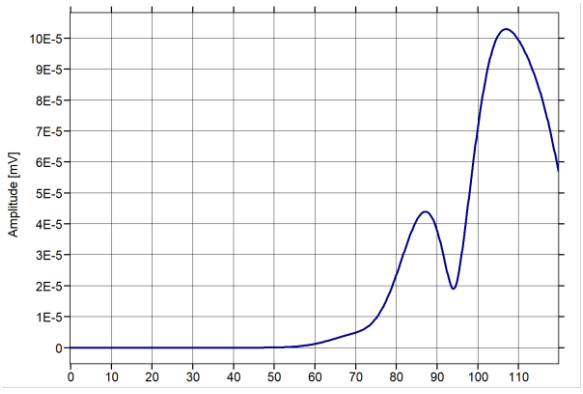

Figure 2.9– An example of a wavelet coefficient plot with 150 kHz frequency

By overlapping the calculated dispersion curves in Section 2.1.4 with wavelet transform diagram, the oncoming wave modes can be clearly distinguished. An example of a wavelet transform diagram overlaid by a dispersion curve was shown in Figure 2.10.

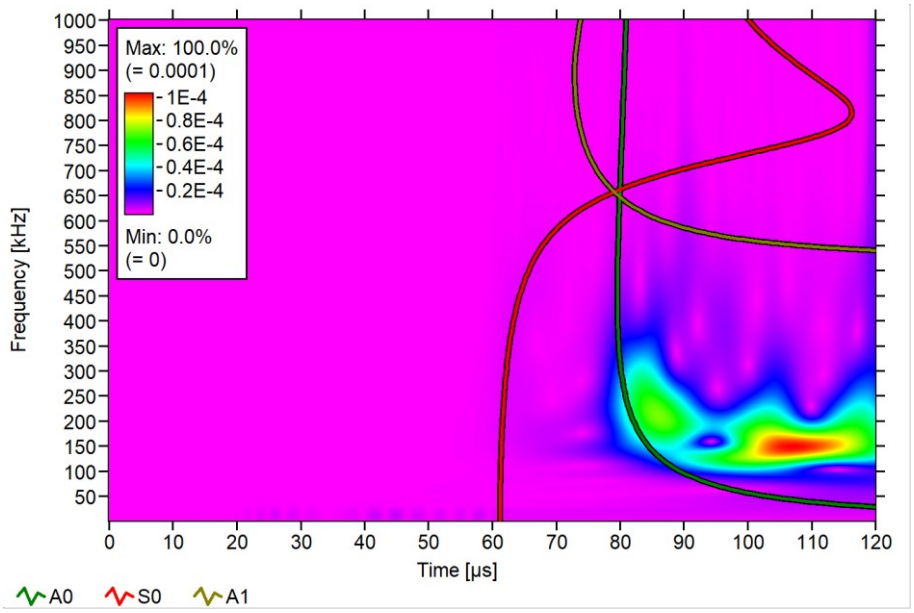

Figure 2.10– An example of a wavelet transform diagram overlaid by a dispersion curve

For identification of the arrival time, consider two harmonic waves of the same unit amplitude and with slightly different frequencies ω_1 and ω_2 traveling in X-direction [56];

$$u(x,t) = e^{-i(k_1 x - \omega_1 t)} + e^{-i(k_2 x - \omega_2 t)} \tag{2.11}$$

where:

k_i The wave numbers corresponding to the frequency ω_i

Introducing:

$$(k_1 + k_2)/2 = k_c$$
$$(k_1 - k_2)/2 = \Delta k \tag{2.12}$$

$$(\omega_1 + \omega_2)/2 = \omega_c \tag{2.13}$$

$$(\omega_1 - \omega_2)/2 = \Delta\omega$$

Equation (2.11) becomes:

$$u(x,t) = 2\cos(\Delta kx - \Delta\omega t)\, e^{-i(k_c x - \omega_c t)} \tag{2.14}$$

As seen in Equation (2.14), the resulting wave consists of two parts i.e. the carrier (the exponential term $e^{-i(k_c x - \omega_c t)}$) and the modulation (the cosine term $\cos(\Delta kx - \Delta\omega t)$). The former travels with the phase velocity $c_p = \omega_c/k_c$, whilst the latter propagate with group velocity $c_g = d\omega/d$ in the limit $\Delta k \to 0$. Substituting Equation (2.14) in Equation (2.6) using the Gabor wavelet (Equation (2.9)), the WT magnitude of $u(x,t)$ can be written as:

$$\begin{aligned} |WT_u(x,a,b)| = \sqrt{a}\Big\{&\left[\hat{\psi}_g(a\omega_1)\right]^2 \\ &+ \left[\hat{\psi}_g(a\omega_2)\right]^2 + 2\hat{\psi}_g(a\omega_1)\hat{\psi}_g(a\omega_2)\cos(2\Delta kx - 2\Delta\omega b)\Big\}^{1/2} \end{aligned} \tag{2.15}$$

If $\Delta\omega$ is sufficiently small such that $\hat{\psi}_g(a\omega_1) \approx \hat{\psi}_g(a\omega_2) \approx \hat{\psi}_g(a\omega_c)$, Equation (2.14) can be written as:

$$|WT_u(x,a,b)| = \sqrt{2a}|\hat{\psi}_g(a\omega_1)|[1 + \cos(2\Delta kx - 2\Delta\omega b)]^{1/2} \tag{2.16}$$

Equation (2.16) shows the largest value of the WT magnitude locates at $a = \omega_0/\omega_g$ and $b = \left(\frac{\Delta k}{\Delta\omega}\right)x = x/c_g$. This location on the (a, b) plane can be used to identify the arrival time of the group velocity c_g at the frequency $\omega_c = \omega_0/a$ i.e. $f = 1/a$.

2.4 Arrival time determination

2.4.1 Introduction

One of the critical aspects of AE-based monitoring is the determination of the arrival time of the AE signals. Accurate determination of arrival time of signals plays a key role in the data

analysis and results interpretation. In this section, several commonly utilized methods for estimating AE arrival times of AE signals were discussed below.

2.4.2 Akaike Information Criterion (AIC)

AIC was a statistical method, which was developed by Akaike [57] to select statistical model in 1974. A decade later, AIC calculation was further developed by Maeda [58] to be applied to a raw transient signal for automatic determination of the onset time. In 2005, two auto-pickers which were based on Hinkley criterion [59] and AIC respectively were adopted and studied by Kurz et al. [60] in order to achieve reliable and automatic onset detection. It was concluded that a considerably better result was achieved by AIC picker than Hinkley picker. The following form of AIC was developed by Maeda [58].

$$AIC_t = t \log_{10}(Var(x[1;t])) + (T - t - 1) \log_{10}(Var(x[t;T])) \quad (2.17)$$

where:

$Var(x)$ The variance of x

$x[1;t]$ x data from time 0 to t

T The end of data set

$x[t;T]$ x data from time t to T

The signal is divided into two part in this function; the first one is from time 0 to time t and the second one is from time t to time T. For a specific time t, the variances of the first part of and second part of the segmented signal are calculated to measure the similarity in entropy between two parts. By increasing the value of time t gradually, the value of AIC_t through the entire signal can be calculated. In an AE waveform, the region of noise before the signal onset has the feature of very little structure which results in high entropy. In contrast to the noise, the region of signal shows substantially higher structure which leads to low entropy. Therefore, the minimum value of AIC_t, i.e. minimum similarity in entropy will be observed when the time t equals to the arrival time of the signal.

The AIC method has several advantages over other arrival time determination methods, including its ability to handle non-Gaussian noise and its flexibility in dealing with waveform distortions. However, it can be computationally intensive and requires careful selection of the candidate arrival times.

2.4.3 Cross-correlation Method

The cross-correlation method is usually utilized to measure the extent of similarity or correlation between two signals [61]. In AE testing, cross-correlation is typically performed on the waveform data acquired from multiple sensors. Due to differences in distance and location to the AE source between sensors, the arrival times of AE signals recorded from the same source can vary slightly. By applying cross-correlation method on the waveform data from each sensor, the time delay between the AE signal at each sensor can be determined.

For discretized AE signals, the correlation between the measured signal $x(n)$ and a reference signal $y(n)$ with the same N samples length can be expressed by the following equations.

$$r_{xy}(l) = \frac{1}{N} \sum_{n=-\infty}^{\infty} x(n) \cdot y(n+l), l = 0, \pm 1, \pm 2 \dots N-1 \tag{2.18}$$

where:

l index l is considered to be the time lag

The time delay between two signals corresponds to the maximum value of r_{xy}.

The cross-correlation method is widely used in AE testing because of its robustness and reliability. It only requires basic mathematical operations, thus being simple to implement. However, the accuracy of the predicted arrival time relies on the selected reference signal in the cross-correlation analysis. In addition, another disadvantage of using cross-correlation method is that it can be sensitive to noise or other types of interference, which can lead to inaccuracy arrival time of signals.

2.4.4 Wavelet Transform (WT)

The WT is a mathematical tool that has been widely used for the analysis and processing of AE signals. In particular, the WT has been used for the determination of the arrival time of AE signals. This is discussed in detail in Chapter 4.

2.5 AE source location

2.5.1 Introduction

During AE testing, elastic waves emitted from a source propagates through the structure and arrives at each sensor. If this signal crosses a predetermined threshold, the AE system will record this time. As the arrival time at each sensor is recorded, AE sources can be located. Source localisation is an essential tool in AE analysis. If locations of AE events are known, grouping of events can be used to identify hot spots and filter bad data. Source localisation is also considered to be one of the key problems in the AE monitoring as the precision of source location will greatly influence the application of AE monitoring. Since a location algorithm will affect the accuracy of AE location, it should be selected carefully to meet monitoring requirements and improve the location accuracy.

In the 20th century, various classical source localization methods were proposed, including iterative method (e.g. Geiger method [62], Thueber method [63] and simplex method [64]) and non-iterative method (e.g. Inglada method [65], US Bureau of Mines method [66,67]). In these classical methods, it is assumed that AE waves travel in a straight line from AE source to sensors and the wave velocity is constant in each direction, creating a circular wave front However, due to the nature of composites, the velocity of the S_0 mode is known to be greater in the direction of fibres than in off-fibre directions [68]. Thus, Paget et al. [69] developed a method of considering the wave front as elliptical, i.e. higher velocities in one direction than another, which was shown to work well in composites.

Much effort have been devoted to improve source localization accuracy. A novel analytical method for the three-dimensional (3D) location of AE sources under a cube monitoring

network with five sensors was proposed by Dong et al. [70]. Equations for localizing AE sources were established and a set of analytical solutions were obtained. Since the proposed method is non-iterative and only requires simple mathematical calculations, convergence problems are eliminated and the live application of this method on the measurement system is possible. The results showed that the proposed solution can achieve high accuracy in source location. However, the issue with this method is that it requires a known wave velocity, which makes it challenging to use in scenarios involving anisotropic materials. In such cases, where velocities are not constant and difficult to measure, the method's effectiveness is compromised. Therefore, to address this issue, analytical solutions were optimized by Dong et al. [71] using five sensors and multiple networks. A notable advantage of this updated method was that the pre-measured velocity was not required. Later, WT and cross-time frequency spectrum were combined by Mostafapour et al. [72] to identify the source of AE in plate-like structures. A signal packet with a frequency range of 0.125-0.25 MHz was selected using wavelet packet decomposition. Afterwards, cross-time frequency spectrum was calculated using the short-time Fourier transform of the cross-correlation between selected signal packets. The time delay corresponded to the peak value of cross-time frequency spectrum. Subsequently, the corresponding frequency at this peak was extracted. Finally, the group velocity of wave velocity at the resulting frequency was determined using the dispersion curve. The proposed algorithm was tested using an artificial AE source (such as PLB) and the location results show a high degree of precision.

With the development of the AE technique, more AE source location methods were proposed by researchers. Since AE source location is very difficult in complex structures, much effort has been devoted to the development of source localisation in complex structures. To localise AE sources in structures where a direct propagation path is blocked, a correlation operator was proposed by Ing et al. [73] and Park et al. [74] to measures the similarity between two AE events using the concept of time-reversal. The correlation between a real AE event and a set of artificial AE sources was assessed and the artificial AE source that returned the highest similarity corresponded to the location of the real source. Later, delta-T source location was proposed by Baxter [40]. The technique requires the structure to be mapped by performing the Hsu-Nielsen (H-N) sources [31] and evaluating the difference of arrival times at the sensor pairs to estimate the source location. Real test data can then be located using these

maps. This technique has been shown to improve AE source location accuracy in complex structures [75–79].

In 2012, an approach similar to time-reversal was implemented by Ciampa and Meo [80] for AE source localisation in complex geometries. By ensuring a diffused wavefield, it is possible localize an impact event with only a single sensor. Similarly, a single-sensor approach was also used by Ebrahimkhanlou and Salamone [81]. In this approach, deep neural networks were trained to map a recorded AE waveform to a source location. Although the results were promising, the neural network's outputs were limited to providing deterministic source location estimates, and therefore did not provide a metric to quantify the level of confidence in the predictions. Later, Hensman et al. [82] utilised Gaussian process regression, which is Bayesian non-parametric method, to describe all source location parameters as posterior probability density functions. The locations of AE sources were predicted by directly learning an inverse mapping from the difference in time-of-flight to the source's location. In each prediction, it was associated with a level of uncertainty. Following that, Jones et al. [83] extended the use of Gaussian process regression and a new approach was proposed for identifying the location of AE sources in complex structures. In contrast to the method proposed by Hensman et al. [82], it involved a forward-model solution, where the source coordinates are mapped to difference-in-time-of-arrival values. With a difference in time-of-flight measurement, the likelihood of source locations across the structure's surface were assessed and a mapping in which the predicted source locations were associated with a level of probability was generated. Recently, A* Location Method (ALM) was proposed by Hu and Dong [84]. In ALM, a grid node model representing the specimen shape is built using node matrix with digits 0 or 1. The travel path of an AE wave between a source and a sensor, which is the shortest, is found in the grid node model using A* search algorithm. The pencil lead test results indicate that the location error on complex structure with circular or square holes can be reduced effectively by using ALM.

For delta-T method, there is no need to take the influence of geometry and wave velocity on source location into account, while it will be quite costly in terms of time and labour as both methods require considerable amount of training and calculation. This means that both

methods might be only suitable for examining key areas of interest. When it comes to monitoring the global structure, the classical method will be a better choice.

2.5.2 Time of Arrival technique

The traditional and most commonly used source localisation method within the field of AE is the Time of Arrival (TOA) technique. This most established technique has been built into all commercially available AE systems as default source location method. A more detailed explanation of this technique can be found in the work by Miller and Mclntire [43] and Rindorf [34].

2.5.2.1 One-dimensional source location

An example of linear source location shown in Figure 2.11 is used to introduce the one-dimensional TOA location methodology in a simple way. An array of three sensors is instrumented along the beam. AE waves emitted from AE source propagate in both directions. The zonal location is considered to be the most basic way to locate the AE source. In this method, the order in which AE waves reach each sensor is examined. As presented in Figure 2.11 a, the first sensor hit is sensor 2 and therefore the expected range of source location is from the midpoint of sensor 1 and 2 to the midpoint of sensor 2 and 3. If the second sensor hit is considered, a source location area with higher accuracy can be defined. As shown in Figure 2.11 b, the second sensor hit is sensor 1 and therefore the source location area can be further refined and reduced to the range from the midpoint of sensor 1 and 2 to sensor 2. A more accurate source location can be determined with known time arrival differences between sensors. As shown in Figure 2.11 c, if the sensor 2 is the first hit sensor and sensor 1 is the second, the time difference between sensor 1 and sensor 2 can be written as the following equation;

$$\Delta t = (d_2 - d_1)/C_{\mathrm{AE}} \tag{2.19}$$

where:

C_{AE} Calculated wave velocity

Δt Time difference between sensors

d_1 Distances from the source to first hit sensor

d_2 Distances from the source to second hit sensor

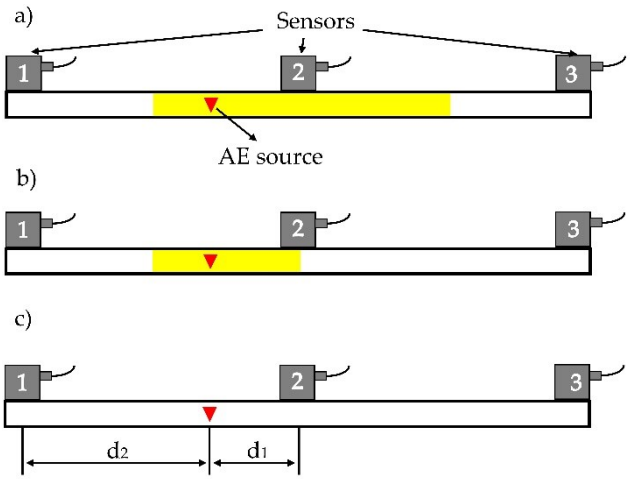

Figure 2.11– TOA linear source location; a) zonal location for first hit at sensor 2, b) zonal location for first hit at sensor 2 and second hit at sensor 1, c) hit sequence and arrival time difference measurement.

2.5.2.2 Two-dimensional source location

The same technique can be expanded to two-dimensional source location. As shown in the Figure 2.12, two sensors (sensor 1 and sensor 2) are located d apart and placed on an infinite plate. Based on the assumptions that the propagation speed of a stress wave generated from an event is constant in all directions, the following equations can be found [43];

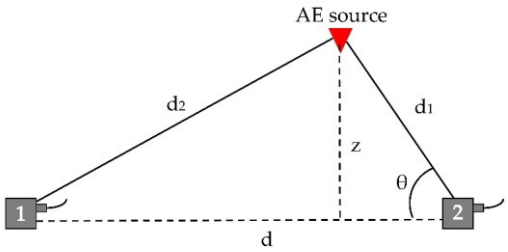

Figure 2.12– Two-dimensional source location with two sensors

$$\Delta t C_{AE} = d_2 - d_1 \tag{2.20}$$

And

$$z = d_1 \sin\theta \tag{2.21}$$

$$z^2 = {d_2}^2 - (d - d_1 \cos\theta)^2 \tag{2.22}$$

Then

$${d_1}^2 \sin^2\theta = {d_2}^2 - (d - d_1 \cos\theta)^2 \tag{2.23}$$

$${d_1}^2 = {d_2}^2 - d^2 + 2d \cdot d_1 \cos\theta \tag{2.24}$$

Substituting d_2 from Equation (2.20) into Equation (2.24) gives:

$$d_1 = \frac{1}{2} \cdot \left(\frac{d^2 - \Delta t^2 C_{AE}^2}{\Delta t C_{\mathrm{AE}} + d \cos\theta} \right) \tag{2.25}$$

Using the given hit sequence and arrival time difference from two sensors, this equation for a hyperbola (Hyperbola 1-2 in Figure 2.13) describes all the potential locations of the source. However, the information is not sufficient to provide one definitive position. The source location with higher accuracy can be reached with a third sensor (sensor 3 in Figure 2.13). A second (1-3) and third hyperbolas (2-3) can be effectively created as shown in Figure 2.13. A more accurate position of the source is given by the intersection of the three hyperbolas. The number of hyperbola will be increased by adding further sensors into the sensor array and therefore the accuracy of source location will be improved.

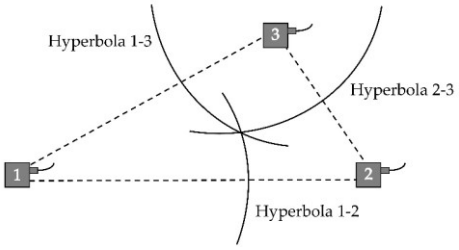

Figure 2.13– Two-dimensional source location with three sensors

Although TOA location technique is a traditional and widely used source location method, the likely source of errors cannot be ignored. The potential errors [41] associated with TOA are summarized and listed as following. A thorough explanation of possible sources of error in this technique can be found in the work by Miller and Mclntire [43] and Rindorf [34].

• Triggering errors. In AE instrumentation, if the amplitude of a signal crosses a pre-set threshold, the arrival timing will be triggered and an AE hit will be recorded. Then the arrival time differences between sensors can be calculated. Typically, the triggering of timing measurement is dependent on the arrival of the extensional mode. Due to wave attenuation, extensional components may have a lower amplitude than pre-set threshold after travelling a considerable distance. This can cause a triggering of different temporal points of the signal. These inaccurate triggering can result in erroneous arrival time differences between sensors and hence incorrect location results. This error can also be found when using AE techniques to record signals with low signal-to-noise ratio. In these AE applications, in order to exclude the background noise, the pre-set threshold is defined with a sufficiently large value. However, the amplitude of the extensional mode components may fail to cross the high threshold at correct point of a signal or even fail to trigger a recording.

• Effect of dispersion. Because of the effect of wave dispersion, the waveform of a signal changes during wave propagation within the structure. These alterations can result in an AE hit detected at different phase points in its arrival.

• The assumption of constant wave velocity and direct wave path. The main assumptions made for TOA techniques are uniform wave speed in the test structure and straight wave path between the AE source and sensor. However, due to the inhomogeneity of some materials such as composites, wave velocities may vary in different directions. Furthermore, the complexity of the real life structures means that a direct wave path may be very difficult to be achieved during AE monitoring. The wave propagation route from the source to the sensor can be influenced by geometric features including stiffeners, holes and thickness change. The irregular wave speeds or indirect wave paths mean that hyperbola equation which describes the possible source locations is no longer correct and hence source locations are not accurate.

2.5.3 Delta-T Mapping technique

As discussed above, the main assumptions made for traditional TOA source location techniques are constant wave speed in the test structure and straight wave paths between an AE source and sensors. However, due to the inhomogeneity of some materials such as composites, wave velocities may vary in different directions. Furthermore, the complexity of the real structures means that a direct wave path may be very difficult to be achieved during AE monitoring.

Therefore, in order to overcome the aforementioned two major assumptions, a methodology called delta-T mapping source location technique was developed by Baxter et al. [75]. Due to the good performance of this technique, it has been adopted in further lab-based studies by Eaton et al. [68], Pearson et al. [76] and Grigg et al. [77]. According to a detailed description of delta-T mapping technique found in Baxter et al. [75], the five procedural steps of implementing this technique are shown in Figure 2.14 and provided below;

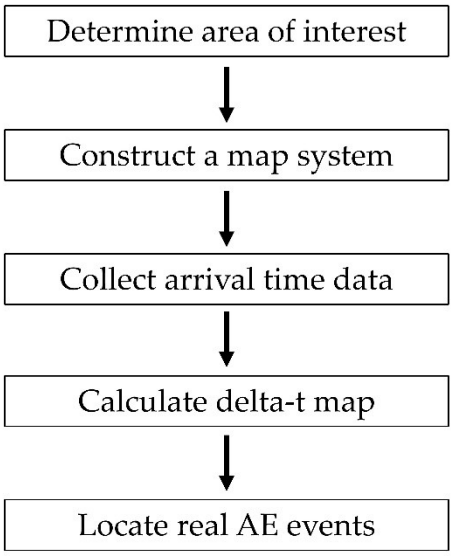

Figure 2.14– Five procedural steps of implementing delta-T technique [75]

• Determine area of interest. Though delta-T mapping technique can offer the ability to provide complete coverage of an entire structure, it is the best to utilize this technique over an area with special interest such as damage susceptible area because ahead of the start of the

testing, the data collection process on the test structure required by delta-T mapping is time consuming. FE modelling can be used to identify those areas of interest due to high stress.

• Construct a map System. After an area of interest is defined, a training grid is placed on this area. The AE events within this area can be located. The location accuracy can be improved with the increasingly high resolution of the grid, while the grid resolution should not be smaller than one wavelength because this is the minimum location resolution [75]. As the reference used in delta-T mapping technique is the training grid rather than sensor locations used in traditional TOA method, there is no need to place AE sensors within the grid and know the sensor positions.

• Collect arrival time data. The generation of artificial AE sources (nominally H-N sources) at each node of the grids can provide data for each sensor. To reduce erroneous data and provide a reliable average result, five sources at each node are considered to be adequate according to practical work [75]. It is acceptable to have some missing data points due to holes on the area because those points can be interpolated from adjacent nodes.

• Calculate delta-T map. The arrival time difference or delta-T can be calculated for each sensor pair using the time arrival information recorded at each sensor after the generation of an H-N source. If four sensors (1, 2, 3 and 4) are used in the tests, there will be six sensor pairs (i.e., 1-2, 1-3, 1-4, 2-3, 2-4 and 3-4). A delta-T map can be generated from one sensor pair. The information stored at each node of a delta-T map includes node coordinates and average delta-T. The delta-T map can be plotted as contours of equal delta-t. The density of a map can be increased through interpolation.

• Locate real AE events. The time arrival difference between each sensor pair from a real AE event can be calculated and used to identity a line with same and equal delta T in corresponding map. This line represents all possible real AE event locations in each map. Theoretically, by overlaying all the resulting maps, the intersections of all lines should converge into one point. However, in practice, it is a different situation due to marginal error at each step. Therefore, all intersection points of lines are calculated and a cluster analysis is applied to find the convergence point which is also the most likely location of a real AE event.

As factors including complex geometric features and damaged regions can be taken into consideration within mapping area and detailed accurate wave speed data are not required, this technique has shown its advantage on source location in aerospace structure and composite materials. However, the disadvantages of this technique are listed as following;

1. As the training grid data are collected manually, this process is lengthy and time consuming. Furthermore, the chances of human error are introduced; for example, not performing the PLB on top of the exact grid point and failing to remove the erroneous training data.

2. Traditional threshold crossing approach, which is used in this technique in order to determine the arrival of waves at each sensor, is considered to be unreliable in determination of the time arrival of an AE event.

3. Since H-N sources are generated to provide AE data, there is a high risk of foreign object debris from broken pencil leads, which is a major problem in some sectors.

These disadvantages of this technique limit its performance and lead to reduced accuracy of source locations.

2.6 Background theory on corrosion and stress corrosion cracking

Corrosion of steel is an electrochemical process, which leads to a degradation in the material properties. Steel structures exposed to extreme environments, such as marine and highly polluted industrial settings, are particularly vulnerable to corrosion. Among the widely differing forms of corrosion, this study focuses on uniform corrosion and SCC which are shown in Figure 2.15.

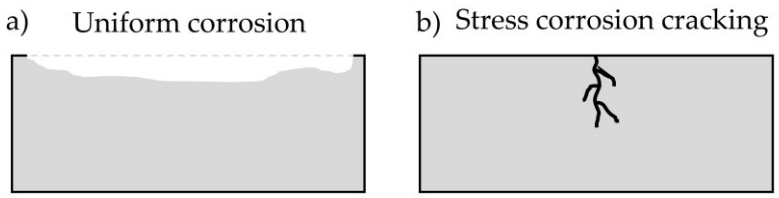

Figure 2.15– Two forms of corrosion; (a) uniform corrosion and (b) SCC

Uniform corrosion is one of the most common forms of corrosion that occur on mild steel. It is widely understood through the reaction of iron (Fe) when exposed to water and oxygen mild steel is exposed to water and oxygen [85], as shown in Figure 2.16.

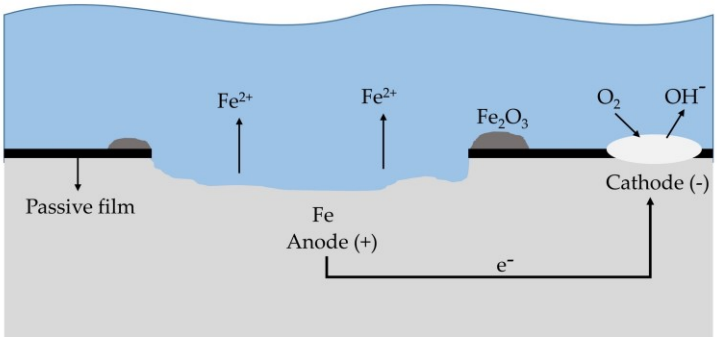

Figure 2.16– Uniform corrosion of mild steel [85]

The process initiates when iron is oxidized at the anodic sites, leading to the formation of ferrous ions (Fe^{2+}), as shown in Equation (2.26), and the release of electrons which travel to the cathodic site via an electronic path within the metal. In the cathodic site, these electrons react with water and oxygen to create hydroxide ions (OH^-), as shown in Equation (2.27). If the solution is acidic without oxygen, the reduction of hydrogen ions (H^+) will generate hydrogen gas (H_2) (Equation (2.28)).

$$Fe \rightarrow Fe^{2+} + 2e^- \tag{2.26}$$

$$O_2 + 2H_2O + 4e^- \rightarrow 4OH^- \tag{2.27}$$

$$2H^+ + 2e^- \rightarrow H_2 \tag{2.28}$$

After that, the resulting OH^- will combine with Fe^{2+} to produce iron hydroxide, $Fe(OH)_2$ (as shown in Equation (2.29)) at the cathodic site. This substance is a solid residue of corrosion and an incomplete form of rust. A further hydration and oxidation reactions of this substance will lead to the formation of a complete corrosion product, which is a complex mixture commonly referred to as ferric oxide (Fe_2O_3) (Equation (2.30)).

$$Fe^{2+} + 2OH^- \rightarrow Fe(OH)_2 \tag{2.29}$$

$$O_2 + 4Fe(OH)_2 \rightarrow 2Fe_2O_3 + 4H_2O \tag{2.30}$$

SCC is a complicated process that results from a combination of mechanical factors, metallurgical effects, and environmental characteristics. The concept of the "stress corrosion spectrum" was firstly introduced by Parkins [86] to evaluate the SCC mechanism. This spectrum takes into account the influence of both electrochemical and mechanical factors, which can vary over time as the SCC damage mechanism evolves [87].

Typically, SCC originates from localized corrosion or mechanical flaws such as pitting, intergranular attack, scratches, or inherent defects [87]. As time progresses, these defects progress into short cracks that grow slowly until they reach a critical length, ultimately resulting in component failure.

2.7 Literature review

As discussed in Chapter 1, this research aims to optimise an advanced AE damage location technique, delta-T mapping using the Finite Element (FE) method and improve the AE techniques and analysis methods required for monitoring corrosion and SCC. Thus, a comprehensive literature review exploring FE modelling of AE and monitoring corrosion and SCC with AE techniques was conducted.

2.7.1 FE Modelling of AE

The FE method, which was developed by engineers in the mid-1950s, has been popular because of fine discretization, efficient and reliable algorithms and fast computing systems.

Numerous studies [87–92] conducted for simulation of AE signals in both steel and carbon-fibre reinforced plastics (CFRP) can be found.

In 1994, a 2-D (two-dimensional) dynamic finite element method (DFEM) was developed and validated by Gary and Hamstad [87] to predict AE waveforms in thin plates. Good agreement between predictions from the FE model and experimental measurements was found. The influence of different variables including the mesh size, source rise time and sensor aperture were investigated. Based on the 2-D DFEM, a 3-D DFEM used for predicting far-filed AE displacement fields was developed by Hamstad et al. [88]. The out-of-plane displacements in the 3-D model were firstly compared with those in 2-D models and good agreement were found. After that, the 3-D FE models were validated by laboratory experiment data which were collected by performing in-plane and out-of-plane H-N sources on a 1.32 m × 0.78 m × 0.254 m plate. It was concluded that in order to simulate the Rayleigh waves properly and accurately, it is necessary to increase the mesh density away from the source.

In the above-mentioned work on simulation of AE using 2-D and 3-D DFEM, only a surface monopole AE source had been studied. However, AE source configurations such as buried dipole sources should be taken into consideration as they are more realistic and more complicated as well. In 1998, Hamstad et al. [93,94] extended the DFEM method to predict the AE waveforms generated from buried transient dipole, which was modelled by applying two closely spaced and simultaneous body forces along opposite directions. FE predictions were shown to be in good agreement with published results. A function of the minimum wavelength was proposed to calculate the maximum source and mesh size in point sources. Until that time, only direct AE signal arrivals were predicted with the DFEM method, and a reflected AE waveform, which is an important part of signals, had not been investigated. Prosser et al. [95] then used 3-D DFEM to predict AE waveforms including direct signal arrivals and reflection components in finite plates. H-N sources on both the surface and the edge of the thin plate were modelled for the experimental confirmation. The reflected AE waveforms, which were predicted by the FE method, were shown to have high accuracy. It was also concluded that A_0 (zero order anti-symmetric Lamb mode) will be preferentially generated with surface lead breaks while S_0 (zero order symmetric Lamb mode) will be

preferentially generated with H-N sources on the edge near the mid-plane of the plate. In addition to DFEM, Mindlin Plate Theory (MPT) was also used by Prosser et al. [96] to predict AE waveforms in thin plate. Predictions from MPT were compared with those from DEFM. Though some discrepancies did exist, AE signals predicted by MPT were in good agreement with those by DFEM. At shorter times, before the reflections, the discrepancies in the waveforms were due to the approximate nature of the MPT. At longer times, after the reflections, the discrepancies were a result of different reflections which were caused by differences in the boundary conditions used in DFEM and MPT.

Later, a FE model in which a piezoelectric transducer was simulated was developed by Hill et al. [97] using commercial FE software PAFEC-FE. A step force was used in the model to excite AE waves. The effect of varied source types and positions was evaluated in the work.

In contrast to source models in which a force-time curve is defined as the source function and the directivity of source couples and their positioning are assumed, a new microscopic source model was presented by Sause and Horn [22] to simulate the excitation of macroscopic plate waves resulting from failures. AE waves generated by matrix cracking, fibre breakage and fibre matrix interface failure in carbon fibre reinforced plastic (CFRP) specimens were investigated using the Structural Mechanics Module of commercial FE software Comsol Multiphysics. Simulated signals were shown to be in systematic agreement with experimental data collected from four-point bending experiments of CFRP structures. Following that, the influence of microscopic elastic properties and varied geometries of AE sources on simulated AE waves were investigated by Sause and Horn [23] using FE modelling approach. The AE wave simulated on the anisotropic, homogeneous model was compared with that on an anisotropic, microscopically inhomogeneous model. The results indicated that microscopic elastic properties of the AE source have a considerable impact on the formation of distinct Lamb wave modes. Later, the studies were extended by Sause [24] in evaluating the influence of internal discontinuities on signal propagation in CFRP plates. It was shown that internal damage had a significant effect on the AE source localisation because the damage resulted in distortions of wave patterns and had a significant effect on the initial arrival time of different wave modes.

Afterwards, a new model using the cohesive zone modelling (CZM) approach was introduced by Sause et al. [98]. The cohesive-like interface included in the model is determined according to the experimental measurements. Through a multi-scale and multi-physics approach, the initiation and propagation of cracks, signal propagation process and the detection process of an AE sensor were considered. Signals generated using the modelling approach had been validated against the data collected from micromechanical experiments. In addition to CZM, Extended Finite Element Method (XFEM) was used by Cuadra et al. [99] to simulate the excitation of AE wave due to the onset of crack. In 3D FEM models, the fracture mechanics were linked to AE by an integrated computational approach. Fracture mechanics parameters in the CZM and XFEM models were defined according to the experimental measurements. Computational results obtained from the two models were compared and analysed to investigate the wave initiation and propagation near and far from the crack tip. The effect of geometry and material properties on the wave characteristics were also investigated. It was observed that a shift of the peak frequency of the modelled waveforms was shown to be a function of distance from the crack source, which can be used as a guide when selecting the sensor type.

In addition to aforementioned methods of simulating AE sources, some simplified methods [100–102] can also be found. A method in which nodes were released to generate AE waves were proposed by Lee et al. [102]. The process contains static and dynamic analyses. As shown in Figure 2.17 a), the FE static analysis, in which the tensile stress was applied to the un-cracked specimen, was firstly performed with the commercial FE code ABAQUS. The boundary condition of the crack surface was defined as symmetric. Following that, the stress field calculated in the static analysis was imported as a predefined filed in the dynamic analysis (Figure 2.17 (b)). The symmetry boundary conditions on crack surface was removed. Therefore, nodes on crack surface was released and AE waves were generated at the same time. The disadvantage of this method is that it cannot be applied on unsymmetrical FE models.

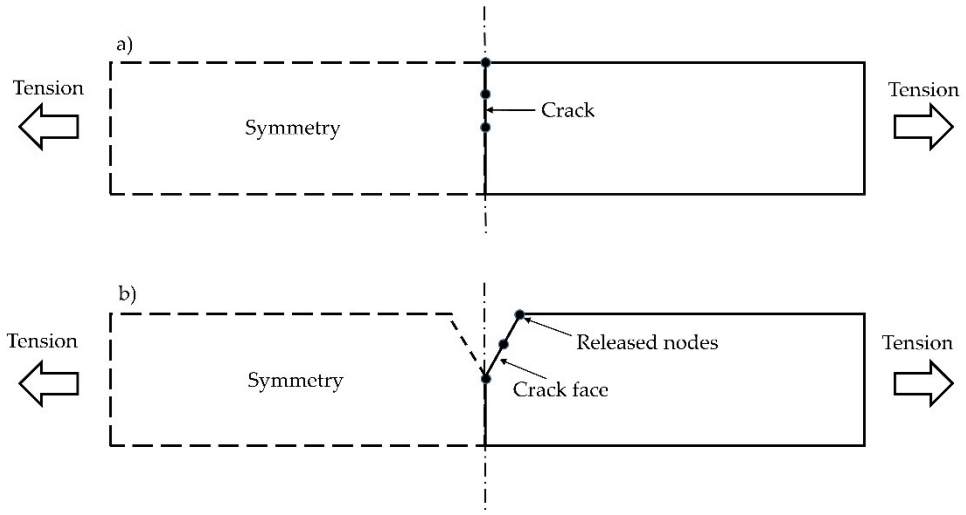

Figure 2.17– Basic procedure of first method; (a) static analysis and (b) dynamic analysis

Later, a similar method was proposed by Tang [101]. In this method, material properties of steel (Material 1 in Table 2.1) were assigned to the model firstly as shown in Figure 2.18 a). Subsequently, as shown in Figure 2.18 b), the material properties of Material 2 in Table 2.1 were assigned to elements at the crack instantaneously. The stiffness (Young's Modulus) of these elements were reduced to nearly zero, which means these elements were artificially deleted, thus producing AE waves.

Table 2.1 – Material properties

	Temperature (°C)	**Young's Modulus (GPa)**	**Poisson's Ratio**	**Density (Kg/m^3)**
Material 1	20	207	0.3	7830
Material 2	0	~0	0.3	7830

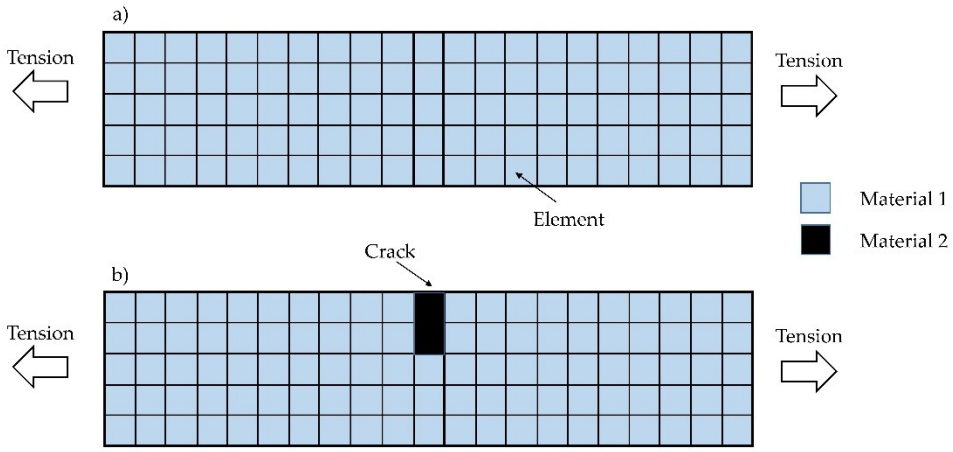

Figure 2.18–Simulating crack growth by reducing Young's Modulus to ~0; (a) material properties of Material 1 were assigned to the model and (b) material properties of Material 2 were assigned to elements at the crack

Recently, a localisation technique utilizing FE simulation in conjunction with Artificial Neural Networks (ANN) was proposed as an efficient approach for source location in complex structures by Cheng et al. [92]. In this technique, AE waves induced from H-N sources were simulated using excitation signals modulated as tone bursts with the central frequency of 150 kHz at the FE model. The onset time of signals were collected using FE simulation results. Based on that, the ANN models were trained. To test the performance of this technique, H-N sources were performed on a steel-concrete composite girder. It was shown that AE source locations were predicted with satisfactory accuracy on a steel-concrete composite girder.

To summarize, FE modelling is a commonly employed technique for predicting the generation and propagation of AE waves in materials. Various types of AE sources, such as crack growth, matrix cracking, or fibre breakage were simulated in FE models and the impact of different factors such as material properties and loading conditions on AE behaviour had been studied. More recently, FE modelling has been utilized to generate training data for AE source localizations.

2.7.2 Monitoring corrosion with AE techniques

In 1992, to quantify AE data with pitting corrosion, AE technique was utilised by Jones and Friesel [103] to detect and investigate the pit initiation and growth on low-carbon type 304

stainless steel. Tests were conducted in 0.05% and 5.5% NaCl solution acidified to pH=1. A significant number of AE signals were recorded during pitting corrosion. Though the exact AE generation sources were not delineated, the authors [103] speculated that the rupture of an oxide or salt cap covering the pits might be a possible AE source. They mentioned that if the guess was correct, mainly large pits, which were only a small percent of the pits, were acoustically active. This could be a problem for monitoring pitting corrosion using AE techniques since the majority of pits cannot be detected. Therefore, to explore this topic further, the AE response of pitting corrosion on 316L austenitic stainless steel was investigated by Mazille et al. [104] in laboratory experiments. Tests were carried out in 3% Nacl solution with pH=2. Results showed that AE events occurring during the pitting corrosion process were easily detected and the AE activity was in a good correlation with the pitting rate during the tests. Though the exact process responsible for the AE generation during pitting corrosion was still not identified clearly, results of the study demonstrated that AE technique is as a useful tool for detecting and monitoring the occurrence of pitting corrosion.

Since the influence of the polarization procedure and the material sensitivity towards pitting corrosion on AE response of pitting corrosion were not clear, the experimental work was conducted by to explore this topic further by Fregonese et al. [105]. Two types of 316L austenitic stainless steels with different sensitivity towards pitting and two polarization procedures (i.e. under potentiostatic or galvanostatic polarization conditions) were adopted to initiate corrosion pits in a 3% NaCl solution (acidified to pH=2). Results showed that the time delay (which was defined as a short time period before a significant AE activity) and AE hit rate when pits propagated were highly related to the material sensitivity towards pitting and the polarization procedure. AE features including rise time and counts number were higher during pit propagation compared to pit initiation, while no obvious change on the amplitudes of AE signals was observed throughout the pitting corrosion tests. Considering different characteristics of AE signals during pitting initiation and propagation, it was of great importance to study the AE responses at different steps of pitting corrosion separately. Thus, following that, the research was extended by Fregonese et al. [106]. Pit initiation and propagation on 316L austenitic stainless steel were investigated separately using AE technique. The results showed that the pit initiation process was not highly acoustically

emissive, while significant number of AE signals were recorded when pits propagated. It was found that the increase AE signals from pit initiation to propagation corresponded to the recording of resonant signals, which were predominant when pits grew in the form of occluded cells and developed with a sufficient rate. It was very likely that these resonant signals were attributed to the evolution of hydrogen bubbles. Moreover, a drastic change of AE features, e.g. rise time and counts number, was observed when the corrosion mechanism changed from pitting corrosion to uniform corrosion, which indicated that it was very promising to use AE technique to detect the change of the corrosion mechanism.

Later, experimental work was conducted by Kim et al. [107] to examine the capability of AE techniques to detect and monitor crevice corrosion on 304 L austenitic stainless steel. During the experiment, the initiation, propagation and repassivation of crevice corrosion were controlled by adding hydrogen peroxide and hydrochloric acid and changing the applied torque of crevice assembly. Results showed that corrosion potential of the specimen, AE activity and AE hit rate were closely correlated with the weight loss and the area of affected metallic surfaces during crevice corrosion. Fluctuations of AE parameters including rise time, counts number, duration and cumulative energy were overserved when crevice corrosion propagated. It was concluded that one of possible AE sources was the bubble formation from cathodic reactions within the crevice.

In 2003, both potentiodynamic method and AE technique were employed by Darowicki et al. [108] to study the pitting corrosion on 304L stainless steel, in 3% sodium chloride solution with pH =2. It was found that potentials of pitting corrosion seemed not to correlate to AE activity and the occurrence of AE events during polarization was random. Hence, they concluded that the AE activity during pitting corrosion process on stainless steel were attributed to formation of hydrogen bubbles rather than pitting corrosion. Later, experimental work were carried out by Jomdecha et al. [109] to characterise and locate four different types of corrosion, i.e., uniform, pitting, crevice corrosion and SCC. It was found that the correlations analysis based on AE parameters such as amplitude and counts can be utilised to distinguish between different types of corrosion. For uniform corrosion, a significant number of AE hits were observed in the first 4 hours, but they decreased rapidly afterwards. In the case of pitting and crevice corrosion, high AE hits with a broad range of amplitudes were

detected. Initially, the count rate was low but increased quickly in later stages. For SCC, large number of AEs hit with a wide range of amplitudes were recorded at the beginning of the process. However, they decreased exponentially with time. In addition, AE sources arising from different corrosion mechanisms were successfully located by the AE system.

Later, Jirarungsatian and Prateepasen [110] performed some experiments to investigate characteristics of AE sources in uniform and pitting corrosion process. The AE activity and electrochemical characteristics were recorded during pitting corrosion tests on 304 stainless steel and uniform corrosion tests on A36 mild steel. Three AE sources, i.e., gas bubbles activation, passive film rupture and pitting propagation were identified in the pitting corrosion tests. In uniform corrosion tests, two AE sources associated with gas bubbles activation and uniform corrosion were identified. Results showed that AE parameters such as duration and average frequency were useful for discriminating between pitting and uniform corrosion.

Since there are still a number of unclarified points regarding characteristics of AE signals and AE sources during pitting corrosion, experimental work on AE monitoring of pitting corrosion of 304 stainless steel in varied solutions with different pH values and Cl concentrations was conducted by Xu et al. [111]. It was found that AE signals in the context of pitting corrosion can be classified into two groups (Type 1 and 2) and signals in Type 2 had higher AE parameters such as rise time, count number, duration and amplitude than those in Type 1. Moreover, it appeared that duration and amplitude were more useful for discriminating between different pitting corrosion stages than other AE parameters such as rise time and count number. It was also found that the hydrogen bubble evolution was one of AE sources during the pitting corrosion.

Although there had been many investigations on AE monitoring of pitting corrosion as discussed above, the AE activity during pitting corrosion on vertically positioned stainless steel wat not fully studied. Hence, an investigation of AE behaviour during pitting corrosion tests on vertically positioned 304 stainless steel specimens was carried out by Wu et al. [112]. Based on the absolute energy of AE signals, two clusters were identified, i.e., a low-energy cluster with mainly continuous signals and a high-energy cluster with mainly burst signals. It

was found that the low-energy cluster was attributed to hydrogen-bubble evolution inside the pits and the high-energy cluster was attributed to the pit cover rupture.

Later, in 2016, a novel approach based on wavelets and Random Forests was proposed by Morizet et al. [113] to classify and characterise AE signals submerged by environment noise. This approach was firstly validated on synthetic data and a software code RF-CAM was developed accordingly by the authors. Then, the real corrosion data related to noise and crevice corrosion conditions were collected and analysed by RF-CAM. It was concluded that the proposed approach can be applied on ground truth data with a high efficiency and is very promising on the application to real data.

In 2019, further experimental work was carried out by Tang et al. [114] to identify AE sources associated with different corrosion mechanisms. In addition to AE technique, the open circuit potential measurement and an optical microscope were utilised for an in-situ monitoring of the corrosion on the carbon steel. A good correlation between open circuit potential measurement and AE evolution was shown. Moreover, a novel method in which the waveform graphics were imported into Matlab and a 2D pattern recognition algorithm was executed to assess the similarities among the various graphics was proposed to classify different types of corrosion damage, i.e. the localized corrosion and uniform corrosion, occurring within a structure. The results showed that the graphics of uniform corrosion exhibited low similarity with those of localized corrosion, which indicated this method can distinguish localized corrosion from uniform corrosion.

Later, a knowledge gaps regarding the AE activity during the pitting corrosion of open morphology was identified by Wu and Kim [115]. To fill the gap, a simple and effective method was proposed and utilised to control the evolution of pits uncovered by lacy covers or corrosion products on a 304 stainless steel specimen. The emitted AE signals during open-morphological pitting corrosion were recorded and discussed. Results showed that the AE activity were not attributed to hydrogen bubble evolution in this study and possible mechanisms for AE generation could be the salt film rupture at pit head and the corrosion products deposition at pit tail.

To eliminate the intervention of different pits on the electrode and better understand the AE sources mechanism during the corrosion, a specific experimental setup that only allows a single pit evolution was presented by Wu et al. [116]. AE techniques along with optical microscopy and potentiodynamic polarization were applied to monitor the pit initiation and propagation on both 304 stainless steel and 17-4 precipitation hardened stainless steel. Dozens of AE signals were recorded during pitting on 17-4 precipitation hardened stainless steel, while a limited number of AE signals were recorded on 304 stainless steel. It was concluded that hydrogen bubbles inside the pit and the perturbation of electrolyte around the pit can be considered as direct AE sources.

Recently, a novel approach based on ensemble empirical mode decomposition and linear discriminant analysis was proposed by Chai et al. [9] to identify different types of AE sources during corrosion. To test the approach, the signals emitted from the induced intergranular corrosion on 316LN stainless steel during corrosion were continuously monitored with an AE system. Three different types of AE signals associated with three damage modes, i.e., environmental noise, intergranular corrosion and crack initiation and propagation were identified using the proposed approach. Results indicated that it was feasible to use the AE characteristic parameters which were based on the energy percentage of the intrinsic mode functions to characterize the evolution of damage during corrosion.

A short time ago, AE and electrochemical testing technology were combined to investigate corrosion mechanism on a Q235B steel specimen by Qiu et al. [10]. During metal dissolution, AE signals were recorded and energy conversion value of anode metal was calculated. Since there is a positive correlation between AE activity and the corrosion rate which reflects the corrosion severity, a quantitative characterization formula based on the characteristics of AE signals such as AE counts rate, amplitude, hits and absolute energy was established to measure the corrosion rate, thus evaluating the severity of Q235B steel corrosion status.

Overall, monitoring corrosion with AE techniques has been widely studied in the literature. Studies have shown that AE monitoring can be effective in detecting and monitoring pitting corrosion, crevice corrosion and uniform corrosion. It has been demonstrated that it is feasible to identify different types of corrosion, predict corrosion rates, and estimate

remaining service life. Other studies have focused on improving the accuracy and sensitivity of corrosion detection.

2.7.3 Monitoring SCC with AE techniques

AE sources during SCC and corresponding source mechanism for SCC phenomena were investigated by Shaikh et al. [117] using AE signal analysis. A compact tension test was carried out by Shaikh et al. [117] in accordance with ASTM E399 [118]. During the test, a specimen made from AISI type 316LN stainless steel was subjected to a constant load and immersed in a 45% $MgCl_2$ solution at a temperature of 140 °C. A continuous AE activity was seen at the beginning of the test until a dramatic increase in AE counts and energy was observed, which was attributed to the SCC initiation. It was found that the cracking mode during SCC initiation and propagation stage was ascertained to be transgranular mode and the majority of AE activities were generated by plastic deformation ahead of the crack tip during SCC propagation stage. Following that, the characterization of AE signals recorded during SCC propagation was investigated by Lapitz et al. [119]. Slow strain rate tensile tests (SSRT) were performed on α-brass specimens, which were under potentiostatic control and exposed to 1 mol/L $NaNO_2$ solution and Mattsson's solution. Test results showed that the number of AE signals emitted from transgranular SCC propagation was much more than that from intergranular SCC propagation, while AE parameters including mean amplitude and rise time of AE signals generated from these two types of SCC were similar. Following that, to investigate the effect of materials on the AE signals measured for SCC propagation, SSRT was performed by Alvarez et al. [120] on a different material, i.e. AISI 304 stainless steel. The specimen was exposed to a 1.0 mol/L NaCl and 1.0 mol/L HCl solution. Similar to test results on brass [119], a much higher AE signal activity was observed during intergranular SCC propagation compared to that during transgranular SCC propagation. Likewise, mean amplitude and rise time of AE signals emitted from these two types of SCC were similar.

Later, Du et al. [121] investigated the capability of electrochemical noise (EN) and AE techniques to detect and characterise the SCC phenomenon, with special interest in the process of corrosion. 304 stainless steel specimen were tested in acidic NaCl solution (1.5 mol/L H_2SO_4 + 0.5 mol/L NaCl) under slow strain rate. EN and AE were monitored

continuously during the test. The characteristics of AE signals emanating from varied sources (pitting, cracking and bubble breaking up) were compared. Results showed that AE signal generated from different sources exhibited considerably different characteristics. Moreover, it was found that EN and AE techniques led to very similar results. Hence, it was suggested that a combination of AE and EN techniques can improve the reliability of the monitoring system during on-site testing.

Afterwards, Xu et al. [122] carried out a constant tensile load test. The AISI 304 stainless steel specimen was subjected to a high temperature aqueous environment and AE was utilised to monitor the SCC initiation and propagation through the entire testing period. It was found that with the increase of stress intensity factor, an increase in the cumulative AE hits was observed. Two different types of AE signals were successfully distinguished by the AE analysis: low amplitude and high amplitude signals; the former was found to correspond to the mechanisms of plastic deformation and the latter was attributed to crack propagation. Following that, the research was extended by Xu et al. [123] to study the AE behaviours during intergranular corrosion (IGC), intergranular stress corrosion cracking (IGSCC) and transgranular stress corrosion cracking (TGSCC). Results showed that, compared with IGSCC and TGSCC, the AE activity throughout the IGC process was relatively low and AE signals were characterized by a relatively low amplitude. It was found that the AE activity detected during IGSCC process was generated from plastic deformation, while that detected during TGSCC was generated from both plastic deformation and crack propagation.

To eliminate the intervention of different SCC cracks on a specimen and better understand the AE sources mechanism during the SCC phenomenon, a chloride droplet SCC test was improved and conducted by Wu et al. [86] to trigger single SCC crack on a stainless steel specimen. A droplet of 1.0 % NaCl solution was placed in the middle of the specimens using a microliter syringe and a high level of humidity was maintained to hinder the fluid evaporation. AE measurements, electron backscattered diffraction (EBSD) and optical microscopy observation were used to investigate the initiation and propagation of SCC. Three stages, i.e. pitting corrosion evolution, slow crack propagation and rapid crack propagation were identified in the SCC phenomenon. An unsupervised clustering analysis based on k-means algorithms was performed and results showed that AE signals were distributed into

two clusters, i.e. low-frequency and high-frequency AE cluster; the former was believed to be generated from plastic deformation and the latter corresponded to crack propagation.

Afterwards, the correlation between SCC behaviours on the storage tank bottom steel and AE behaviours was investigated by Bi et al. [11]. A three-point bending test was carried out on a v-notched plate specimen cut from storage tank bottom plates. During the test, the stress was applied on the specimen using a hydraulic jack and the v-notch tip was in contact with a 3.0% sodium chloride solution to induce SCC. Throughout the test, AE in combination with electrochemical techniques were utilised to monitor the SCC initiation and propagation. Results indicated that the main AE sources during SCC were microcrack creeping, macrocrack propagation and pitting corrosion. It was found that, compared to AE signals generated from microcracks, signals from macrocracks were characterised by larger AE counts and higher energies.

Recently, experimental work was carried out by Soltangharaei et al. [12] to identify the AE signal signatures during SCC propagation. During the test, a notch on a stainless-steel specimen was exposed to a 1% Potassium Tetrathionate solution and an almost uniform tensile stress was applied along the notch. An unsupervised clustering analysis was performed based on Features derived from the collected AE signals. The clustering results showed that the AE signal signatures attributed to SCC initiation and propagation were successfully identified. Furthermore, a method based on linear regression was proposed for identification and quantification of SCC damage with AE techniques.

Overall, AE techniques have been shown to be effective in detecting and monitoring the onset and progression of SCC in different materials. The use of AE techniques for estimating the rate of crack growth had also been investigated. Some work was found on using the AE method for detecting and characterizing SCC. In addition, some studies suggested that AE techniques can be a valuable tool for identifying different AE sources during SCC.

2.8 Conclusions

This chapter provides theoretical and background knowledge on AE techniques. In addition, a structured literature review on FE modelling of AE and monitoring corrosion and SCC with AE techniques is presented. According to the literature review, AE methods have been extensively studied and used to detect and monitor corrosion and SCC related issues due to its high sensitivity. Despite the advancements in AE techniques, detecting unknown corrosion and SCC damage sources on complex and large specimens remains challenging. Overcoming these challenges is crucial in advancing the real-world applications of AE techniques for monitoring SCC and corrosion on in-service structures. Hence, this study seeks to fill this research gap. Since the delta-T mapping technique has been shown to predict AE source location with good accuracy in complex structures, it is regarded to be a suitable method for AE source location of corrosion and SCC damage in complicated geometric structures. To automate the delta-T mapping technique, FE method, which is a widely used numerical simulation technique for solving complex engineering problems was used in this study to produce simulated data required for delta-T mapping, and the arrival time of simulated signals was estimated using the AIC method. Additionally, as little research has been done on identifying corrosion signals during SCC, the clustering method was employed in this study to differentiate between signals from two sources.

Chapter 3 Experimental Techniques

3.1 Data acquisition and timing parameters

A fully digital, four channel computerised AMSY-6 system consisting of parallel measurement channels was used during this research to perform AE data acquisition. It was manufactured by Vallen Systeme GmbH, Wolfratshausen, Germany. Generally, AE sources including material failure, leakage, partial discharge, friction, wear and particle impact can be detected, measured and located with this system.

As shown in Figure 3.1, a measurement channel is made up of an AE sensor that converts the displacement of elastic waves into an electrical signal, a preamplifier that amplifies the weak signal from the AE sensor into a stronger signal and an acoustic signal processor which is one of the channels of ASIP-2 in Figure 3.1.

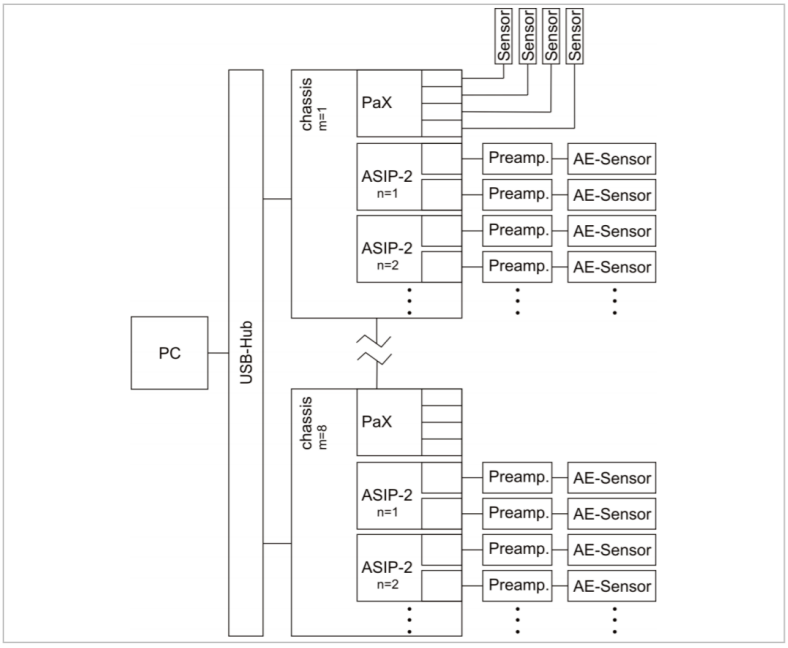

Figure 3.1– Block diagram of AMSY-6 system [124]

An ASIP-2 can perform 18bit analog-to-digital conversion at a 40MHz sampling rate, which means that high resolution data can be provided. The merit of the ASIP-2 is its high

sensitivity because the system noise is very low. An ASIP-2 must be plugged into a chassis. The chassis is connected to a personal computer via an USB interface. The acquisition data can be stored, displayed and analysed in real time on the computer [124].

Additionally, the AMSY-6 system can record up to four parametric channels. Thus, environmental conditions such as strain, temperature, humidity, wind speed, etc. can be measured and parameters such as load and displacement from a test machine in a fatigue test can be logged using parametric channels (PaX shown in Figure 3.1).

The acquisition set up is controlled through the Vallen AE Suite software, which consists of the acquisition system, which controls the measurement hardware and analysis software, which displays and analyses the acquired data. A thorough review of the acquisition setup should be conducted in order to select the most appropriate values for a particular AE monitoring application. Amongst the acquisition setup, it is of great importance to select timing parameters includes Duration Discrimination Time (DDT) and Rearm Time (RAT). DDT defines the length of time during which there is no threshold crossing in order to determine the end of a hit. As shown in Figure 3.2, during hit based AE testing, a signal is recorded by an acquisition system once the amplitude of this signal crosses the user defined threshold. If this amplitude falls below the threshold, the DDT timer will be started. Within the duration of the DDT, if a threshold crossing occurs, the DDT timer will be reset. If there is no threshold crossing, the time of the last threshold crossing will be stored by the channel. The hit duration is the time difference between the first and the last threshold crossing. The waveform and all the AE features of a hit are saved to the computer's hard drive. The DDT setting is used to prevent the merging of individual hits which are recorded in the same channel.

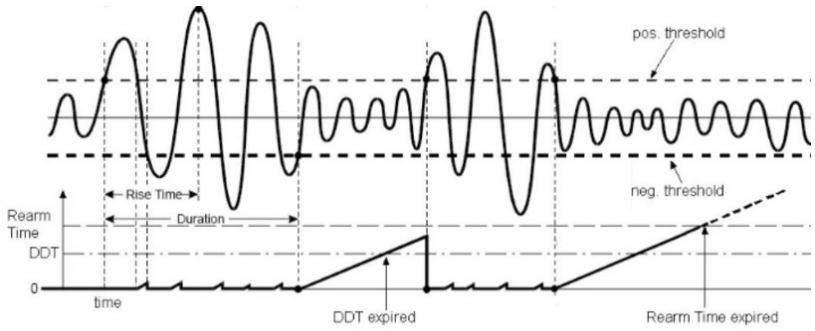

Figure 3.2– Illustration of DDT and RAT [124]

RAT specifies the time period that acquisition system will wait for before being ready to record again. Similar to DDT, if the amplitude of a signal falls below the threshold, the RAT timer will be started. Within the duration of the RAT, if a threshold crossing occurs, the RAT timer will be reset; if not, a new hit will be recorded.

It is crucial to choose an appropriate RAT value during an AE testing. If a RAT is set to be too low, the late arriving reflections will be logged. Consequently, multiple hits rather than one hit from a single wave will be recorded. Conversely, if a RAT is set too high, the system may miss the incoming AE signals which occur shortly after the recorded hit. Recommended threshold, DDT and RAT values for general-purpose testing [124] are presented in Table 3.1.

Table 3.1 – Recommended values for general-purpose testing from Vallen Systeme GmbH [124]

Materials	Threshold (dB)	DDT (µs)	RAT (µs)
Metals	30-40	400-2000	1000-4000
Fibre-reinforced plastic	30-40	150-1000	300-2000

3.2 Transducers

Piezoelectric transducers are the most commonly used in AE monitoring. The mechanical movement of the specimen surface can be detected by the piezoelectric element and converted into an electrical response. The architecture of a typical AE piezoelectric sensor is shown in Figure 3.3. The piezo element sits against the wear plate. Typically, there is an electrode on each face of piezo element within an AE sensor. One of the electrodes is linked to an electric ground and the other one is connected to a signal lead. Molding materials which

have vibration-damping property can be found behind the piezo element. With these damping materials, reflections back to the piezo element can be minimized and signals around the piezo's natural resonance can be suppressed. An integrated mechanical package is provided by the case which also acts as a shield to reduce electromagnetic interference [125].

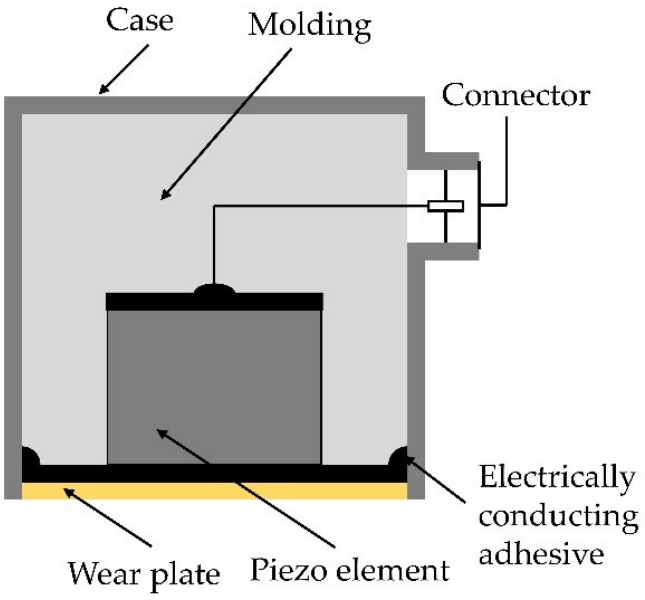

Figure 3.3– Structure of a typical piezoelectric transducer [126]

There are two categories of piezoelectric sensors produced for use in a wide range of industries: resonant and wideband. For resonant sensors, their sensitivity is the highest at certain frequency, i.e., sensors' resonant frequency. An example of the frequency response of a resonant sensor is shown in Figure 3.4. The resonant sensor is a VS150-RIC sensor manufactured by Vallen Systeme GmbH, Wolfratshausen, Germany. This sensor is characterized by a resonant frequency of 150 kHz. The output signal with frequencies close to 150 kHz produced a larger amplitude than that of signal with the other frequencies. Due to this feature, in a given AE application, consideration should be made to match the frequency response of resonant sensors with expected frequency content from AE source, the material and the structure. Hence, comparison of these AE parameters should only be made between AE applications utilising similar resonant sensors. In spite of these considerations, resonant sensors remain more commonly used in the field than wideband sensors due to their low cost and good sensitivity to signals from the preferred frequency range [124].

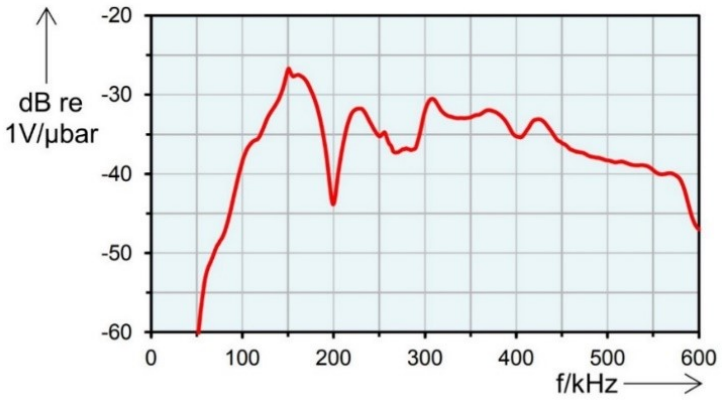

Figure 3.4–The frequency response of a VS150-RIC sensor [124].

For wideband sensors, they show a relatively flat response in wide frequency spectrum. An example of the frequency response of a wideband sensor, which is a VS900-RIC sensor manufactured by Vallen Systeme GmbH, Wolfratshausen, Germany, is presented in Figure 3.5. A good response in both standard and high frequency ranges is achieved on this sensor. Typically, the level of damping on the piezoelectric element of a wideband sensor is increased. Hence the sensitivity of the sensors is reduced.

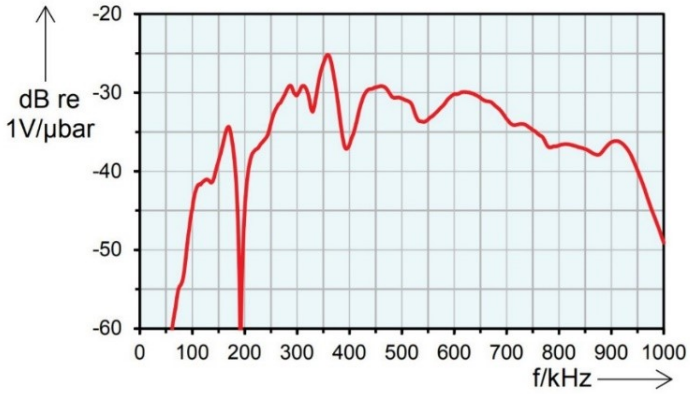

Figure 3.5– The frequency response of a VS900-RIC sensor [124].

3.3 AE preamplifier

A small voltage will be generated by a piezoelectric element when a sensor picks up an AE wave. A preamplifier is used to amplify this small voltage to a strong and useable voltage before transmitting to the measurement circuitry. As part of a measurement channel, a

preamplifier has the merit of enabling a long cable transmission of an output signal, which means that the acquisition system can be placed several hundred meters far away from the testing structure when long distance monitoring is required. Commercially available preamplifiers with different gains range from 20 dB to 60 dB can be chosen depending on the application. For some specific applications, using a preamplifier with the highest gain might not be the best choice. A high gain can improve small signal resolution, while may lead to saturation of strong signals and losses of signals. Hence, with regard to strong AE sources such as crack propagation in a metallic vessel, a gain of 34 dB is adequate. With respect to weak AE sources such as corrosion, a gain of 46 dB might be a better choice.

Commercially available preamplifiers can either be integral or external preamplifiers. An integral preamplifier is completely enclosed in the case of an AE sensor as part of the sensor, while an external preamplifier has its own housing and is connected to an AE sensor with a cable. In general, compared with external preamplifiers, the integral preamplifiers are considered to be more cost effective because the number of cables used during a test is reduced and the risk of mixed-up connections is minimized. The permanent installation of AE sensors as an essential industry application is possible with integrated preamplifiers [1].

3.4 Couplants

In most AE tests, a sensor must be placed on the surface of a test object, the exception being if a non-contact sensor with higher cost is used. A couplant is typically used between the sensors and surface, which improves the transmission of AE wave between the measurement surface and a sensor [127].

Without applying a couplant, the air at the structure-to-sensor interface is introduced because of the microstructure and surface roughness of the two attaching surface. The acoustic impedances of the test specimen (usually steel) and sensor surface (usually piezo-ceramic) are around 5 orders of magnitude higher than that of the air, which substantially decreases the transmission of wave energy between two surfaces [128]. A thin layer of couplant material with higher acoustic impedance can replace the air gap and produce better transmission.

When selecting a couplant material for an AE test, there are a number of factors which need to be taken into consideration. These factors include coulpant stability within the test duration, sensor removal and reapplication, test environment, vibration sources, etc. There are various types of couplants can be used including liquid, gel, grease and bonding agent.

The liquid and gel have the characteristics of low viscosity and good wetting ability compared with grease and bonding agent, which means that air bubbles can be easily expelled from the contacting interface. Therefore, the air at the structure-to-sensor interface will be less. Results showed that, for all liquid and gel couplants used in AE tests, the minimum thickness which is 5 to 6 μm of the couplant layer can be produced and an optimal energy transmission can be achieved [129]. However, because of the low viscosity of liquid and gel, couplants tend to dry up quickly over time and to drip when a sensor is vertically mounted. Therefore, liquid and gel couplants are not appropriate for long-term tests of ones with vertically mounted sensors.

Compared with liquid and gel, the viscosity of grease based couplants is much higher. Therefore, grease based couplants are less likely to drip and dry up with time, which means that they are more suitable for rough surfaces and long-term monitoring. However, due to high viscosity of grease, it is hard to remove the air at the structure-to-sensor interface. A mounting fixture can be used to force all the trapped air bubbles. Furthermore, compared with ultrasound gel, poorer sensitivity was found at higher frequencies with silicone grease [128]. And this signal loss at high frequency will be substantially higher with the increase of the thickness of the couplant layer. Therefore, special attention need to be paid on the thickness of the grease couplants [129].

Different from liquid, gel or grease based couplings, bonding agents can be used without a mounting fixture. They can be found in AE applications where absolute coupling and sensor stability are relatively important. In AE testing, many types of bonding agents can be applied, two of which, cyanoacrylate and silicon rubber compounds, are most commonly used. Moreover, because of the strong and stable bond between AE sensors and measuring structures, better transmission of shear motions can be provided with bonding agent. A thin and bubble free layer of this type of coupling can be achieved and provide a permanent bond between AE transducers and measuring surface. During AE tests, this thin layer couplings

can display high resistance to bond failure under situation of surface movement. Furthermore, silicone rubber compound can be applied on rough surfaces. Compared with cyanoacrylate, it is much easier to be removed from the test structures or AE transducers, which means that silicone rubber compound is less likely to cause damage to the structures or delicate AE sensors.

It is necessary to mount the AE sensor correctly to the surface as it helps achieve high sensitivity and good repeatability of signals. Poor coupling between sensors and testing structures can result in low sensitivity, which causes failure to detect low-amplitude AE signals and unreliable AE detection. Measures to prepare the surface of the testing structure should be done to make the surface smooth and clean before mounting the AE sensors. AE recordings with unreliable coupling may lead to misjudgement of actual status of monitored structure. The application of AE monitoring cannot be successful without the means of effectively mounting sensors.

According to the ASTM guidelines [31], two requirements must be fulfilled to correctly mount an AE sensor. Firstly, the movement of sensors must be restrained. Secondly, the constant and adequate acoustical coupling between the sensor and measurement surface must be provided. There are generally two categories of mounting methods; compression mounts and bonding. Through the use of the compression mount, the force is applied to ensure intimate contact between the sensor and tested structure. It is strongly advised to use the compression mounts together with the couplant to achieve the optimum transmission of acoustic energy between sensor and tested structure. Typical and well-tested compression mount methods are listed below.

• Electrical tape – Sufficient mounting pressure can be provided when adhering electrical tape to the surface of the structure and top of a sensor, as shown in Figure 3.6. However, the limitation is that it can only be used on small size specimens.

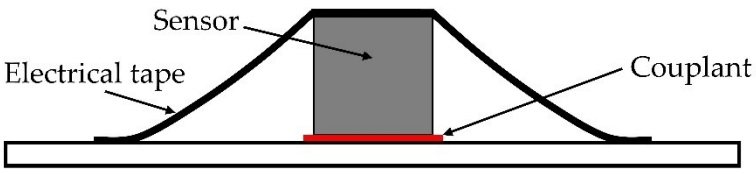

Figure 3.6– Electrical tape mounting [130]

• Magnetic clamps – There are two types of magnetic clamps (small and large) which can be chosen for different material inspection situations. For the large magnetic clamp, as shown in Figure 3.7 a), the magnets secure the clamp and the spring provides a repeatable mounting force on the sensor. For the small magnetic clamp, which is well suited for use on miniature sensors as shown in Figure 3.7 b), a mounting force is applied to the sensor through a foam tab. In terms of nonmagnetic materials, such as carbon fibre composites or aluminium, the magnetic clamps can still be used with slight modification. In order to provide a clamping force to the surface, small steel tabs bonded to the surface of the specimen (Figure 3.8 a)) or another magnet positioned on the opposite surface (Figure 3.8 b)) can be utilised.

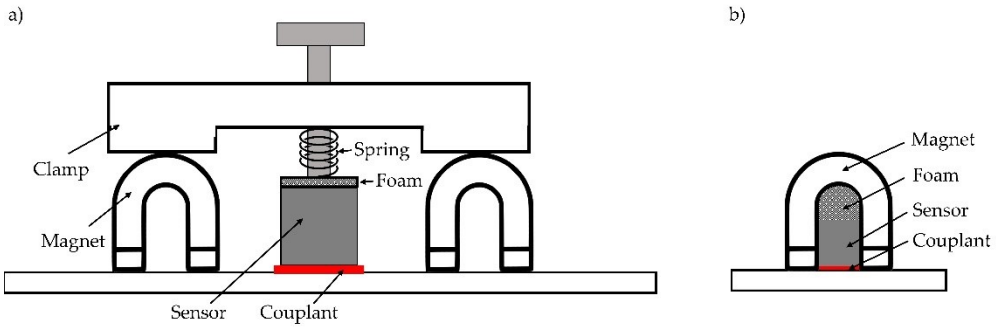

Figure 3.7– Magnetic clamps (a) for large sensor and (b) for small sensor [130]

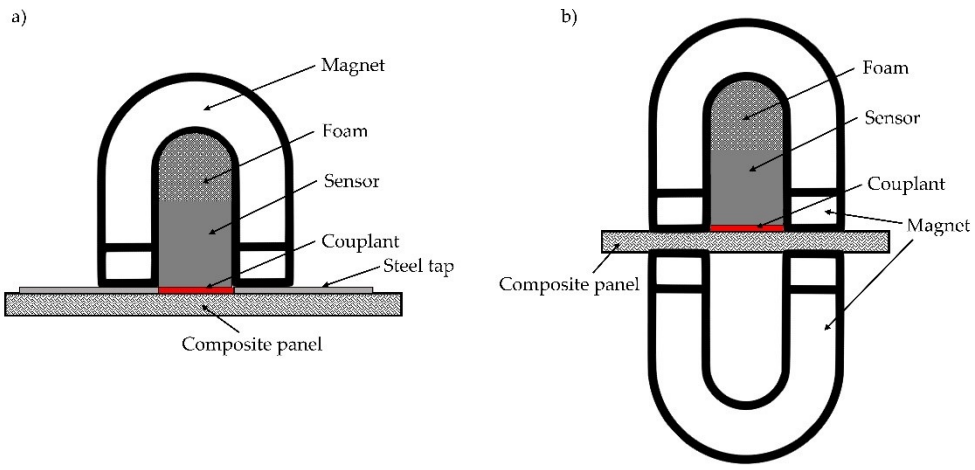

Figure 3.8– Magnetic clamps for nonmagnetic specimen using (a) steel tabs and (b) two magnetic clamps [130]

• Self-adhesive tabs and cable ties –As shown in Figure 3.9, self-adhesive tabs are boned to a specimen either side of the sensor. The position of the sensor is secured by looping and tightening the cable tie over the top of the sensor. The mounting force applied on the sensor can be regulated by the foam between the cable tie and the sensor.

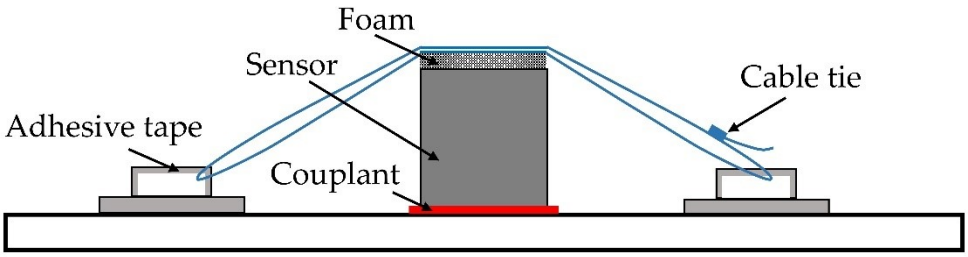

Figure 3.9– Self-adhesive tab and zip tie sensor mounting [131]

A sensor can also be mounted to a structure using an adhesive couplant such as cyanoacrylate or silicone sealant. When using an adhesive, appropriate pressure must be applied to the sensor before the adhesive is set to achieve intimate contact between the sensor and measurement surface, and there is no need to utilise additional couplant because the adhesive itself is one type of couplants. In some cases, compression mounts are not suitable to be used because of geometrical obstructions on tested structure, while bonding a sensor with an adhesive provides an alternative. Compared with compression mounts, the fixation resulted by bonding a sensor is more permanent, which means that bonding a sensor is a better solution for long-term monitoring. However, an adhesive couplant may cause damage to the sensor and the specimens upon removal. Therefore, it is rarely used in research applications.

3.5 Conclusions

In this study, a four-channel computerised AMSY-6 system manufactured by Vallen Systeme GmbH was used throughout the laboratory tests. Data acquisition and timing parameters including DDT and RAT were used in AE waveform measurement. Values of these parameters were determined according to the recommended suitable values in the Vallen AMSY-6 manual [124] and those found in the open literature. A value of 0.8 ms was used for both RAT and DDT. For the threshold, since the H-N sources are characterised by high amplitude, a larger threshold, 45 dB, was used for testing with H-N sources, while a threshold of 30 dB was used for low-amplitude AE sources such as corrosion and SCC.

The sensors used in this study were resonant VS150-RIC sensors manufactured Vallen Systeme, which have a resonance frequency equalling to 150 kHz and a bandwidth of 100-450 kHz and resonant Nano-30 sensors manufactured by Mistras Group Inc., which have a resonance of 300 kHz with operating range of 125-750 kHz.

According to the literature review, the commonly used type of sensor in metallic applications for monitoring corrosion and SCC has been the sensor which is nominally resonant at 150 kHz. Therefore, VS150-RIC sensor was selected. In addition, one sensor from Mistras Group Inc. was selected for trial, since it is responsive at a wide range of frequencies. Compared to VS150-RIC, the smaller size of the Nano-30 means that a more precise prediction of time of arrival can be made.

In this study, ultrasonic gel, which was found to give satisfactory coupling, and magnetic clamps have been used to couple the VS150-RIC sensors to the surface of the ferromagnetic specimens for the whole duration of test. A constant pressure for optimal coupling between the specimen surface and the sensor was provided by the magnetic holder. Additionally, The Nano-30 sensor was adhered on the surfaces of the specimens using a bonding agent, loctite 595 transparent sealant, which provided a mechanical fixture and acted as an acoustic couplant between the specimens and the sensors.

Chapter 4 Acoustic Emission Source Location Using Finite Element Generated Delta-T Mapping

4.1 Introduction

Ageing-induced cracks, human-caused hazards and natural disasters such as earthquakes or hurricanes can result in the deterioration of in-service metallic structures and the loss of structural integrity in the oil and gas industry [132]. Without appropriate remedial measures, structural integrity is likely to deteriorate with the potential to cause catastrophic damage with the risk of loss of lives and capital. In order to eliminate unplanned shutdowns and reduce inspection and maintenance costs, there is a need for a proactive monitoring approach to assess existing structural conditions and facilitate safe operation. As a method of monitoring the structural behaviour, evaluating structural performance and identifying damage at an early stage, SHM systems such as those which include strain and vibration monitoring are gaining significant interest and increased application. Recent industrial studies suggest that detecting damage at early stage can reduce costs and increase the life expectancy of a structure [5]. Therefore, a practical and cost-efficient SHM method that can identify micro and nano defects at an early stage and continually assess the structural health is desirable to ensure structures operate safely and efficiently throughout the service life. Adaptation of Non Destructive Evaluation (NDE) techniques for SHM is gathering significant interest because of the ability to provide quantitative information on defects based on measured physical parameters [133]. Inspection of large-scale complex structures using NDE techniques such as X-ray and ultrasonic techniques can be laborious and expensive. However, if the damage location can be identified accurately in advance through one of the NDE techniques, such as AE measurement, only the specific area of concern would require inspection. AE is defined as the transient elastic energy released by a material when it experiences a change of deformation in its structure [7]. As a passive technique, only active defects can be detected by AE testing.

Difficulties were reported by Baxter et al. [75] and Pearson et al. [76] in applying the most commonly used source-locating method within the field of AE, the Time of Arrival (TOA) technique, for locating active defects in complex structures. The main assumptions of a constant wave speed and unobstructed wave paths between the AE source and the sensor in the TOA technique are not easily met due to inhomogeneity of some materials such as composites and the complexity of the real structures that contain features such as welds, holes and thickness. In order to overcome these difficulties, the delta-T mapping technique was developed by Baxter et al. [75]. This has been shown to improve AE source location accuracy in complex structures. In this technique, a training grid is placed on an area of special interest. The generation of a well-established and widely used artificial source of AE, Hsu-Nielsen (H-N) source [31], at each node of the grid can provide arrival time data of waves for each sensor. The difference in the arrival time of waves (or delta-T) for each sensor pair can be found at each point; this data can be used to generate maps. Once real test data has been collected, the actual delta-Ts can be used to identity a line with same and equal delta T in corresponding map. By overlaying all the resulting maps, the intersections of all lines should converge into one point, which is the most likely location of a real AE event. Due to the good performance of this technique, it has been adopted in many lab-based studies by Eaton et al. [68], Pearson et al. [76] and Grigg et al. [77]. Details of the delta-T mapping technique can be found in [75]. However, there is a disadvantage of this technique in that the manual collection and processing of the training data requires significant time and human input. This lengthy and time-consuming process has prevented this technique from broad applications on large complex structures.

To overcome these problems, simulated data were collected by Marks [134] from a Local Interaction Simulation Approach (LISA) model to train the delta-T map and to locate real damage events on a plane of a complex structure. Results of fatigue crack events location using simulated training data were compared to those of the experimental training data. Similarity in the accuracy of the two results demonstrated the potential for using modelling data to locate real AE events. The commercially available package based on LISA, cuLISA3D, has high computational efficiency and thus has a short runtime (for example, running a 370 mm × 200 mm × 3 mm model takes approximately 3 minutes [134]). However, as reported by Marks [10], there are some disadvantages with cuLISA3D. Firstly,

the user was not allowed to define irregular mesh sizes in the model. Secondly, anisotropic materials such as composites cannot be modelled. Furthermore, it is very difficult to run multi-scale, multi-physics models in cuLISA3D.

Though using the FE method to generate data for training of delta-T maps has not been seen reported in open literature following an extensive search, it can be applied on monitoring active defects in complex structures as an accurate, low-cost and time-efficient approach. As a widely used numerical simulation technique for solving complex engineering problems, FE method was used in this study to produce simulated data required for delta-T mapping.

In this chapter, considerable efforts have been devoted to automating the delta-T mapping technique using FE method for the location of AE activities on specimens with complex geometries. A numerical method for simulation of an H-N source was validated and applied on a complex plate to train a delta-T map for localization of experimental H-N sources. Results of the present investigation indicated that the FE generated delta-T map reduces the time and effort required for manually collection and processing of the training data, whilst keeps a reasonable degree of accuracy for source locations

4.2 Numerical method for simulating H-N sources and its validation

In this section, a numerical method in which a monopole point force pulse acts in the out-of-plane direction was used to model an H-N source. Before applying this approach to a complex plate model, it was used to simulate an H-N source on a simple plate. And the FE model were validated by experimental results.

4.2.1 Numerical method for simulating H-N sources

Using the break of a pencil lead to generate acoustic waves, an H-N source [29,30,135] creates a step-function from a maximum compressive contact force to zero value in a very short period of time [46]. A broadband range of frequencies is excited by the step-function force, which has been used for the primary sensor calibration in codes and standards [136]. A

commonly used step-function, the ‘cosine bell’ function, which was proposed by Hamstad [90], was selected to simulate the time-dependent deflection on the surface of the plate caused by an H-N source. The 'cosine bell' force pulse is described by Equation (4.1). The ’cosine bell’ function is shown in Figure 4.1.

$$F(t) = \begin{cases} 0\ N & ,t \leq 0 \\ 0.5 - 0.5 \times \cos\left(\frac{\pi \times t}{T}\right) N & ,0 < t < T \\ 1\ N & ,t > T\ (T = 1.5\ \mu s) \end{cases} \quad (4.1)$$

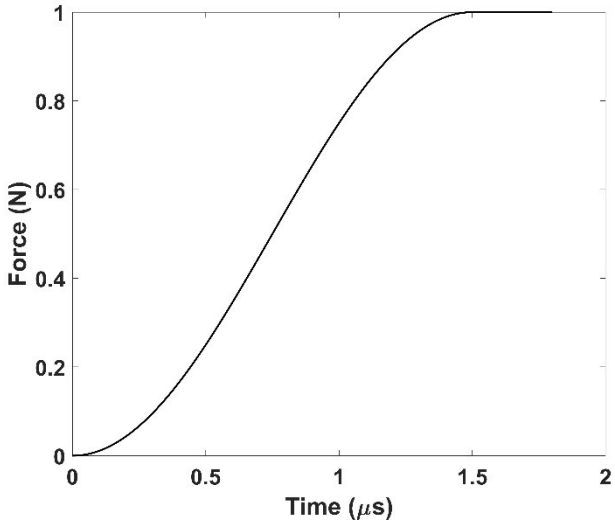

Figure 4.1– ‘Cosine bell’ source characteristics

As the actual load during an H-N source is unknown, the magnitude of the force is assumed to be 1 N according to literature [96]. With respect to the force development on the surface, as shown in Figure 4.1, the force pulse ramps up from 0 N to 1 N over a time duration of 1.5 µs, with a temporal resolution of 0.1 µs and then stays constant in the modelling.

4.2.2 FE model for simulating an H-N source on a simple plate

To test the effectiveness of the numerical method described in Section 4.2.1, a simple plate model was created using a commercial code ABAQUS (Dassault Systèmes Simulia Corp., Providence, RI, USA). This model has a width of 300 mm in the X direction, a length of 625 mm in the Y direction and a thickness of 3 mm in the Z direction. The steel plate has a

density value of 7850 kg/m^3, Young's modulus of 210 GPa, and Poisson's ratio of 0.3. A schematic layout of sensors and the simulated H-N source is shown in Figure 4.2.

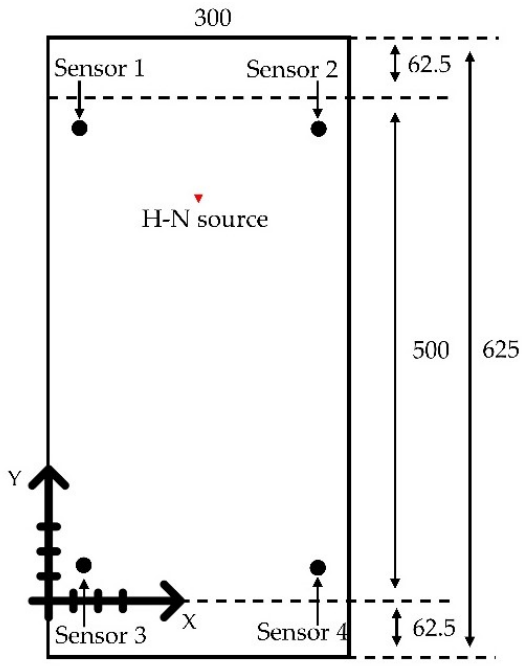

Figure 4.2– A schematic layout of the sensors and H-N source (units: mm)

The point force pulse described in Section 4.2.1 was excited at the location of the simulated H-N source. For simplicity and saving of computing time [92], it was decided not to model sensors but only the out-of-plane displacement because the focus of the work was to model the delta-T mapping process. A single node was the basis of the output signal; displacements in Z direction (out-of-plane) over time of all nodes at locations of the sensors were used for the analysis. The central 500mm section of the specimen plate was considered as the test area in the investigation for the purpose of minimizing the influence of edge reflections on the recorded waves. A coordinate system was introduced and the origin was placed at the bottom left corner of the test area. Coordinates relative to the origin of four sensors and the H-N source are summarized in Table 4.1. The four outermost nodes at the bottom surface of the plate (Z= 0 mm) were fixed in X, Y, Z directions (Ux=Uy=Uz=0) to prevent rigid body motion.

Table 4.1 – Coordinates of sensors and H-N source (units: mm).

	X coordinate	Y coordinate
Sensor 1	35	465
Sensor 2	265	465
Sensor 3	35	35
Sensor 4	265	35
H-N source	150	400

Convergence of the numerical results is strictly dependent upon the temporal and the spatial resolution used in the FE model. To avoid numerical instability and to enhance wave propagation accuracy, the shortest wavelength of simulated elastic waves needs to be resolved by the mesh resolution [137–139].

According to the wavelength formula, the relationship between the wavelength λ and the frequency f is described by the following simple equation:

$$\lambda = \upsilon / f \tag{4.2}$$

where υ is the wave velocity.

The VS150-RIC sensor (Vallen Systeme GmbH, Germany) used in experiments has a resonant frequency of 150 kHz and a frequency bandwidth of 100-450 kHz. As shown in Figure 3.4, there is a drop off around 500 kHz, making it challenging for the VS150-RIC to detect signals above this frequency [140,141]. Hence, the maximum frequency of the wave was set as 500 kHz. Assuming the longitudinal and shear wave velocities in steel are 5940 m/s and 3220 m/s, respectively [142], the smallest wavelength, thereby the maximum mesh size for 500 kHz was calculated to be 6.44 mm. As reported by Le Gall et al. [91], at least 5 nodes per wavelength are needed to simulate AE waves accurately with frequencies in the range of 500 kHz. Therefore, the mesh resolution of 1 mm, which gives 6 nodes per wavelength, was used for the simulations for both the accuracy and computational efficiency. The mesh convergence test also showed that 1 mm was sufficient as the mesh resolution for accurate simulation of elastic wave propagation. The general purpose 8-node linear brick element, C3D8R, provided by ABAQUS was used. The FE model and mesh are shown in Figure 4.3.

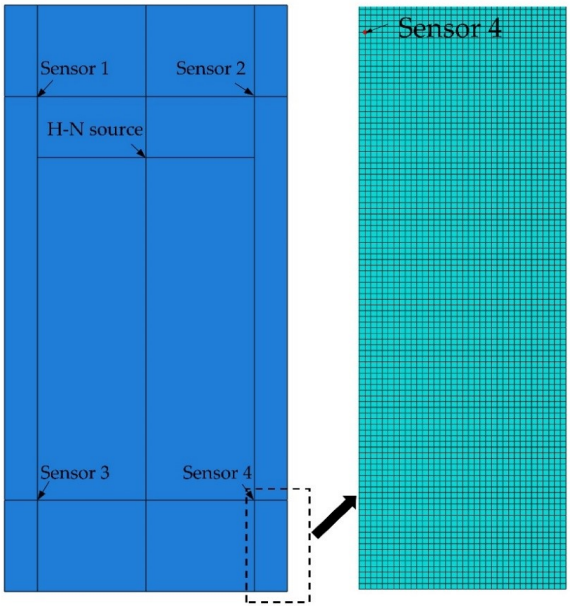

Figure 4.3– FE model and mesh in ABAQUS

Choosing an appropriate time integration step is also critical to achieve numerical stability and resolve the high frequency components accurately. An equation shows the relationship between the time increment Δt and the maximum of frequency f_{max} was recommended by Moser et al. [143] and is expressed as:

$$\Delta t < 1/(20 f_{max}) \tag{4.3}$$

Given that the highest frequency of interest is 500 kHz, a maximum time integration step of 0.1 μs was calculated. In order to save computational time while maintaining a sufficient temporal resolution, a time integration step was set as 0.01 μs in accordance to the reference [89], giving the time increment equalled to a sampling rate of 100 MHz, which did not correspond to the sample rate in experimental tests (5 MHz). However, it should be noted that both sampling rates used in the modelling and experiments are sufficient to resolve the signals' highest frequency content of interest (500 kHz). Therefore, errors caused by different sampling rates were marginal on time estimations between experiments and modelling.

4.2.3 Experimental verification of FE model for simulating an H-N source on a simple plate

In parallel, experimental testing of H-N sources on a simple mild steel plate was performed to validate the FE model. Dimensions of the plate were 625 mm × 300 mm × 3 mm, same as those of the FE model in Section 4.2.2. The setup of the experiment is shown in Figure 4.4. In order to easily specify the locations of AE sensors and H-N sources on the plate, a grid with 10 mm spacing was drawn on the central 500mm section of the specimen. A coordinate system identical to that of FE model was introduced. The coordinates relative to the origin of the four sensors and the H-N source are the same as those presented in Table 4.1.

AE waveforms were measured by four VS150-RIC sensors, which were acoustically coupled using ultrasound gel. Pressure force was applied on each of the sensor using magnetic clamps. The integral pre-amplifiers with 34 dB gain were used for signals from the sensors and the outputs of the transducers were connected to a Vallen 4-channel AMSY-6 System. Signals were acquired with the settings shown in Table 4.2. The amplitude of recorded noise was around 25 dB. Therefore, a 45 dB amplitude threshold was set.

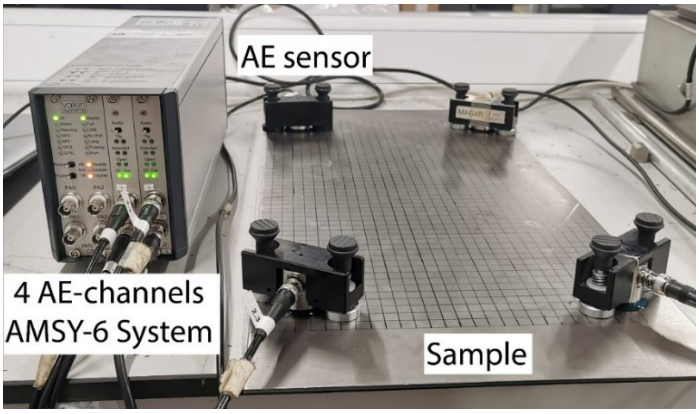

Figure 4.4–AE sensors mounted on 10×10 mm spaced grid specimen and connected to the AE systems.

Table 4.2 – AE acquisition settings.

Threshold (dB)	Sample Length (ms)	Sample Rate (MHz)	Pre-Trigger (ms)	Rearm time (ms)	Duration discrimination time (ms)
45	1.6	5	0.1	0.8	0.8

Experiments were carried out in the lab at TWI Ltd., Cambridge, UK. Bubble wrap was used to acoustically de-couple the sample from the workbench surface. Before starting the experiment, an H-N source was generated close to each AE sensor to assess sensor sensitivity and coupling between the sensors and testing plate. Hits with amplitude above 98 dB were recorded at each sensor, which verified the coupling. A total of three H-N sources using 0.5 mm 2H type pencil were performed to reduce erroneous data and provide a reliable average result. Recorded signal amplitudes showed virtually constant in the range of 80 dB to 100 dB with discrepancies of only a couple of dB for each sensor. Signals by the three H-N sources (H-N 1-1, H-N 1-2 and H-N 1-3) were presented in Figure 4.5 for each of the four sensors. A high consistency of signals at each sensor can be observed.

Because the four sensors were positioned symmetrically about the central axes of the plate and the H-N source is located on the central of the mild steel plate, which can be considered as isotropic and homogeneous, it was observed that the difference between the arrival time of the signals at Sensor 1 and Sensor 2 was very small, same as at Sensor 3 and Sensor 4. For simplicity, only results from Sensor 1 and Sensor 3 are displayed and discussed in the following sections.

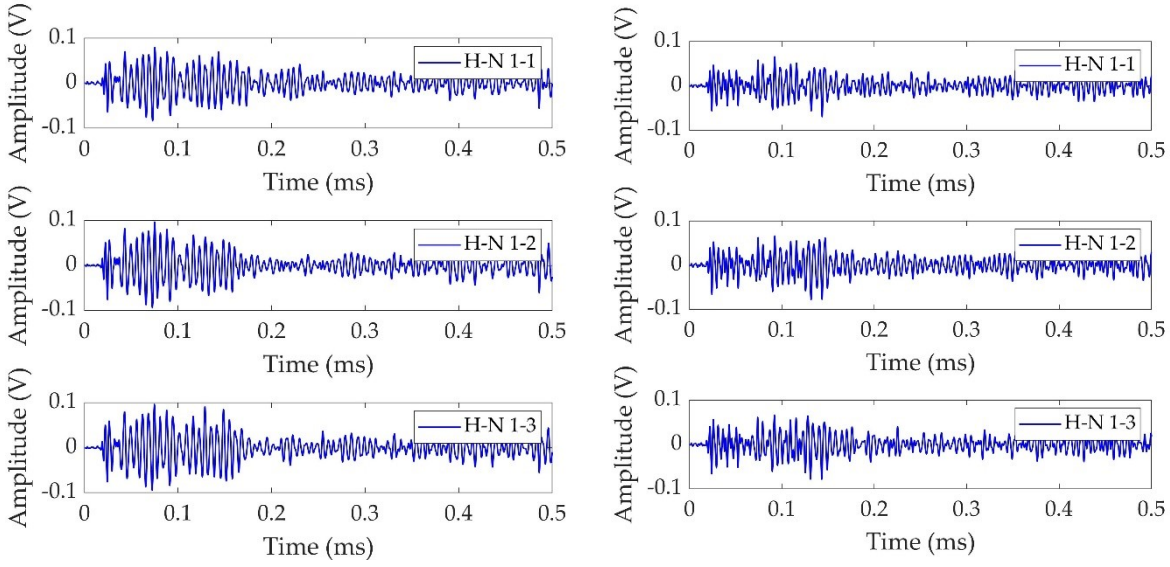

(**a**) sensor 1 (**b**) sensor 2

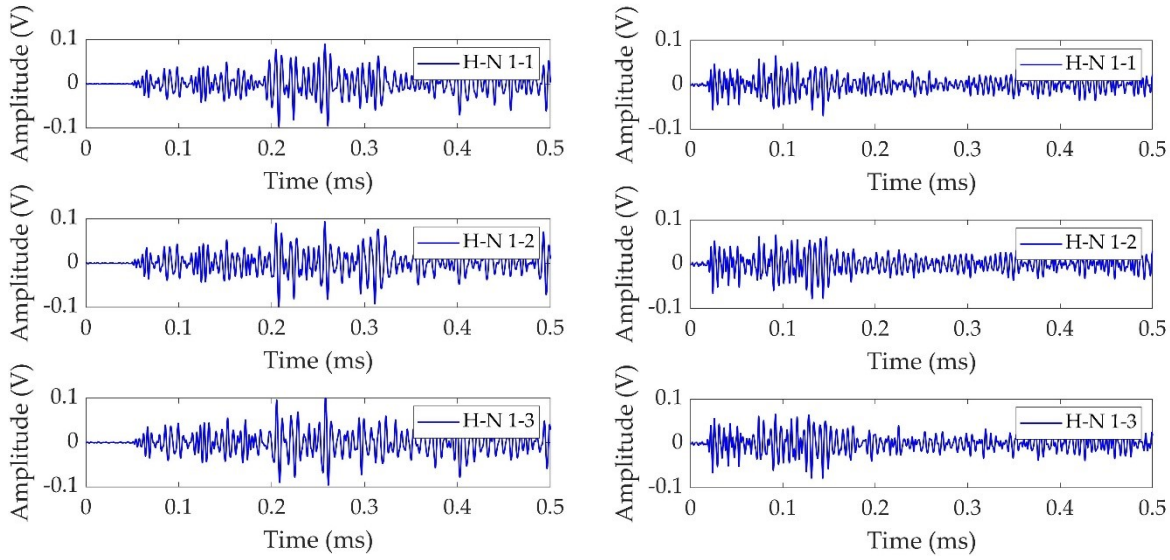

(**c**) sensor 3 (**d**) sensor 4

Figure 4.5–Signals recorded from H-N 1-1, 1-2 and 1-3 at (a) sensor 1, (b) sensor 2, (c) sensor 3 and (d) sensor 4.

4.2.3.1 Modal analysis

As discussed in Section 2.1.3, when two surfaces are introduced in a medium (i.e., a plate-like structure), the longitudinal and transverse waves couple at the surfaces and form new surface waves known as Lamb waves. Two major Lamb waves are S_0 and A_0 modes. Given the dispersive properties of elastic waves in flat plates, each wave mode with different frequencies has varied phases and group velocities, resulting in overlapping of some modes. As discussed in Section 2.3, WT is one of the most useful analysis tools for transient signals. It can be used to plot a time-domain graph showing the magnitude of the frequency spectrum of the signal. Hence, the amplitude of the AE waveform in both time and frequency domains can be viewed simultaneously. By overlapping the calculated dispersion curves with WT, the oncoming wave modes can be clearly distinguished.

Numerical and experimental signals at Sensors 1 and 3 are presented with WT diagrams processed using a Gabor wavelet in Figure 4.6 and Figure 4.7, respectively. Dispersion curves for Lamb wave propagation in a 3 mm steel plate has been superimposed onto the WT diagrams. These have been shifted manually to achieve a best fit between the arrival of the fastest S_0 mode in the dispersion curve with the arrival of S_0 mode on the WT color plot.

The movements of particles are mainly parallel to the plate for S_0 mode and perpendicular to the plate for the A_0 mode [36]. When an H-N source is conducted in plane to the sensor face, a large portion of the resulting displacement is normal to the plane of the plate giving rise to the A_0 mode, while there is still a small portion of displacement which is tangential to the plate because of Poisson effect, giving rise to the S_0 mode. Consequently, the A_0 mode has substantially larger out-of-plane amplitudes than the S_0 mode [49]. WT for each signal were then analyzed under two time periods before and after A_0 arrival.

As can be seen in Figure 4.6 and Figure 4.7, S_0 and A_0 are discernible within both experimental and numerical signals even though S_0 and A_0 components were not well separated in Sensor 1 signals. S_0 components have a faster velocity than the A_0 components [144]. It is shown that the arrival of the low amplitude S_0 component was followed by the high amplitude A_0 component. The first-arrival wave were attributed to the S_0 mode with low amplitude, followed by the A_0 mode with very high amplitude.

It can be seen that experimental and numerical WT diagram show a reasonably good agreement. The discrepancy in magnitude between the experimental and numerical WT magnitude at Sensor 1 can be explained by the fact that the frequency response of actual sensors was not simulated in the FE modelling.

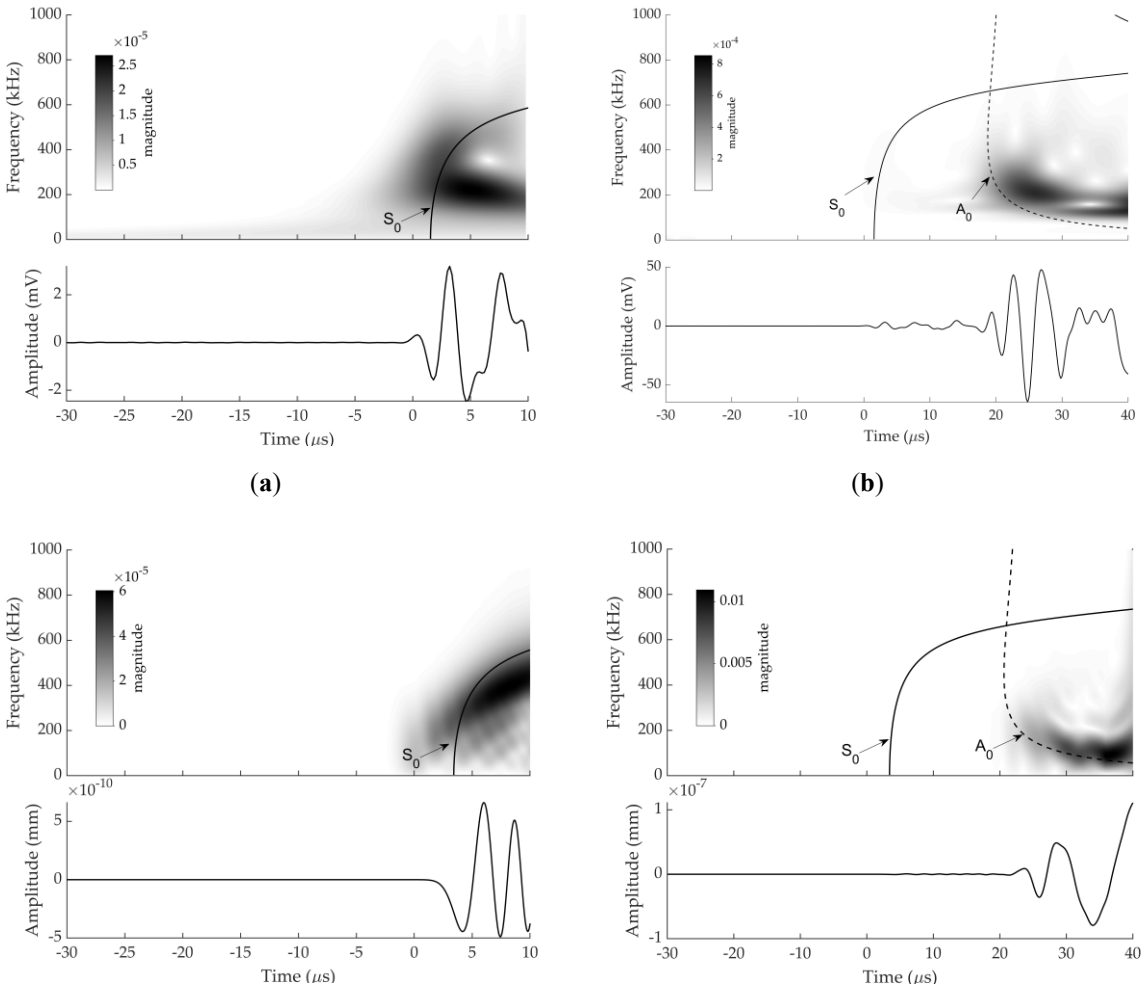

Figure 4.6–The signal at sensor 1 and corresponding WT diagram with superimposed dispersion curves; the experimental signal from (a) -30 to 10 μs, (b) -30 to 40 μs and the numerical signal from (c) -30 to 10 μs, (d) -30 to 40 μs (scale was changed to make the S_0 visible).

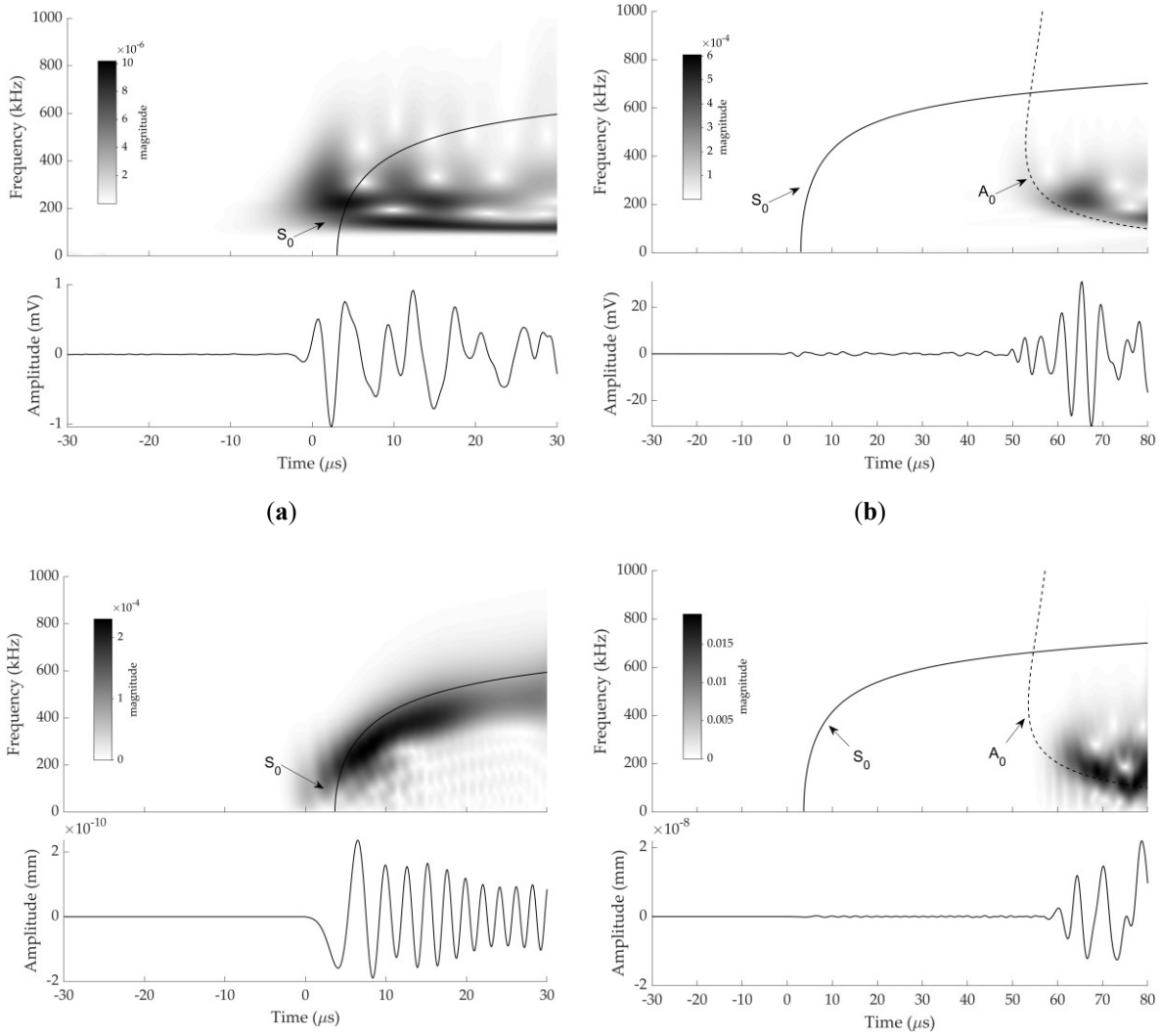

Figure 4.7–The signal at sensor 3 and corresponding WT diagram with superimposed dispersion curves; the experimental signal from (a) -30 to 30 μs , (b) -30 to 80 μs and the numerical signal from (c) -30 to 30 μs, (d) -30 to 80 μs (scale was changed to make the S_0 visible)

4.2.3.2 Velocity calculation

As discussed in Section 2.3, the arrival time can be predicted by considering the peak WT magnitudes at a known frequency [41- 43]. The maximum magnitude of WT in the time-frequency domain corresponds to the arrival time of the wave mode at the particular frequency traveling at the group velocity. Hence, the arrival times of specific frequency component can be determined. The frequency component of 200 kHz was used in the WT analysis to determine the arrival time of mode waves because both S_0 and A_0 modes can be

observed at this frequency according to the spectral analysis of captured signals, and the peak wavelet coefficients of both S_0 and A_0 modes are very clear at this frequency. The arrival time of S_0 and A_0 modes at 200 kHz was determined based on the peaks of the WT coefficients at 200 kHz shown in Figure 4.8 and Figure 4.9.

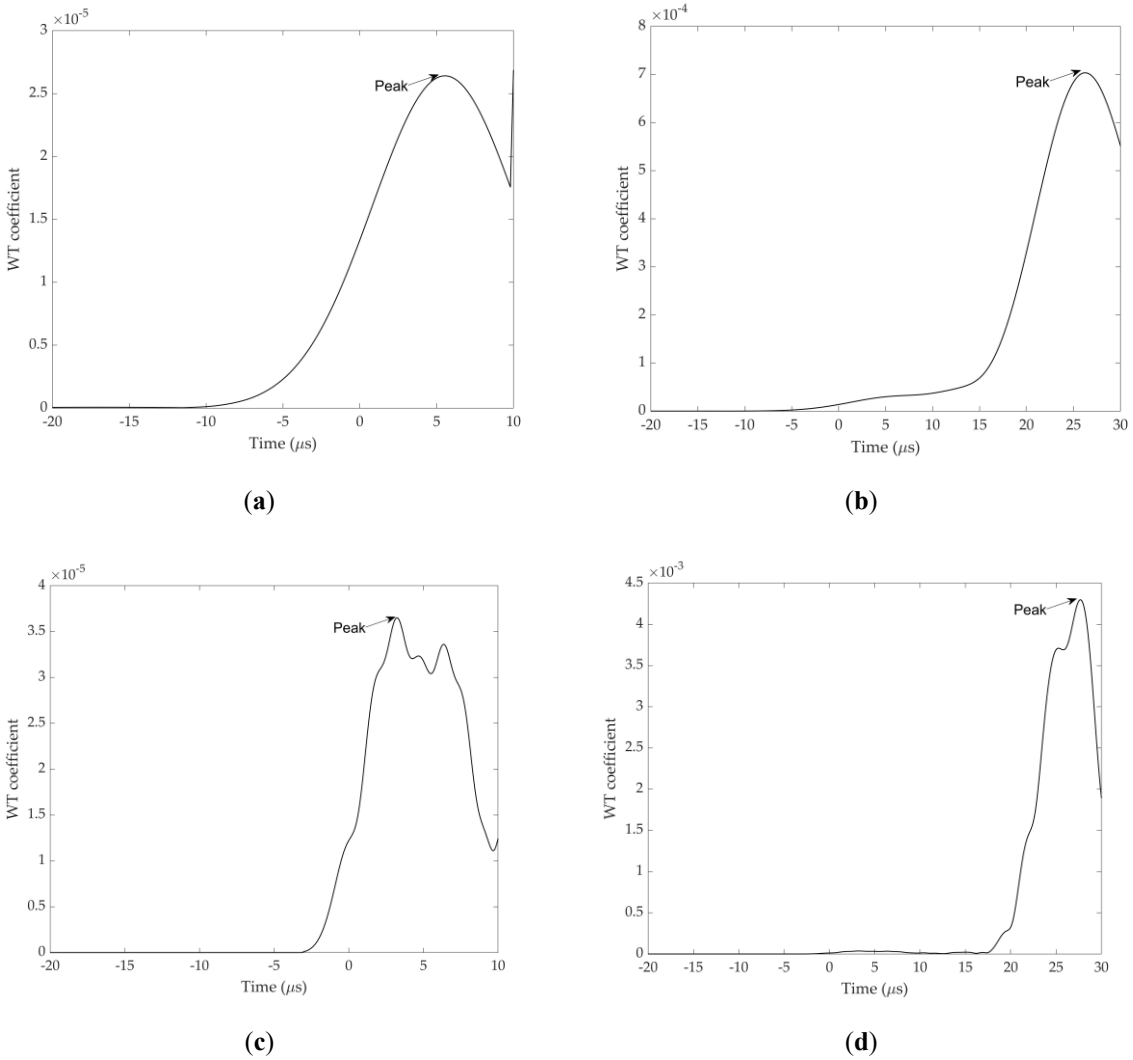

Figure 4.8– WT coefficient at 200 kHz of the signal at sensor 1; (a) the peak during S_0 arrival and (b) the peak during A_0 arrival in the experimental signal and (c) the peak during S_0 arrival and (d) the peak during A_0 arrival in the numerical signal (scale was changed to make the peak during S_0 arrival visible)

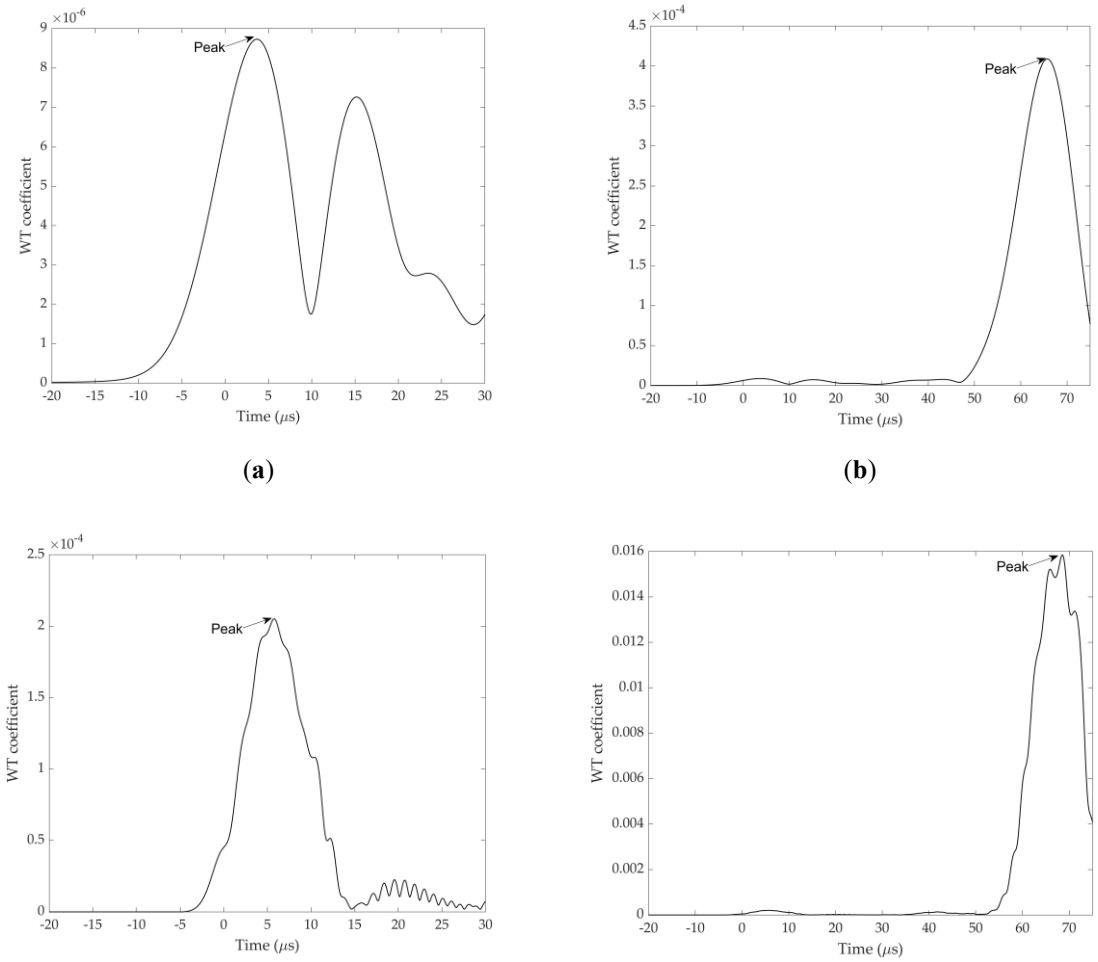

Figure 4.9– WT coefficient at 200 kHz of the signal at sensor 3; (a) the peak during S_0 arrival and (b) the peak during A_0 arrival in the experimental signal and (c) the peak during S_0 arrival and (d) the peak during A_0 arrival in the numerical signal (scale was changed to make the peak during S_0 arrival visible)

Using the following equation, the speed of S_0 and A_0 modes can be determined,

$$C = \frac{D_3 - D_1}{t_3 - t_1} \tag{4.4}$$

where:

C velocity of the wave mode

D_3 distance between the H-N source and sensor 3

D_1 distance between the H-N source and sensor 1

t_3 arrival time of the wave mode recorded at sensor 3

t_1 arrival time of the wave mode recorded at sensor 1

The velocities of S_0 and A_0 can also be predicted by classical plate theory. The results are summarized in Table 4.3. It can be seen that the discrepancy between experimental and numerical velocities of S_0 and A_0 is small. Numerical predictions are in good agreement with measured velocities. A reasonably good agreement can also be observed between experimentally measured velocities and theoretically predicted ones. The small discrepancies may be due to the resonant sensors used in the tests as they have higher sensitivity in particular frequency ranges and hence do not show a true reflection of the signal.

Table 4.3 – The theoretical, numerical and experimental velocities of S_0 and A_0 modes at 200 kHz (units: mm).

	Velocity of the S_0 mode	**Velocity of the A_0 mode**
Theoretical	5.200	2.961
Numerical	5.381	2.861
Experimental	5.309	2.848
Discrepancy*	1.356%	0.456%

*Discrepancy= (Numerical -Experimental)/Experimental

4.2.3.3 Arrival time estimation

Determination of arrival time of signals is crucial for localization of AE source. As discussed in Section 4.2.3.2, the arrival time can be predicted by considering the peak WT magnitudes at a known frequency. In addition to WT analysis, arrival time estimation methods including threshold crossing and AIC which were discussed in Chapter 2 were used in this study.

Because of many of the factors involved, such as the assumptions on the magnitude of the force, the time duration of an H-N source, and a simplified sensor model, etc., accurate prediction of AE signals' amplitudes in FE modelling were not achieved and is not of interest in this work. Moreover, as displacement was measured in the FE model while voltage was measured in the experiment, consequently, it is impossible to have the same threshold level for both experimental and numerical signals in the threshold crossing method. Therefore, this method was only used to estimate the arrival time of experimental signals. However, AIC and

WT analyses were used on both experimental and numerical signals. For simplicity, the delta-T for Sensors 1 and 3 was calculated. Results are summarized in Table 4.4.

Table 4.4 – Delta-T for sensor 1 and sensor 3 in the experiment and FE modelling (units: μs).

	Threshold crossing	**AIC**	**WT analysis**
Experiment	48.4	46.8	47.2
FE modelling	-	46.74	46.57
Difference	-	0.06	0.63

The estimated delta-T produced by the threshold crossing, AIC and WT analyses in the experiment showed very little difference. Compared with delta-T determined by AIC, threshold crossing and WT analyses showed a discrepancy of 1.6 μs and 0.4 μs respectively. Simulation predictions are well in agreement with experimental observations. For the delta-T estimated by AIC, a discrepancy of 0.06 μs was noted between experiment and FE modelling results. Good agreement was also demonstrated between delta-T in the experiment predicted by WT analysis and that of modelling, with a discrepancy of 0.63 μs. Moreover, for the simulation results, delta-T given by WT analysis was very similar to that given by AIC.

Overall, experimental and numerical WT diagrams show a reasonably good agreement. And the FE method is seen to give accurate results for velocities of S_0 and A_0. A high level of accuracy of the delta-T from FE modelling is found. It can thus be concluded that the numerical method for simulation of an H-N source on a simple plate was validated. This makes it potentially a useful tool for predicting arrival times of AE waveforms on a complex plate model. For estimations of the arrival time, results show that AIC is a viable option for estimating the onset of signals. As the accuracy of threshold crossing depends on the pre-set threshold level and the arrival time determined by WT analysis is the time at a single frequency, AIC was used to estimate arrival time of signals in numerical and experimental delta-T techniques.

4.3 Experimental and numerical delta-T mapping training on complex plate

Experimental delta-T maps were generated on a complex plate for the localization of experimental AE events. In parallel, using the numerical method validated in Section 4.2, H-

N sources were simulated on a complex plate model. Information including arrival times of signals at each sensor was collected to build numerical delta-T maps. Localization results produced by numerical and experimental delta-T mapping were compared.

4.3.1 Experimental delta-T mapping training on complex plate

The delta-T mapping technique requires the structure to be mapped and the training maps are created by performing H-N sources. Following the procedural steps of implementing delta-t mapping technique [75] which are presented in Section 2.4.3, an experimental delta-T map was built.

A mild steel plate with four holes, thus termed a 'complex plate' to differentiate with the simple plate which has no holes, was used for experimental delta-T mapping training. The dimensions of the specimen with coordinates of the centers of four holes and radiuses are shown in Figure 4.10.

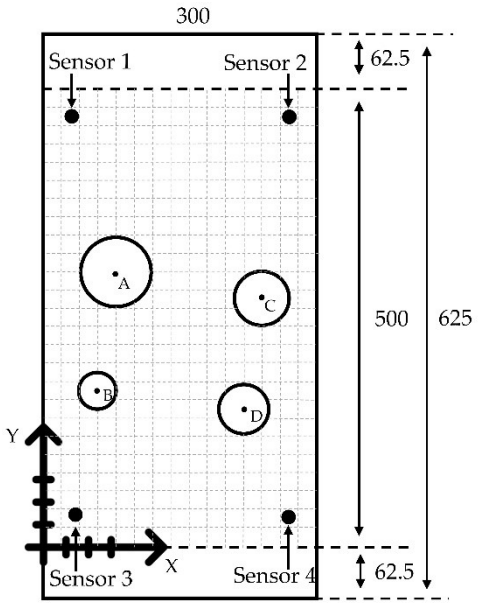

	X coordinate	Y coordinate	Radius
A	80	300	40
B	60	170	20
C	240	270	30
D	220	150	30

Figure 4.10–Schematic layout of the sensors and H-N sources on complex plate model with 20mm spacing grid (unit: mm).

The locations of all sensors were the same as those in the experiment on the simple plate described in Table 4.1. The central 500mm section was the area of interest and a coordinate system was introduced. A training grid was placed on this area. The spacing of the grid was

20 mm as prior research [76] has shown that further reduction in size has minimal influence on accuracy. The arrival time data, which were determined by AIC, were collected after the generation of an H-N source at each node of the grids. For each sensor pair, a delta-T map was produced. An example of a delta-T map produced for Sensor 1 and Sensor 2 and plotted as contours of equal delta-t is shown in Figure 4.11. The information stored at each node of a delta-T map includes node coordinates and average delta-T.

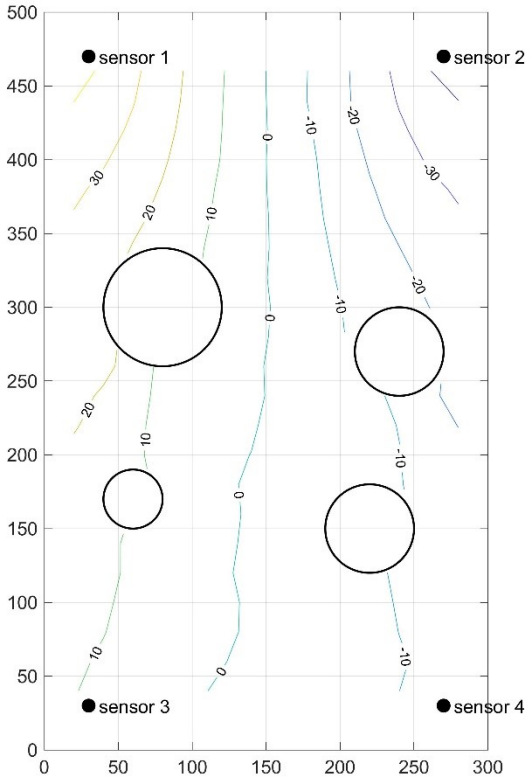

Figure 4.11– A delta-T map produced for sensor 1 and sensor 2.

The number of maps to be produced is given by $N * (N - 1)/2$, where N is the number of sensors in the network. For example, for 4 sensors (i.e. Sensors 1 to 4) in the network, a total of 6 delta-T maps (i.e., 1-2, 1-3, 1-4, 2-3, 2-4 and 3-4) will be produced.

The delta-Ts for each sensor pair from a real AE event can be calculated and used to identity a line with equal delta-T in the corresponding map. This line represents all possible real AE event locations in each map. By overlaying all resulting maps, the location of the real AE event can be determined. An example of overlaid delta-T maps is presented in Figure 4.12. Each line in the figure represents contour with constant delta-T corresponding to that of the

H-N sources identified on the map of each sensor pair. The convergence point indicates the location of the AE source.

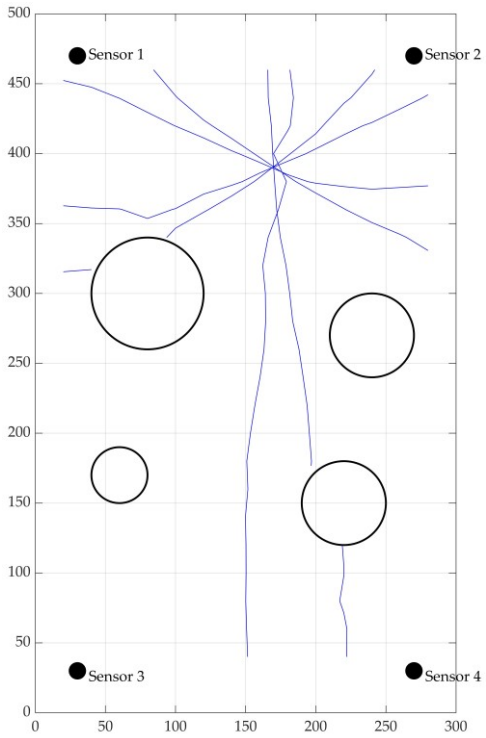

Figure 4.12– An example of overlaid delta-T maps.

4.3.2 FE generated delta-T mapping training on complex plate

In parallel, FE modelling was performed to produce a FE generated delta-T map or numerical delta-T map. As shown in Figure 4.13, a complex plate model was created in ABAQUS. As in the FE modelling of H-N sources on the simple plate in Section 4.2.2, steel material properties, mesh resolution of 1 mm, time integration step of 0.01 μs, C3D8R element and the same boundary conditions were used for simulation. The locations of sensors and the gird were chosen to be the same as those in the experiment on the complex plate described in Section 4.3.1. The validated numerical method described in Section 4.2.2 was used to simulate an H-N source on each node of the grid. Displacements in Z direction (out-of-plane) over time of all nodes at locations of sensors were recorded in FE modelling to estimate the arrival time. AIC was used to determine the arrival times of simulated signals. The FE

generated delta-T map was built in the same way as experimental delta-T maps in Section 4.3.1.

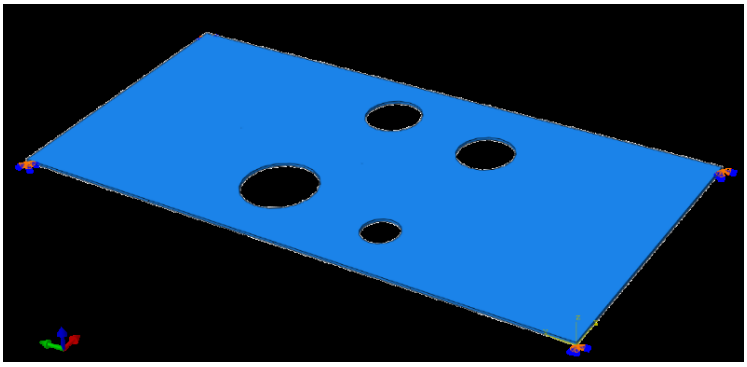

Figure 4.13– Complex geometry plate modelled in ABAQUS.

4.3.3 Experimental test data on complex plate

In order to test the performance of experimental and numerical delta-T maps, six extra H-N sources (H-N source 1 to 6) were conducted at six off-grid locations on the complex plate in the experiment. The schematic layout of the six extra H-N sources on the complex plate is presented in Figure 4.14. Coordinates of the location of the extra H-N sources relative to the origin are given in Table 4.5.

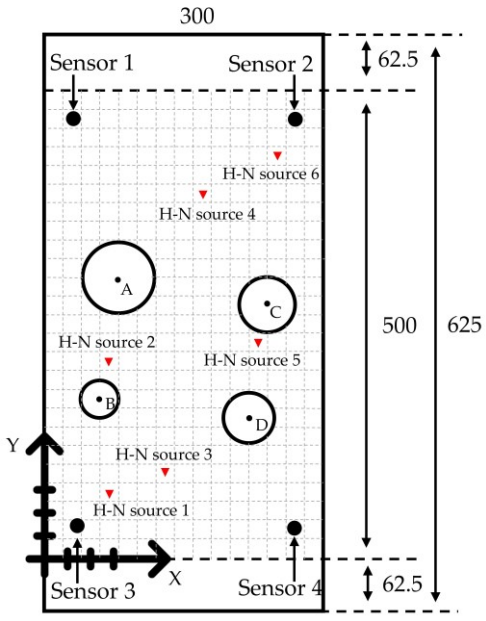

Figure 4.14– Schematic layout of six extra H-N sources on complex plate.

4.3.4 Results

The AE test data collected from H-N source 1 to 6 were assessed with the traditional TOA location approach based on threshold crossing (TOA-TC for short), TOA location approach based on AIC method (TOA-AIC), experimental delta-T mapping (experimental delta-T) and numerical delta-T mapping (numerical delta-T) techniques. Table 4.5, Figure 4.15 and Figure 4.16 document source location results and the associated Euclidian distance errors.

Table 4.5 – Actual locations of six extra H-N sources and results calculated by TOA-TC, TOA-AIC, numerical delta-T and experimental delta-T (units: mm).

	H-N source 1			**H-N source 2**			**H-N source 3**			**H-N source 4**			**H-N source 5**			**H-N source 6**		
	X	**Y**	**Error**	**X**	**Y**	**Error**	**X**	**Y**	**Error**	**X**	**Y**	**Error**	**X**	**Y**	**Error**	**X**	**Y**	**Error**
Actual	70	70	-	70	210	-	130	90	-	170	390	-	230	230	-	250	430	-
TOA-TC	74.42	59.19	11.68	83.04	207.21	13.34	134.54	79.42	11.51	168.99	397.51	7.58	213.60	223.92	17.49	244.54	438.59	10.18
TOA-AIC	77.13	61.63	11.00	81.29	210.88	11.32	133.89	83.19	7.84	167.79	393.18	3.87	222.44	224.29	9.47	246.58	434.70	5.81
Numerical delta-T	74.82	67.80	5.30	73.99	211.46	4.25	132.26	91.41	2.66	169.33	386.67	3.40	225.27	229.86	4.73	251.17	432.7	2.94
Experimental delta-T	71.54	66.80	3.55	67.39	210.13	2.61	132.89	90.03	2.89	169.93	390.35	0.36	231.13	230.45	1.22	248.96	433.33	3.49

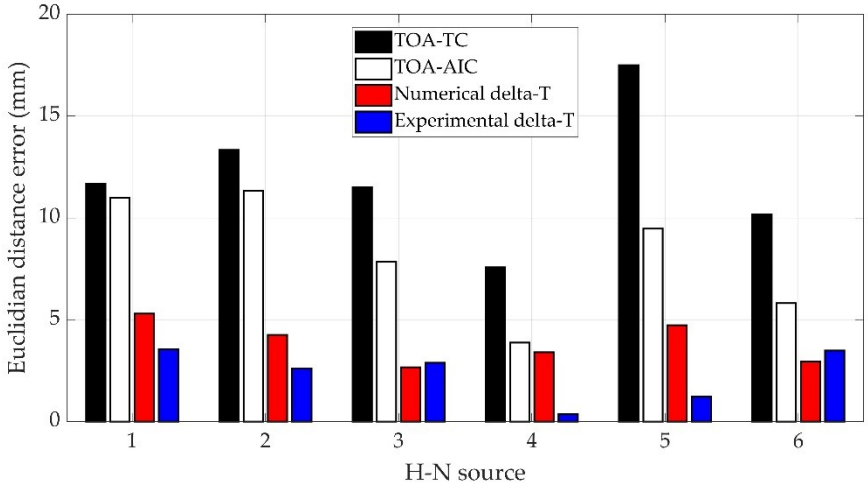

Figure 4.15–Euclidian distance errors of source location results.

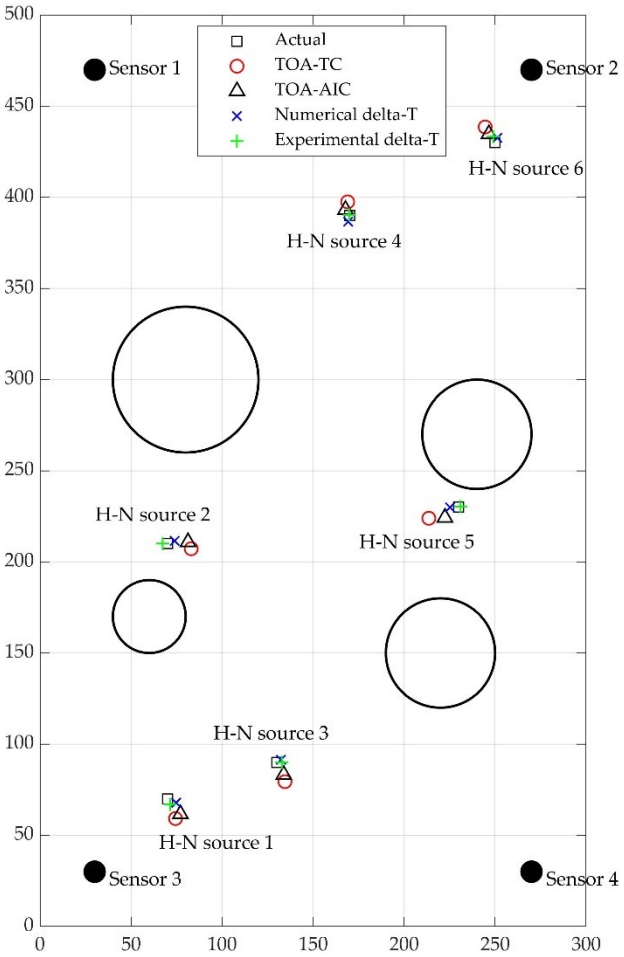

Figure 4.16–Actual locations of H-N sources and results calculated by TOA-TC, TOA-AIC, numerical delta-T and experimental delta-T (units: mm).

For H-N sources 1 and 2 shown in Figure 4.16 respectively, it can be clearly seen from Fig. 4.18 that a small improvement in accuracy was observed after AIC method was used in the TOA localization technique. For H-N source 1, the error for TOA-TC and TOA-AIC were 11.68 mm and 11.00 mm respectively, or a 5.82 % reduction using AIC. For H-N source 2, the error for TOA-TC and TOA-AIC were 13.34 mm and 11.32 mm respectively, a 15.14% reduction using AIC. Compared with TOA-AIC, experimental and numerical delta-T reduced the error by more than half. The locations located with the experimentally trained delta-T maps were more accurate than those located with numerically trained delta-T maps.

H-N source 3 was located in the lower part of the specimen close to the central line. The TOA-AIC produced a location error of 7.84 mm compared with 11.51 mm by TOA-TC, a

reduction in error of 31.89%. The experimental and numerical delta-T gave similar levels of error, with a slightly higher accuracy by experimental delta-T.

H-N source 4 was located on the upper part of the specimen close to the central line. The location error produced by the TOA-TC was 7.58 mm, which was the smallest amongst all the location errors gave by TOA-TC. TOA-AIC reduced the location error to 3.87 mm, a 48.95% reduction. The results showed small difference in location errors when TOA-AIC and numerical delta-T were used, with the latter having slightly higher accuracy. The accuracy of location H-N sources was significantly better when using the experimental delta-T with a Euclidean error distance of 0.35 mm.

H-N source 5 sits on the middle right of the specimen. The TOA-TC, TOA-AIC and numerical delta-T all located the H-N source slightly to the left of the actual position with a Euclidean error distance of 17.49 mm, 9.47 mm and 4.73 mm, respectively, while DTM located the source to the right of the actual location with an error of 1.22 mm.

H-N source 6 locates near sensor 2 in the up-right corner of the specimen. The TOA-TC, TOA-AIC predicted the source locations with a error of 10.18 mm and 5.81 mm respectively. Similar to H-N source 3, a slightly lower location error at 2.94 mm was given by the numerical delta-T, compared to 3.49mm given by the experimental delta-T.

In general, as it had been found also by some other researchers [75] [134] that the delta-T mapping technique improved the source location accuracy on complex structures. Results obtained show noticeable improvements in source location accuracy when using the two delta-t mapping methods over the TOA technique. Furthermore, other than H-N sources 3 and 6, a higher degree of accuracy of location was shown when using the experimental delta-T over the numerical delta-T. As as for the TOA technique, the AIC method led to a marked improvement in accuracy. This was expected since the AIC method is considered to be more accurate in the arrival time determination than the threshold crossing [76].

To identify areas where the numerical delta-T is less accurate, the difference in the delta-T values between the numerical and experimental delta-T for each node was plotted and presented in Figure 4.17.

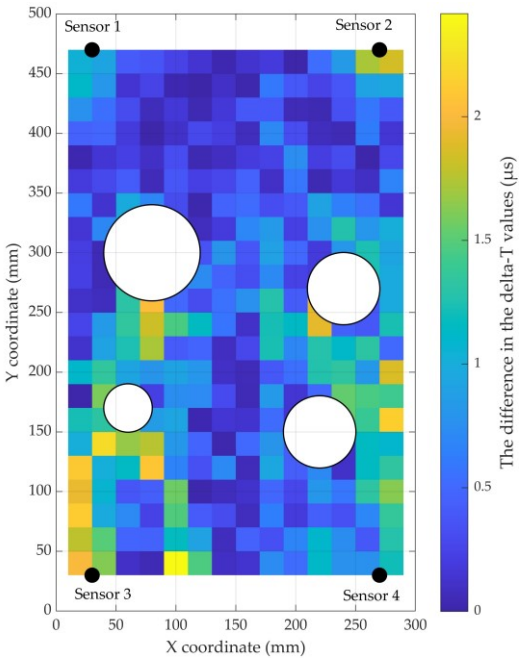
Sensor 1
Sensor 2
Sensor 3
Sensor 4
Y coordinate (mm)
X coordinate (mm)
The difference in the delta-T values (µs)

(**a**)

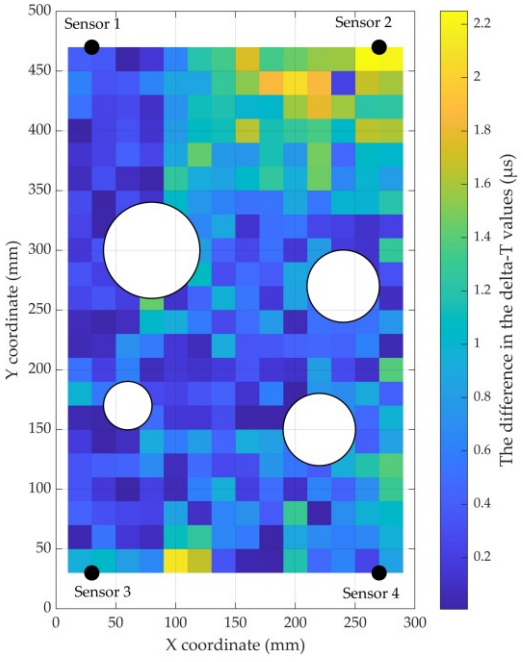
Sensor 1
Sensor 2
Sensor 3
Sensor 4
Y coordinate (mm)
X coordinate (mm)
The difference in the delta-T values (µs)

(**b**)

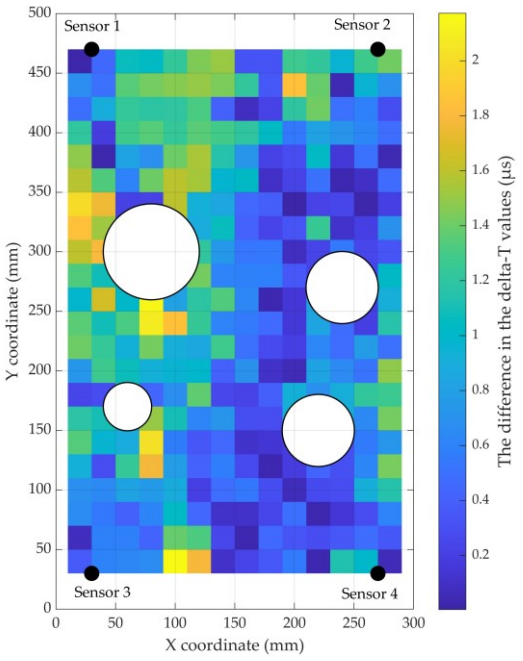
Sensor 1
Sensor 2
Sensor 3
Sensor 4
Y coordinate (mm)
X coordinate (mm)
The difference in the delta-T values (µs)

(**c**)

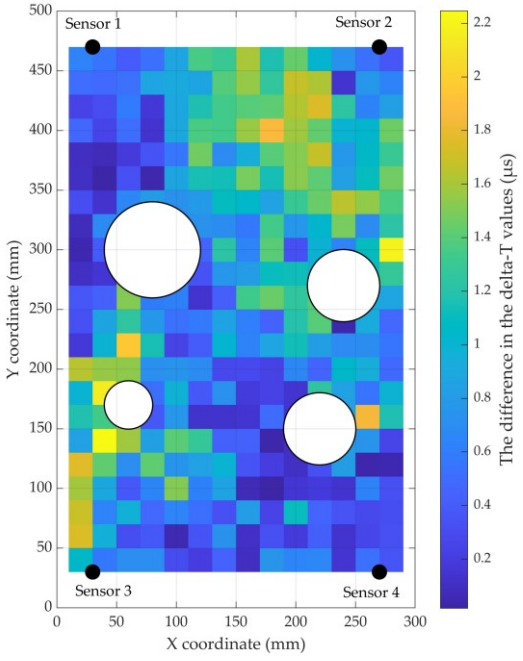
Sensor 1
Sensor 2
Sensor 3
Sensor 4
Y coordinate (mm)
X coordinate (mm)
The difference in the delta-T values (µs)

(**d**)

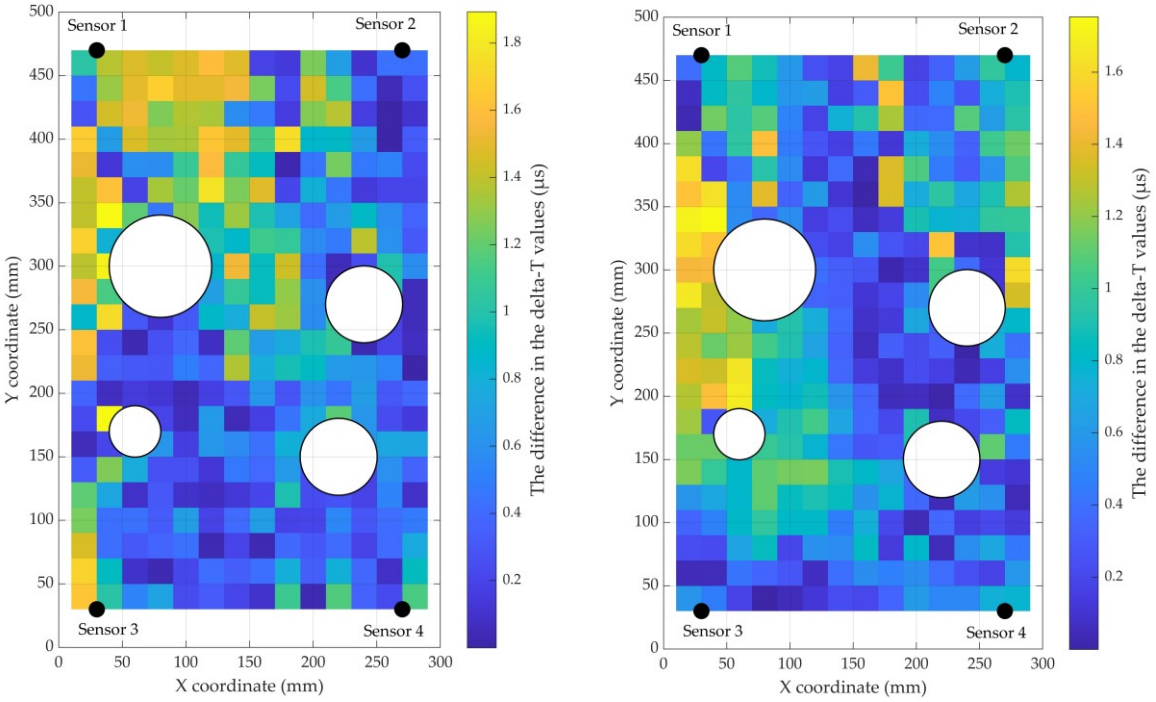

Figure 4.17– The difference in the delta-T values between the numerical and experimental delta-T maps for (a) sensor pair 1-2, (b) sensor pair 1-3, (c) sensor pair 1-4, (d) sensor pair 2-3, (e) sensor pair 2-4 and (f) sensor pair 3-4.

As shown in Figure 4.17, for sensor pair 1-2, errors around 2 mm can be seen in zones close to Senor 2 and 3, and between the holes. For sensor pair 1-3, the FE modelling was able to produce a delta-T map with high accuracy over the whole complex plate, other than zones close to the sensor 2. For sensor pair 1-4, it can be seen that zones with large errors are located around the biggest hole, i.e., hole A. For sensor pair 2-3, the delta-T map generated by the FE modelling has a large error in zones close to Sensor 2 and around the smallest hole B. For sensor pair 2-4, good accuracy can be seen in the majority of zones, other than those near Sensor 1 and hole A. For sensor pair 2-4, errors occur mainly in zones between hole A and the plate edge.

In general, it is evidential that for the majority of nodes on the delta-T maps, the delta-T values have been accurately predicted using the FE method. Nodes where the numerical delta-T is less accurate are mainly close to the sensors and around the holes. This can be attributed partially to the boundary conditions used in the FE model, which are not exact as

those of the physical structure in experiment, and may influence wave propagation and result in differences between the arrival time recorded in experiments and from the FE modelling.

4.4 Discussions

Using numerical approaches such as FE to generate delta-T mapping offers some advantages over experiments. Firstly, for experimental delta-T, it takes a number of days to set up the experiment, perform H-N sources on all the grid points, select and prepare the AE data to build the delta-T maps. For the numerical delta-T, it takes 0.5 days to build a FE model. The computation time for simulation of an H-N source on each node of the grid is 5 minutes on a personal laptop. There is a total of 285 nodes in the present model, which results in a computation time of 1 day. The total time for the whole process is 1.5 days. This reveals that the numerical delta-T decreases the time required for constructing a delta-T map. It is worth noting that processes of experimental and numerical delta-T mapping could be optimised to reduce these times. To ensure maximum accuracy, an operator with an AE background is required to manually sort and discard useless arrival time data being captured experimentally [79]. With numerical delta-T, data is captured autonomously, which means that collection and processing of training data do not rely on experience and human errors are removed. Moreover, the expenses associated with the equipment and labour required for experiments can be eliminated. Furthermore, numerical delta-T mapping method scales better compared with experimental delta-T. With FE method, large-scale models with numerical sensors can be easily created for collection of training data, whilst experimental collection of delta-T data may be limited by several factors including large size or complex structures. Moreover, instead of artificial AE sources which can only be performed on the surface in experiment, FE method allows multiple training sources such as fatigue [99] and fibre breaks [147] and internal damage to be modelled. This might be a solution to a 3-D delta-T location problem. A final benefit of numerical delta-T is that the risk of foreign object debris from broken pencil leads is eliminated, which in some sectors is a major consideration.

However, numerical delta-T also has some disadvantages. One of the main difficulties lies in modelling of wave propagation in highly complex structures, such as composites which are

being used abundantly in safety critical structures in recent years. Furthermore, the fine mesh is required to model AE waves with high accuracy. The amount of degrees of freedom in a large complex FE model will be huge, leading to a significant demand for computational resources such as memory space and processor time. The solution for this could be using fine meshes over the area of interest and coarse meshes over other areas.

The source location errors associated with experimental delta-T techniques were found. There are numerous factors which contributed these errors. Firstly, the VS150-RIC sensors used in the test have a sensor face diameter of 28.6 mm, which is relatively large. Since the arrival time error is directly proportional to the size of the sensor face [134], the use of VS150-RIC sensors may lead to relatively large arrival time errors, thus resulting in source location errors. Moreover, AE signals usually contain a wide range of frequencies. Higher sample rates allow for better representation of higher frequency content in AE signals. Using an inadequate sample rate can cause crucial frequency contents to be lost, leading to errors in arrival time estimations and ultimately resulting in inaccurate source location predictions. In addition, the boundary conditions within a complex plate may result in a loss of energy of an AE wave. Therefore, the signal amplitudes may be strongly attenuated during wave propagation, which in turn can adversely impact the accuracy of arrival time calculations, thus affecting source location determination.

It was also found that numerical delta-T techniques had a larger magnitude of average source location error compared to experimental delta-T techniques. There are several reasons why this is the case. Firstly, a source of error is that the AE sensor face is not considered as the sensor is simplified as a point in the modelling. It could be stated that the signal in experimental training is captured at the sensors' circumference rather than sensors' center point where simulated sensors locate, thereby resulting in different arrival times. Numerical study conducted by Tsangouri and Aggelis [148] shows that the size of simulated AE sensor has a direct effect on wave content in time domains. The source location accuracy produced by finite element generated delta-T map may be improved if the AE sensor with the sensor face can be modelled.

Moreover, the limitation is that TOA-TC, TOA-AIC, numerical delta-T and experimental delta-T have not been trialled to locate real AE data. As real damage sources [134] usually

have smaller amplitude and different frequency content compared with H-N sources, It will be of interest to examine the performance of four methods with AE signals generated from real damage mechanism. Secondly, only holes were considered in the complex plate in the present study, However, other complexities of real structures include multiple thickness changes, stiffeners, holes, nozzles, welds, etc. need to be considered in the future study. Thirdly, the defined boundary conditions in the model were not the same as real boundary conditions of the plate. The wave propagation will be slightly influenced by the edge of the hole on the complex plate and thus might result in errors in arrival time. By applying realistic boundary conditions in FE model, the influence of the edges of holes on the first arrival of AE waves can be eliminated. The accuracy of arrival time of signals recorded in complex FE model can be improved. Furthermore, the material defined in the FE model was an isotropic homogenous metallic material. As composites are increasingly used in oil and gas industry, it would be beneficial to examine the performance of a modelled delta-T training dataset on composite material. Besides, it should be noted that delta-T mapping technique and other localization technique do not account for factors such as temperature, loading and changing sensor coupling. It will be of interest to investigate how these factors will influence the delta-T maps and how to update delta-T maps accordingly. Finally, currently, commercial AE systems are not capable of applying experimental and numerical delta-T mapping techniques live. However, it will be beneficial to integrate these methods with commercial AE systems to observe online AE events.

4.5 Conclusions

In this investigation, a numerical method from literature was used to simulate the H-N source on a simple plate and validated by the experiment results. The validation of the FE model showed great promise for applying the FE method to a planar location problem on a complex plate. Using the same numerical method, H-N sources were simulated on a complex plate and a numerical delta-T map were generated. The location results of numerical delta-t map technique were compared with those of traditional TOA techniques and experimental delta-t map technique. It has been demonstrated the viability of using FE method to decrease the time and man-power required for manually collecting and processing the training data whilst

keeping a reasonable degree of source location accuracy with an average error of 3.88 mm. With such a high source location accuracy, the particular area of concern which needs to be inspected using other NDE techniques can be reduced greatly. Moreover, if the specific location of an AE event is identified on an area with particular geometric features or loading condition, the number of potential damage source mechanisms can be decreased.

Although the FE generated delta-T mapping has been carried out successfully, it will be preferable to examine the performance of present FE generated delta-T maps with AE signals from real damage mechanism. Development of FE model such as improved boundary conditions, realistic AE sensors, additional complexity and anisotropic materials needs to be investigated for further study.

Chapter 5 Improved Acoustic Emission Source Location of Corrosion with Delta-T Mapping

5.1 Introduction

Corrosion is a natural phenomenon and a major cause of the steel structures deterioration. In some extreme cases, it can lead to the reduction of a structure's load-bearing capacity, thus resulting in life-threatening situations and catastrophic failure. Therefore, it is essential to address this issue for safety, environmental, and economic reasons.

Carbon steel is the most commonly used and popular engineering material, comprising approximately 85% of the annual global steel production [149]. It has a higher concentration of carbon than other types of steel and a limited alloy content, which is generally below 2% (by weight) of the total additions [150]. Unfortunately, this level of additions do not have a significant impact on the corrosion behaviour of carbon steel [150]. In general, under industrial operation conditions found in the oil and gas exploration where acidic solutions are used extensively and as such carbon steel used in these environments shows susceptibility to corrosion. Despite its relatively weak corrosion resistance in industrial environments, it is widely employed in substantial tonnages for the oil and gas industry [151] because of the low cost and high resistance to wear and tear. With regard to both tonnage and total cost, carbon steel is the largest single class of alloys in use. Therefore, the carbon steel corrosion is an enormously important problem [152].

Hence, it is necessary to carry out periodic inspections to prevent destruction from corrosion. Various types of conventional NDT methods such as ultrasonic thickness measurement [153] and magnetic flux leakage [154] are utilised in corrosion monitoring. Though good accuracy in corrosion measurement is achieved by NDT methods, many components need to be removed from the testing equipment and refitted thereafter, thus requiring a long period of downtime. Moreover, areas of difficult access and complex geometry are particularly difficult

to examine by the NDT techniques, thus making the evaluation laborious, high-cost, and usually inconclusive.

Additionally, electrochemical methods such as electrochemical noise measurement [155,156], linear polarization resistance probe [157] and electrical resistance probe [158,159] have been implemented to examine and evaluate corrosion. They are very useful to predict the initiation of corrosion events [160]. However, it is very difficult to interpret the recorded data and investigate the underlying mechanisms during corrosion propagation [114].

Compared to the above-mentioned alternative methods of corrosion monitoring, AE directly measures failure mechanisms related to corrosion. AE offers a number of advantages; it is a desirable technique that has the capability to globally monitor large-scale structures using a suitable array of sensors. AE also allows for damage in areas inaccessible for physical inspection with current NDT methods to be detected. Moreover, it provides the ability to monitor structures without requiring a total stoppage or shutdown. Furthermore, the locations of AE sources can be determined with an appropriate sensor array. However, no literature references were found for monitoring corrosion with AE techniques on a complex structure. Hence, this study seeks to fill this research gap. Since delta-T mapping technique was developed by Baxter et al. [75] and an improvement in AE source location accuracy in complex structures has been shown. Hence, delta-T mapping is regarded to be a suitable method for AE source location of corrosion damage in complicated geometric structures.

The objectives of this chapter are to gain an understanding of the characteristics of the AE signals generated from corrosion, and to enhance the capability of AE in detecting and locating corrosion damage with delta-T mapping technique in complex structures.

In this chapter, a corrosion test was performed on a simple plate and a novel time estimation method was proposed to identify the onset time of signals. The velocities and source locations of AE events were calculated. It was found that the first arrival mode of signals recorded by AE sensors were was attributed to the A_0 mode. Following that, methods aimed towards determining the arrival of the A_0 mode with a lot of S_0 arrivals were discussed because the current delta-T mapping technique relies on identifying the arrival time of the S_0

mode. Afterwards, delta-T mapping technique based on the arrival of the A_0 mode was developed and tested using real AE data generated from corrosion.

5.2 Corrosion test on simple plate

5.2.1 The corrosion process

Corrosion is the disintegration of an engineered material into its constituent atoms as a result of electrochemical reactions with surroundings [161]. The type and rate of corrosion mechanism are dependent on multiple factors, including the type of material and corrosive environment [162]. Since the most prevalent type of corrosion is uniform corrosion [163], which is defined as the attack proceeding evenly over the entire metal surface area exposed to a corrosive environment. This leads to a uniform thinning rather than appreciable localised attack of the metal from the exposed surface [164]. There are two basic theoretical stages of a uniform corrosion mechanism; in the initial stage, the primary surface of the metal is attacked by chemical solutions. Secondly, a corrosion nucleus propagates on the surface area of the metal as a uniform corrosive engine.

5.2.2 Experimental setup

As discussed above, since this study focuses on monitoring carbon steel corrosion, a commercial sheet of grade S275 mild steel (Lakeland Steel Ltd., Cumbria, UK) was used for the experiment. The chemical composition of this mild steel is given in Table 5.1.

Table 5.1 – Chemical composition of S275 mild steel.

Element	C	Si	Mn	P	S	Ni	Cr	Mo	Cu
wt%	0.15	0.01	0.86	0.006	0.014	0.031	0.016	0.003	0.052

The specimen (500 mm × 300 mm × 3 mm) was washed in de-ionised water and then rinsed with acetone solution. After rinsing, the specimen was dried under a stream of cold air. The investigations were carried out in 3.5 % sodium chloride solution (pH was measured by a

calibrated pH meter to be 5.7). The test setup, a schematic diagram and an associated section view are shown in Figure 5.1, Figure 5.2 and Figure 5.3 respectively.

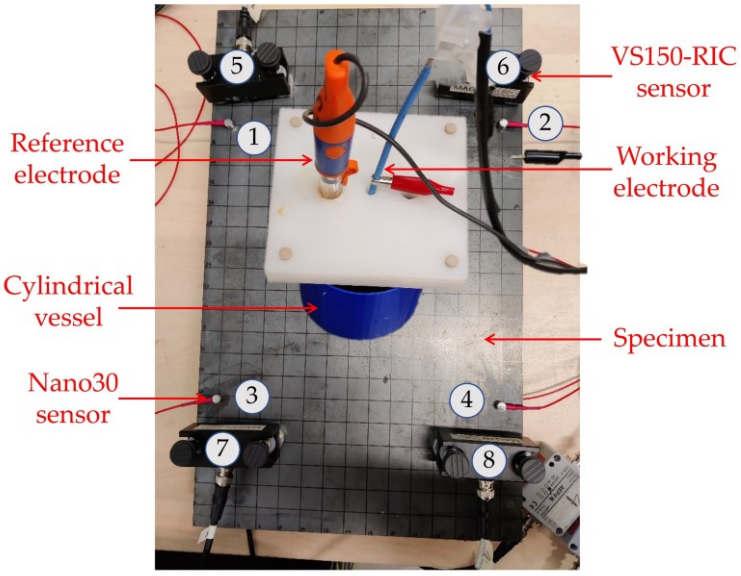

Figure 5.1–The test setup of the corrosion test

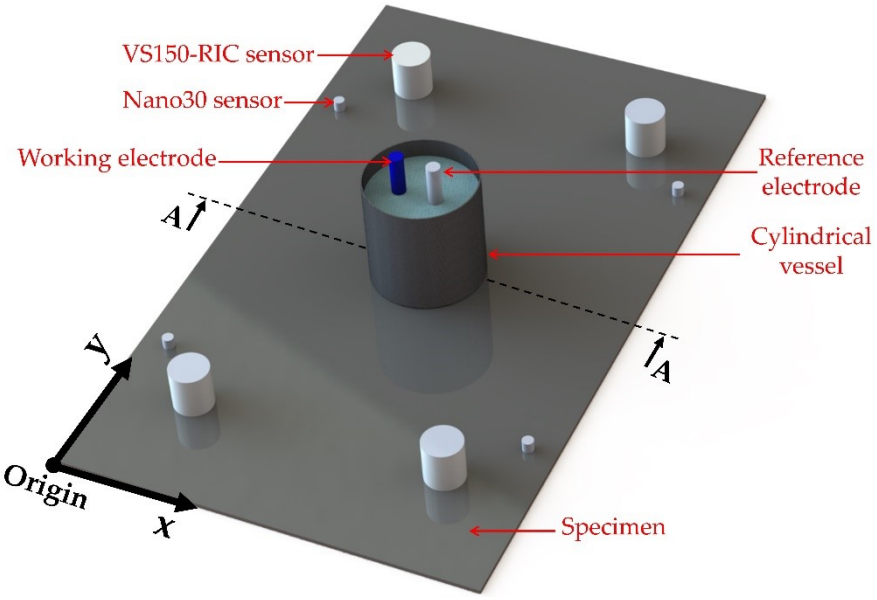

Figure 5.2– A schematic diagram of the test setup

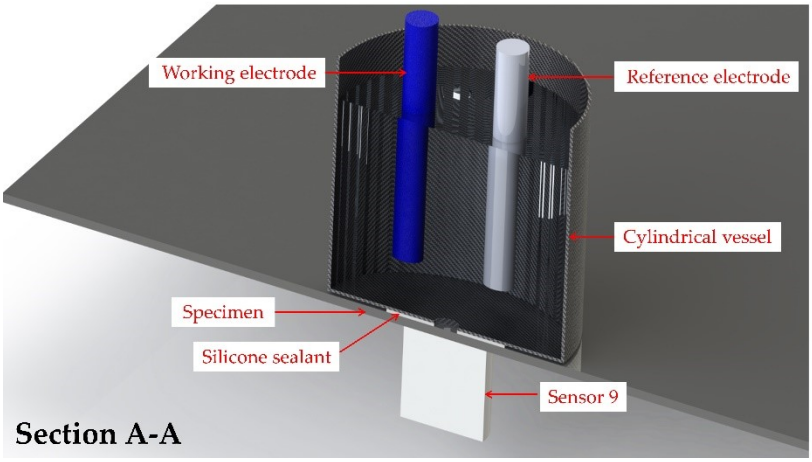

Figure 5.3– A an associated section view of the test setup

As seen, the solution was placed in a cylindrical thin-walled plastic vessel (outer diameter= 80 mm, height= 80 mm and thickness= 2 mm). There was a small hole (radius =4 mm) on the bottom to allow for the specimen to be in contact with the solution, that is, providing an exposed surface area of 16 π mm^2. A waterproof silicone sealant (Everbuild Building Products Ltd., Leeds, UK) was applied around the hole to attach the cylindrical vessel to the specimen and prevent the leaking of the test solution.

The uniform corrosion process was controlled in typical three-electrode electrochemical cell at room temperature. The specimen was served as the working electrode and a coiled platinum wire was used as a counter electrode. The measurement of the potential was made against a reference saturated Ag/AgCl/NaCl electrode. The electrochemical corrosion process at the static corrosive potential was controlled using a potentiostat/galvanostat system Gill AC (ACM Instruments, Cumbria, UK).

In addition to the potentiostatic measurements carried out by application of electrochemical, digital measurement system, measurements of uniform corrosion by AE method were carried out simultaneously. As shown in Figure 5.2, four resonant Nano-30 sensors (Mistras Group Inc.,New Jersey, United States), which have a resonance of 300 kHz with operating range of 125-750 kHz and four resonant VS150-RIC sensors (Vallen Systeme GmbH, Germany),which have a resonance frequency equalling to 150 kHz and a bandwidth of 100-450 kHz, were mounted at the top surface of the specimen. In addition, a VS150-RIC sensor,

which was sensor 9, was installed at the centre point of bottom surface of the specimen, below the corrosion site as shown in Figure 5.3. A two-dimensional coordinate system was introduced and the origin was placed on the bottom left corner of the specimen. The centre of the surface area exposed to sodium chloride solution coincided with the centre point (X coordinate = 150 mm, Y coordinate =250 mm) of the top surface of the specimen. The coordinates of nine sensors relative to the origin are summarized in Table 5.2. Sensor 1-4 are Nano-30 sensors and sensor 5-9 are VS150-RIC sensors.

Table 5.2 – Coordinates of sensors and H-N source (units: mm).

	Sensor type	**X coordinate**	**Y coordinate**
Sensor 1	Nano-30	20	380
Sensor 2		280	380
Sensor 3		20	120
Sensor 4		280	120
Sensor 5	VS150-RIC	40	420
Sensor 6		260	420
Sensor 7		40	80
Sensor 8		260	80
Sensor 9		150	250

The VS150-RIC sensors were acoustically coupled using ultrasound gel and pressure was applied using magnetic clamps. The integral pre-amplifiers with 34 dB gain amplified the signals recorded by sensors. The Nano-30 sensors were coupled with the specimen by the way of Loctite 595 Transparent Sealant (Henkel Loctite Corporation, Helsinki, Finland) and amplified with AEP4H (Vallen Systeme GmbH, Germany) at 34 dB gain. Outputs of all the sensors were linked to a Vallen 16-channel AMSY-6 AE System (Vallen Systeme GmbH, Germany) with the acquisition settings shown in Table 5.3.

Table 5.3 – AE acquisition settings.

Threshold (dB)	**Sample Length (ms)**	**Sample Rate (MHz)**	**Pre-Trigger (ms)**	**Rearm time (ms)**	**Duration discrimination time (ms)**
30	1.6	5	0.5	0.8	0.8

Prior to the corrosion test, H-N sources [31] were generated close to each AE sensor to assess the sensor sensitivity and the coupling between the sensors and the specimen. Hits with amplitude above 98 dB at each sensor were recorded, which verified the coupling.

5.2.3 Test result

Since the sensors were placed symmetrically around the plate centre on the top surface and the corrosion area was located at the centre of the plate, signals recorded at the same type of sensor were similar. Therefore, one of each type of sensors on the top surface, i.e., sensor 1 (Nano-30) and sensor 5 (VS150-RIC), as well as the sensor 9 on the bottom surface were chosen for further data analysis of the collected results.

AE amplitudes of hits over time in the corrosion test are presented in Figure 5.4. The duration of the corrosion test was chosen to be around 5 hours to ensure that sufficient AE data for further analyses can be provided. As seen in Figure 5.4, a short delay of around 1.5 hours was observed before significant AE activity resulting from the corrosion was recorded. It was speculated that the different stages of AE behaviours were attributed to different stages of corrosion process, which were associated with the corrosion current density as proposed by Andrade and Alonso [165].

As expected, sensor 9 received a significantly greater number of hits than the other sensors, recording 23,388 rather than 1,796 from sensor 1 and 696 from sensor 5. AE hits at sensor 9 had high amplitude levels up to 65 dB. Compared to sensor 9, a smaller number of hits were observed at sensor 1 and 5. AE hits at both sensor 1 and 5 had low amplitude levels up to 45 dB.

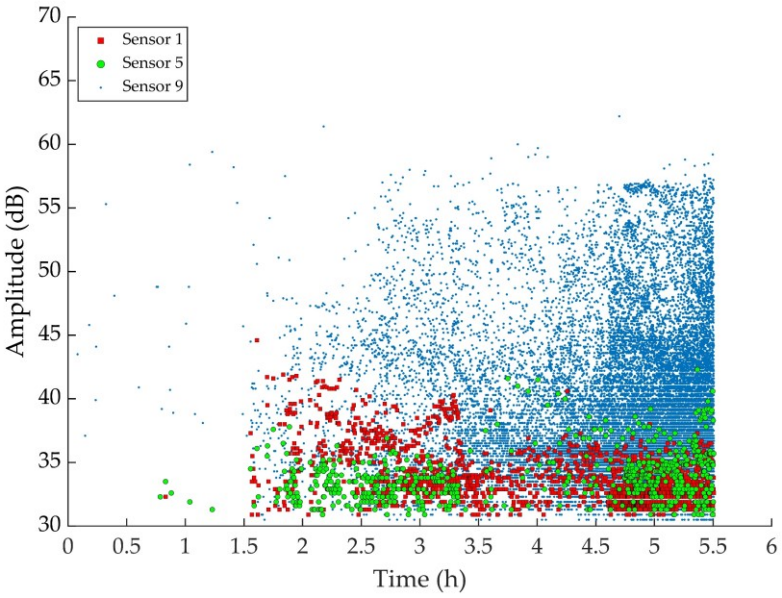

Figure 5.4– AE amplitudes of hits over time in the corrosion test

The normalised cumulative energy and current over time are shown in Figure 5.5. It can be seen that the current gradually increased throughout the corrosion test. The normalised cumulative energy at sensor 9 showed a steady and constant increase. Figure 5.5 also shows that the normalised cumulative energy at sensor 1 and sensor 5 followed similar trend.

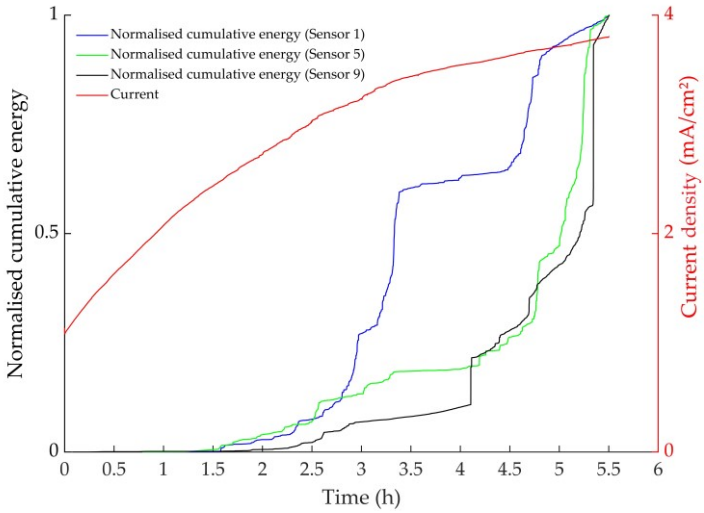

Figure 5.5– Normalised cumulative energy and current over time in the corrosion test

5.2.3.1 Frequency

Fast Fourier Transform (FFT), which is a commonly used tool for providing information about the frequency domain of a signal, was carried out on signals recorded at sensor 1 (Nano-30) and sensor 5 (VS150-RIC). Examples of waveforms at sensor 1 and sensor 5 and corresponding frequency domain are shown in Figure 5.6 and Figure 5.7 respectively.

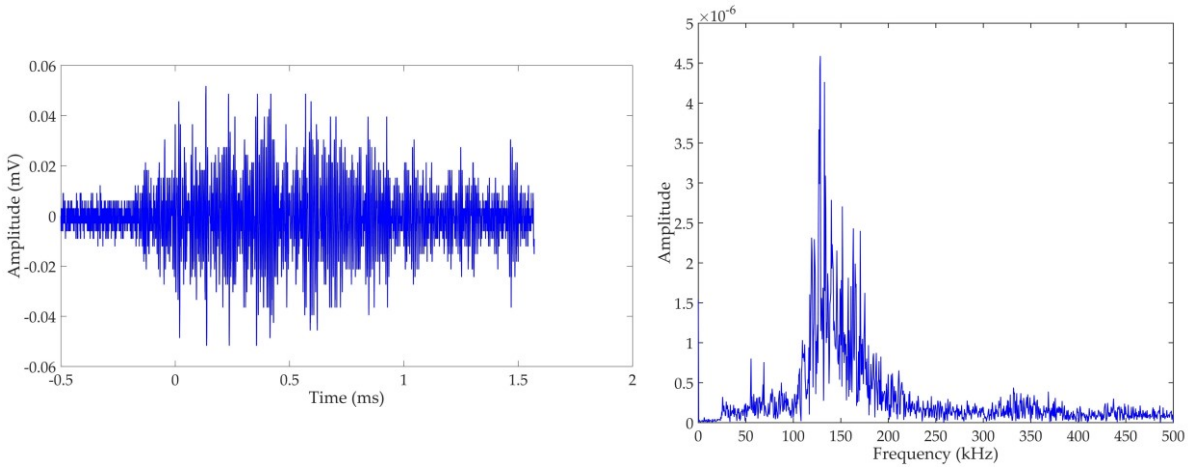

(**a**) (**b**)

Figure 5.6– An example of a waveform at sensor 1 (a) and corresponding frequency domain (b).

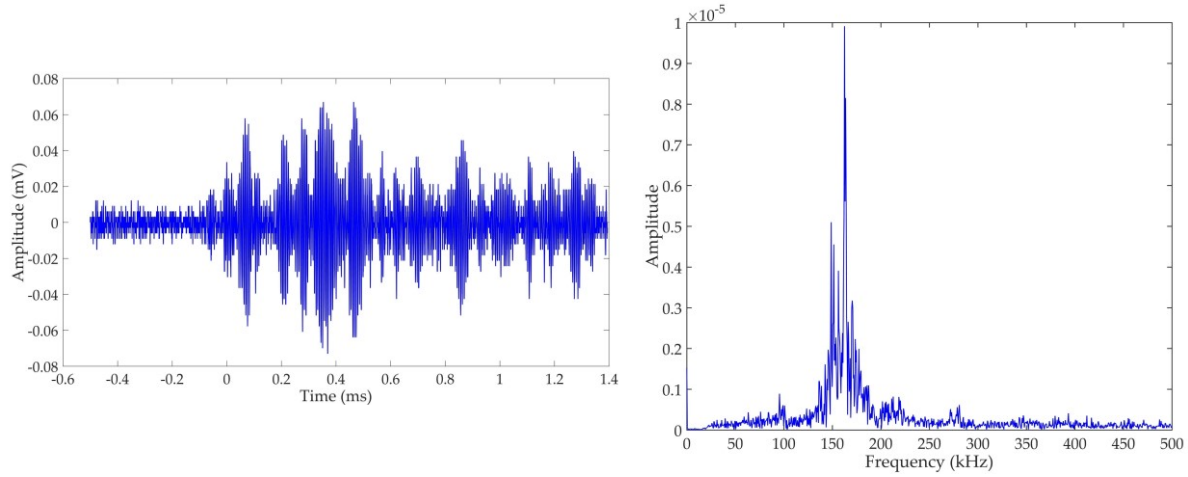

(**a**) (**b**)

Figure 5.7– An example of a waveform at sensor 5 (a) and corresponding frequency domain (b).

From the FFT results, the peak frequencies of AE signals were extracted, which are shown in Figure 5.8. It can be seen that, for both signals, the majority of their peak frequencies lied in the 50- 200 kHz range. Additionally, sensor 1 and sensor 5 detected some AE signals with

peak frequency between 50 kHz and 100 kHz from around 1.5 h to around 3.5 h. Figure 5.8 also shows the variation in peak frequencies observed between sensor 1 and sensor 5. In particular, from around 1.5 h to around 3.5 h, peak frequencies of some signals at sensor 1 were around 100 kHz, which those of some signals were around 150 kHz at sensor 5. This can be attributed to the difference in the frequency responses of sensor 1 and sensor 5.

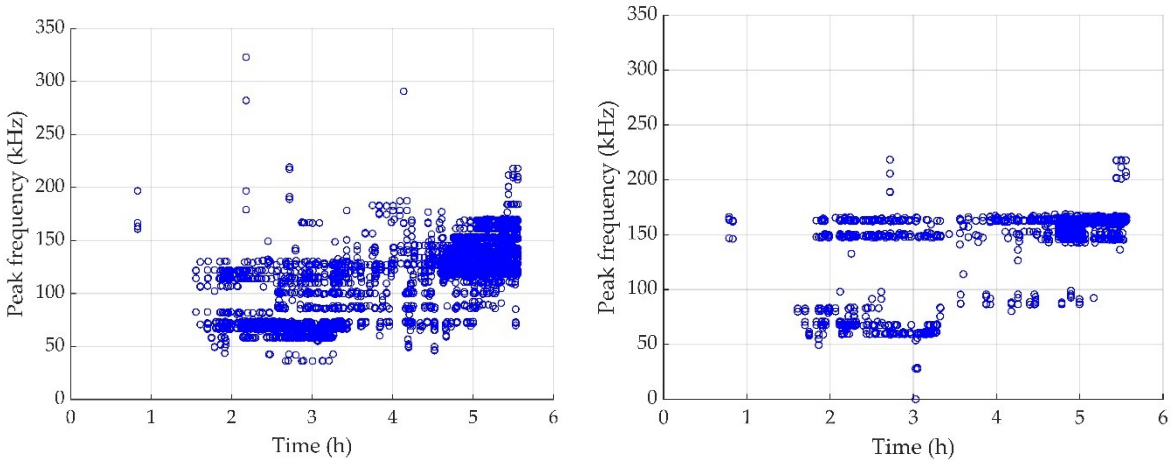

(a) **(b)**

Figure 5.8– Peak frequencies of AE signals recorded at: (a) sensor 1 (Nano-30) and (b) sensor 5 (VS150-RIC).

In addition, the partial power was calculated using Equation (5.1) by dividing the summation of the power spectrum over the frequency range of interest by the total power and multiplied by 100 [166].

$$p = \int_{f_1}^{f_2} \widehat{U}^2(f)df \,/\, \int_{0\ kHz}^{1000\ kHz} \widehat{U}^2(f)df \tag{5.1}$$

where:

$\widehat{U}(f)$	Fourier-Transformation of the signal
Partial Power 0-100 kHz	$f_1 = 0\ kHz,\ f_2 = 100\ kHz;$
Partial Power 100-200 kHz	$f_1 = 100\ kHz,\ f_2 = 200\ kHz;$
Partial Power 200-300 kHz	$f_1 = 200\ kHz,\ f_2 = 300\ kHz;$
Partial Power 300-400 kHz	$f_1 = 300\ kHz,\ f_2 = 400\ kHz;$

Scatterplot of partial power from 0 to 100 kHz (blue), 100 to 200 kHz (red), 200 to 300 kHz (black) and 300 to 400 kHz (magenta) of AE hits are shown in Figure 5.9 (a) for sensor 1 and Figure 5.9 (b) for sensor 5.

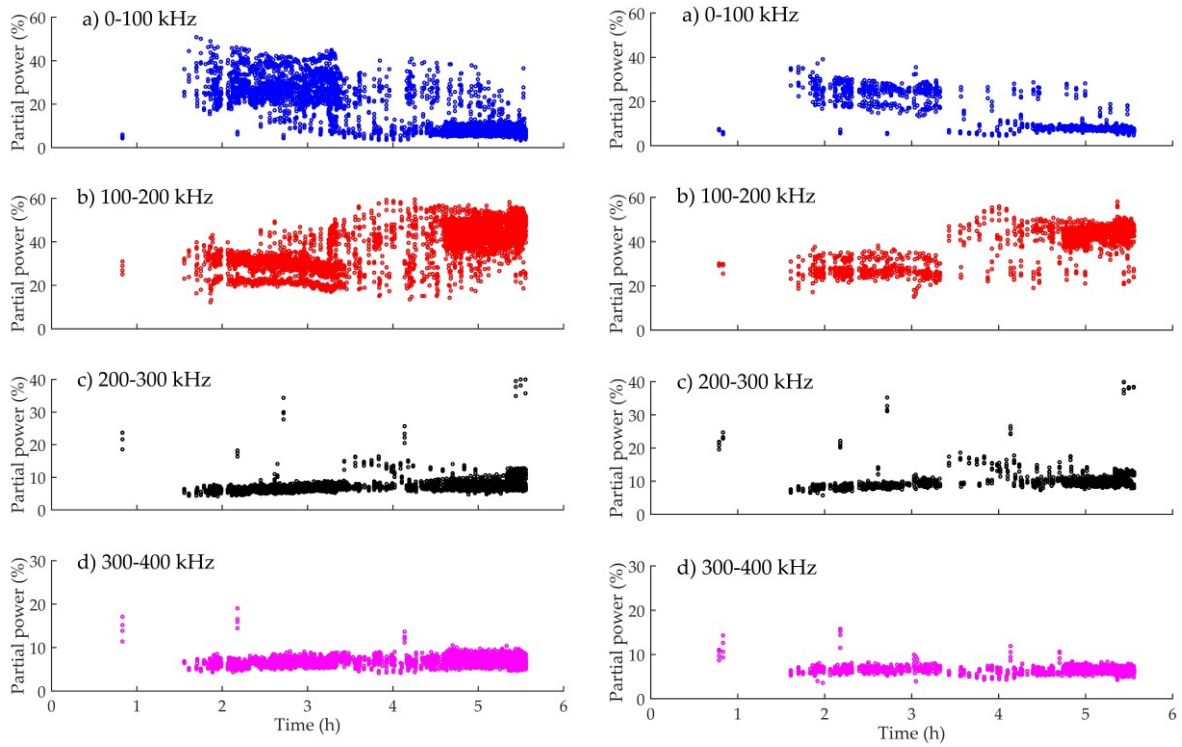

Figure 5.9– partial power from 0 to 100 kHz, 100 to 200 kHz, 200 to 300 kHz and 200 to 300 kHz of AE signals at: (a) sensor 1 (Nano-30) and (b) sensor 5 (VS150-RIC).

Generally, two parts of signals at both sensor 1 and sensor 5 can be observed; the first part of signals, which was from around 1.5 h to around 3.5 h, had similar magnitude of partial power from 0 to 100 kHz and from 100 to 200 kHz. The second part of signals, from around 4.5 h to around 5.5 h, had notably larger magnitude of partial power from 100 to 200 kHz than that from 0 to 100 kHz. Despite the differences between partial powers of signals, it can be summarized that the majority of signals had large magnitude of partial power from 0 to 200 kHz. This indicates that these signals had large amount of energy in frequency components from 0 to 200 kHz.

The resonance frequency of VS150-RIC sensors is 150 kHz, and their bandwidth ranges from 100-450 kHz, which align with the frequency components of signals generated from

corrosion. In contrast, Nano-30 sensors have a frequency response that spans from 125 to 750 kHz, with a resonant frequency of 300 kHz. Hence, in terms of frequency response, VS150-RIC sensors may be a more suitable option for monitoring corrosion.

5.2.3.2 Velocity calculation

As described in Section 5.2.2, besides sensors placed on the top surfaces of the plate, an AE sensor, i.e., sensor 9, was installed on the bottom surface of the plate and below the surface area exposed to corrosion. Since sensor 9 was very close to the AE source from corrosion damage, it is assumed that the onset time of waves recorded at sensor 9 is the time when waves were emitted from the corrosion source. Additionally, since the area exposed to corrosion was small and circular with a radium of 4 mm, the sensor-source distance on the top surface of the plate is assumed to be the distance between the centre of circular exposed area and the sensor. The velocity v of waves were calculated using Equation (5.2) .

$$v = D/(t_i - t_9) \tag{5.2}$$

Where:

D	The distance between the centre of exposed area and the sensor i.
t_i	The arrival time of a signal at sensor i.
t_9	The arrival time of the same signal at sensor 9.

The arrival time of signals were estimated using the traditional threshold crossing method and AIC picker, which was regarded as a reliable tool for automatic onset detection in Chapter 4. In addition, the arrival time can be estimated by using a wavelet coefficient threshold crossing technique [167]. The arrival time of a signal is the time when the wavelet coefficients are larger than a certain value or a threshold. However, signals recorded during the corrosion test were characterized by a low signal-to-noise ratio. It was very difficult to choose an appropriate wavelet coefficient threshold. For example, the signal in Figure 5.7 (a) was firstly estimated to be -73.4 μs by AIC picker as shown in Figure 5.10. Then, the wavelet analysis of this waveform was conducted using the free software AGU-Vallen Wavelet from

Vallen System and the 2D contour diagram of WT coefficients of the waveform was shown in Figure 5.11. Since the peak frequency of the waveform (as shown in Figure 5.7 (b)) was around 150 kHz. The WT coefficients at 150 kHz was extracted and presented in Figure 5.12.

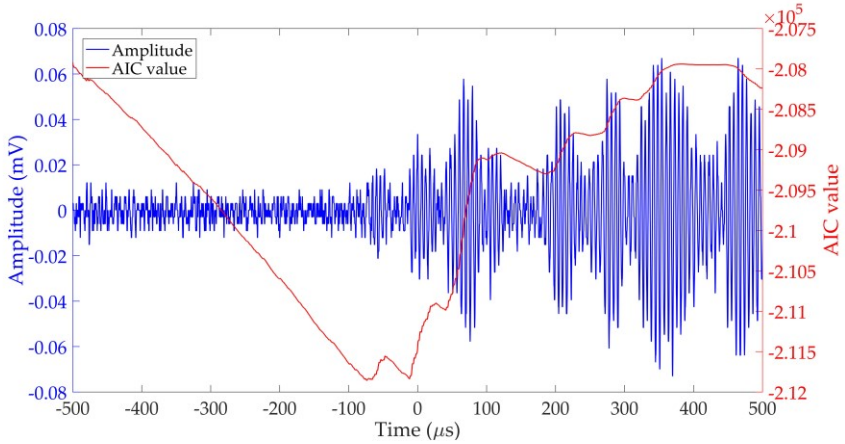

Figure 5.10–The waveform shown in Figure 5.7(a) with overlapped AIC value

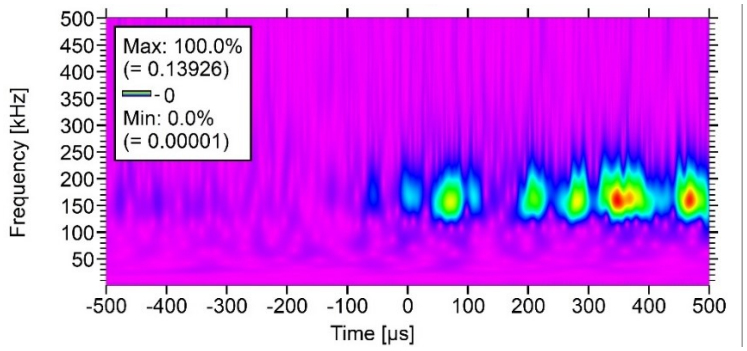

Figure 5.11– 2D contour diagram of WT coefficients of the waveform

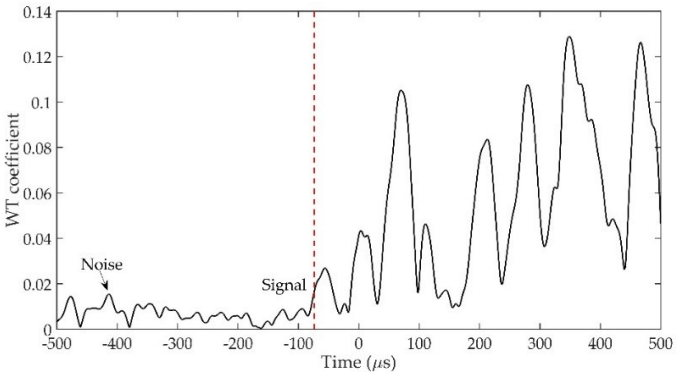

Figure 5.12– WT coefficients at 150 kHz

As seen, the WT coefficient of the signal at -73.4 μs was 0.017, which was very close to 0.015 of the background noise at -414 μs. Hence, a low WT coefficient threshold is likely to result in the early triggering by the background noise, while a high WT coefficient threshold will lead to an inaccuracy in arrival time estimation. Therefore, WT coefficient threshold crossing technique was not used to determine the arrival time of signals from corrosion.

Moreover, it can be seen that the first and second minimum of AIC value were very close in Figure 5.10. This indicated that AIC picker is very likely to be unreliable for estimating the arrival time of signals with such low signal-to-noise ratios. Therefore, to improve the reliability on predicting onset time of low signal-to-noise signals, a novel method, window AIC method, which was based on AIC function is proposed in this study. In this method, AIC function is applied twice on the transient signals.

The visual description of each step of this window AIC method is presented in Figure 5.13. The 3 steps associated with the window AIC method are detailed below;

- **Step a)**. Firstly, since the time window is assumed to be starting in noise and ending just after the peak amplitude of the signal, AIC function is applied on time window which is set to start at the beginning of signal and ending on time when the signal reaches its global maximum value. Time t_a which attains the minima of the AIC value indicates the estimated point of the signal onset. As seen in Figure 5.13 (a), the time window is shortened again to time window A. Similar to a time window proposed by Sedlak et al. [168], it starts at time $t_a - t_{ba}$, and ends on $t_a + t_{aa}$. A value of 30 µs (300 samples) was selected for t_{ba} and 10 µs (100 samples) for t_{aa} by Sedlak et al. Since the proposed method aimed towards low-amplitude signals with low signal-to-noise ratios rather than high-amplitude signals in Sedlak et al.'s work, a larger t_{ba}= 150 µs (750 samples) and t_{aa}= 50 µs (250 samples) were selected and verified by trial and error. The errors associated with selection of t_{ba} and t_{aa} are discussed in Section 5.4.

- **Step b)**. In the second step, as shown in Figure 5.13 (b), time window B, which contains noise records, is extracted from a signal. The noise record is roughly estimated by experience and the same time window B was used for all the signals.

The length of time window B is specified to be the same as time window A. Since the ambient noise recordings are similar, the samples of time window B used in all the calculations are the same.

- **Step c)**. The samples of time window B are placed before and after samples of time window A to form a new signal as shown in Figure 5.13 (c). The AIC function is recalculated and applied on this updated signal. The onset time of this updated signal as well as the original signal is now represented by the global minimum the recalculated AIC function.

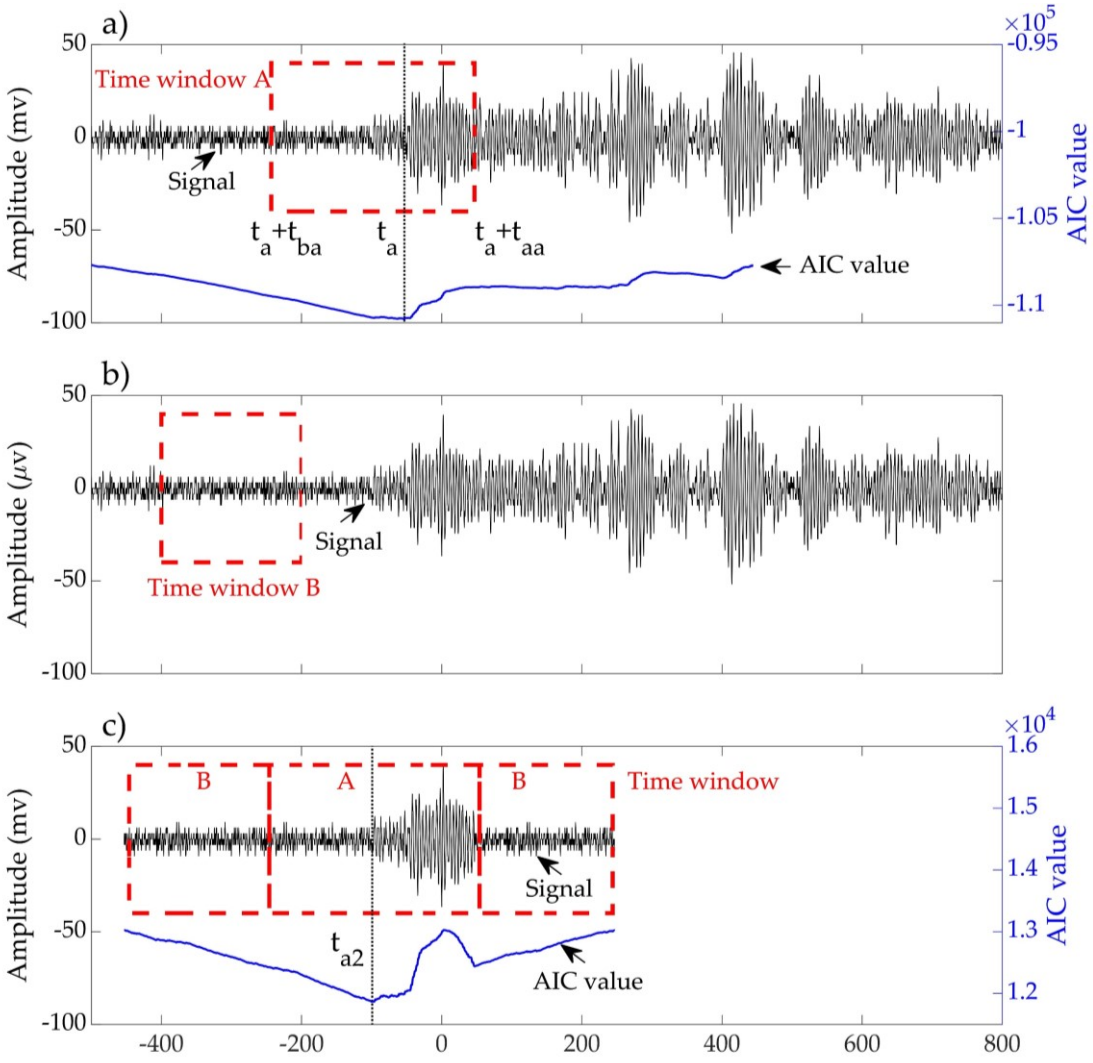

Figure 5.13– Description of each step of window AIC method.

Compared with AIC function, window AIC usually predicts an earlier arrival time. Examples of time arrival estimated by window AIC and AIC function are shown in Figure 5.14 (a) and (b) respectively (The waveform is the signal from VS150-RIC sensors during corrosion test on a simple plate). To view the signals clearly, signal in Figure 5.14 (b) is shown in Figure 5.14 (c) with a shortened time frame.

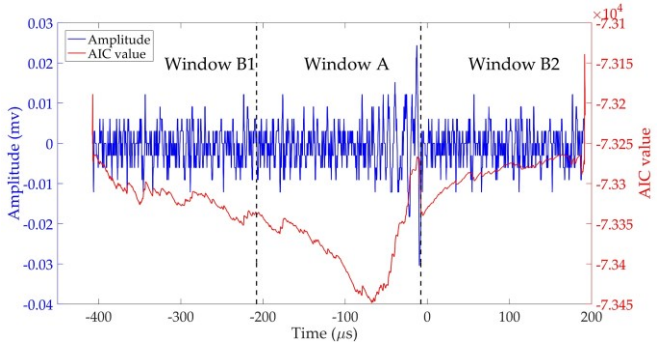

(**a**)

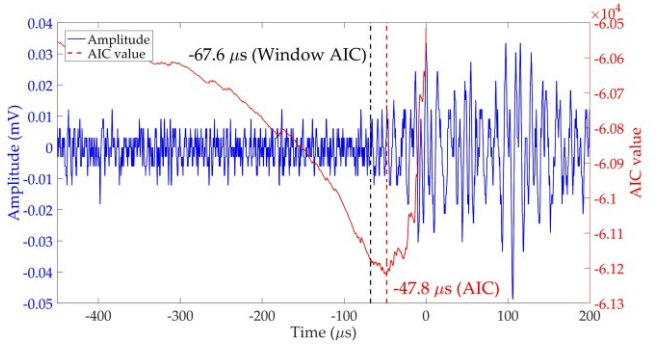

(**b**)

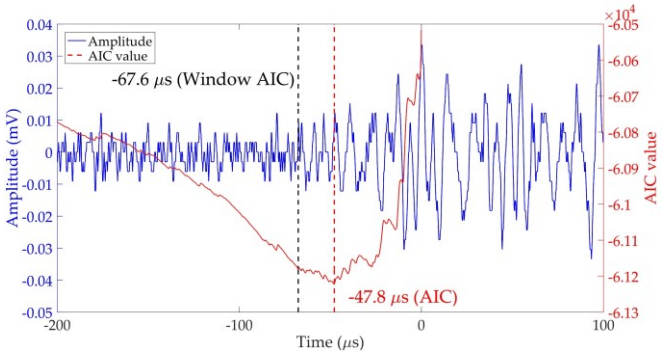

(**c**)

Figure 5.14–Examples of time arrival estimated by (a) window AIC, (b) AIC function and (c) signal in (b) with a shortened time frame.

As seen in Figure 5.14 (a), the signal was reconstructed with time window A and B according to window AIC method in Section 5.2.3.2. The arrival time predicted by window

AIC method was -67.6 μs rather than -47.8 μs by AIC function as shown in Figure 5.14 (b). Since AIC function [60] compares the difference in classic variance before and after each point in the wave, typically when it is at its minimum represents the point where the transition from noise to waveform is occurring, and therefore the arrival time of the wave. By adding time window B (B1 and B2 are the same and from background noise) to the original signal component (time window A), the majority after time= -67.6 μs are samples from background noise. Therefore, the classic variance after time= -67.6 μs is more sensitive to the transition from noise to waveform, while the classic variance after time= -47.8 μs in Figure 5.32 (b) is less sensitive to this transition. This is because the amplitude of waveform around this time is almost the same as the noise and this transition does not have a significant impact on the value of the classic variance after time= -47.8 μs.

The selection of the length of time window A, B1 and B2 are very important to achieve a higher accuracy in time estimation. A short window A may miss the onset of the signal and a long window A may include some samples from reflection or background noise with high amplitude, resulting an early triggering. For this study, time window B1 is the same as time window B2, which equals to 1000 samples. However, as shown in Figure 5.15, if a window B1 is too short (100 samples) or window B2 is too long (2000 samples), the arrival time determined by window AIC method is time at the wrong transition, which is the transition from the waveform to the noise at the end of window A. In addition, if a window B1 is too long, the computation time will increase. If window B2 is too short, the window AIC will estimate the arrival time similar to AIC function in Figure 5.14 (b).

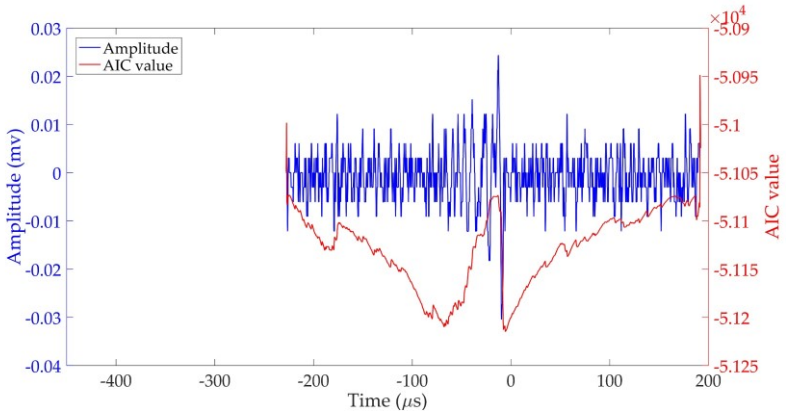

(a)

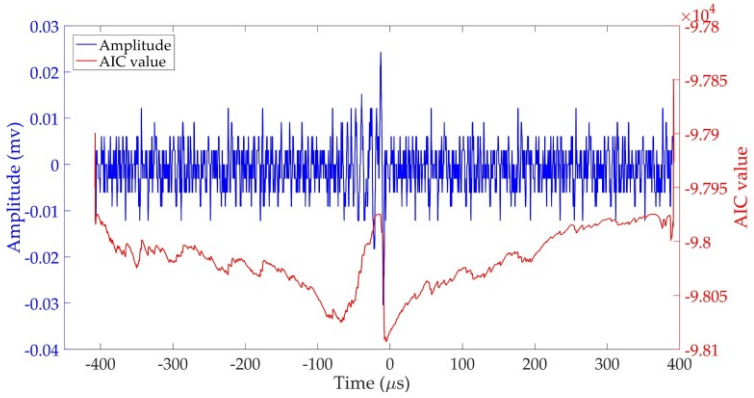

(b)

Figure 5.15–Examples of time arrival estimated by window AIC with wrong triggering; (a) window B1= 100 samples (20 μs) and window B2=1000 samples (200 μs), (b) window B1= 1000 samples (200 μs) and window B2= 2000 samples (400 μs).

After the arrival time of signals were determined by threshold crossing, AIC picker and window AIC method, velocities of AE signals were calculated using Equation (5.2). Scatter plots of velocities of signals at sensor 1-4 and sensor 5-8 are shown in Figure 5.16 and Figure 5.17 respectively.

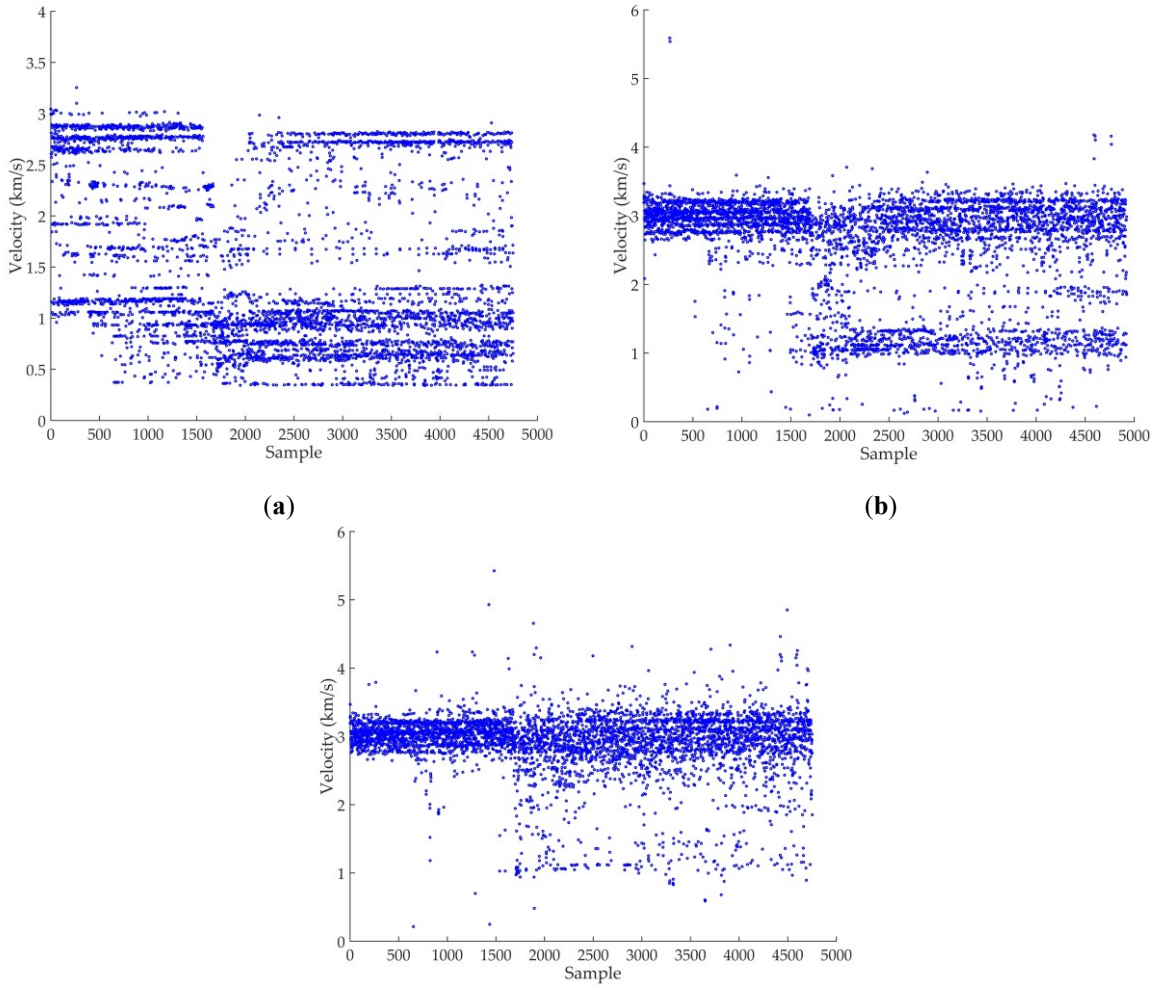

Figure 5.16–Velocities of AE signals at sensor 1-4 (Nano-30 sensors), which were calculated based on arrival time determined by (a) threshold crossing, (b) AIC function and (c) window AIC method.

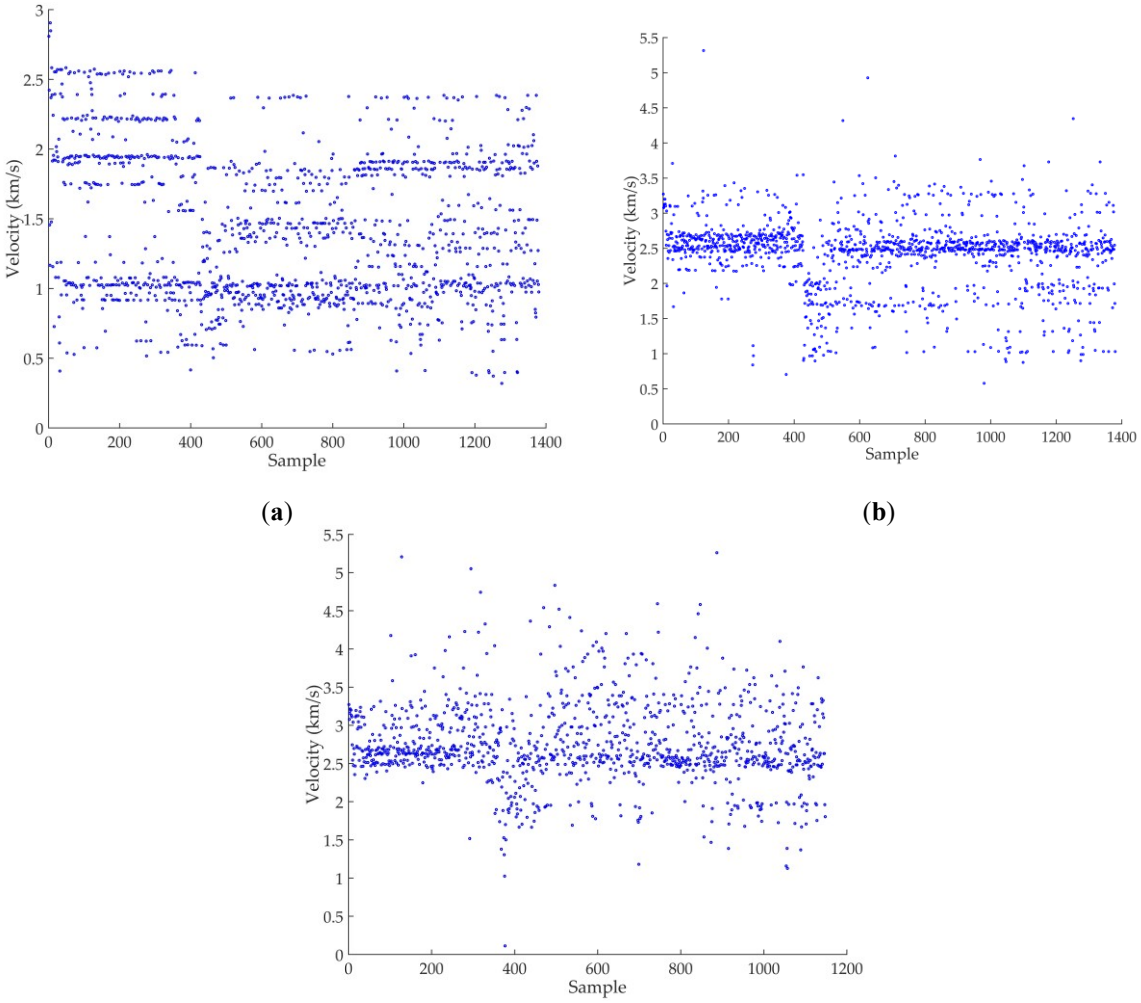

Figure 5.17–Velocities of AE signals at sensor 5-8 (VS 150-RIC sensors), which were calculated based on arrival time determined by (a) threshold crossing, (b) AIC function and (c) window AIC method.

Percentages of different velocity ranges (i.e., 0-1, 1-2, 2-3, 3-4, 4-5, 5-6 km/s) were summarized and documented in Figure 5.18 and Figure 5.19.

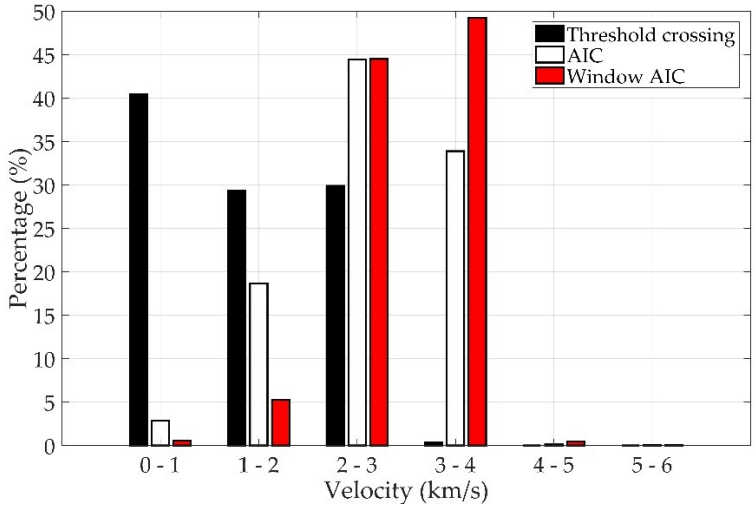

Figure 5.18–Percentages of velocities of AE signals recorded at sensor 1-4 (Nano-30 sensors)

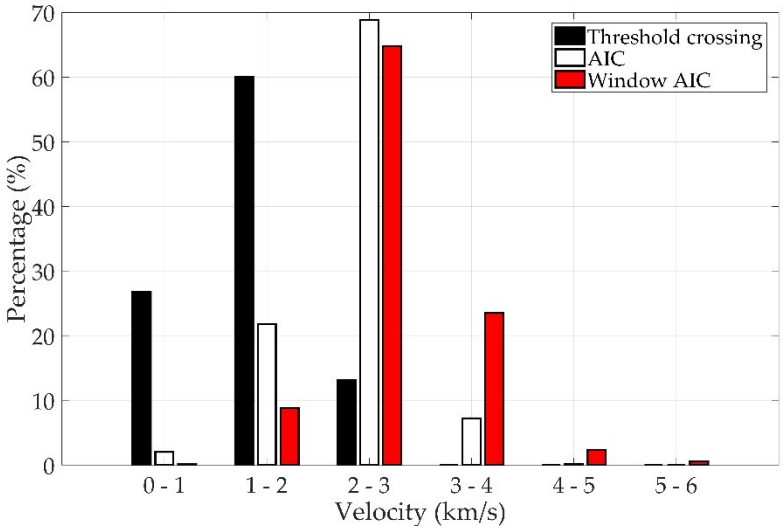

Figure 5.19– Percentages of velocities of AE signals recorded at sensor 5-8 (VS150-RIC sensors).

Considering the velocities calculated from Nano-30 sensors shown in Figure 5.18, based on arrival time determined by threshold crossing, 40.5% of velocities (in black) were between 0-1 km/s and 29.3% were between 1-2 km/s. Some of measured velocities were found to be between 2-3 km/s, with a percentage of 29.9%. After AIC function (in white) was applied, the percentage of velocities between 0-1 and 1-2 km/s reduced significantly to 2.9% and 18.7% respectively. Compared to threshold crossing, an obvious increase in the percentages of velocities in the range of 3-4 km/s was seen. With window AIC method (in red), a further increase in the percentage of velocities between 3-4 km/s was observed. A gradual decrease

in the percentage of velocities between 0-1 and 1-2 km/s and a gradual increase in the percentage of velocities between 3-4 and 4-5 km/s was seen as threshold crossing, AIC function and window AIC method were used successively to estimate the onset time of AE signals. The average velocity calculated based on threshold crossing, AIC and window AIC are 1.47, 2.54 and 2.87 km/s respectively.

As for the velocities from VS150-RIC sensors shown in Figure 5.19, based on arrival time determined by threshold crossing, all the measured velocities were below 3 km/s and the majority of velocities lied in the range of 0-2 km/s, with a percentage of 26.8% between 0-1 km/s and 60.0% between 1-2 km/s. Percentages of velocities between 2-3 were relatively small, with a value of 13.2% respectively. A gradual decrease in the percentages of velocities between 0-1 and 1-2 km/s and a gradual increase in percentages of velocities between3-4, 4-5 and 5-6 km/s was seen as threshold crossing, AIC function and window AIC method were used successively to estimate the onset time of AE signals. For window AIC method, a large number of velocities lied in the range of 2-3 km/s, with a percentage of 64.8%. The average velocity calculated based on threshold crossing, AIC and window AIC are 1.42, 2.41 and 2.86 km/s respectively.

As discussed in Chapter 2, dispersion curves present the propagation velocities with respect to the plate thickness and the frequency of each Lamb wave mode. The curves depicting the relationship among group velocities and frequencies of different Lamb modes, for a plate of thickness 3 mm are shown in Figure 5.20. Since the high frequency contents of the higher wave modes were not seen according to peak frequencies in Figure 5.8 and partial power in Figure 5.9, only S_0 and A_0 modes are shown in Figure 5.20.

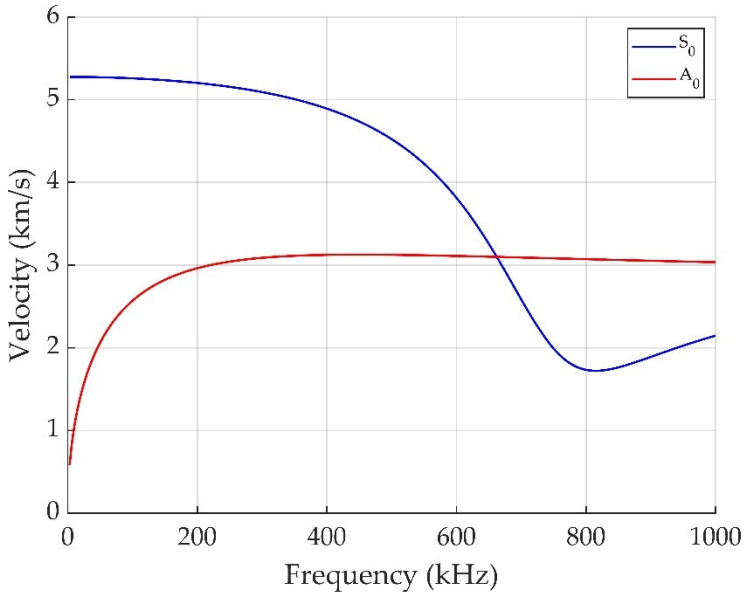

Figure 5.20– Dispersion curves for a steel plate of thickness 3 mm.

According to FFT analysis shown in Figure 5.6 (b) and Figure 5.7 (b) and partial power in Figure 5.9, if a frequency between 150kHz and 200 kHz is assumed, a group velocity of around 5.20-5.24 km/s is seen for S_0 mode and around 2.83-2.96 km/s for A_0 mode from the dispersion curves in Figure 5.20. Therefore, the majority of measured velocities from Nano-30 and VS150-RIC match the velocity of the A_0 mode predicted by the dispersion curve. Hence, the first arriving component of signals that was detected is likely to be the A_0 mode from the corrosion signals.

5.2.3.3 Source location results

As mentioned above, three methods, i.e., threshold crossing, AIC function and window AIC were applied to identify wave arrival times of sensor 1-8. Afterwards, locations of sources were calculated using the traditional TOA approach with experimentally collected velocities (2.87 km/s for Nano-30 sensors and 2.86 km/s for VS150-RIC sensors). The source location results from sensor 1-4 and sensor 5-8 are documented in Figure 5.21 and Figure 5.23.

Since the corrosion area was a circle, the associated Euclidian distance errors d in this section was defined as the distance from the localised event to the circular area and calculated using Equation (5.3). If the calculated Euclidian distance error is zero or below zero, this means

that the localised corrosion damage is within the corrosion area and the Euclidian distance error is considered to be zero.

$$d = \sqrt[2]{(x - x_c)^2 + (y - y_c)^2} - r \tag{5.3}$$

Where:

x, y	The X-coordinate and Y-coordinate of a localised corrosion event.
x_c, y_c	The X-coordinate and Y-coordinate of the centre of the corrosion area.
r	The radius of the corrosion area.

The associated Euclidian distance errors are documented in Figure 5.22 and Figure 5.24 respectively.

For the results from the Nano-30 sensors (1-4), which are shown in Figure 5.21 (a) and Figure 5.22, it can be seen in that none of the location results calculated from arrival times based on threshold crossing with a fixed threshold of 30 dB threshold were within the corrosion area and the majority of located AE events had a location error larger than 100 mm. After AIC function was used in arrival time estimation, as seen in Figure 5.19 (b), some AE events were located within the corrosion area and a large number of AE events clustered on the top left of the corrosion area. Compared with threshold crossing, most events were concentrated in the centre of the sensor array, i.e., the corrosion area. Moreover, in Figure 5.22, percentage of AE events with errors larger than 100 mm reduced by more than half from 89.6% to 34.3%. An obvious increase in the percentages of AE events with errors between 0-10, 10-30 and 30-50 mm. A gradual decrease in the percentages of AE events with errors above 100 mm and a gradual increase in percentages of 0, 0-10, 10-30 and 30-50 mm were seen as threshold crossing, AIC function and window AIC method were used successively to estimate the onset time of AE signals.

For the VS150 sensors (5-8), similar to results from the Nano-30 sensors , a poor localisation accuracy was shown as none of the AE events given by threshold crossing were located within the corrosion area and 84.0% of AE events had a location error above 100 mm in

Figure 5.23 (a) and Figure 5.24. Both the AIC function and window AIC function showed an improvement over the threshold crossing where a reduction in the percentages of errors above 100 mm and an increase in the percentages of errors below 50 mm was observed respectively. However, it should be noted that compared with AIC function, the location results given by window AIC had a higher percentage of errors between 10-30, 30-50 and 50-100 mm, which a smaller percentage of errors below 10 mm was seen. The reason is discussed below.

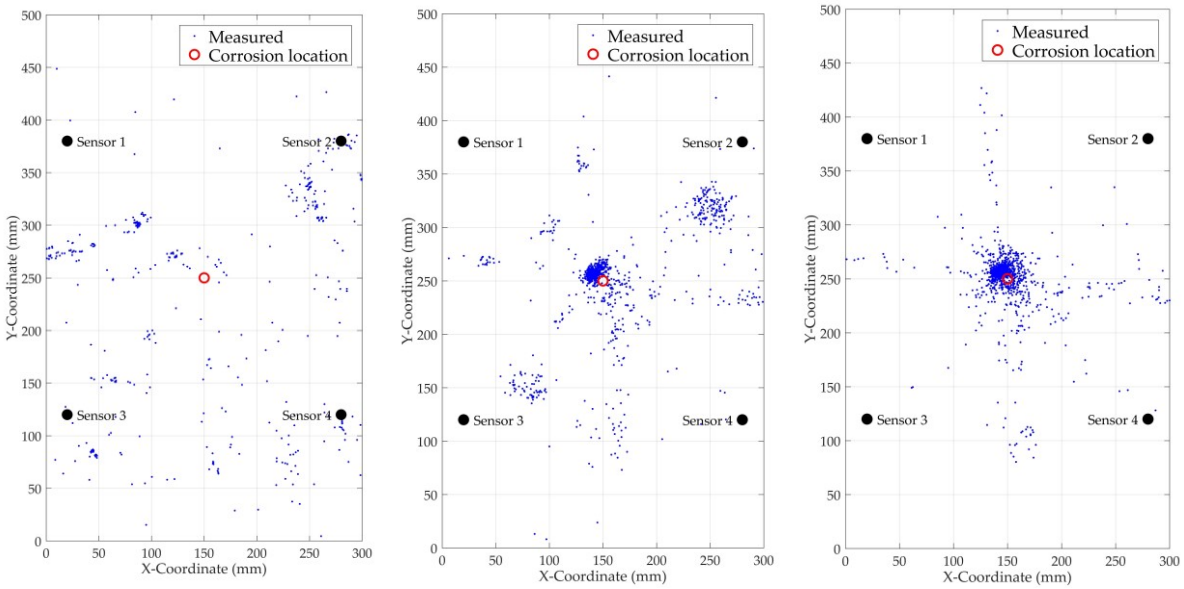

Figure 5.21– Source location results (sensor 1-4, Nano-30 sensors) based on arrival times estimated by: (a) threshold crossing, (b) AIC function and (c) window AIC method.

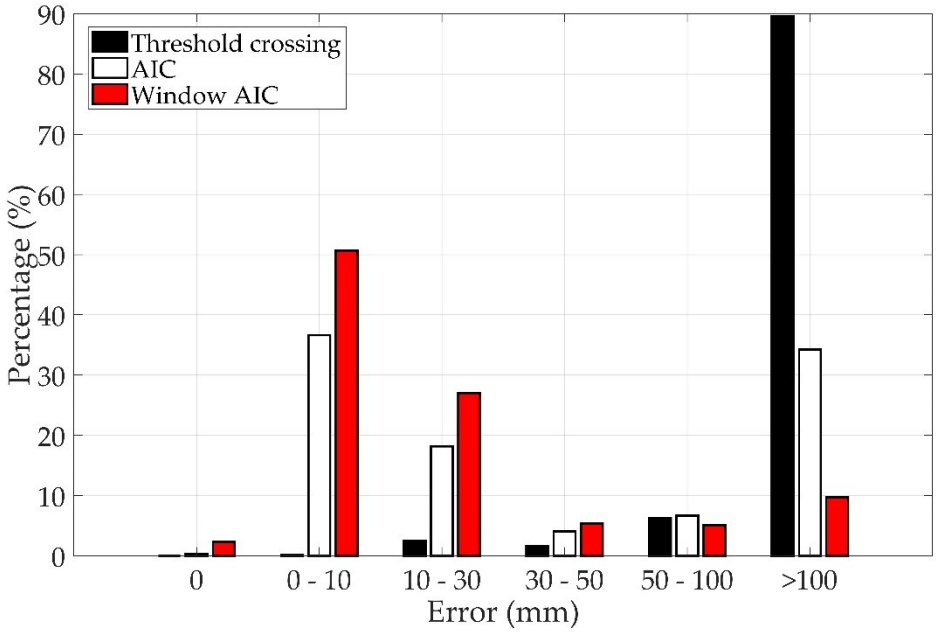

Figure 5.22–Errors of source location results from sensor 1-4.

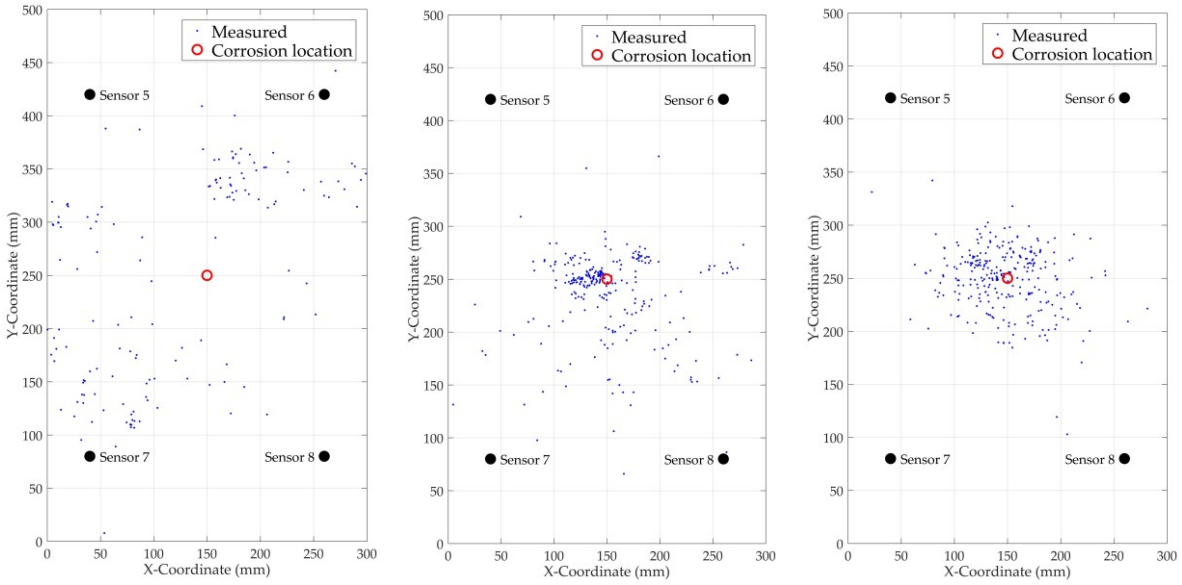

(**a**) (**b**) (c)

Figure 5.23– Source location results (sensor 5-8, VS150-RIC sensors) based on arrival times estimated by: (a) threshold crossing, (b) AIC function and (c) window AIC method.

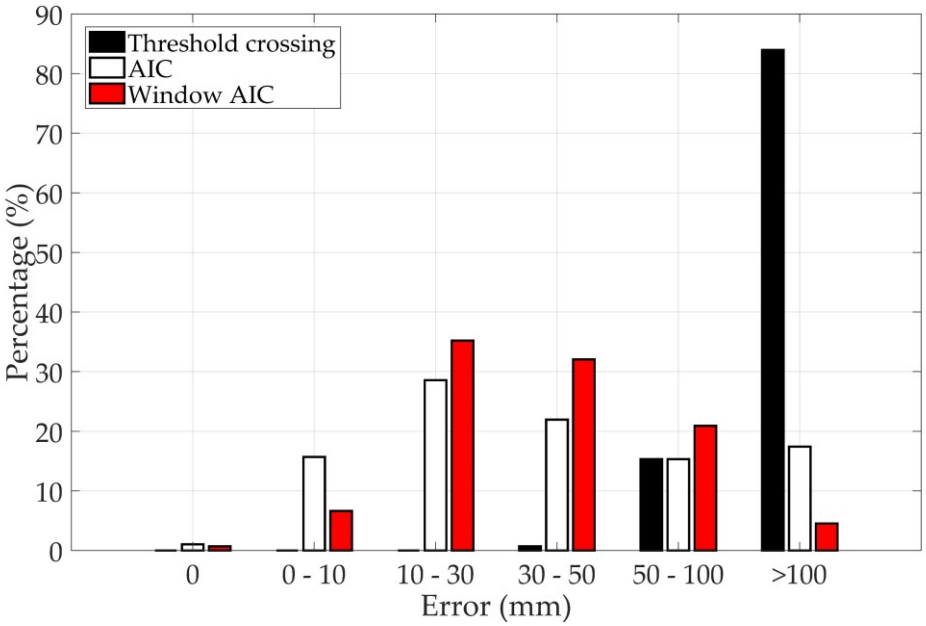

Figure 5.24– Errors of source location results from sensor 5-8.

An example of arrival time estimated by AIC and window AIC for a signal from sensor 5-8 (VS150-RIC sensors) and corresponding locations determined by TOA. The time = 0 μs was set as the arrival time of signal at sensor 9. As seen, the window AIC gave a smaller arrival time for signals at sensor 7 and 8 than AIC function.

Table 5.4 –An example of arrival time estimated by AIC and window AIC for a signal from sensor 5-8 and corresponding location determined by TOA.

	Arrival time (AIC), μs	**Arrival time (window AIC), μs**
Sensor 5	75.4	75.2
Sensor 6	81.4	81.4
Sensor 7	81	68.8
Sensor 8	75.2	71.4
Location (X, Y)	155.3, 245.9 mm	139.9, 236.5 mm
Errors	2.7 mm	12.8 mm

Due to the earlier time arrival, the associated location errors increase from 2.7 mm to 12.8 mm. Some signals from VS150-RIC sensors were similar to that in Figure 5.14 (b). The arrival time determined by Window AIC was earlier than that of AIC, potentially due to reflections or background noise, leading to a greater location error in the results.

Therefore, compared with AIC function, the location results from VS150-RIC sensors given by window AIC had a smaller percentage of errors below 10 mm in Section 5.2.3.3.

However, since the sensors had a smaller distance to the corrosion area than VS150-RIC sensors and the amplitudes of signals from Nano-30 sensors are usually larger than VS150-RIC sensors, this was not found among the location results from Nano-30 sensors.

5.3 Localisation of corrosion damage on a complex plate

Delta-T mapping, which is regarded as a suitable method for the location of AE sources in complicated geometric structures, is used in this study to locate corrosion damage on a complex plate. As discussed in Chapter 4, current delta-T maps are built by performing H-N sources and collecting the arrival time of the S_0 mode. However, it was found in Section 5.2.3 that the first arrival mode of signal generated from corrosion was the A_0 mode. Hence, the methods for identifying the arrival of the A_0 mode are required and current delta-T maps should be built on the basis of the A_0 mode arrival. Different from the methods presented in Section 5.2.3.2 which are aimed towards low signal-to-noise corrosion signals without S_0 arrival, the methods presented in the following Section 5.3.1 are aimed towards signals generated from H-N sources with a lot of S_0 arrivals. Afterwards, delta-T maps based on A_0 arrival were built on a complex plate and corrosion tests were performed on the same complex plate. Localisation results produced by a traditional TOA method and delta-T mapping were compared.

5.3.1 Method for determining A_0 arrivals

Different methods for determining A_0 arrivals on signals with a lot of S_0 arrivals can be found in the open literature. A method based on Continuous Wavelet Transform (CWT) was proposed by Aljets et al. [167]. In this method, the signal is transformed into the time-frequency domain by means of the Gabor wavelet transform and WT coefficients at a certain frequency component of interest are extracted. The time when the WT coefficient is larger than a pre-set dynamic threshold is regarded as the arrival time of the A_0 mode. This dynamic threshold is dependent on the test setup and not consistent throughout Aljets's work [167,169,170] with a range from 40% to 90% of the maximum amplitude of each event. This method had been shown to be successfully used in the A_0 mode arrival measurement

[167,169,170]. The major disadvantage of this method is that the user-defined WT coefficient threshold can introduce errors in accuracy of the source location results. However, it can be easily utilised to predict the arrival of the A_0 mode arrival. Therefore, it was used in this study and discussed in the following Section 5.3.1.1. Recently, a novel second differential method was proposed by Grigg et al. [8] to detect the arrival of the A_0 mode. The procedural steps of implementing this step include applying bandpass filter, identifying peaks and finding second differential. However, this method is highly complicated. Considering that the signals generated from H-N sources in this study have high amplitudes with clear S_0 and A_0 arrivals, the identification of A_0 arrival are straightforward. Hence, this method was not used in this study.

5.3.1.1 Wavelet coefficient threshold method

An example of an AE signal generated by an H-N source with a distance of around 345 mm to the Nano-30 sensor on a complex structure is shown in Figure 5.25 a). Since the wave velocity shows a strong dependency on wave modes, frequency content and plate thickness [34], a frequency was chosen to estimate the mode arrival time for the A_0 mode according to Aljets et al. [167]. In the test set-ups presented in this study, the frequency of 150 kHz was best suited since the A_0 mode were present at this frequency and the corrosion test in Section 5.2 showed that most signals generated from corrosion had a peak frequency for the tests around 150 kHz. The two-dimensional wavelet transform diagram of the AE signal in Figure 5.25 a) was calculated and shown in Figure 5.25 b), with an example of the WT coefficient at 150 kHz frequency shown in Figure 5.25 c). Since the earlier arriving S_0 mode had a much smaller amplitude in comparison to the A_0 mode, a threshold was set just above the S_0 mode level to detect the arrival of the A_0 mode. Since the testing structure is relatively small with large reflections, a fixed threshold rather than a variable threshold typically used in the literature [167] was adopted in this study to ensure the consistency of the results. A threshold was specified to be 3×10^{-5} (units: Hz/Hz)by trial and error. As shown in Figure 5.25 c), t_W , which corresponds to the threshold crossing of the wavelet coefficient was considered to be the arrival time of A_0 mode.

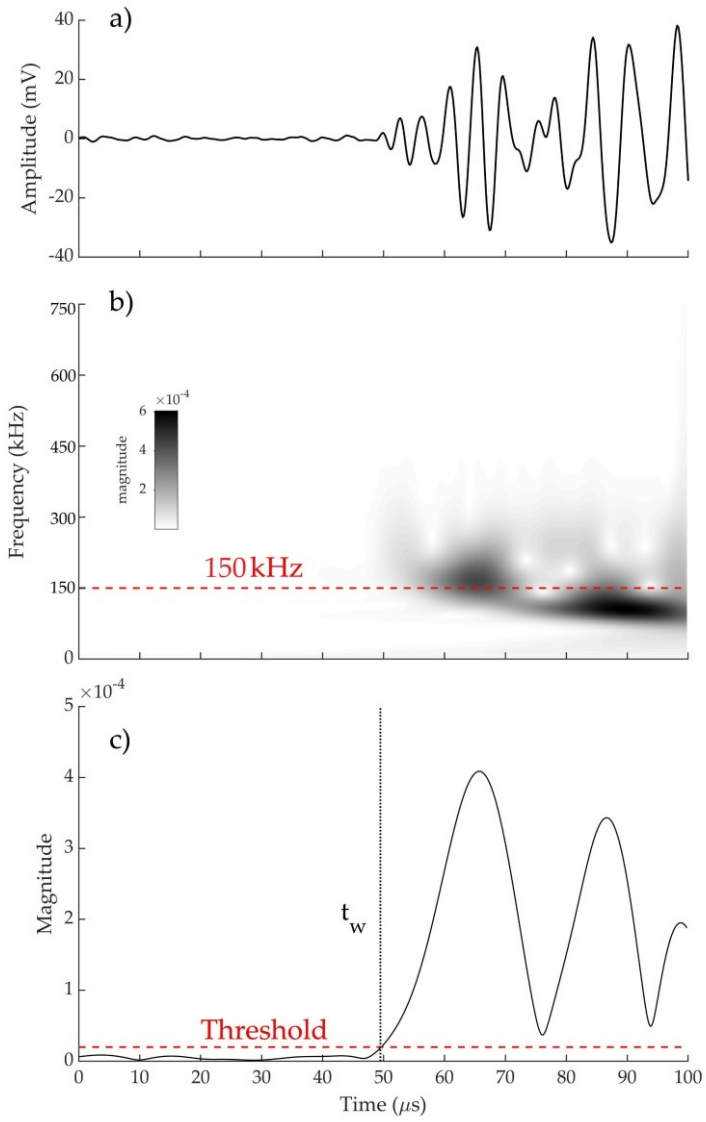

Figure 5.25–Visual description of wavelet coefficient threshold method: (a) an AE signal generated by an H-N source, (b) two-dimensional wavelet transform diagram of the AE signal and (c) WT coefficient at 150 kHz.

5.3.1.2 Modified two-step AIC picker

A two-step AIC picker was proposed by Sedlak et al. [168] to determine the arrival of the S_0 arrival. In this method, the AIC function was applied twice on the transient signals to eliminate the influence of ambient noise. In contrast to the two-step AIC picker, a modified two-step AIC picker was proposed in this study to estimate the arrival time of the A_0 mode. The AIC function was firstly applied to identify the arrival of the S_0 mode. Since the AIC function is based on the measurement of similarity in entropies and the frequency contents

and dispersion characteristics of the S_0 mode are significantly different from those of the A_0 mode, thus resulting in the difference between the entropy of the S_0 mode and that of the A_0 mode, it might provide reliable outcomes when identify the arrival of the A_0 mode and present two clearly distinct regions, e.g., an entropy portion where the S_0 mode dominates, and an entropy segment where the A_0 mode dominates. Therefore, it was applied again on signals with the S_0 mode to determine the A_0 arrival time.

The 3 steps associated with modified two-step AIC picker are detailed below. Procedural steps of implementing modified two-step AIC picker are presented in Figure 5.26. The visual description of each step of modified two-step AIC picker algorithm is presented in Figure 5.27. The AE signal in Figure 5.27 was generated by an H-N source with a distance of around 207 mm to the Nano-30 sensor on a complex structure.

- **Step a)**. When performing H-N sources with a short distance to sensors on the surface of a plate, the S_0 mode are usually hidden in the high-amplitude A_0 mode. Only a short period of the S_0 mode or no S_0 mode can be observed. In this circumstance, it is very difficult to use modified two-step AIC picker to estimate the arrival of the A_0 mode correctly. Therefore, in the first step of this method, the arrival time of the A_0 mode is estimated using traditional threshold crossing. As shown in Figure 5.26, if the time t_t, which is the time when the amplitude of signals is above the threshold, exceeds 6 μs (which are 30 samples, the minimum number of samples required for correctly identifying the A_0 mode using AIC function), the computation will continue and the following steps will be performed. Otherwise, the computation will terminate and t_t is considered to be the arrival time of the A_0 mode. Since this threshold crossing is used to determine the A_0 arrival time of signals generated from H-N sources close to sensors and characterised with the high initial A_0 mode peak, a high threshold of 15 mV was selected in the study by trial and error.

- **Step b)**. AIC function is applied on a time window which is set to start at the beginning of signal and ending on time when the signal reaches its global maximum value. Time t_a which attains the minima of the AIC value indicates the estimated point of signal onset. The time window is updated and starts at time t_a and ends on $t_a + t_{aa}$, where t_{aa} is a time delay. Since the maximum time difference between

the S_0 arrival and A_0 arrival was around 50 µs, a value of 100 µs (200 samples) was specified for t_{aa}.

- **Step c)**. The AIC function is recalculated and applied on an updated time interval at Step b). The arrival of the A_0 mode is now represented by the global minimum the recalculated AIC function.

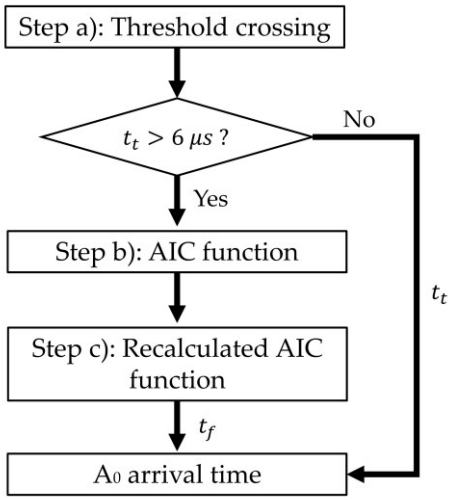

Figure 5.26–Procedural steps of implementing modified two-step AIC picker.

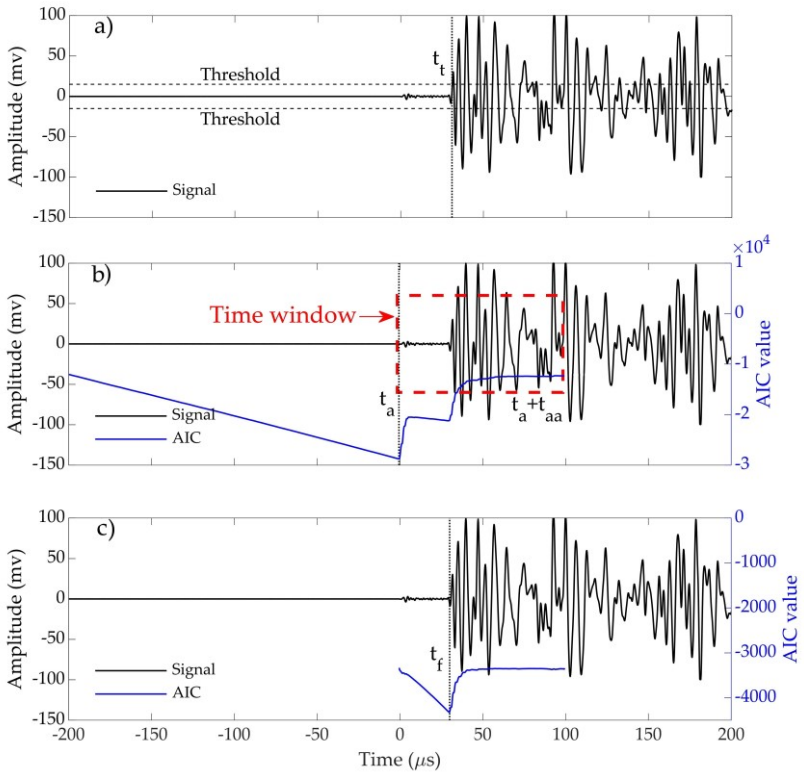

Figure 5.27–Visual description of each stage of modified two-step AIC picker algorithm.

5.3.2 Delta-T mapping based on A_0 arrivals

A complex geometry mild steel plate with four holes was used for experimental delta-T mapping training. This plate has a length of 500 mm, width 300 mm and thickness 3 mm. The material of this plate is the same as that of the simple plate in Section 5.2. Though it was found in Section 5.2.3 that VS150-RIC sensors are the better choice for monitoring corrosion, Nano-30 sensors have much smaller dimensions and wider response than VS150-RIC sensors. Considering that the testing structure is relatively small, Nano-30 sensors were used in the corrosion test on a complex plate to decrease the influence from the size of a sensor on results. As shown in Figure 5.28, a coordinate system was introduced and the origin was placed on the bottom left corner of the test area. The dimensions of the specimen with coordinates of the centres of four holes and radiuses are presented in Figure 5.28. The coordinate of four Nano-30 sensors (sensor 1, 2, 3 and 4) are the same as those documented

in Table 4.1. Four sensors were coupled with the specimen by the way of Loctite 595 Transparent Sealant and amplified with AEP4H (Vallen Systeme GmbH, Germany) at 34 dB gain. Outputs of all the sensors were linked to the same AE System as that in Section 5.2 with the acquisition settings shown in Table 5.5.

Table 5.5 – AE acquisition settings.

Threshold (dB)	Sample Length (ms)	Sample Rate (MHz)	Pre-Trigger (ms)	Rearm time (ms)	Duration discrimination time (ms)
40	1.6	5	0.1	0.8	0.8

The procedural steps of implementing delta-t mapping technique [75] which are presented in Section 2.4.3 were followed. A training grid of 20 mm spacing was placed on the plate. The A_0 mode arrival time data, which were determined by either of two methods presented in Section 5.3.1.2 and 5.3.1.1, were collected after the generation of an H-N source at each node of the grid. For each sensor pair, a delta-T map was produced. The information stored at each node of a delta-T map includes node coordinates and average delta-T. Examples of delta-T maps produced for sensor 1 and sensor 2 and built based on arrival time of the A_0 mode determined by wavelet coefficient threshold method and window AIC method were shown in Figure 5.29.

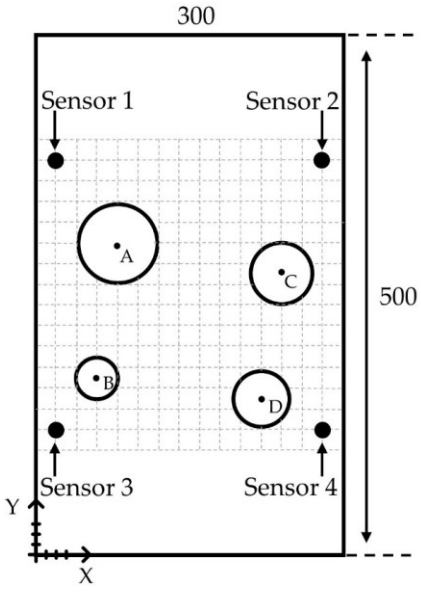

	X coordinate	Y coordinate	Radius
A	80	300	40
B	60	170	20
C	240	270	30
D	220	150	30

Figure 5.28–Schematic layout of the sensors on the complex plate model with grid (unit: mm).

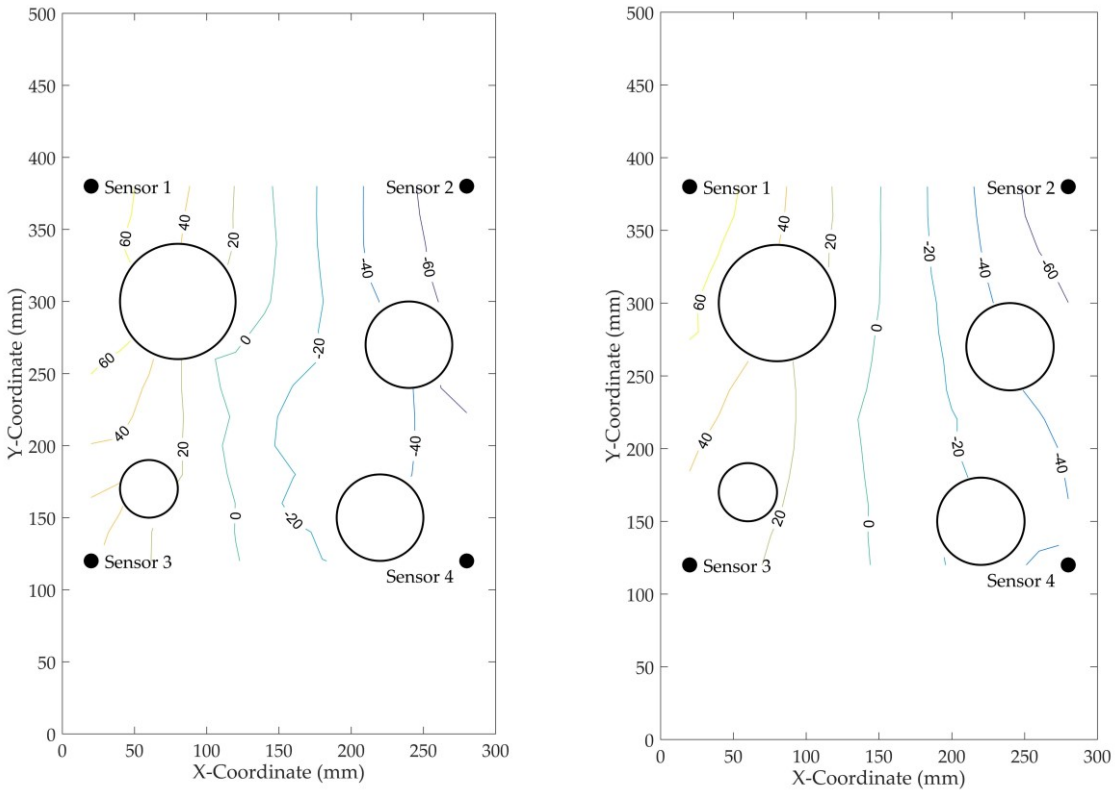

Figure 5.29–Examples of delta-T maps produced for sensor 1 and sensor 2 and built based on arrival time of the A_0 mode determined by (a) wavelet coefficient threshold method and (b) modified two-step AIC method.

5.3.3 Corrosion test data

In order to test the performance of the produced delta-T map based on A_0 arrival, the test setup for delta-T mapping was used again to generate real damage data. The AE acquisition settings are the same as those in Table 5.3. Similar to the test setup for corrosion in Section 5.2.2, a cylindrical thin-walled plastic vessel with 3.5 % sodium chloride solution (pH= 5.7) inside was placed on the plate. The surface area of plate exposed to sodium chloride solution, i.e., the area of corrosion, is off grid and circular with a centre point of X coordinate = 70 mm, Y coordinate =230 mm and a radius of 4 mm. To establish an active uniform corrosion process, a typical three-electrode electrochemical cell (used in Section 5.2.2) was used.

After collecting all the data during corrosion test, AIC function and window AIC method in Section 5.2.3.2 were used to determine the arrival time of signals. The delta-Ts for each sensor pair were calculated and used to identity a line with same and equal delta-T in

corresponding map. This line represented all possible locations of corrosion damage in each map. By overlaying all the resulting maps, the locations of corrosion damage were determined. Examples of overlaid delta-T maps are shown in Figure 5.30.

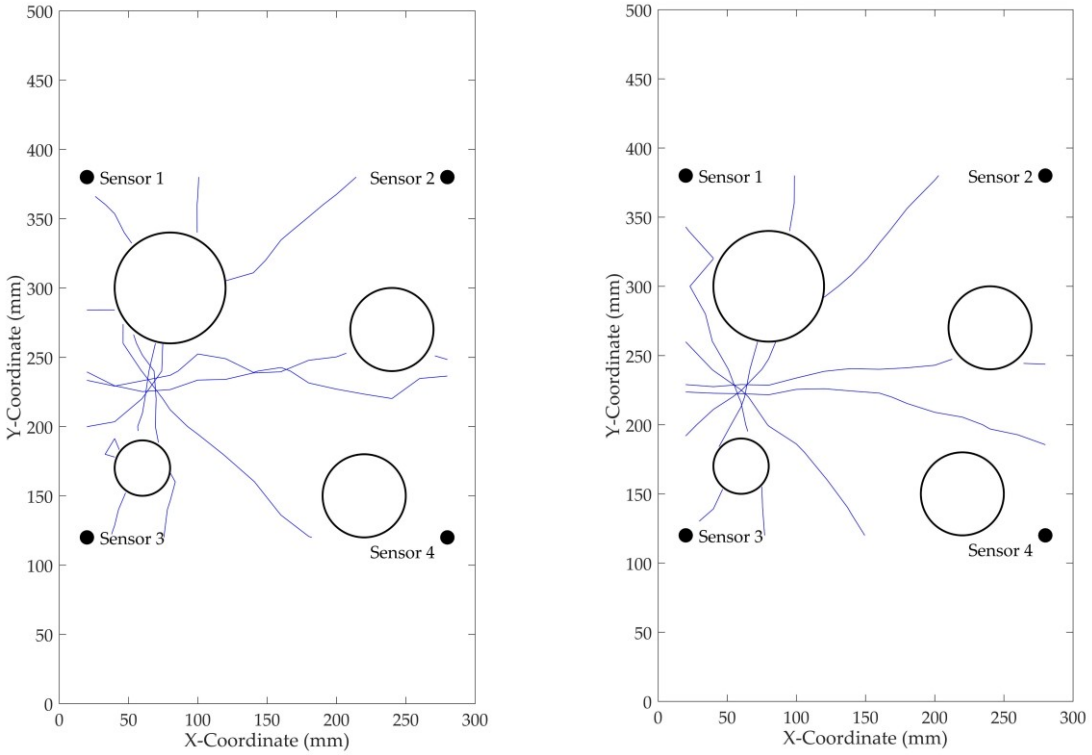

(**a**) (**b**)

Figure 5.30–Examples of overlaid delta-T maps based on arrival time of the A_0 mode determined by (a) wavelet coefficient threshold method and (b) modified two-step AIC method.

5.3.4 Results

The real AE event data collected from the corrosion test were assessed with different time estimation methods and location approaches, which are summarised in Table 5.6.

Figure 5.31 documented Euclidian distance errors calculated using Equation (5.3). The percentages of localised events in varied Euclidian distance error ranges (i.e., 0, 0-5, 5-10, 10-20, 20-30, 30-40, >40 mm) were shown.

Table 5.6 – AE event data assessed with varied time estimation methods and location approaches.

`	Time estimation method	Location approaches	For short
Signal →	Threshold crossing	TOA location approach	TC-TOA
	AIC function	TOA location approach	AIC-TOA
	Window AIC method	TOA location approach	WAIC-TOA
	AIC function	Delta-t mapping based on modified two-step AIC picker	AIC-Delta-T-M
	Window AIC method	Delta-t mapping based on modified two-step AIC picker	WAIC-Delta-T-M
	AIC function	Delta-t mapping based on wavelet coefficient threshold method	AIC-Delta-T-W
	Window AIC method	Delta-t mapping based on wavelet coefficient threshold method	WAIC-Delta-T-W

As seen, TC-TOA gave large location errors and the majority of Euclidian distance errors (in black) are higher than 40 mm. After AIC method was used in the TOA localization technique (in white), it can be clearly seen that a significant improvement in accuracy was observed. The percentage of Euclidian distance errors larger than 40 mm reduced significantly from 80.1% to 25.5% and the majority location errors lie between 5 mm to 40 mm. Compared with AIC-TOA, WAIC-TOA (in red) gave a higher accuracy since the percentage of Euclidian distance errors larger than 40 mm reduced significantly and the percentages of Euclidian distance errors including 0-5, 5-10, 10-20 increased. The location results given by WAIC-TOA have an error of 18.3 mm.

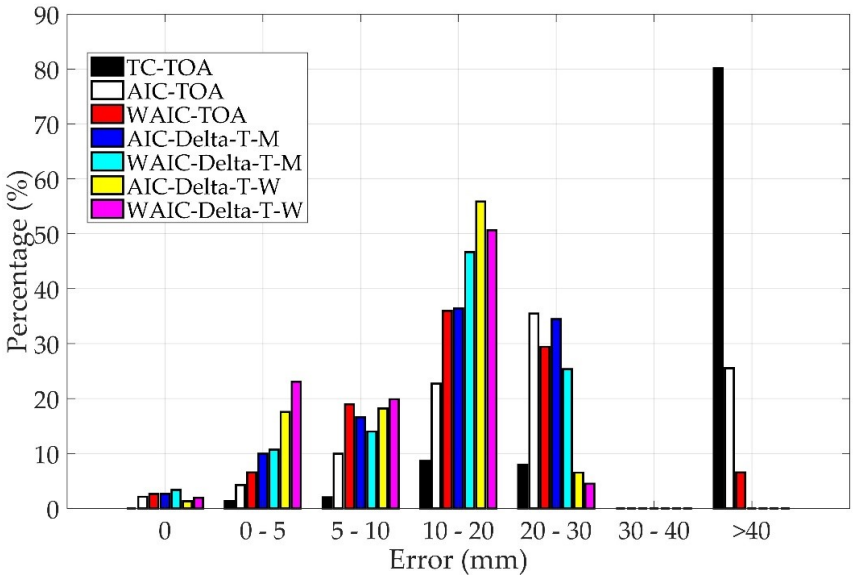

Figure 5.31–Euclidian distance errors of source location results.

Compared with WAIC-TOA, the average error given by AIC-Delta-T-M (in blue) reduced to 15.9 mm and that given by WAIC-Delta-T-M (in cyan) reduced to 15.2 mm. All the location errors are below 40 mm. A slight increase in percentages of both Euclidian distance errors 0-5 and 5-10 mm are observed.

Moreover, a further reduction in location errors was observed after the delta-T mapping based on wavelet coefficient threshold method was used. The average error given by AIC-Delta-T-M (in yellow) was 12.5 mm and that given by WAIC-Delta-T-M (in magenta) was 10.7 mm. As seen in Figure 5.31, compared with AIC-Delta-T-M and WAIC-Delta-T-M, there was an increase in the percentage of Euclidian distance errors 0-5 mm given by AIC-Delta-T-W and WAIC-Delta-T-W; in addition, an obvious reduction in errors 20-30 mm was seen, while it should be noted the percentages of AE events located within the corrosion area also reduced. Moreover, it seemed that location results produced by WAIC-Delta-T-W were more accurate than those by AIC-Delta-T-M since location results given by WAIC-Delta-T-W showed a reduction in average error from 12.5 mm to 10.7 mm and a higher percentage of Euclidian distance errors 0, 0-5 and 5-10 mm.

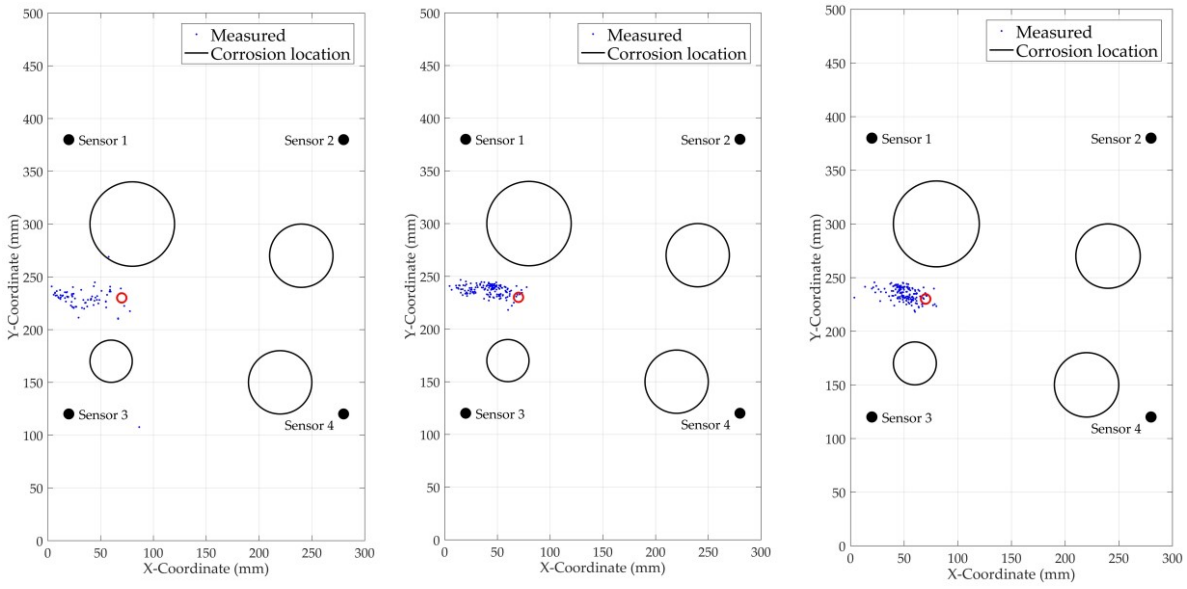

(**a**) (**b**) (**c**)

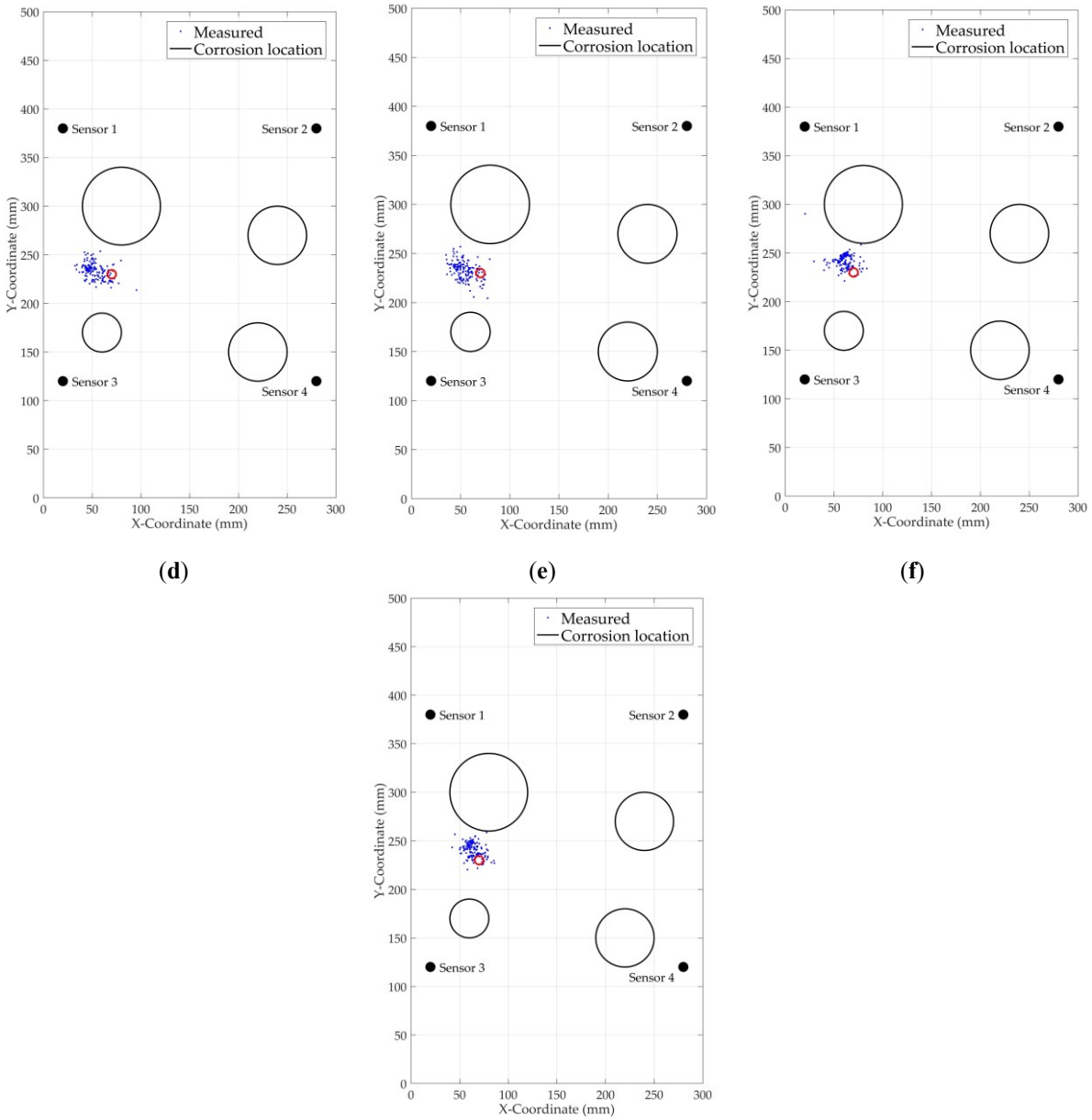

(**d**) (**e**) (**f**)

(**g**)

Figure 5.32– Source location results produced by: (a) TC-TOA, (b) AIC-TOA, (c) WAIC-TOA, (d) AIC-Delta-T-M, (e) WAIC-Delta-T-M, (f) AIC-Delta-T-W and (g) WAIC-Delta-T-W.

5.4 Discussions

In the first part of the study, a corrosion test was performed on a simple plate and it was found that the AE signals recorded during the corrosion test were characterised by a low signal-to-noise ratio. In addition to time estimation methods including threshold crossing and

AIC function, a novel method, window AIC method was proposed. TOA source location approach is a traditional and widely-used location approach and can achieve high location accuracy on simple structures. However, a known wave velocity is required as the input of the TOA algorithm. An inaccurate wave velocity can result in poor performance of the TOA algorithm, thus leading to poor location accuracy. Therefore, based on the signal arrival time and the distance between the source and the sensor, the propagation velocities of AE signals were calculated. It was found that the wave velocities of signals were close to those of the A_0 mode and it was speculated that the first arrival wave mode of signals was A_0 mode. As discussed in Chapter 4, the S_0 mode has substantially smaller out-of-plane amplitudes than A_0 modes and signals generated from corrosion are of low energy. Moreover, the S_0 mode attenuates when travelling from the source to the sensor. Hence the S_0 arrival might be too small to be seen in the waveform.

It should be noted that some of the calculated wave velocities had some discrepancy with the wave velocities of the A_0 mode calculated from the dispersion curve. Some velocities are much larger than and some are smaller than that from dispersion curve, which are due to an early and late triggering. Since corrosion is low-energy source and wave attenuated, corrosion signals were characterized by a low amplitude and low signal-to-noise ratio. Hence signal reflections or high-amplitude background noise might result in an early triggering.

There are various factors that could explain the velocity outliers seen in Figure 5.16 and Figure 5.17. Firstly, corrosion is a low-energy source and signals generated from corrosion are characterized by low amplitudes and low signal-to-noise ratios. The amplitude of the noise can be very similar to that of the signal around the signal onset time. This can make it difficult to accurately identify the arrival of the signal, which can also lead to errors in the velocity measurement. Additionally, due to the fact that certain frequencies will be lost because of wave attenuation, which may result in the fast arrival mode being missed. This can further contribute to inaccuracies in the velocity measurement.

Due to wave attenuation and the fact that certain frequencies will be lost, the fast arrival mode may not be picked. Additionally, for signals with a low signal-to-noise ratio, the amplitude of noise is very close to that of signal around the signal onset time, thus leading to

difficultly in accurately picking up the arrival of the signals and resulting in a late signal arrival and small velocities.

Moreover, it was assumed that the AE source was a point and an AE event generation time at the AE source was the arrival time of this AE event recorded at sensor 9. However, the corrosion area was a circle with a radius equals to 4 mm and there was a small distance, i.e., the thickness of the plate between the AE source and the sensor 9. Therefore, this assumption led to an inaccuracy in signal propagation time from the source to sensors, thus resulting in an inaccuracy in the calculation of wave velocities.

Within Section 5.2.3.3, the accuracy and precision of the estimated source locations based on arrival time predicted by not only threshold crossing and AIC function, but window AIC method are compared. It is clear from corrosion testing on a simple plate that window AIC method is more accurate and sensitive than threshold crossing and AIC function. The percentage of event located within the corrosion area increased from 0% to 0.2% and finally to 2.3% as threshold crossing, AIC function and window AIC method were used successively. The window AIC method however was at a significant disadvantage as it is dependent on the test setup and may require the user input of the time window length. The accuracy of window AIC function depends on the time window. With a properly chosen time window, window AIC function can identify an accurate arrival time. However, with an improper time window length, the arrival time prediction may be inaccurate.

The errors in location accuracy from both Nano-30 and VS150-RIC sensors may relate to the variance in velocity calculation and the difficulty in accurate estimation of arrival times. Additionally, the fact that all signals won't have exactly the same velocity due to varying frequency content/ what is picked up by the sensors also contributed to the errors in location accuracy.

In the second part of the study, based on a good understanding of signals generated by corrosion, the research was extended further to investigate the localisation of corrosion damage on a complex plate. A significant improvement in location accuracy was achieved after delta-T mapping was used as the average error was reduced from 18.3 mm by WAIC-TOA to 15.2 mm by WAIC-Delta-T-M and further reduced to 10.7 mm by WAIC-Delta-T-

W. The location results given by WAIC-Delta-T-W has the highest accuracy. However, it should be noted that, even for WAIC-Delta-T-W, only a very limited events were located within the corrosion area. The reason for this is inconsistencies in the wave arrival prediction. In addition, minor variation in wave velocity will play a part.

Investigation on monitoring corrosion damage on a simple and complex plate has been carried out successfully and the corrosion damage had been located accurately with an average error of 10.7 mm given by WAIC-Delta-T-W. It is worth highlighting that the selection of sensors can have an impact on this source location error. The Nano-30 and VS150-RIC sensors used in this study have distinct frequency responses, meaning they are more sensitive to certain frequency ranges than others. This difference in frequency response can lead to limitations in their ability to accurately identify specific types of frequency components present in AE signals associated with corrosion. Consequently, the estimation of arrival time and source location for such signals can vary across different sensors. Additionally, VS150-RIC sensors have a larger size than Nano-30 sensors. Since the signal is captured at the sensors' circumference rather than sensors' centre point, the sensor's physical dimensions can impact the time it takes for the acoustic waves to reach the sensor. Sensors with different sizes can lead to varying estimates of arrival time, thereby impacting the accuracy of source location.

As real damage sources [134] usually have smaller amplitude compared with H-N sources, it would be of interest to build delta-T maps with AE signals generated from repeatable low-amplitude AE sources and examine the performance of these delta-T maps on localisation of low-amplitude real damage sources such as corrosion. Moreover, it will be beneficial to examine the location accuracy of delta-T mapping with more corrosion at different locations on a complex plate.

5.5 Conclusions

In this investigation, a corrosion test was firstly performed on a simple plate and it was found that the AE signals recorded during the corrosion test were characterised by low amplitude and low signal-to-noise ratio. To accurately identify the onset time of this kind of signals, a

novel time estimation method, which is called window AIC method was proposed and a high accuracy in arrival time estimation was achieved. Moreover, the propagation velocities of AE signals were calculated. It was found that the calculated wave velocities of signals, when compared to a dispersion curve, were in the range of the velocity of the A_0 mode, therefore it was speculated that the arrival prediction techniques were detecting the arrival of the A_0 mode. Therefore, the velocity of the A_0 mode was used in TOA location approach and a high accuracy of source location results was achieved.

The successful localisation of AE events generated from corrosion on a simple plate showed great promise for locating corrosion damage on a complex plate. To achieve that, the delta-T mapping method presented in Chapter 4 need to be updated and built on the basis of the A_0 mode arrival. Hence, one novel method, i.e., modified two-step AIC picker and a method found in the literature, i.e., wavelet coefficient threshold method were used to determine the arrival time of the A_0 mode.

A corrosion test was performed on a complex plate. The recorded AE data was processed with varied time estimation method (i.e., threshold crossing, AIC function and window AIC method) and examined with different source location approaches (i.e., TOA location approach delta-t mapping based on modified two-step AIC picker and delta-t mapping based on wavelet coefficient threshold method). The results showed the source location results with highest accuracy were given by a combination window AIC method and delta-t mapping based on wavelet coefficient threshold method, which had a smallest average error of 10.7 mm and showed a significant improvement in source location accuracy over the TOA location approach.

Although the localisation of corrosion damage on a complex plate has been carried out successfully, development of delta-T maps built from repeatable low-amplitude AE sources examining the location accuracy of delta-T mapping with more corrosion at different locations on a complex plate will be beneficial.

Chapter 6 Acoustic Emission Monitoring of Stress Corrosion Cracking

6.1 Introduction

Stainless steels have remained important in structures and are used in a wide variety of applications because of their comprehensive performance of strength, stiffness, toughness and high temperature tolerance. However, the interactions between stainless steels and diverse in-service environments are inevitable and can lead to impaired physical and mechanical properties. As a result of these interactions, SCC has been a major cause of the premature failures of various structures and components made of stainless steels in various industries, such as the oil and gas industry.

Three working conditions must be present simultaneously to induce SCC: a moderately corrosive environment, sufficient tensile stress and a susceptible material [171], as shown in Figure 6.1. Eliminating or limiting any of these conditions can prevent SCC.

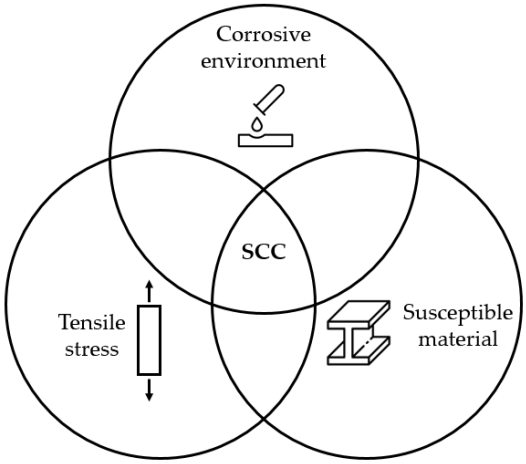

Figure 6.1–Requirements to induce SCC

In 1972, the concept of "stress corrosion spectrum" was first put forward by Parkins [172]. It was proposed that the evidence of different mechanisms of stress corrosion may be

rationalised in a continuous spectrum of mechanisms. It was suggested that SCC damage mechanism is predominantly controlled by a changing contribution from electrochemical to mechanical factors depending on SCC evolution. A schematic diagram which represents a three-stage model for SCC progression [86] based on Parking Stress Corrosion Spectrum is shown in Figure 6.2.

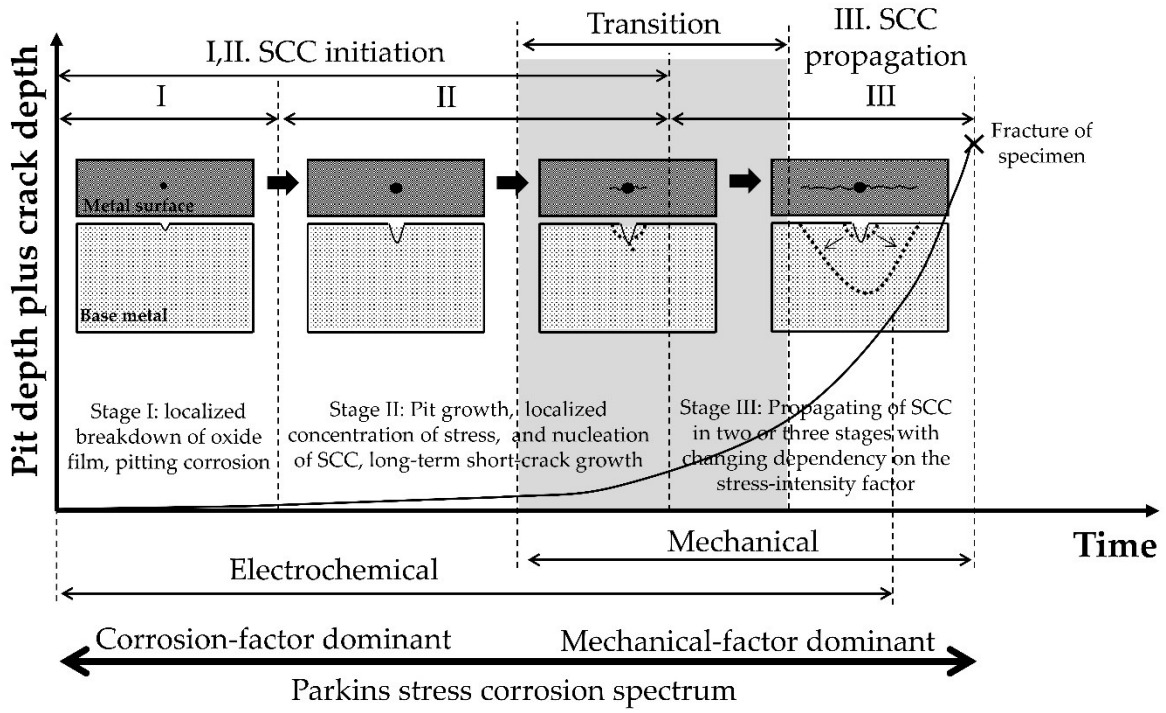

Figure 6.2– A schematic diagram of a three-stage model for SCC progression based on Parking Stress Corrosion Spectrum [86]

Despite the fact that SCC involves a complex interaction of mechanical conditions, metallurgical effects and characteristics of the surrounding environment, in most cases it initiated at the early localized corrosion or mechanical flaws such as pitting, local intergranular attack, scratches or initial defects [86]. Subsequently, the crack initiation evolves to slowly growing short cracks, until a critical crack length is reached and eventually the component fails. It is perceived that SCC development in the initiation stage is a very slow process with long duration, which can be used to estimate the expected service lifetime of an exposed component [173,174]. Thus, advanced continuous in-situ monitoring of SCC and thus identifying the initiation and propagation stages of the SCC phenomenon accurately is important for an accurate evaluation of the lifetime of the components susceptible to SCC.

Generally, the initiation and propagation of SCC are greatly influenced by localized electrochemical processes, alongside the stress and strain fields at the crack tip. Therefore, predicting this phenomena is difficult because the conventional electrochemical methods cannot be used directly and integrally [175], and mathematical based models have the problem of obtaining good input parameters experimentally [176].

Due to the high sensitivity of AE, it has been extensively studied and used to detect and monitor corrosion [9,115,177–179] and SCC related issues [11–13,86,180–184]. However, specimens used in the majority of these studies were small [11,13,86,180–184], which only allows one or two AE sensors to be coupled and the damage locations were known. There are still a number of challenges regarding the detection capabilities of AE techniques to locate unknown SCC damage sources on a large specimen with additional complexity, addressing these should take us a step closer to real-world applications of monitoring SCC with AE techniques on in-service structures.

The aims of this section are to conduct experimental investigations for identifying different source mechanisms during SCC, to assess the ability of AE techniques on the identification and localization of AE signals from SCC in metallic specimens with added complexity, and to demonstrate a discrimination method between AE signals generated from corrosion and SCC.

According to the accelerated SCC test standards: ASTM G129 [185], ASTM G36 [186], and NACE TM0177 [187], the specimens are required to be immersed in a bulk solution and exposed to elevated temperature, which is difficult to facilitate condition monitoring using AE techniques. In an attempt to perform the drop evaporation test recommended by ISO 15324 [188], it was found that a large number of noise with amplitudes higher than 60 dB were emitted by evaporation of falling drops and the salt crystallization. Therefore, in this section, an improved chloride droplet SCC test was undertaken with the dog-bone stainless steel specimen and circulating solution to trigger the SCC crack evolution.

6.2 Experimental procedure

6.2.1 Material and specimen

For the SCC tests, the tested material was 304 stainless steel, which is susceptible to SCC [189]. Two specimens were manufactured in Lakeland Steel Ltd., Cumbria, UK. The chemical composition of 304 stainless steel, used in this study, is given in Table 6.1. The specimens are plates measuring 440 mm by 200 mm and 10 mm thick, as shown in Figure 6.3.

Table 6.1 – Chemical composition of 304 stainless steel specimen.

Element	C	Si	Mn	P	S	Ni	Cr	Mo	Cu
wt%	0.066	0.58	0.82	0.029	0.002	8.75	18.29	0.14	0.14

Figure 6.3–304 stainless-steel specimens for SCC tests

Dimensions of the specimens are shown in Figure 6.4. To match the size of the fixture of the test rig and reduce the concentration of the stresses in central holes on specimens, four small plates were used on the both sides and both ends of each specimen. The dimensions of these plates are shown in Figure 6.5.

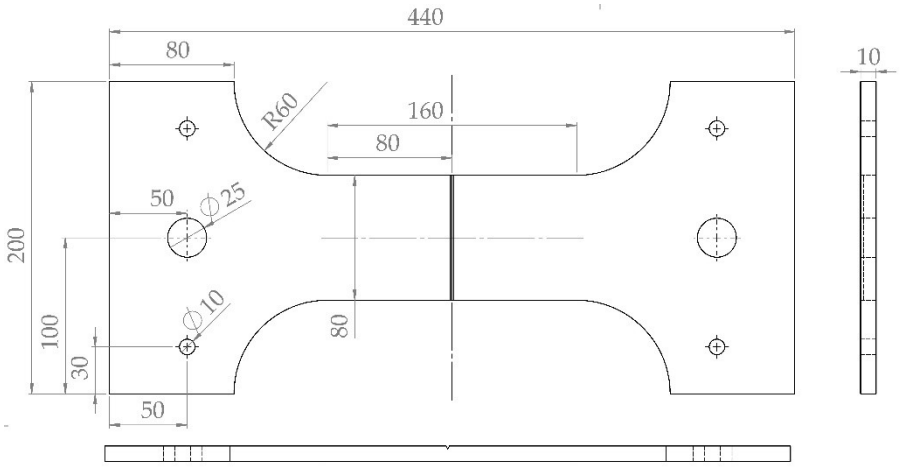

Figure 6.4– Dimensions of the 304 stainless-steel specimens

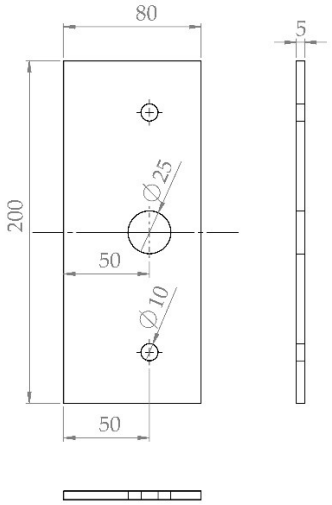

Figure 6.5– Dimensions of small plates.

To accelerate the SCC test, stress concentration was induced by manufacturing a V-notch in the middle of specimens with electrical discharge machining (EDM). The V-notch had a length of 80 mm, a depth of 2 mm and an opening angle of 60°. Dimensions of the V-notch are shown in Figure 6.6. The notch was ground with 120, 320, and then 600 grit abrasive paper. The mechanical grinding was performed on part of the specimen surface surrounding the notch using a multi-purpose micro grinder (Nakanishi Inc., Kanuma, Japan) with abrasive

papers of grit 120, 320 and 600. After that, specimens were thoroughly degreased well with acetone. Shortly before the SCC experiments begun, the notch was manually ground once again with abrasive paper of grit 600 and rinsed several times with deionized water.

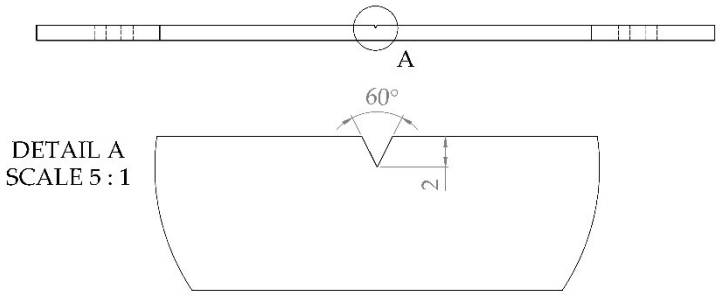

Figure 6.6– Dimensions of the V-notch on specimens.

6.2.2 SCC testing and AE measurement

The experimental setup is shown in Figure 6.7. Small plates were installed firmly at the end of the specimens and mounted in the fixture attached to the testing machine, which is a Horizontal Tensile Testing Machine (TWI Ltd., Cambridge, UK) with maximum loading capacity of 250 kN. The tensile stress on the specimen was applied through a loading frame equipped with an electrical hydraulic pump. A dead load of 120 kN was applied on the ends of the specimen.

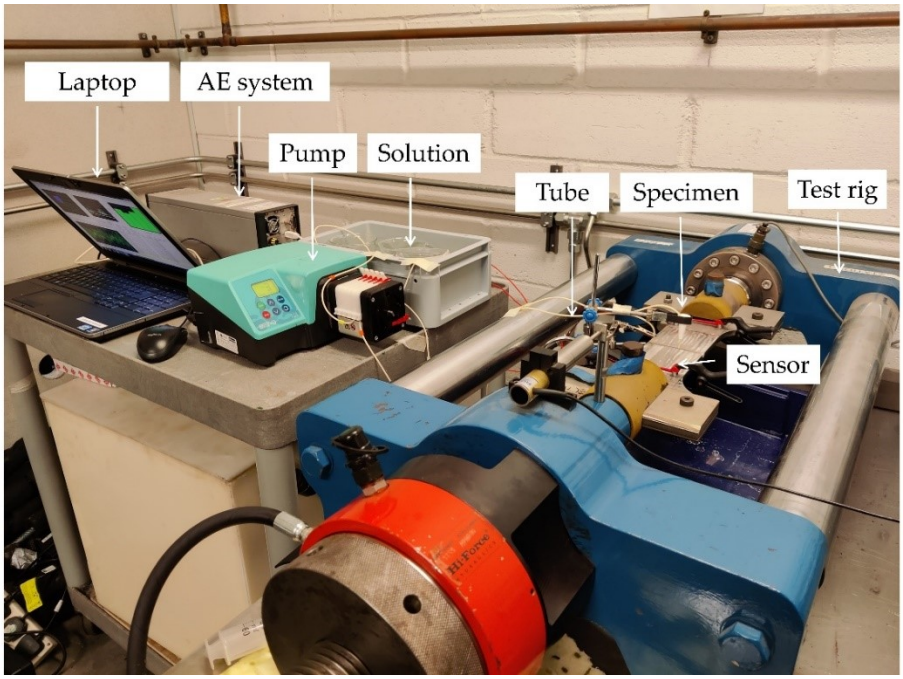

Figure 6.7– The experimental setup of SCC experiments

In addition to application of mechanical stresses on the specimen, the continued contact of the plate surface with the corrosive environment is also crucial to produce SCC. A weak acid solution was used during the test to create a controlled corrosive environment at the notch. The acid solution was mixed by adding two drops of 18% hydrochloric acid solution to every 300 ml 3.5% sodium chloride solution. As determined by a calibrated pH meter, the pH value of the mixed solution was around 2.89. The solution was freshly prepared and put into a glass beaker before the test. A plastic lid was placed on the top of the glass beaker to prevent fluid evaporation.

In order to make sure the specimens were continuously exposed to corrosive environment, a Watson-Marlow 323s peristaltic pump (Watson-Marlow Limited, Falmouth, UK) and a 314MC five channel microcassette pumphead (Watson-Marlow Limited, Falmouth, UK) compatible to the 323s peristaltic pump were used during experiments.

Peristaltic pumps are a type of positive displacement pump, which can be utilized to deliver a wide variety of fluids. The underlying mechanism of pumping involves the compression of a hose or tube via the rotation of rollers, which results in the transfer of liquid via the pulsation of multiple rollers. Due to this process, the peristaltic pumps have proved to deliver correct

and stable flows with excellent repeatability, making them the most precise solution available today. Without valves, seals and glands, the peristaltic pump represents a simple and inexpensive pumping solution. In addition, as fluids being pumped are completely contained within a tube, the cross-contamination by the fluids and any moving parts on the pump can be avoided during the liquid transfer process.

During the SCC test, two Marprene tube with 0.5 mm internal diameter (item number: 979.0050.000; Watson-Marlow Limited, Falmouth, UK) were mounted in the two channels of the pumphead. According to the manufacture's (Watson-Marlow Limited, Falmouth, UK) chemical compatibility guide, the solution used in the tests is compatible with the tube materials. Pumping segments were fitted in the pump cassette in accordance with manufacturer's instructions. To maintain a continuous volume of the solution at the notch, a two-channel system was formed; one for feeding the acid solution to the notch on the specimen, and the other for sucking the remaining solution back. The pump ran at 3 rpm yielding a flow rate of 0.05 mL/min at both channels. A zoomed-in view of the experimental setup showing this two-channel system and locations of sensors is presented in Figure 6.8.

During the SCC test, AE was continuously monitored by piezoelectric sensors. Specimens were tested with four Nano-30 sensors (MISTRAS Group Inc., Princeton Junction, USA) with a frequency domain of 125-750 kHz and diameter of 8 mm, positioned around the corners of specimens as shown in Figure 6.9. To easily identify locations of sensors, a coordinate system was introduced and the origin was placed on the bottom left corner of the specimen as shown in Figure 6.9. The coordinates relative to the origin of four sensors are summarized in Table 6.2.

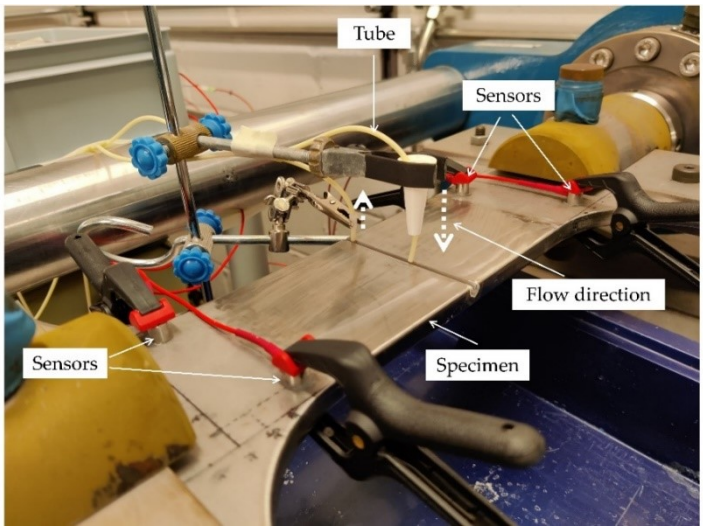

Figure 6.8– A zoomed-in view of the experimental setup showing the two-channel pumping system and locations of sensors.

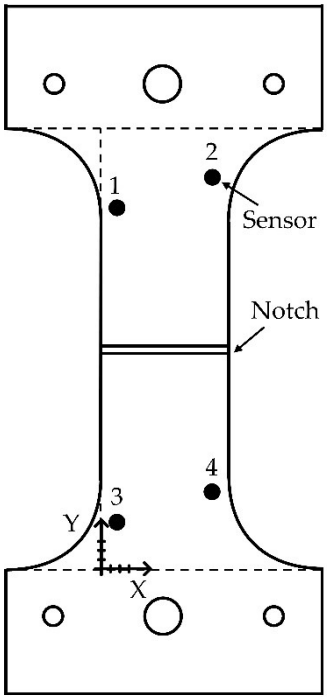

Figure 6.9– A schematic layout of the coordinate system and sensors.

Table 6.2 – Coordinates of sensors (units: mm).

	X coordinate	Y coordinate
Sensor 1	10	230
Sensor 2	70	250
Sensor 3	10	30
Sensor 4	70	50

Throughout the entire testing period, a wide range of signals were detected by theses sensors. All sensors were coupled with the stainless-steel plates by way of Loctite 595 Transparent Sealant (Henkel Loctite Corporation, Helsinki, Finland). For a strong and stable bond and an optimal energy transmission between sensors and plates, a small force was applied to the top of sensors by using nylon spring clamps. The sensors were connected to general-purpose wideband AEP4H pre-amplifiers (Vallen Systeme GmbH, Wolfratshausen, Germany) with a gain of 34 dB and a band-pass filter of 20–1000 kHz. From the pre-amplifier, the signal was collected using a Vallen AMSY-6 monitoring system (Vallen Systeme GmbH, Wolfratshausen, Germany) where the signals were stored for feature and waveform processing. The acquisition setup, which is a crucial factor for AE data collection, is shown in Table 6.3.

Table 6.3 – AE acquisition settings.

Threshold (dB)	Sample Length (ms)	Sample Rate (MHz)	Pre-Trigger (ms)	Rearm time (ms)	Duration discrimination time (ms)
35	1.6	5	0.5	0.8	0.8

In parallel, using the same setup as the SCC test except that no load was applied on the test specimen, a test (hereinafter referred to as the corrosion test) was performed to collect AE data generated from the corrosion. An initial threshold of 35 dB was selected for the corrosion test. However, only a limited number of AE events were recorded. Therefore, the corrosion test was repeated with a threshold of 30 dB.

6.2.3 Material velocity determination

Prior to the SCC test, to check the sensitivity of the AE sensors and determine the wave velocity in the specimens, H-N sources were performed near each sensor. To achieve repeatable results, H-N sources were performed at least three times at the same point.

Results obtained from H-N sources showed that AE events with amplitudes above 98 dB were recorded at each sensor, which confirmed the sensitivity of AE sensors and verified the good acoustic coupling between the specimen and sensors. The results also showed that the amplitude remained constant with variation of 3 dB or less when performing H-N sources at each sensor. An excellent level of reproducibility can be seen for the test results.

The wave speed in the specimens could be determined using the arrival time difference of signals at sensors and the difference between the measured distances from sensors to the AE source. The AIC function was used to determine the arrival time of the signals. For an H-N source at each sensor, the wave velocity was determined at the two remaining sensors on the other side of the notch. For example, if H-N sources are performed at sensor 1, signals recorded at sensor 3 and 4 will be used to calculate the wave velocity. This was repeated for all sensors and average experimental wave velocities for S_0 and A_0 modes were determined and presented in Table 6.4.

Table 6.4 –Average of experimentally measured S_0 and A_0 velocity.

Lamb modes	Average wave velocity (km/s)
S_0	5.17
A_0	2.99

6.3 Results

6.3.1 AE results

AE features such as energy and amplitude are useful indicators of acoustic activity associated with damage in materials. Therefore, they can be utilized to contribute to a better understanding of underlying mechanism during the SCC test and the corrosion test. In this

case, AE amplitude of a single hit and the cumulative energy over time in the SCC test are presented in Figure 6.10.

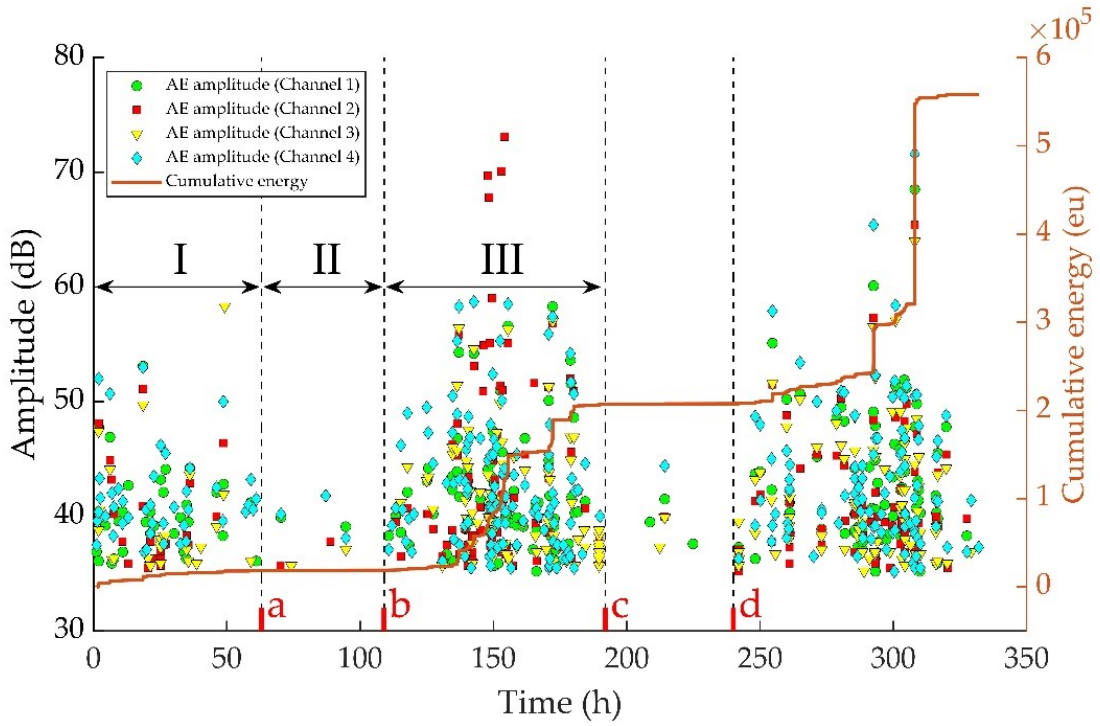

Figure 6.10–AE amplitude of a single hit and the cumulative energy over time in the SCC test.

Based on the analysis of the time evolution of the amplitudes throughout the SCC test, three distinct stages are identified in Figure 6.10, i.e., stage I (from the start of the test to $a = 63\ h$) with moderate AE activity, stage II with rare AE activity (from $a = 63\ h$ to $b = 109\ h$) and stage III with significantly higher AE activity (from $b = 109\ h$ to $c = 192\ h$). In stage I, which was the first 63 hours, the rate of AE hits remained moderate. The great majority of AE hits had amplitudes in the range from 35 to 45 dB. In stage II, the AE activities of the four channels were almost nil over a period of 46 h. In stage III, the major part of AE events had amplitudes in the range from 35 to 50 dB. The start of a high AE activity can be seen since after about 130 hours of the test. Compared to stage I, there were higher numbers of AE hits with amplitude levels above 50 dB in stage III.

A visual inspection of the notch tip occurred at the end of stage III, using a Dino-Lite 10x-220x digital USB 2.0 microscope (Dunwell Tech, Inc, Torrance, USA). Before the inspection, the AE system was paused. The solution at the notch was removed and the notch

tip was dried with air. Since the specimen was exposed to the solution for a relatively short exposure period in testing, the samples did not show distinguishable micro cracks in this visual inspection.

After a three-hour visual inspection, the drops of solution were applied to the notch again and the AE acquisition process was resumed. Because the solution was temporarily removed from notch tip, the SCC was interrupted. A region (from $time = 195\ h$ to $d = 240\ h$) similar to stage II was recognized. A very low AE activity persisted in this region over a period of 45 h until time $d = 240\ h$. Following that, a region with a high AE activities, which was similar to stage III, can be observed. In this region, AE signals with high energy and high amplitude around 70dB were recorded, which led to distinct jumps in the plotted cumulative AE energy versus time. These noticeable jumps in the cumulative AE energy curve likely corresponded to a new cracking event or propagation along an existing crack.

Figure 6.11 shows the variation of AE amplitude and cumulative energy with time in the corrosion test. Similar to the SCC test, three distinct stages were recognized, i.e. stage I (from the start of the test to $a = 24\ h$) with low AE activity, stage II with rare AE activity (from $a = 24\ h$ to $b = 71\ h$), and stage III with moderate AE signals (from $b = 71\ h$ to $c = 164\ h$). In stage I, which was the first 24 hours, there were very few signals but some of them had high amplitudes of around 50 dB. Stage II showed almost no AE activity with only two hits over a period of 47 h. In stage III, a total of 156 AE hits were recorded with an average of around 1.7 hits per hour during a period of 93 h.

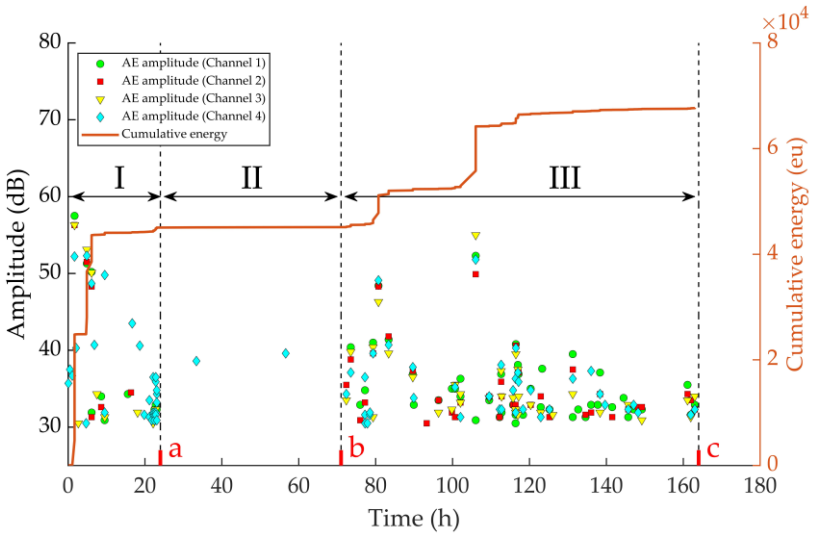

Figure 6.11–AE amplitude of a single hit and the cumulative energy over time in the corrosion test.

AE amplitude of extracted AE signals from the SCC test and the corrosion test were compared over the time evolution and shown in Figure 6.12. Overall, similar three-stage AE evolution trends can be identified in signals from the SCC test and the corrosion test. The duration of stage II in the SCC test was very similar to that in the corrosion test, while the duration of stage I in the SCC test was longer than that in the corrosion test. More AE activity with higher amplitude level was produced during stage I and stage III in SCC tests compared to the corrosion test.

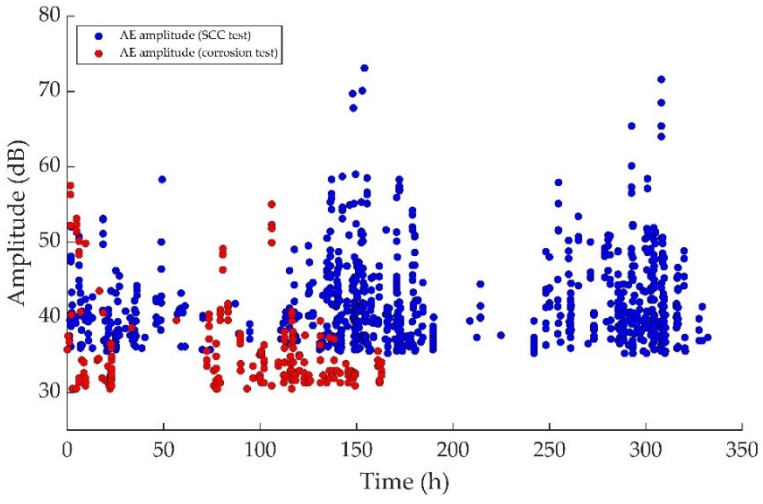

Figure 6.12–Comparison of AE amplitude over time in SCC test and the corrosion test.

6.3.2 AE Source location and microscopic inspection results in the SCC test

One of the most important and beneficial attributes of AE techniques is its ability to locate sources of damage within the testing structure. In this section, this was achieved through traditional TOA source location technique, a triangulation method which is described in Chapter 2. As at least three sensors are required to apply the triangulation method, only AE events having been detected by at least three sensors were utilised in the following analysis.

The accuracy of the TOA localization method depends on the precision of the velocity determination. As discussed in Chapter 2, with a known plate thickness, dispersion curves depict the relationship among the propagation velocities and the frequency of each mode. The dispersion curves for steel (longitudinal wave velocity 5900 m/s, transverse wave velocity 3100 m/s, and thickness 10 mm) were calculated with the commercial software (Vallen Dispersion, version R2017.0504.2, from Vallen Systeme GmbH) and presented in Figure 6.13. In the diagram, each individual curve represents the group velocity curve of a specific mode in a frequency range from 0 to 900 kHz (horizontally).

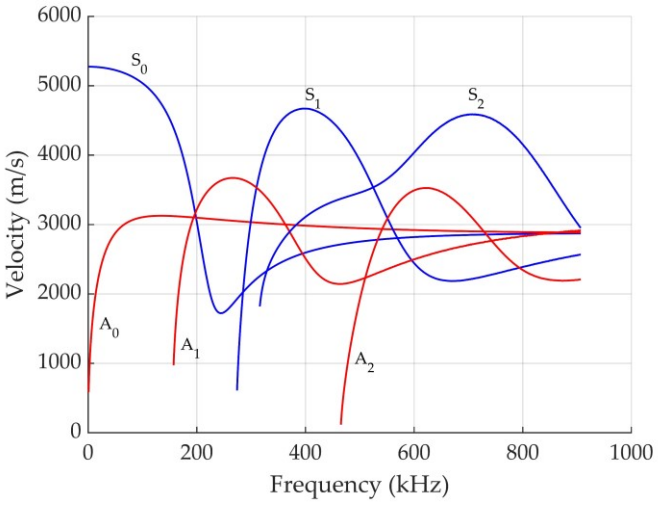

Figure 6.13– Group velocity dispersion curves for steel (longitudinal wave velocity 5900 m/s, transverse wave velocity 3100 m/s, and thickness 10 mm).

In order to calculate the frequency spectrum of recorded waveforms, the Fast Fourier Transform (FFT) was utilised to convert waveforms from the time domain to the frequency

domain. Prior to the FFT analysis, the arrival time of the waveform was determined by the AIC function. Since the propagation velocities only depend on the frequencies of the first arrival of the waveform rather than the frequencies of the whole waveform, the FFT analysis was performed on the waveform data with the time window starting 5 us before the arrival time and ending 30 us after the arrival time. Figure 6.14 documents the peak frequency of AE hits in the SCC test. As shown in Figure 6.14, peak frequency ranging from 200 to 400 kHz are the majority (around 75%). In addition, the partial power is calculated by dividing the summation of the power spectrum over the frequency range of interest by the total power and multiplied by 100. A scatterplot of partial power from 0 to 200 kHz (blue), 200 to 400 kHz (red) and 400 to 600 kHz (black) of AE hits is shown in Figure 6.15.

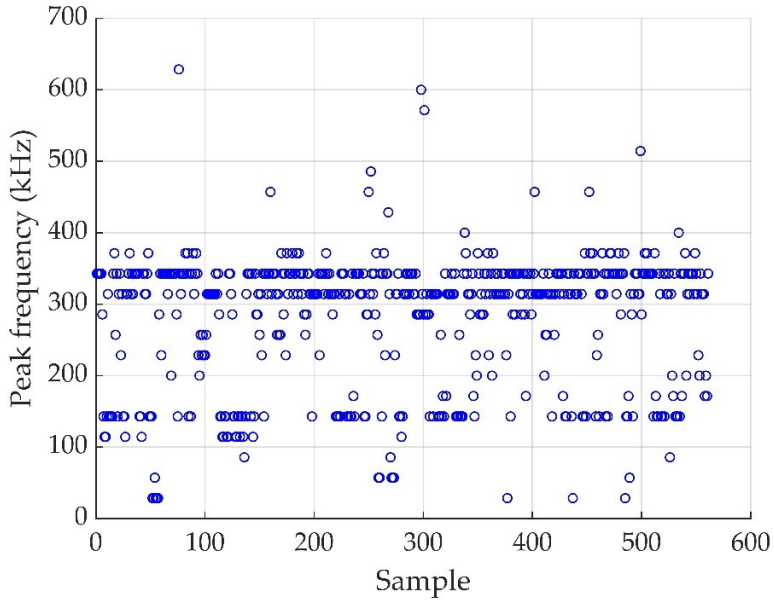

Figure 6.14–Peak frequency of AE hits in the SCC test.

The average magnitude of partial power from 200 to 400 kHz is 47.0%, which is larger than that of partial power from 0 to 200 kHz (21.2%) and that of partial power from 400 to 600 kHz (15.3%). It can also be found the majority of signals had large magnitude of partial power from 200 to 400 kHz. This indicates that these signals had larger amount of energy in frequency components from 200 to 400 kHz.

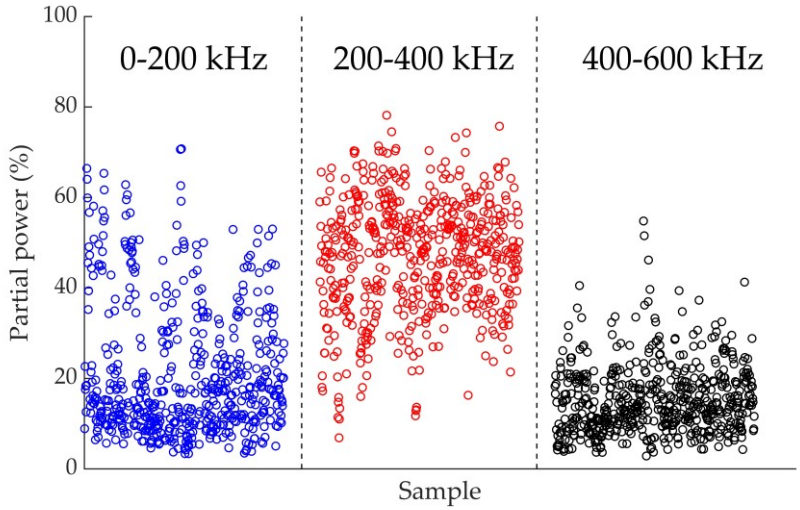

Figure 6.15–Partial power from 0 to 200 kHz, 200 to 400 kHz and 400 to 600 kHz of AE hits in SCC test.

Since only low frequencies were seen, higher modes are unlikely to be occurred. In addition, higher modes usually propagate with a much lower energy than two major Lamb wave modes, S_0 and A_0 modes, in low frequency regime. Therefore, group velocity dispersion curves of the A_0 and S_0 modes were considered and discussed. However, if triggering modes of AE waves were higher modes, using the wave velocities of S_0 and A_0 modes in the source location algorithm will decrease the accuracy of the source locations.

As shown in Figure 6.13 , in the frequency region from 200 to 400 kHz, the group velocity of around 3000 m/s for the A_0 mode is larger than that for the S_0 mode. Therefore, it is very likely that the recorded wave mode of first arrivals of AE hits was the A_0 mode and the experimentally measured velocity for the A_0 mode should be utilised in TOA source location techniques.

For comparison, velocities for both the S_0 mode and the A_0 mode in Table 6.4 were used in source location calculations and results are documented in Figure 6.16 and Figure 6.17 respectively with locations of cracks which were visually detected using an optical Olympus GX 41 microscope (Olympus Corporation, Tokyo, Japan) after the test. For simplicity, the dogbone shaped specimen is plotted as a square. By studying the results of the TOA in both Figure 6.16 and Figure 6.17. It is apparent that more AE events were located in notch when using the velocity of the A0 mode. Although there were still some AE events in Figure 6.17

which were located far away from the notch and outside the specimen boundary, it is apparent that when comparing the location of the AE events and cracks visually observed, there is a smaller error in the accuracy of the location in Figure 6.17 than that observed in Figure 6.16.

A plot showing source location for AE hits that occur in time is presented in Figure 6.18, where the colour bar indicates the time. As seen, at the early stage of the tests, the events (marked in blue dots) initially were located very close to the centre of the notch. Later, the events (marked in green and yellow dots) were mainly located around the edges of the plate. Photos of some typical cracks detected by the optical microscope are shown in Figure 6.19.

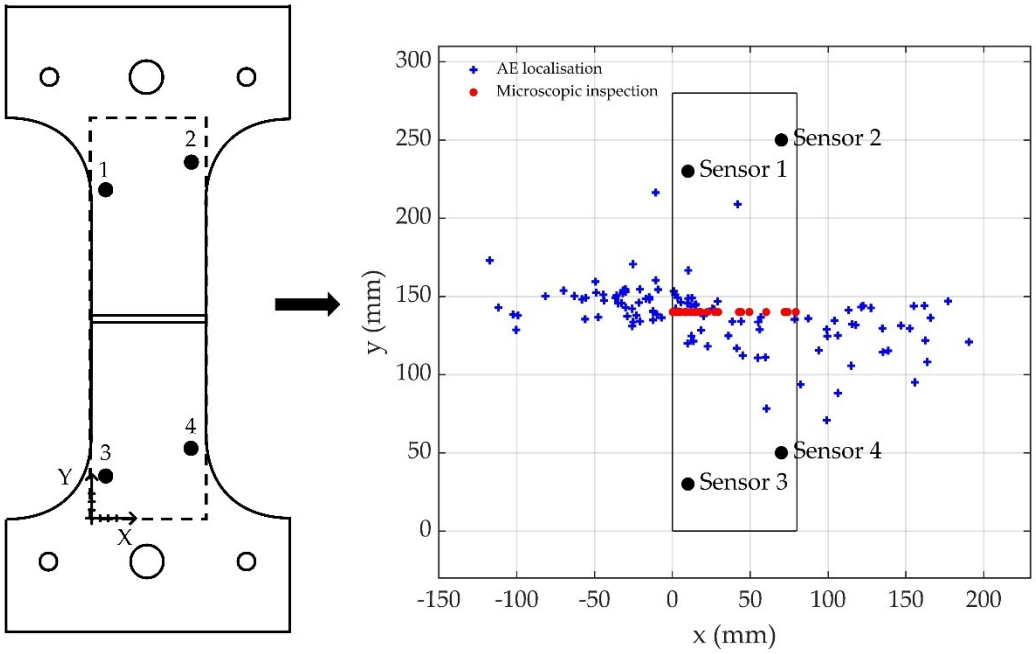

Figure 6.16–AE Source location results using the velocity of the S_0 mode and locations of cracks detected by an optical microscope.

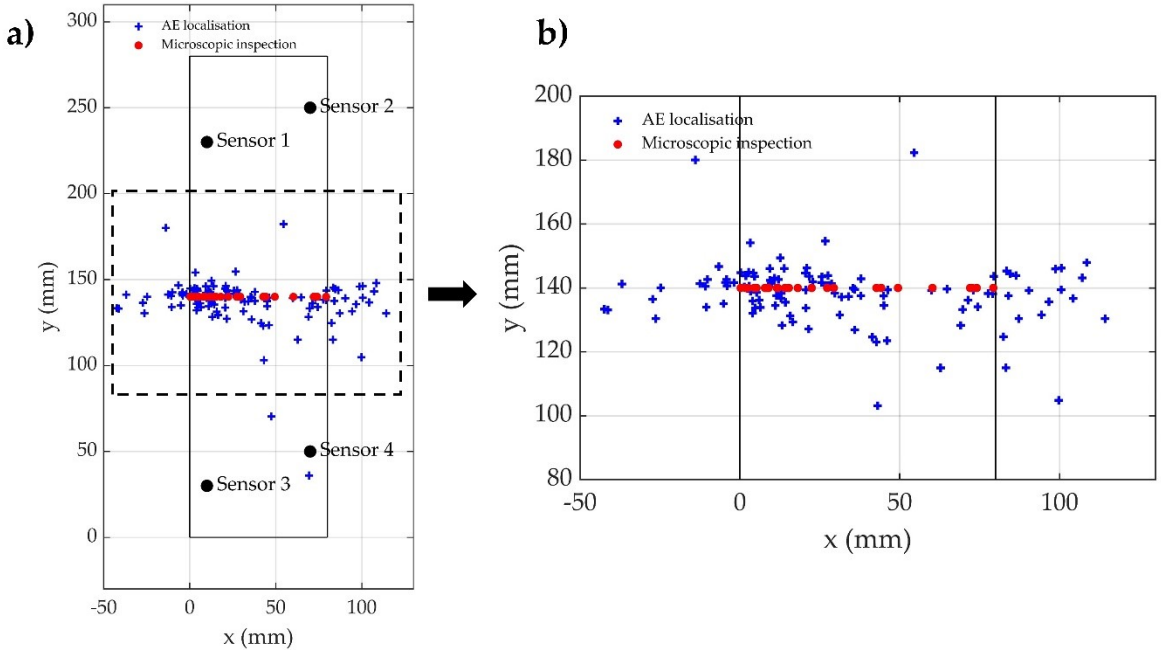

Figure 6.17–AE Source location results using the velocity of the A_0 mode and locations of cracks detected by an optical microscope (a) and a zoomed-in view (b).

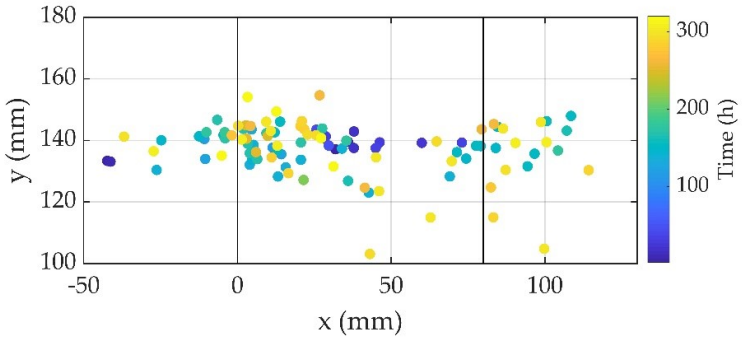

Figure 6.18– source location for AE hits that occur in time.

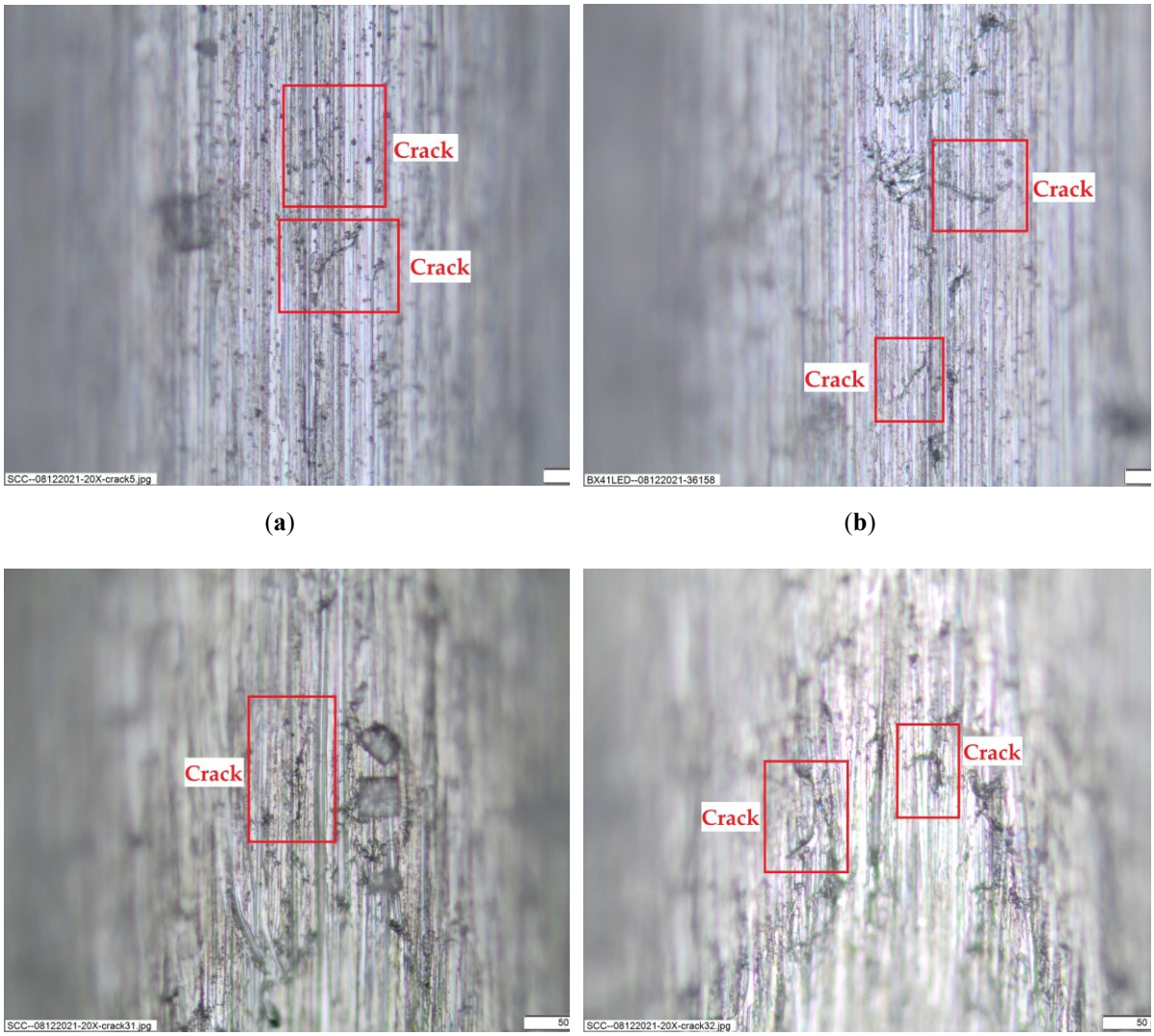

Figure 6.19– Virtually observed cracks.

6.3.3 Cluster analysis of AE data

To further investigate the different damage mechanisms and distinguish between SCC related AE signals and corrosion related AE signals, principal component analysis (PCA) and unsupervised pattern recognition algorithms are adopted. The AE data recorded in the SCC test and the corrosion were mixed as the input of the onward clustering analysis.

6.3.3.1 Feature normalisation

In the multivariable clustering process, It has been shown that normalization of data is an essential step which should be taken to ensure that all parameters receive equal weighting [190]. When processing AE data, all parameter were normalised with Z-score standardization method [191].

The original AE parameters are transformed to corresponding standard score (z-score) forms in the Z-score standardization process. Given a raw data set in d dimensions,

$$Y = \{X_1, X_2, \cdots, X_n\} \tag{6.1}$$

a $n \times d$ data matrix can be written as [191]:

$$X_1, X_2, \cdots, X_n = \begin{bmatrix} x_{11} & \cdots & x_{1d} \\ \vdots & \ddots & \vdots \\ x_{11} & \cdots & x_{nd} \end{bmatrix} \tag{6.2}$$

The specific expression to calculate the standardized Z-score (z_{ij}) is defined as:

$$z_{ij} = \frac{x_{ij} - \mu_j}{\sigma_j} \tag{6.3}$$

Where:

x_{ij} The i^{th} value of the j^{th} attribute

μ_j The arithmetic mean value of the j^{th} attribute

σ_j The sample standard deviation of the j^{th} attribute

The transformed variable with new location and scale information will replace the original variables and have a mean value of 0 and a standard deviation of 1 [192]. A major limitation to the Z-score standardization it that it cannot be used to perform a within-cluster standardization [193].

The AE features commonly used for damage identification in SCC tests [12,86] are listed in Table 6.5. The detailed description about these features can be found in Chapter 2. P1, P2, P3, P4, P5, P6 are the partial powers which are calculated by dividing the summation of the power spectrum over 0-100 kHz, 100-200 kHz, 200-300 kHz, 300-400 kHz, 400-500 kHz, 500-600 kHz by the total power respectively. These features were used to carry out the onward feature selection analysis.

Table 6.5 –AE features for analysis.

Number	AE features	Abbreviation	Number	AE features	Abbreviation
1	Amplitude	A	5	Duration	D
2	Rise time	R	6	Root mean square	RMS
3	Energy	E	7	Average frequency	AF
4	Counts	CNTS	8	Partial power	P1, P2, P3, P4, P5, P6

6.3.3.2 Feature selection

To reduce the volume of computations during pattern recognition, only independent AE features were used in the clustering calculations. The Pearson correlation coefficient was calculated to filter the selected features and the volume of computation can be reduced by using independent parameters. The Pearson correlation coefficient between two variables is formally defined as the covariance of the two variables divided by the product of their standard deviations. A cross-correlation coefficient analysis using Matlab's (The MathWorks Inc., Natick, US) function corrcoef was performed to form the matrix of Pearson correlation coefficients for the AE features. A correlation coefficient level of 0.8 (A correlation coefficient of 1 between two variables means that they are theoretically totally correlated) was used in this work [194]; two features are deemed to be highly correlated with correlation coefficients (absolute values) greater than 0.8. The correlation calculation results are shown in Table 6.6 and a heat map which was produced based on calculated correlation coefficient is displayed in Figure 6.20. The values of correlation coefficients are represented by colours in the heat map.

Table 6.6 – The Pearson correlation calculation results.

Features	A	R	E	CNTS	D	RMS	AF	P1	P2	P3	P4	P5	P6
A	1.00	-0.08	0.42	0.77	0.60	0.78	0.64	-0.20	0.08	0.34	0.27	-0.06	-0.38
R	-0.08	1.00	-0.02	0.03	0.16	-0.01	-0.12	0.24	-0.12	-0.05	-0.09	-0.05	0.00
E	0.42	-0.02	1.00	0.38	0.28	0.77	0.18	-0.05	0.09	0.09	0.03	-0.02	-0.15
CNTS	0.77	0.03	0.38	1.00	0.85	0.61	0.59	-0.33	-0.11	0.50	0.34	-0.05	-0.31
D	0.60	0.16	0.28	0.85	1.00	0.47	0.27	-0.19	-0.04	0.50	0.13	-0.14	-0.31
RMS	0.78	-0.01	0.77	0.61	0.47	1.00	0.37	0.01	0.07	0.17	0.10	-0.11	-0.31
AF	0.64	-0.12	0.18	0.59	0.27	0.37	1.00	-0.48	-0.21	0.27	0.57	0.19	-0.08
P1	-0.20	0.24	-0.05	-0.33	-0.19	0.01	-0.48	1.00	-0.08	-0.48	-0.53	-0.23	-0.01
P2	0.08	-0.12	0.09	-0.11	-0.04	0.07	-0.21	-0.08	1.00	-0.15	-0.50	-0.23	-0.23
P3	0.34	-0.05	0.09	0.50	0.50	0.17	0.27	-0.48	-0.15	1.00	0.08	-0.13	-0.25
P4	0.27	-0.09	0.03	0.34	0.13	0.10	0.57	-0.53	-0.50	0.08	1.00	0.12	-0.13
P5	-0.06	-0.05	-0.02	-0.05	-0.14	-0.11	0.19	-0.23	-0.23	-0.13	0.12	1.00	0.43
P6	-0.38	0.00	-0.15	-0.31	-0.31	-0.31	-0.08	-0.01	-0.23	-0.25	-0.13	0.43	1.00

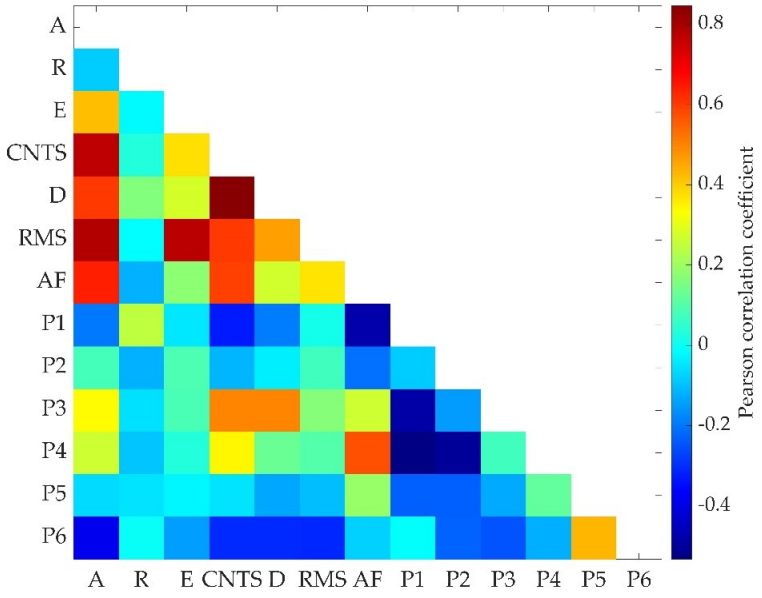

Figure 6.20– The heat map of correlation coefficients between AE features.

A high degree of correlation between certain features can be clearly identified from Figure 6.20. It can be concluded from correlation study that duration and counts are highly correlated (Pearson correlation coefficients >0.8). After the Pearson correlation coefficient study, features including A, R, E, RMS, AF and P1, P2, P3, P4, P5, P6 were selected for PCA since weak correlations between these AE features were found. Because D is widely used as

cluster parameters in the literature [12,86], it was selected among two correlated AE features, i.e. D and CNTS.

6.3.3.3 Feature extraction

To allow a simpler analysis by reducing the number of AE features into a smaller number of 'dimensions', a classical statistical method, PCA, is implemented. PCA utilizes an orthogonal transformation to simplify high-order data sets to linearly uncorrelated lower-dimensional data sets known as principal components, while the majority of data's variation can be preserved [195,196].

In this work, the less correlated features selected using Pearson correlation coefficient study were inputted through the PCA. A PCA typically consists of the following steps [194];

1, Subtract the empirical mean vector from each column of the data set to centre the data around the origin.

2, Compute the covariance matrix from the data set matrix.

3, Compute the eigenvalues and corresponding eigenvectors of the covariance matrix.

4, Project the data from multidimensional space into a two- or low-dimensional space.

Figure 6.21 presents the percentage variance explained by twelve principal components. Eight principal components, which accounted for over 94% of the total variance of the original data set, were generated as a new set of signal features and used in the following clustering analysis.

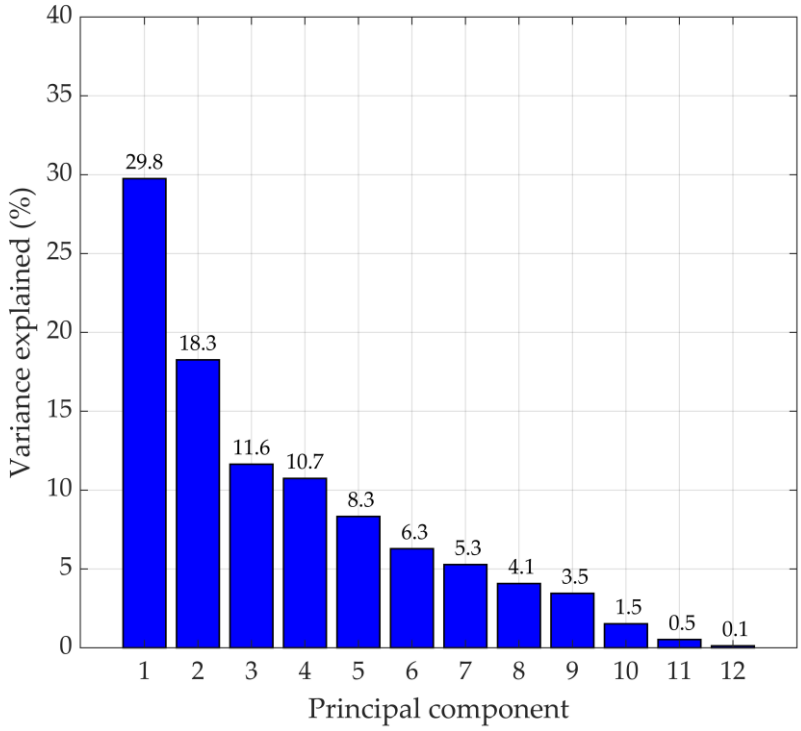

Figure 6.21– The percentage variance explained by twelve principal components.

Figure 6.22 presents the PCA results in the principal component spaces. As seen in Figure 6.22 (a) and (b), most of the signals are overlapping and no distinct separation can be noticed of signals, which a distinct separation can be noticed of signals in Figure 6.22 (c). In addition, it can be found that signals of the corrosion test gathered together in a dense region.

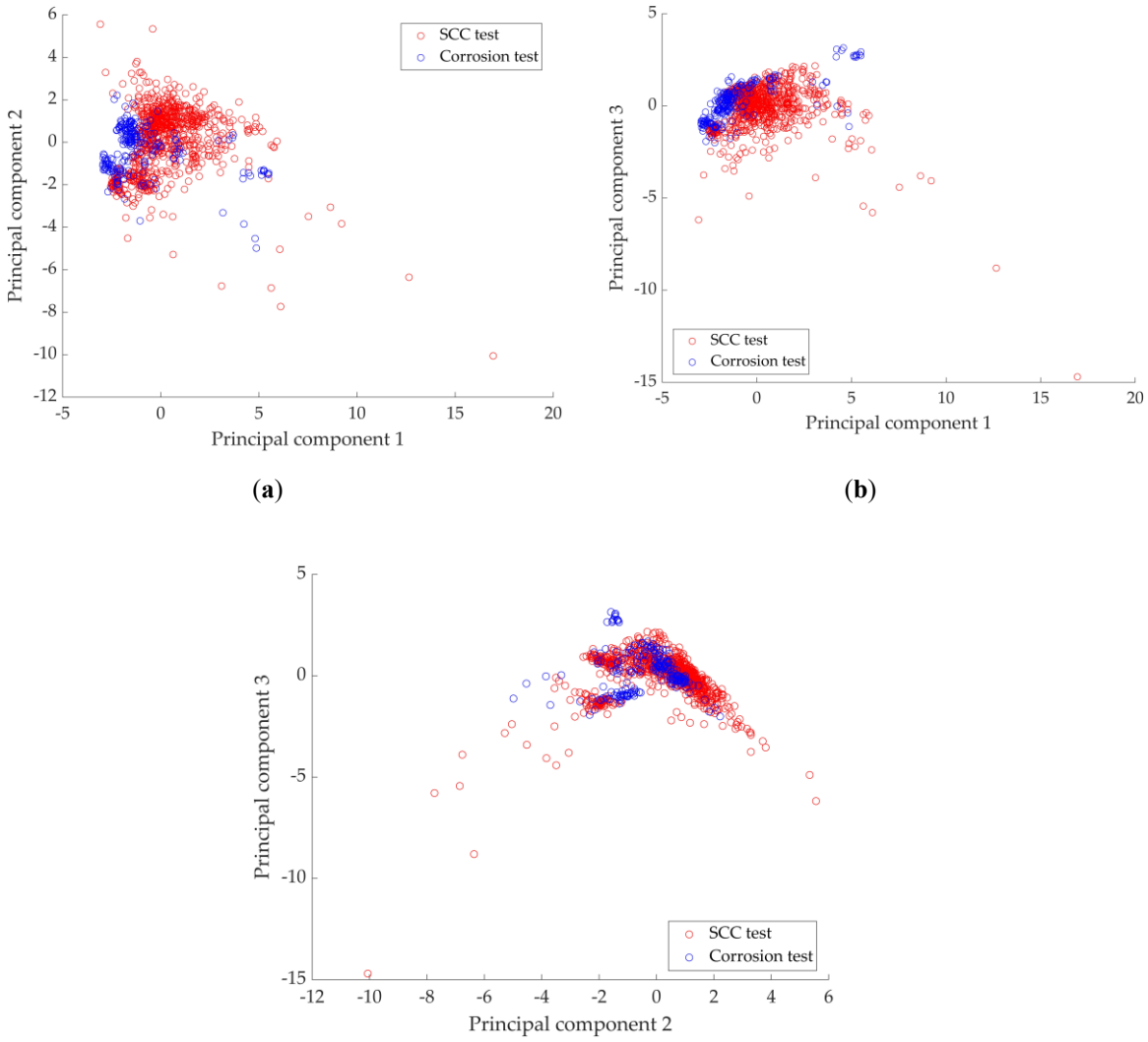

Figure 6.22–PCA results; (a) principal component 2 versus principal component 1, (b) principal component 3 versus principal component 1 and (c) principal component 3 versus principal component 2

6.3.3.4 Unsupervised clustering and cluster quality

Classifying several parameters including energy, duration, and amplitude into clusters forming patterns plays an important role on the pattern recognition techniques. There are two types of pattern recognition techniques: supervised and unsupervised. For the supervised techniques, a class or cluster is given from trained examples with known failure modes. The algorithm will associate the input parameters with this given class or cluster. For the

unsupervised techniques, the algorithm divides the signals into one group according to their similarities.

The classifiers which are able to group signals with similarities into clusters are widely used in the discrimination of different types of damage occurring in the composite material [197–203]. Both k-means clustering method and neural networks are used in the identification of different AE pattern [200]. Other method such as k-means ++ [201], self-organising map[202] [203]and competitive neural network [197] have also been reported.

K-means and Fuzzy c-means clustering algorithms are simple and widely used in AE signal analysis to identify and classify different types of damage mechanisms, such as cracking. They have been shown to be effective in identifying different AE source mechanisms [201]. Hence, in this work, these two classical multivariable clustering techniques were used to group AE signals into classes. Alternative unsupervised machine learning algorithms, such as the self-organizing map and neural network, were not utilized due to their complexity in understanding and implementation. Additionally, their computational requirements, including the need for extensive computational resources and time, made them less suitable for the purposes of this study.

6.3.3.4.1 Fuzzy c-means

The objective of the Fuzzy c-means is to minimise the within-cluster scatter (i.e., the Euclidean distance between each data element in a cluster) and maximise the global compactness of the clusters. The main advantage of Fuzzy c-means clustering is that one piece of data has a degree of belongingness in [0,1] as membership value to each of the clusters and thus it can belong to two or more clusters at the same time rather than belonging completely to one cluster.

Given the feature vector X with n observations,

$$X = \{x_1, x_2, \cdots, x_n\} \tag{6.4}$$

the Fuzzy c-means algorithm can be stated by the following steps;

1, Select number of clusters M and randomly initialise membership matrix U.

$$U = \begin{bmatrix} u_1(x_1) & u_1(x_2) & \cdots & u_1(x_n) \\ u_2(x_1) & u_2(x_2) & \cdots & u_2(x_n) \\ \vdots & \vdots & \vdots & \vdots \\ u_M(x_1) & u_M(x_2) & \cdots & u_M(x_n) \end{bmatrix} \tag{6.5}$$

where $u(x)$ is the membership value to each of the clusters.

2, Calculate the matrix of the cluster centres V by using the matrix U.

$$V = [C_1|C_2|\cdots C_M] \tag{6.6}$$

where C_i is Cluster centre.

3, Update membership matrix U and ensure that the memberships of each sample to all clusters should sum to 1.

4, Iterate steps 2 and 3 to update membership matrix and matrix of the cluster centres until the minimum value of function $J(U,V)$ is achieved or the improvement over the previous iteration $\left\|U^{(q+1)} - U^{(q)}\right\|$ is below a termination criterion, whereas q is the iteration step.

$$J(U,V) = \sum_{j=1}^{n}\sum_{i=1}^{M}\left[u_i(x_j)\right]^f d^2(x_j, C_i) \tag{6.7}$$

By updating the cluster centres as well as the membership values at each iteration, the cluster centres were iteratively shifted to the "right" location within the data set. This procedure will lead to convergence of the fuzzy c-means algorithm to either a local minimizer or saddle point of the object function $J(U,V)$.

6.3.3.4.2 K-means

K-means clustering is a popular clustering algorithm used in unsupervised machine learning. It is fast and efficient in terms of computational cost, and can produce tight clusters. Given the feature vector X in Equation (6.4) with n observations, the basic principle of k-means is

to assign n observations to all the clusters. The steps for performing k-means clustering analysis are as follows;

1, Select the number of clusters M and randomly assign initial cluster centroids C_i.

2, Calculate the Euclidean distance between each data observation x_j and the cluster centroids C_i.

3, Assign each data observation x_j to the cluster with the minimum Euclidean distance.

4, Calculate the new cluster centroids after all data observations feature vector X have been assigned.

5, Repeat Step 2, 3 and 4 until the solution converges (i.e. the cluster centroids centre coordinates do not change any more).

K-means clustering is similar in approach to Fuzzy c-means clustering. The main difference is that, in k-means clustering, each data point belongs to only one cluster centroid, but in Fuzzy c-means each data point can belong to two or more cluster centroids with degrees of membership to the clusters.

6.3.3.4.3 Cluster quality

In an unsupervised clustering process, Fuzzy c-means and k-means algorithms depend on the features of the data set and certain assumptions on the number of clusters. Therefore, some sort of evaluation as regards to the clustering quality in feature vector X is required. In this work, two popular cluster quality criterion, Silhouette and Calinski-Harabasz indexes were used to evaluate the clustering results of Fuzzy c-means and k-means clustering algorithm. The number of clusters was gradually increased to perform the typical incremental clustering until a predefined threshold value was exceeded. The number of clusters which returns the peak value of Silhouette and Calinski-Harabasz indexes was deemed to be optimal.

Silhouette validation index [204] show compactness of data points within a cluster and separation between clusters based on calculating the average distance between each data point within the cluster and smallest average distance between clusters. The largest silhouette

value which represents a better clustering quality correspond to the optimum number of cluster. For a data point i in a cluster, the Silhouette indexes can be calculated using Equation (6.8);

$$s(i) = \frac{b(i) - a(i)}{\max\{a(i), b(i)\}} \tag{6.8}$$

Where $a(i)$ is the mean distance calculated from the data point i to the other data points within the same cluster and $b(i)$ is the minimum mean distance calculated from the data point i to all data points in any other cluster.

Calinski-Harabasz index [205] shows the clustering quality based on the average sum of between-cluster and within-cluster dispersion for all clusters. Given the feature vector X of n observations which has been clustered into M cluters, it can be defined as follows;

$$s = \frac{tr(B_M)}{tr(W_M)} \times \frac{n - M}{M - 1} \tag{6.9}$$

Where $tr(B_M)$ is the overall between-cluster variance and $tr(W_M)$ is the overall within-cluster variance. Similar to Silhouette validation index, a larger value of Calinski-Harabasz index reflects a better data partition result.

The cluster quality results for the Fuzzy c-means and k-means clustering approaches are presented in Figure 6.23 (a) and (b) respectively. For the Fuzzy c-means, it can be seen that the optimal number of clusters determined by Silhouette coefficient is four, while that determined Calinski-Harabasz Index is two. Since the value of Calinski-Harabasz Index at four clusters is very similar to that of Calinski-Harabasz Index at two clusters, the optimal number of clusters is determined to be four for the Fuzzy c-means. For the k-means, the optimal number of clusters estimated by Silhouette coefficient is two, while that estimated by Calinski-Harabasz Index is five. As the difference between the value of Silhouette coefficient at five clusters and at two clusters is small, the optimal number of clusters is determined to be five for the k-means and is used for the onwards analysis of data presented below.

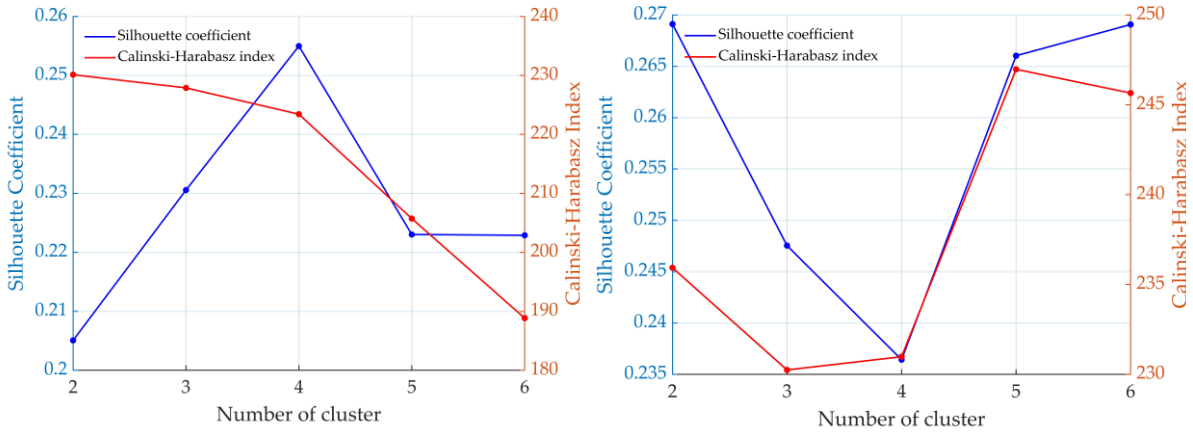

Figure 6.23– The cluster quality results for the Fuzzy C-means (a) and k-means clustering approaches (b).

6.3.3.5 Cluster analysis of AE data

The data was classified into four clusters (cluster 1, cluster 2, cluster 3 and cluster 4) using the Fuzzy c-means method and into five clusters (cluster 1, cluster 2, cluster 3, cluster 4 and cluster 5) using k-means method and results are presented in the principle component spaces as shown in Figure 6.24 and Figure 6.25 respectively. In these figures, the signals were marked in different shapes to differentiate different clusters and different colours to differentiate signals from the SCC tests and those from the corrosion test. As shown, although there was an extra cluster in the k-means clustering, observations in the same cluster of k-means and Fuzzy c-means can be treated as similar. Therefore, only the results of Fuzzy c-means are used for the onwards analysis.

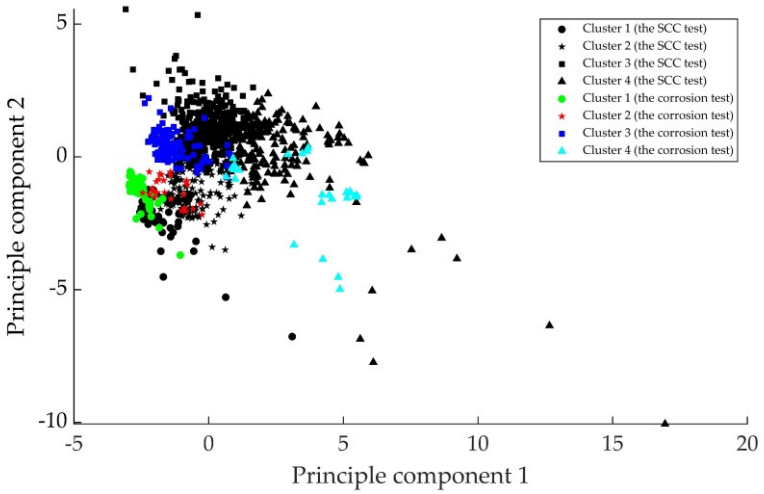

(**a**)

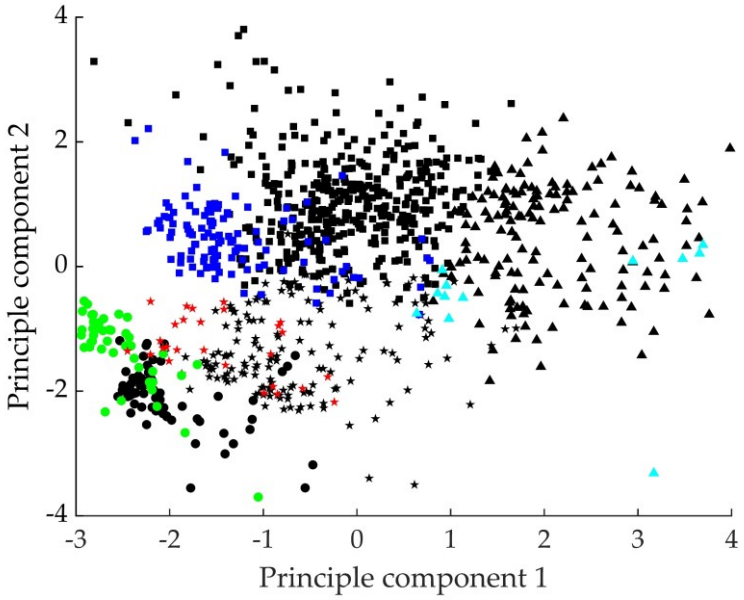

(**b**)

Figure 6.24– The clustering results obtained using Fuzzy c-means algorithm (a) and a zoomed-in view (b).

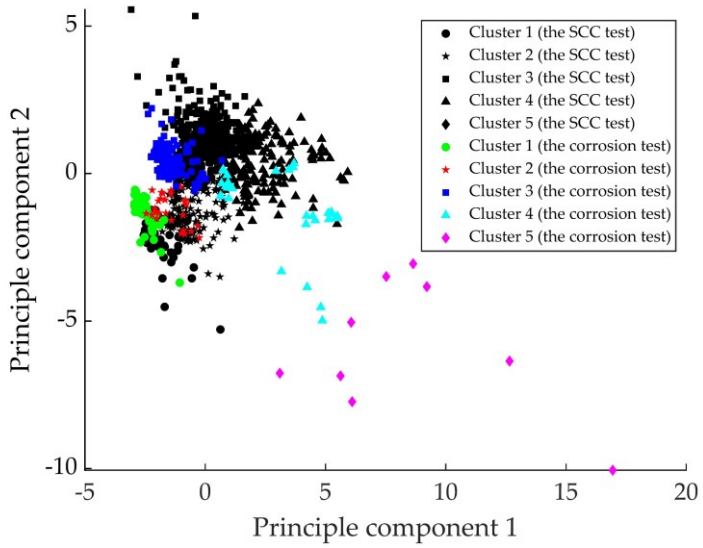

(**a**)

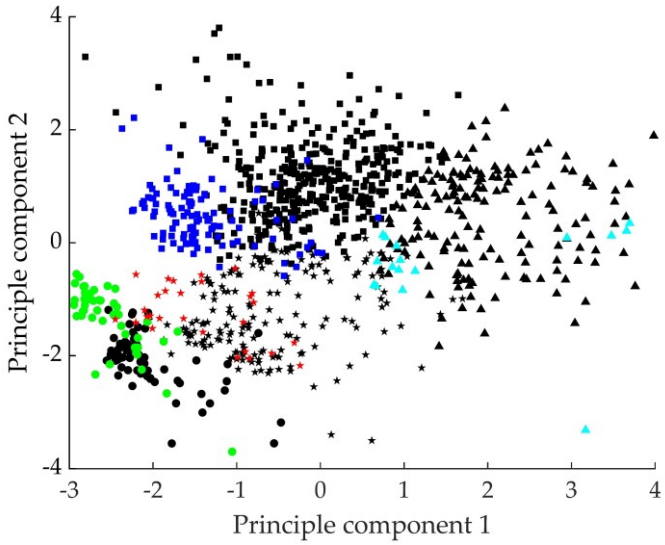

(**b**)

Figure 6.25– The clustering results obtained using k-means algorithm (a) and a zoomed-in view (b).

It can be found in Figure 6.24 that large majority (marked in blue square) of signals of the corrosion test gathered together in a dense region, which indicated the similarity between signals in the corrosion test. The results of the classification are presented in terms of amplitude for the SCC test and the corrosion test in Figure 6.26 and Figure 6.27 respectively. The three stages same as Figure 6.10 and Figure 6.11 are marked in Figure 6.26 and Figure 6.27 respectively.

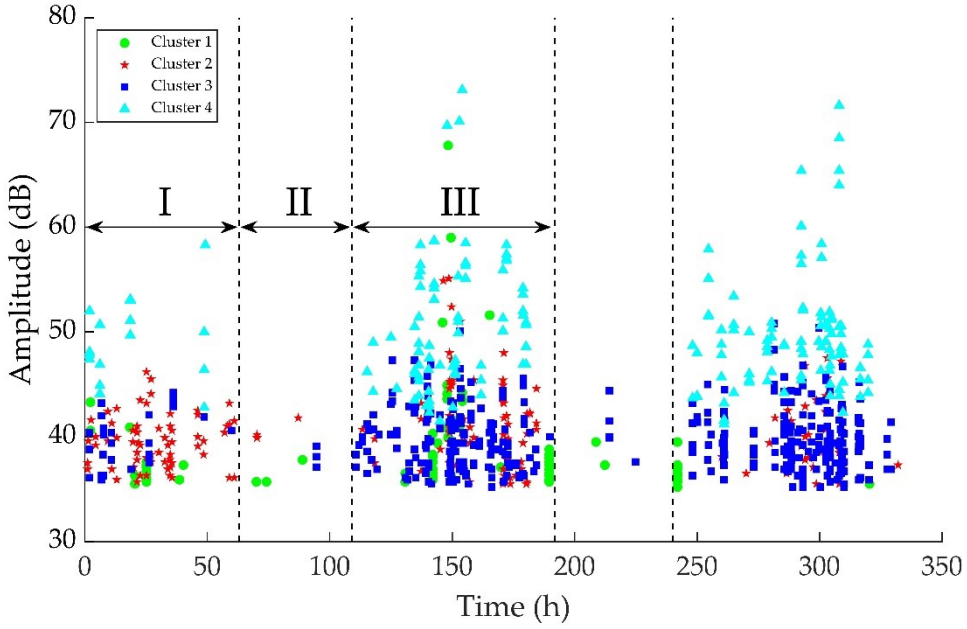

Figure 6.26– The clustering results of Fuzzy c-means method in terms of amplitude versus time for the SCC test.

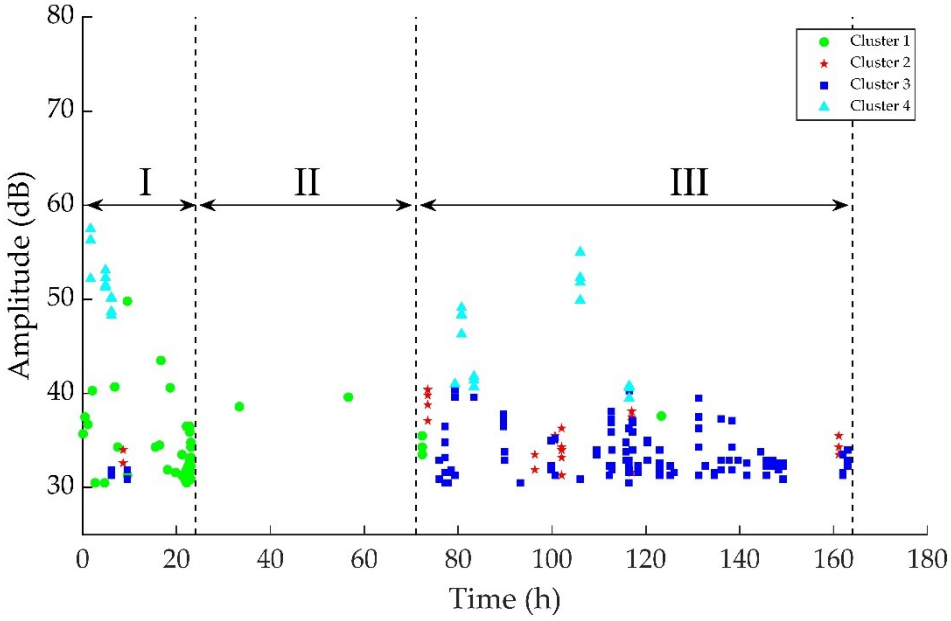

Figure 6.27– The clustering results of Fuzzy c-means method in terms of amplitude versus time for the SCC test.

In the stage I shown in Figure 6.26, which was the early stage of the SCC test, the main mechanism was the pit nucleation with local breakdown of passive film and the localized corrosion of pitting. There were 11.6% of AE hits for cluster 1, 52.9% of hits for cluster 2, 22.3 % for cluster 3 and 13.2% for cluster 4. The partial powers of AE signals for the four clusters are shown in Figure 6.28. As seen, signals in cluster 1 have the highest energy contribution (46%) in the frequency band of 0-100 kHz among the clusters. Signals in cluster 2 has 36% of its energy in the frequency range of 100-200 kHz and contributes to a large portion of AE hits released at the stage I during the SCC test. Signals in cluster 3 and those in cluster 4 have a similar frequency distribution; both of them have a low energy contribution in the frequency band of 0-200 kHz and a high energy contribution in the frequency range of 200-400 kHz. The amplitudes of the majority of hits in cluster 4 are above 45 dB. An example waveform of signals for each cluster is shown in Figure 6.29.

Compared with AE signals in other clusters, the signals in cluster 1 exhibit lower frequencies and characterized by the frequency band energy of signals mainly concentrated between 0 kHz to 100 kHz. In addition, it should be noted that there are no localized AE events in the cluster 1. Therefore, according to Du et al [121], it is very likely to be background noise which gives rise to this low-frequency cluster 1.

In the stage II shown in Figure 6.26, pits from the nucleation stage grew stably and deepened and the sizes of pits increased. The main mechanism at this stage was the stable pit growth. As seen, AE hits observed at this stage were close to zero. Since the main AE sources during stable pitting corrosion are pit growth [112,121,206–208] and hydrogen bubble break-up [112,121,206–209], almost nil AE activities in stage II indicated that AE hits generated from these two sources were not or rarely recorded during the test and thus not considered in the following discussions. From stage I to stage II, the activity of AE signals gradually reduced with the elapsed time. Similarly, Xu et al. [123] found that the amplitudes and activity of AE signals gradually reduced with the elapsed time during transpassive dissolution in the early stage of the test, which was explained by the fact that ruptures of passive films mainly occurred at the start of the test. According to Jirarungsatian and Prateepasen [110], the rapid rupture of passive film would release more energy than corrosion since the atom dislocation forces in corrosion are smaller in comparison to surface tension forces in the film breakdown,

which was very likely to be the reason why the AE hits from the film rupture rather than the pitting corrosion were recorded during the SCC test.

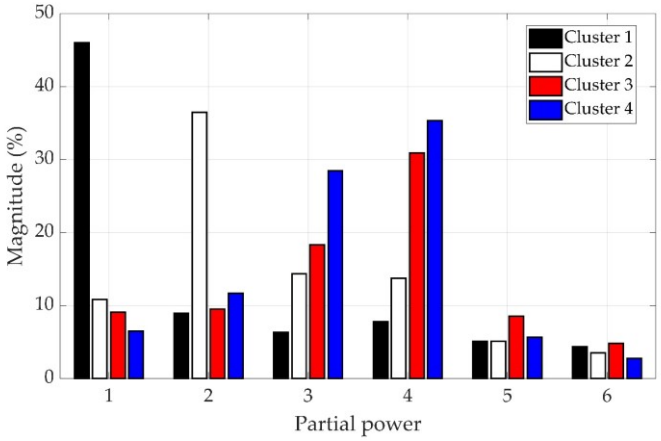

Figure 6.28– Partial powers of AE signals for the four clusters.

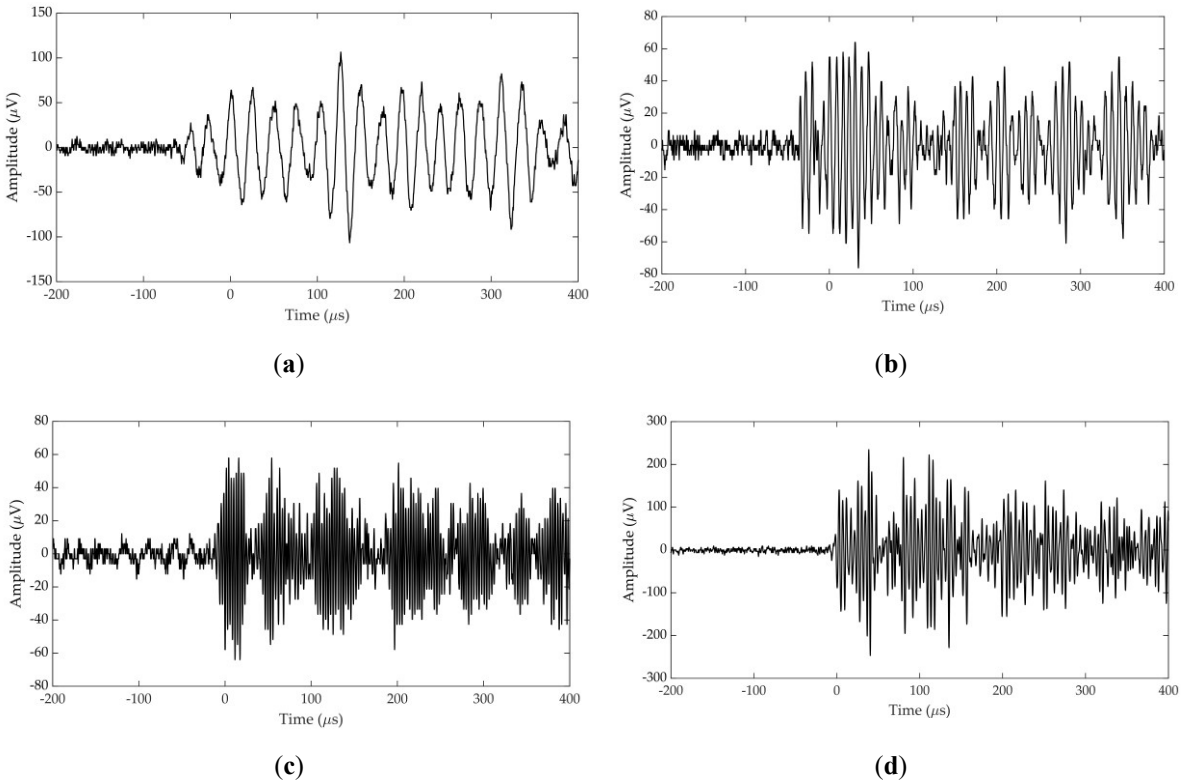

Figure 6.29– An example waveform of signals for: (a) cluster 1, (b) cluster 2, (c) cluster 3 and (d) cluster 4.

Thus, it can be concluded that in the stage I, the main AE source is the passive film rupture. Source locations of AE events in the SCC test during stage I is presented in Figure 6.30. As seen, the locations of events in cluster 2 are very close to those in cluster 3. As discussed above, signals in cluster 3 and those in cluster 4 have very similar frequency band. Therefore, it is very likely that all the AE signals from cluster 2, cluster 3 and cluster 4 mainly originated from passive film breakdown. As cluster 2 possesses the largest number of AE hits at this stage (52.9%), it can conclude that most of AE signals produced due to the breakdown of the passive films are characterised by a low amplitude (below 45 dB) and a middle frequency the frequency band energy of signals mainly concentrated between 100 kHz to 200 kHz. High-frequency signals in cluster 3 and cluster 4 can also be produced since the dissipated energy may be very high as the film rapidly ruptures due to the high stress at the notch tip [210].

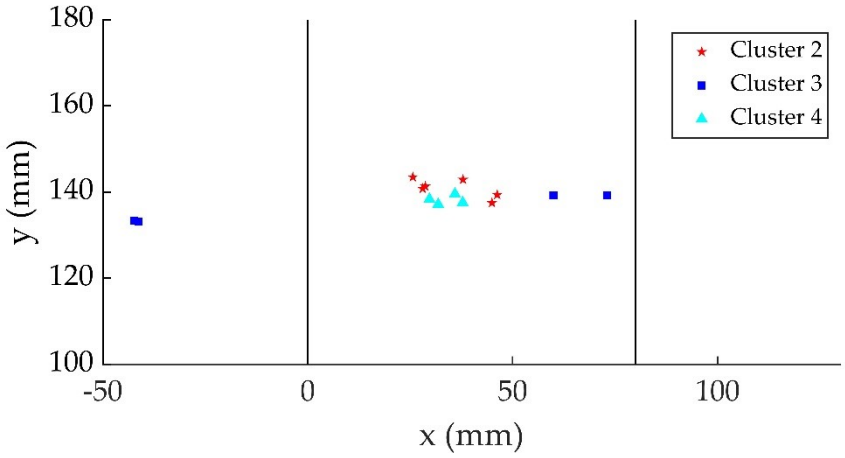

Figure 6.30– Source locations of AE events in the SCC test during stage I.

After stage II, the main mechanism is the SCC initiation and propagation and there were 8.3% of AE hits for cluster 1, 14.4% of hits for cluster 2, 53.7 % for cluster 3 and 23.6% for cluster 4. The source locations of AE events after stage II in the SCC test for cluster 2, cluster 3 and cluster 4 are shown in Figure 6.31. The percentages of localized events for Cluster 2, 3, 4 are 11.6%, 44.7%, and 43.7% respectively. The large majority of the located events are associated with cluster 3 and 4. Most of the localized AE sources are situated around the edges of the plate. As discussed above, although the signals in cluster 4 have a larger amplitude than those in cluster 3, the signals in cluster 3 and cluster 4 have similar frequency band with a large energy concentration between 200 to 400 kHz. The signals in

cluster 2 exhibit lower frequencies and characterized by the frequency band energy of signals mainly concentrated between 100 kHz to 200 kHz.

Recently, Soltangharaei et al. [12] found that signals with frequencies ranges concentrated mostly between 150 to 300 kHz are attributed to the macro cracks due to SCC in the steel plate and signals have a large energy concentration for the frequencies less than 200 kHz and have much small AE energy contributions during the SSC process can mostly associated with micro crack initiation and propagation. Similarly, an approach based on frequency spectrum was proposed by Bi et al. [11] to discriminate the main differences between micro crack AE source and macro crack AE source during the SCC test. It was found that the AE signals emitted by micro cracks have the frequency mainly concentrated in the range of 110–190 kHz, while those emitted by macro cracks are characterized by high frequency components ranges from 260 to 350 kHz.

Therefore, it was concluded that, after stage II, cluster 3 and cluster 4 can be associated most likely with the initiation and propagation of macro cracks. And signals in cluster 2 can be attributed to micro cracks due to SCC in the steel plate.

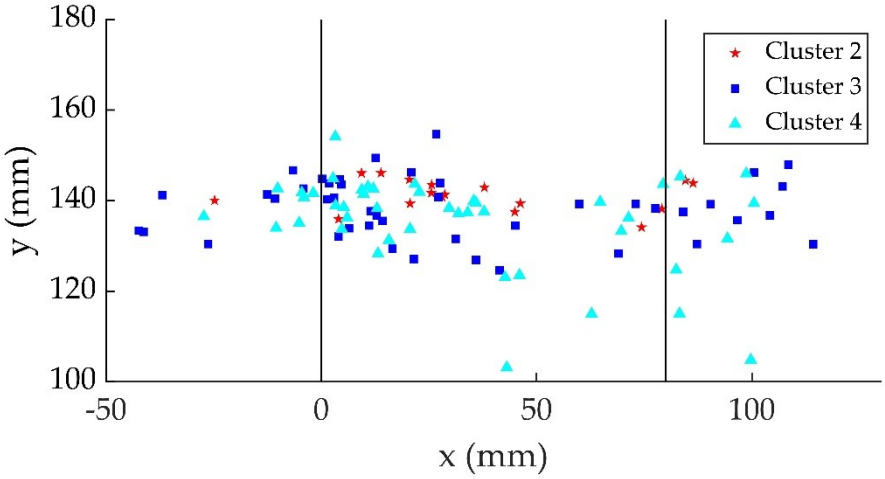

Figure 6.31– Source locations of AE events in the SCC test after stage II.

Similar to the SCC test, three stages can be observed for the corrosion test shown in Figure 6.27. There are 20.4% of hits for cluster 1, 12.6% for cluster 2, 54.4% for cluster 3 and 12.6% for cluster 4. Similarly, the cluster 1 can be attributed to the background noise during the test.

Almost nil AE activities in stage II indicated that AE hits generated from pit growth and hydrogen bubbles were not or rarely recorded during the test and thus not considered. According to Wu et al. [182], it can be concluded that, in stage I, signals in the cluster 2, 3, and 4 are associated with the film rupture, while in stage III, signals in the cluster 2, 3, and 4 are associated with the crack in corrosion products.

6.4 Discussions

Although three distinct stages were observed in AE signals and the transition from SCC initiation to SCC propagation can be identified using AE techniques, the number of AE events detected in the stable pit growth was close to zero. It should be noted that AE response to pitting corrosion is largely dependent on the experimental conditions, corrosion rate and pit shape/size. Although data are available in the literature [112,206,207] governing AE monitoring of pitting corrosion , it should be noted that the onset of pitting corrosion was controlled by an electrochemical reaction with quick pit growth, thus resulting into large pit. However, the pitting corrosion in the current chloride droplet is characterized by a moderate pit growth rate and pit size, which is quite different from the electrochemically controlled pitting corrosion. Moreover, the distance between the sensors and the AE sources is relatively large in the current experimental setup and signals emitted by pitting corrosion are characterized by low amplitude. These factors may account for the difficultly in AE monitoring of pitting corrosion in the current setup.

Furthermore, the clustering results are affected by the frequency response of the sensor. In this study, resonant sensors were carefully selected based on available literature. However, there is a possibility that these sensors may exhibit reduced sensitivity to the frequency content of a particular damage mode. Thus, their ability to effectively detect or classify such modes might be compromised compared to other modes. Unless an ideal non-resonant sensor is used, there will always be some level of impact on source classification due to variations in the frequency response of the sensors. Therefore, it is crucial to carefully select AE sensors.

Due to complex nature of the damage evolution in SCC, a complete understanding of the process evolution and whole morphology is challenging. From this work, a comparative study

on monitoring SCC evolution with in-situ AE techniques was carried out. A good correlation was found between the localized AE sources and microscope observations of crack. However, it should be stressed that uncertainties in clustering AE signals and identifying AE sources still remain for the following reasons. First, a one-on-one correspondence cannot be achieved between post-mortem characteristics obtained with a conventional optical microscope and AE response on the order of microseconds. The concluding remarks in this work were drawn on the basis of some assumptions and speculations. Therefore, in the future, an accurate in-situ observation method will be needed to correlate the recorded AE signals with observed damage events. Second, it should be emphasized that a universal clustering method or strategy which can achieve a perfect recognition accuracy between different populations of AE signals doesn't exist. Although reasonable classification and interpretation were produced by the unsupervised Fuzzy c-means and k-means algorithm used in this work presented reasonability in AE, it will be beneficial to adopt improved clustering algorithm like supervised machine learning and deep neural networks to provide further proof in future studies.

6.5 Conclusions

To investigate the ability of AE techniques on locating SCC damage sources on a large specimen with additional complexity, an improved chloride droplet SCC test was undertaken with the dog-bone stainless steel specimen and circulating solution to trigger the SCC crack evolution. A comparative study of SCC evolution and corrosion were conducted using AE techniques. The following concluding remarks are drawn.

(a) The velocity for the A_0 mode should be utilised in TOA source location techniques and source locations results show that a good correlation can be found between the localized AE sources and microscope observations of crack. The ability of AE to locate SCC damage on a large specimen with addition complexity (i.e., the notch) was demonstrated.

(b) Based on the analysis of the time evolution of the amplitudes throughout the SCC test, three distinct stages were recognized, i.e., stage with moderate AE activity, stage with rare

AE activity and stage with massive AE signals. The transition from SCC initiation to SCC propagation can be identified using AE techniques.

(c) In the SCC test, most of AE signals produced by film rupture during stage I are characterised by a low amplitude (below 45 dB) and a middle frequency the frequency band energy of signals mainly concentrated between 100 kHz to 200 kHz.

(d) In the stage III of the SCC test, cluster 3 and cluster 4 can be associated most likely with the initiation and propagation of macro cracks. And signals in cluster 2 can be attributed to micro cracks due to SCC in the steel plate.

(e) A three-stage AE evolution trends can also be recognized in the corrosion test, the majority of AE signals were emitted in stage III. At this stage, most of signals are characterised by a low amplitude (below 45 dB) and a high frequency with the frequency band energy mainly concentrated between 200 kHz to 400 kHz.

(f) AE hits generated from pitting corrosion and hydrogen bubbles were not or rarely recorded during the SCC and corrosion test.

Chapter 7 Conclusions and Recommended Future Work

7.1 Conclusions

The research has presented three studies that advance the methodologies of AE for SHM applications, with an emphasis on the monitoring of corrosion and SCC. The studies are backed by experimental data, with some aspects supported by robust numerical modelling.

Both the experimental and numerical approaches for the study of FE generated delta-T mapping techniques were adopted. A numerical method from literature was used to simulate the H-N source on a simple plate and validated by the experiment results. The validation of the FE model showed great promise for applying the FE method to a planar location problem on a complex plate. Using the same numerical method, H-N sources were simulated on a complex plate and a numerical delta-T map were generated. The location results of numerical delta-t map technique were compared with those of traditional TOA techniques and experimental delta-t map technique. It has been demonstrated the viability of using FE method to decrease the time and man-power required for manually collecting and processing the training data whilst keeping a reasonable degree of source location accuracy with an average error of 3.88 mm. With such a high source location accuracy, the particular area of concern which needs to be inspected using other NDE techniques can be reduced greatly. Moreover, if the specific location of an AE event is identified on an area with particular geometric features or loading condition, the number of potential damage source mechanisms can be decreased.

Following that, a corrosion test was firstly performed on a simple plate and it was found that the AE signals recorded during the corrosion test were characterised by low amplitude and low signal-to-noise ratio. To accurately identify the onset time of this kind of signals, a novel time estimation method, which is called window AIC method was proposed and a high

accuracy in arrival time estimation was achieved. Moreover, the propagation velocities of AE signals were calculated. It was found that the calculated wave velocities of signals, where compared to a dispersion curve, were in the range of the velocity of the A_0 mode, therefore it was speculated that the arrival prediction techniques were detecting the arrival of the A_0 mode. Therefore, the velocity of the A_0 mode was used in TOA location approach and a high accuracy of source location results was achieved. The successful localisation of AE events generated from corrosion on a simple plate showed great promise for locating corrosion damage on a complex plate. To achieve that, the delta-T mapping method presented in Chapter 4 need to be updated and built on the basis of the A_0 mode arrival. Hence, one novel method, i.e., modified two-step AIC picker and a method found in the literature, i.e., wavelet coefficient threshold method were used to determine the arrival time of the A_0 mode. Afterwards, a corrosion test was performed on a complex plate. The recorded AE data was processed with varied time estimation method (i.e., threshold crossing, AIC function and window AIC method) and examined with different source location approaches (i.e., TOA location approach delta-t mapping based on modified two-step AIC picker and delta-t mapping based on wavelet coefficient threshold method). The results showed the source location results with highest accuracy were given by a combination window AIC method and delta-t mapping based on wavelet coefficient threshold method, which had a smallest average error of 10.7 mm and showed a significant improvement in source location accuracy over the TOA location approach.

To investigate the ability of AE techniques on locating SCC damage sources on a large specimen with additional complexity, an improved chloride droplet SCC test was undertaken with the dog-bone stainless steel specimen and circulating solution to trigger the SCC crack evolution. A comparative study of SCC evolution and corrosion were conducted using AE techniques. The following concluding remarks are drawn. The velocity for the A_0 mode should be utilised in TOA source location techniques and source locations results show that a good correlation can be found between the localized AE sources and microscope observations of crack. The ability of AE to locate SCC damage on a large specimen with addition complexity (i.e., the notch) was demonstrated. Based on the analysis of the time evolution of the amplitudes throughout the SCC test, three distinct stages were recognized, i.e., stage with moderate AE activity, stage with rare AE activity and stage with massive AE signals. The

transition from SCC initiation to SCC propagation can be identified using AE techniques. In the SCC test, most of AE signals produced by film rupture during stage I are characterised by a low amplitude (below 45 dB) and a middle frequency the frequency band energy of signals mainly concentrated between 100 kHz to 200 kHz. In the stage III of the SCC test, cluster 3 and cluster 4 can be associated most likely with the initiation and propagation of macro cracks. And signals in cluster 2 can be attributed to micro cracks due to SCC in the steel plate. A three-stage AE evolution trends can also be recognized in the corrosion test; the majority of AE signals were emitted in stage III. At this stage, most of signals are characterised by a low amplitude (below 45 dB) and a high frequency with the frequency band energy mainly concentrated between 200 kHz to 400 kHz. AE hits generated from pitting corrosion and hydrogen bubbles were not or rarely recorded during the SCC and corrosion test.

7.2 Recommended future work

Despite a large body of research and findings presented in this thesis, there remain multiple aspects that can be taken forward for further investigation and study.

For the study of the FE generated delta-T mapping, although it has been carried out successfully, it will be preferable to examine the performance of present FE generated delta-T maps with AE signals from real damage mechanism. Development of FE model such as improved boundary conditions, realistic AE sensors, additional complexity and anisotropic materials is required. This would be highly desirable for applying this methodology to real-world engineering structures.

It would be highly desirable to carry out further tests with corrosion at different locations on a complex plate and examine the location accuracy of delta-T mapping. It would also be interesting as part of a future work to investigate corrosion damage detection on full sized safety critical structures using the AE technique. Additionally, additional tests will be required to facilitate a comparison between the current NDT and AE testing, which will build more confidence in the AE technique.

The ability of AE techniques on locating SCC damage sources on a specimen with additional complexity was investigated in the work. It would be beneficial to develop an accurate in-situ observation method to correlate the recorded AE signals with observed damage events. In addition, it would be highly desirable to adopt improved clustering algorithm like supervised machine learning and deep neural networks to provide further proof in future studies. This could potentially result in a more rational classification and interpretation, warranting further investigation.

In this work, the FE method allows for the creation of large-scale models with numerical sensors, which facilitates the collection of training data. These data have shown a high level of validity when compared with experimental results. Based on these data, delta-T maps can be generated automatically and used to effectively monitor corrosion and SCC within complex structures. In addition, instead of artificial AE sources, the FE method enable many damage scenarios such as corrosion, SCC and fatigue to be modelled. Moreover, the FE method allows for the modelling of various internal training sources, which may provide a solution to the challenge of 3D monitoring of corrosion and SCC with delta-T mapping techniques. These advancements hold the potential to enhance the application of delta-T mapping techniques. Furthermore, the study on AE monitoring of SCC damage has revealed promising potential in differentiating between corrosion and SCC mechanisms, as well as identifying the different stages of the SCC mechanism. This can be valuable for operators in making decisions.

Overall, the techniques and methodologies developed in this work have shown great promise in the field of corrosion and SCC monitoring in real-world engineering structures, particularly through the innovative use of FE modelling techniques.

References

1. Koch, G.; Varney, J.; Thompson, N.; Moghissi, O.; Gould, M.; Payer, J. International Measures of Prevention, Application, and Economics of Corrosion Technologies Study. *NACE Int.* **2016**, 216.

2. Roberge, P.R. *Corrosion Inspection and Monitoring*; John Wiley & Sons, 2007; Vol. 2; ISBN 0470099755.

3. Iannuzzi, M. Environmentally Assisted Cracking (EAC) in Oil and Gas Production. In *Stress corrosion cracking*; Elsevier, 2011; pp. 570–607.

4. Putri, E.D.W.S.; Triyono, T.; Prabowo, A.R. Estimating Failure Mechanism of Steel Specimens Using Stress Corrosion-Cracking (SCC) Testing Methods: State and Development. *Procedia Struct. Integr.* **2022**, *41*, 266–273.

5. Jinachandran, S.; Rajan, G. Fibre Bragg Grating Based Acoustic Emission Measurement System for Structural Health Monitoring Applications. *Materials (Basel).* **2021**, *14*, 897.

6. Lu, Q.Y.; Wong, C.H. Applications of Non-Destructive Testing Techniques for Post-Process Control of Additively Manufactured Parts. *Virtual Phys. Prototyp.* **2017**, *12*, 301–321.

7. Miller, R.K.; Hill, E. v. K.; Moore, P.O. Nondestructive Testing Handbook, Vol.5, Acoustic Emission Testing. *Am. Soc. Nondestruct. Testing, Inc.* 2005, 541.

8. Grigg, S.; Pullin, R.; Featherston, C.A. Acoustic Emission Source Location in Complex Aircraft Structures Using Three Closely Spaced Sensors. *Mech. Syst. Signal Process.* **2022**, *164*, 108256.

9. Chai, M.; Gao, Z.; Li, Y.; Zhang, Z.; Duan, Q.; Chen, R. An Approach for Identifying

Corrosion Damage from Acoustic Emission Signals Using Ensemble Empirical Mode Decomposition and Linear Discriminant Analysis. *Meas. Sci. Technol.* **2022**.

10. Qiu, F.; Bai, Y.; Qu, D.; Shan, G.; Han, L.; Chen, W. Quantitative Characterization of Q235B Steel Electrochemical Corrosion by Acoustic Emission. *Int. J. Press. Vessel. Pip.* **2022**, 104686.

11. Bi, H.; Li, H.; Zhang, W.; Wang, L.; Zhang, Q.; Cao, S.; Toku-Gyamerah, I. Evaluation of the Acoustic Emission Monitoring Method for Stress Corrosion Cracking on Aboveground Storage Tank Floor Steel. *Int. J. Press. Vessel. Pip.* **2020**, *179*, 104035.

12. Soltangharaei, V.; Hill, J.W.; Ai, L.; Anay, R.; Greer2b, B.; Bayat, M.; Ziehl1c, P. Acoustic Emission Technique to Identify Stress Corrosion Cracking Damage. *Struct. Eng. Mech.* **2020**, *75*, 723–736.

13. Calabrese, L.; Galeano, M.; Proverbio, E.; Di Pietro, D.; Donato, A. Topological Neural Network of Combined AE and EN Signals for Assessment of SCC Damage. *Nondestruct. Test. Eval.* **2020**, *35*, 98–119.

14. Calabrese, L.; Proverbio, E. A Review on the Applications of Acoustic Emission Technique in the Study of Stress Corrosion Cracking. *Corros. Mater. Degrad.* **2020**, *2*, 1–30.

15. Hinton, Y.L. Acoustic Emission. *Stand. News* **1995**, *23*, 36–39, doi:10.4294/zisin.61.535.

16. Huang, M.; Jiang, L.; Liaw, P.K.; Brooks, C.R.; Seeley, R.; Klarstrom, D.L. Using Acoustic Emission in Fatigue and Fracture Materials Research. *JOM* **1998**, *50*, 1–14.

17. Kaiser, J. Doctoral Thesis: Untersuchung Über Das Auftreten von Geräuschen Beim Zugversuch 1950.

18. Charles J. Hellier *Handbook of Nondestructive Evaluation, 2nd Edition*; Mcgraw-hill New York, 2013; Vol. 10; ISBN 9780071777148.

19. Portevin, A.; Le Chatelier, F. Sur Un Phénomène Observé Lors de l'essai de Traction d'alliages En Cours de Transformation. *Comptes Rendus l'Académie des Sci.* **1923**, *176*, 507–510.

20. Drouillard, T.F. A History of Acoustic Emission. *J. Acoust. Emiss.* **1996**, *14*, 1–34.

21. Friedman, D.; Yan, H. An Experiment on the Core. *SSRN Electron. J.* **2011**, *9*, 177–180, doi:10.2139/ssrn.1282227.

22. Scheil, F.F.; E. Acoustical Study of Formation of Martensite Needles. *Naturwissenschaften* **1936**, *28*, 245–247.

23. Carlyle, J.M. Acoustic Emission Signal Analysis 1982.

24. Schofield, B.H. *Acoustic Emission under Applied Stress. Report ARL-150*; LESSELLS AND ASSOCIATES INC WALTHAM MA, 1961;

25. Dunegan, H.L.; Tatro, C.A.; Harris, D.O. *ACOUSTIC EMISSION RESEARCH. Status Report, December 1963--August 1964.*; Lawrence Radiation Lab., Univ. of California, Livermore, 1964;

26. Blahousek, J.; Koula, V.; Cermak, F. Application of Acoustic Emission Techniques To Fracture Mechanics Research. In *Cong on Mater Test, 7th, Lect*; ASTM International, 1978; Vol. v, pp. 789–792.

27. Green, A.T.; Lockman, C.S.; Steele, R.K. Acoustic Verification of Structural Integrity of Polaris Chambers. *Mod. Plast.* **1964**, *41*, 137–139.

28. Dunegan, H.L.; Harris, D.O.; Tatro, C.A. Fracture Analysis by Use of Acoustic Emission. *Eng. Fract. Mech.* **1968**, *1*, 105–122, doi:10.1016/0013-7944(68)90018-0.

29. Hsu, N.N.; Breckenridge, F.R. Characterization and Calibration of Acoustic Emission Sensors. *Mater. Eval.* **1981**, *39*, 60–68.

30. Nielsen, A. *Acoustic Emission Source Based on Pencil Lead Breaking*; 1980; Vol. 80;.

31. ASTM International ASTM E650 - Standard Guide for Mounting Piezoelectric

Acoustic Emission Sensors. **2017**, *97*, 1–4.

32. Ibitolu, E.O.; Summerscales, J. Acoustic Emission Source Location in Bidirectionally Reinforced Composites Part 1: Source Location Algorithm. In *Non-Destructive Testing*; Elsevier, 1988; pp. 2881–2891.

33. Pollock, A.A. Classical Wave Theory in Practical AE Testing. *Prog. Acoust. Emiss. III-JAP Soc. Non-Destructive Test.* **1986**, 708–721.

34. Rindorf, H.J. *Acoustic Emission Source Location in Theory and in Practice.*; Brüel & Kjær, 1981;

35. Gorman, M.R.; Prosser, W.H. AE Source Orientation by Plate Wave Analysis. *J. Acoust. Emiss.* **1991**, *9*.

36. Gorman, M.R. Plate Wave Acoustic Emission. *J. Acoust. Soc. Am.* **1991**, *90*, 358–364, doi:10.1121/1.401258.

37. Rayleigh, Lord On Waves Propagated along the Plane Surface of an Elastic Solid. *Proc. London Math. Soc.* **1885**, *1*, 4–11.

38. Lamb, H. On Waves in an Elastic Plate. *Proc. R. Soc. London. Ser. A, Contain. Pap. a Math. Phys. character* **1917**, *93*, 114–128.

39. Worden, K. Rayleigh and Lamb Waves-Basic Principles. *Strain* **2001**, *37*, 167–172.

40. Baxter, M. Damage Assessment by Acoustic Emission (AE) during Landing Gear Fatigue Testing, Cardiff University (United Kingdom), 2007.

41. Holford, K.M. Acoustic Emission - Basic Principles and Future Directions. *Strain* **2000**, *36*, 51–54, doi:10.1111/j.1475-1305.2000.tb01173.x.

42. Ochôa, P.; Infante, V.; Silva, J.M.; Groves, R.M. Detection of Multiple Low-Energy Impact Damage in Composite Plates Using Lamb Wave Techniques. *Compos. Part B Eng.* **2015**, *80*, 291–298.

43. Miller, R.K.; McIntire, P. NDT Handbook Vol. 5. *Am. Soc. Nondestruct. Test.* **1987**,

652.

44. Pollock, A.A. Classical Plate Theory in Practical AE Testing. *Eighth Int. Acoust. Emiss. Symp.* **1986**, 708–721.

45. Swindlehurst, W. Acoustic Emission-1 Introduction. *Non-destructive Test.* **1973**, *6*, 152–158.

46. Grosse, C.U.; Ohtsu, M. *Acoustic Emission Testing*; Springer Science & Business Media, 2008; ISBN 3540699724.

47. Sause, M.G.R. *In Situ Monitoring of Fiber-Reinforced Composites: Theory, Basic Concepts, Methods, and Applications*; Springer, 2016; Vol. 242; ISBN 3319309544.

48. Carter, D. Acoustic Emission Techniques for the Structural Integrity Monitoring of Steel Bridges 2000.

49. Pullin, R.; Holford, K.M.; Baxter, M.G. Modal Analysis of Acoustic Emission Signals from Artificial and Fatigue Crack Sources in Aerospace Grade Steel. In Proceedings of the Key Engineering Materials; Trans Tech Publ, 2005; Vol. 293–294, pp. 217–224.

50. Sachse, W.H.; Sancar, S. Acoustic Emission Source Location on Plate-like Structures Using a Small Array of Transducers. *J. Acoust. Soc. Am.* **1987**, *81*, 206.

51. Maji, A.K.; Satpathi, D.; Kratochvil, T. Acoustic Emission Source Location Using Lamb Wave Modes. *J. Eng. Mech.* **1997**, *123*, 154–161, doi:10.1061/(asce)0733-9399(1997)123:2(154).

52. Dunegan, H. Global Flaw Location with One Transducer. *DECI Rep.* **1997**.

53. Holford, K.M.; Carter, D.C. Acoustic Emission Source Location. In Proceedings of the Key Engineering Materials; Trans Tech Publ, 1999; Vol. 167, pp. 162–171.

54. Mohd, S. Acoustic Emission for Fatigue Crack Monitoring in Nuclear Piping System 2013.

55. Nesvijski, E.; Marasteanu, M. Wavelet Transform and Its Applications to Acoustic

Emission Analysis of Asphalt Cold Cracking. *Analysis* **2001**, *12*, 1–13.

56. Jiao, J.; He, C.; Wu, B.; Fei, R.; Wang, X. Application of Wavelet Transform on Modal Acoustic Emission Source Location in Thin Plates with One Sensor. *Int. J. Press. Vessel. Pip.* **2004**, *81*, 427–431.

57. Akaike, H. Markovian Representation of Stochastic Processes and Its Application to the Analysis of Autoregressive Moving Average Processes. In *Annals of the Institute of Statistical Mathematics*; Springer, 1974; Vol. 26, pp. 363–387.

58. MAEDA, N. A Method for Reading and Checking Phase Time in Auto-Processing System of Seismic Wave Data. *Zisin (Journal Seismol. Soc. Japan. 2nd ser.)* **1985**, *38*, 365–379, doi:10.4294/zisin1948.38.3_365.

59. Grosse, C.U. Winpecker Version 1.2: Instruction Manual. *Univ. Stuttgart* **2000**.

60. Kurz, J.H.; Grosse, C.U.; Reinhardt, H.W. Strategies for Reliable Automatic Onset Time Picking of Acoustic Emissions and of Ultrasound Signals in Concrete. *Ultrasonics* **2005**, *43*, 538–546, doi:10.1016/j.ultras.2004.12.005.

61. Proakis, J.G.; Manolakis, D.G. Digital Signal Processing 3rd Edition (Book Style) 1996.

62. Geiger, L. Probability Method for the Determination of Earthquake Epicenters from the Arrival Time Only. *Bull. St. Louis Univ* **1912**, *8*, 56–71.

63. Thurber, C.H. Nonlinear Earthquake Location: Theory and Examples. *Bull. Seismol. Soc. Am.* **1985**, *75*, 779–790.

64. Nelder, J.A.; Mead, R. A Simplex Method for Function Minimization. *Comput. J.* **1965**, *7*, 308–313.

65. Inglada, V. Die Berechnung Der Herdkoordinated Eines Nahbebens Aus Den Dintrittszeiten Der in Einingen Benachbarten Stationen Aufgezeichneten P-Oder P-Wellen. *Gerlands Beitrage zur Geophys.* **1928**, *19*, 73–98.

66. Leighton, F.; Blake, W. *Rock Noise Source Location Techniques*; US Department of

Interior, Bureau of Mines, 1970; Vol. 7432;.

67. Leighton, F.; Duvall, W.I. *Least Squares Method for Improving Rock Noise Source Location Techniques*; Bureau of Mines, Washington, DC (USA), 1972;

68. Eaton, M.J.; Pullin, R.; Holford, K.M. Acoustic Emission Source Location in Composite Materials Using Delta T Mapping. *Compos. Part A Appl. Sci. Manuf.* **2012**, *43*, 856–863.

69. Paget, C.A.; Atherton, K.; O'Brien, E. Triangulation Algorithm for Damage Location in Aeronautical Composite Structures. In Proceedings of the Proceedings of the 4th International Workshop on Structural Health Monitoring (F. Chang, ed.),(Stanford, CA, USA); 2003; pp. 363–370.

70. DONG, L.; LI, X. Three-Dimensional Analytical Solution of Acoustic Emission or Microseismic Source Location under Cube Monitoring Network. *Trans. Nonferrous Met. Soc. China* **2012**, *22*, 3087–3094.

71. Dong, L.; Li, X.; Zhou, Z.; Chen, G.; Ju, M.A. Three-Dimensional Analytical Solution of Acoustic Emission Source Location for Cuboid Monitoring Network without Pre-Measured Wave Velocity. *Trans. Nonferrous Met. Soc. China* **2015**, *25*, 293–302.

72. Mostafapour, A.; Davoodi, S.; Ghareaghaji, M. Acoustic Emission Source Location in Plates Using Wavelet Analysis and Cross Time Frequency Spectrum. *Ultrasonics* **2014**, *54*, 2055–2062.

73. Ing, R.K.; Quieffin, N.; Catheline, S.; Fink, M. In Solid Localization of Finger Impacts Using Acoustic Time-Reversal Process. *Appl. Phys. Lett.* **2005**, *87*, 204104.

74. Park, B.; Sohn, H.; Olson, S.E.; DeSimio, M.P.; Brown, K.S.; Derriso, M.M. Impact Localization in Complex Structures Using Laser-Based Time Reversal. *Struct. Heal. Monit.* **2012**, *11*, 577–588.

75. Baxter, M.G.; Pullin, R.; Holford, K.M.; Evans, S.L. Delta T Source Location for Acoustic Emission. *Mech. Syst. Signal Process.* **2007**, *21*, 1512–1520.

76. Pearson, M.R.; Eaton, M.; Featherston, C.; Pullin, R.; Holford, K. Improved Acoustic Emission Source Location during Fatigue and Impact Events in Metallic and Composite Structures. *Struct. Heal. Monit.* **2017**, *16*, 382–399, doi:10.1177/1475921716672206.

77. Grigg, S.; Featherston, C.A.; Pearson, M.; Pullin, R. Advanced Acoustic Emission Source Location in Aircraft Structural Testing. In Proceedings of the IOP Conference Series: Materials Science and Engineering; IOP Publishing, 2021; Vol. 1024, p. 12029.

78. Al-Jumaili, S.; Pearson, M.; Holford, K.; Eaton, M.; Pullin, R. Fast and Reliable Acoustic Emission Source Location Technique in Complex Structures. *J. Mech. Syst. Signal Process.* **2016**.

79. Al-Jumaili, S.K.; Pearson, M.R.; Holford, K.M.; Eaton, M.J.; Pullin, R. Acoustic Emission Source Location in Complex Structures Using Full Automatic Delta T Mapping Technique. *Mech. Syst. Signal Process.* **2016**, *72*, 513–524.

80. Ciampa, F.; Meo, M. Impact Detection in Anisotropic Materials Using a Time Reversal Approach. *Struct. Heal. Monit.* **2012**, *11*, 43–49.

81. Ebrahimkhanlou, A.; Salamone, S. Single-Sensor Acoustic Emission Source Localization in Plate-like Structures Using Deep Learning. *Aerospace* **2018**, *5*, 50.

82. Hensman, J.; Mills, R.; Pierce, S.G.; Worden, K.; Eaton, M. Locating Acoustic Emission Sources in Complex Structures Using Gaussian Processes. *Mech. Syst. Signal Process.* **2010**, *24*, 211–223.

83. Jones, M.R.; Rogers, T.J.; Worden, K.; Cross, E.J. A Bayesian Methodology for Localising Acoustic Emission Sources in Complex Structures. *Mech. Syst. Signal Process.* **2022**, *163*, 108143.

84. Hu, Q.; Dong, L. Acoustic Emission Source Location and Experimental Verification for Two-Dimensional Irregular Complex Structure. *IEEE Sens. J.* **2019**, *20*, 2679–2691.

85. Hou, Y.; Lei, D.; Li, S.; Yang, W.; Li, C.-Q. Experimental Investigation on Corrosion

Effect on Mechanical Properties of Buried Metal Pipes. *Int. J. Corros.* **2016**, *2016*.

86. Wu, K.; Briffod, F.; Ito, K.; Shinozaki, I.; Chivavibul, P.; Enoki, M. In-Situ Observation and Acoustic Emission Monitoring of the Initiation-to-Propagation Transition of Stress Corrosion Cracking in SUS420J2 Stainless Steel. *Mater. Trans.* **2019**, MT-MAW2019004.

87. Gary, J.; Hamstad, M.A. On the Far-Field Structure of Waves Generated by a Pencil Lead Break on a Thin Plate. *J. Acoust. Emiss.* **1994**, *12*, 157–170.

88. Hamstad, M.A.; Gary, J.; O'Gallagher, A. Far-Field Acoustic Emission Waves by Three-Dimensional Finite Element Modeling of Pencil-Lead Breaks on a Thick Plate. *J. Acoust. Emiss.* **1996**, *14*, 103–114.

89. Sause, M. Investigation of Pencil-Lead Breaks as Acoustic Emission Sources. *J. Acoust. Emiss.* **2011**, *29*, 184–196.

90. Hamstad, M.A. Acoustic Emission Signals Generated by Monopole (Pencil Lead Break) versus Dipole Sources: Finite Element Modeling and Experiments. *J. Acoust. Emiss.* **2007**, *25*, 92–106.

91. Le Gall, T.; Monnier, T.; Fusco, C.; Godin, N.; Hebaz, S.-E. Towards Quantitative Acoustic Emission by Finite Element Modelling: Contribution of Modal Analysis and Identification of Pertinent Descriptors. *Appl. Sci.* **2018**, *8*, 2557.

92. Cheng, L.; Xin, H.; Groves, R.M.; Veljkovic, M. Acoustic Emission Source Location Using Lamb Wave Propagation Simulation and Artificial Neural Network for I-Shaped Steel Girder. *Constr. Build. Mater.* **2021**, *273*, 121706.

93. Hamstad, M.A.; Gary, J.M.; O'Gallagher, A. Wideband Acoustic Emission Displacement Signals as a Function of Source Rise-Time and Plate Thickness. **1998**.

94. Hamstad, M.A.; O'Gallagher, A.; Gary, J. Modeling of Buried Acoustic Emission Monopole and Dipole Sources with a Finite Element Technique. *J. Acoust. Emiss* **1999**, *17*, 97–110.

95. Prosser, W.H.; Hamstad, M.A.; Gary, J.; O'Gallagher, A. Reflections of AE Waves in Finite Plates: Finite Element Modeling and Experimental Measurements. **1999**.

96. Prosser, W.H.; Hamstad, M.A.; Gary, J.; O'Gallagher, A. Finite Element and Plate Theory Modeling of Acoustic Emission Waveforms. *J. Nondestruct. Eval.* **1999**, *18*, 83–90, doi:10.1023/A:1021888009896.

97. Hill, R.; Forsyth, S.A.; Macey, P. Finite Element Modelling of Ultrasound, with Reference to Transducers and AE Waves. *Ultrasonics* **2004**, *42*, 253–258.

98. Sause, M.G.R.; Richler, S. Finite Element Modelling of Cracks as Acoustic Emission Sources. *J. Nondestruct. Eval.* **2015**, *34*, 4.

99. Cuadra, J.; Vanniamparambil, P.A.; Servansky, D.; Bartoli, I.; Kontsos, A. Acoustic Emission Source Modeling Using a Data-Driven Approach. *J. Sound Vib.* **2015**, *341*, 222–236.

100. Angulo, Á.; Yang, H.; Tang, J.; Khadimallah, A.; Soua, S. Structural Health Monitoring of Crack Initiation and Growth in Mooring Chains Using FEA Methods for Acoustic Emission Characterisation. *J. Acoust. Emiss.* **2019**, *36*.

101. Tang, J. Characterization of Fatigue Damage Types in Fibre Reinforced Composites Utilizing Pattern Recognition Techniques Applied to Acoustic Emission Signals 2019.

102. Lee, C.K.; Wilcox, P.D.; Drinkwater, B.W.; Scholey, J.J.; Wisnom, M.R.; Friswell, M.I. Acoustic Emission during Fatigue Crack Growth in Aluminium Plates. *Proc. ECNDT, Berlin, Ger.* **2006**, 25–29.

103. Jones, R.H.; Friesel, M.A. Acoustic Emission during Pitting and Transgranular Crack Initiation in Type 304 Stainless Steel. *Corrosion* **1992**, *48*.

104. Mazille, H.; Rothea, R.; Tronel, C. An Acoustic Emission Technique for Monitoring Pitting Corrosion of Austenitic Stainless Steels. *Corros. Sci.* **1995**, *37*, 1365–1375.

105. Fregonese, M.; Idrissi, H.; Mazille, H.; Renaud, L.; Cetre, Y. Monitoring Pitting Corrosion of AISI 316L Austenitic Stainless Steel by Acoustic Emission Technique:

Choice of Representative Acoustic Parameters. *J. Mater. Sci.* **2001**, *36*, 557–563.

106. Fregonese, M.; Idrissi, H.; Mazille, H.; Renaud, L.; Cetre, Y. Initiation and Propagation Steps in Pitting Corrosion of Austenitic Stainless Steels: Monitoring by Acoustic Emission. *Corros. Sci.* **2001**, *43*, 627–641.

107. Kim, Y.P.; Fregonese, M.; Mazille, H.; Féron, D.; Santarini, G. Ability of Acoustic Emission Technique for Detection and Monitoring of Crevice Corrosion on 304L Austenitic Stainless Steel. *Ndt E Int.* **2003**, *36*, 553–562.

108. Darowicki, K.; Mirakowski, A.; Krakowiak, S. Investigation of Pitting Corrosion of Stainless Steel by Means of Acoustic Emission and Potentiodynamic Methods. *Corros. Sci.* **2003**, *45*, 1747–1756.

109. Jomdecha, C.; Prateepasen, A.; Kaewtrakulpong, P. Study on Source Location Using an Acoustic Emission System for Various Corrosion Types. *Ndt E Int.* **2007**, *40*, 584–593.

110. Jirarungsatian, C.; Prateepasen, A. Pitting and Uniform Corrosion Source Recognition Using Acoustic Emission Parameters. *Corros. Sci.* **2010**, *52*, 187–197.

111. Xu, J.; Wu, X.; Han, E.-H. Acoustic Emission during Pitting Corrosion of 304 Stainless Steel. *Corros. Sci.* **2011**, *53*, 1537–1546.

112. Wu, K.; Jung, W.-S.; Byeon, J.-W. In-Situ Monitoring of Pitting Corrosion on Vertically Positioned 304 Stainless Steel by Analyzing Acoustic-Emission Energy Parameter. *Corros. Sci.* **2016**, *105*, 8–16.

113. Morizet, N.; Godin, N.; Tang, J.; Maillet, E.; Fregonese, M.; Normand, B. Classification of Acoustic Emission Signals Using Wavelets and Random Forests: Application to Localized Corrosion. *Mech. Syst. Signal Process.* **2016**, *70*, 1026–1037.

114. Tang, J.; Li, J.; Wang, H.; Wang, Y.; Chen, G. In-Situ Monitoring and Analysis of the Pitting Corrosion of Carbon Steel by Acoustic Emission. *Appl. Sci.* **2019**, *9*, 706.

115. Wu, K.; Kim, J.-Y. Acoustic Emission Monitoring during Open-Morphological Pitting

Corrosion of 304 Stainless Steel Passivated in Dilute Nitric Acid. *Corros. Sci.* **2021**, *180*, 109224.

116. Wu, Y.; Nong, J.; Yuan, S.; Guo, Q.; Xu, J. Acoustic Emission Behaviour during the Evolution of a Single Pit on Stainless Steels. *Corros. Sci.* **2021**, *183*, 109308.

117. Shaikh, H.; Amirthalingam, R.; Anita, T.; Sivaibharasi, N.; Jaykumar, T.; Manohar, P.; Khatak, H.S. Evaluation of Stress Corrosion Cracking Phenomenon in an AISI Type 316LN Stainless Steel Using Acoustic Emission Technique. *Corros. Sci.* **2007**, *49*, 740–765.

118. ASTM International. ASTM E399-20a Standard Test Method for Linear-Elastic Plane-Strain Fracture Toughness of Metallic Materials 2022.

119. Lapitz, P.; Ruzzante, J.; Alvarez, M.G. AE Response of α-Brass during Stress Corrosion Crack Propagation. *Corros. Sci.* **2007**, *49*, 3812–3825.

120. Alvarez, M.G.; Lapitz, P.; Ruzzante, J. AE Response of Type 304 Stainless Steel during Stress Corrosion Crack Propagation. *Corros. Sci.* **2008**, *50*, 3382–3388.

121. Du, G.; Li, J.; Wang, W.K.; Jiang, C.; Song, S.Z. Detection and Characterization of Stress-Corrosion Cracking on 304 Stainless Steel by Electrochemical Noise and Acoustic Emission Techniques. *Corros. Sci.* **2011**, *53*, 2918–2926.

122. Xu, J.; Han, E.-H.; Wu, X. Acoustic Emission Response of 304 Stainless Steel during Constant Load Test in High Temperature Aqueous Environment. *Corros. Sci.* **2012**, *63*, 91–99.

123. Xu, J.; Wu, X.; Han, E.-H. Acoustic Emission Response of Sensitized 304 Stainless Steel during Intergranular Corrosion and Stress Corrosion Cracking. *Corros. Sci.* **2013**, *73*, 262–273.

124. Vallen Systeme GmbH AE-Suite Software Manual. *Acquis. Vis. Vis. Vallen Syst. GmbH Publ. Munich Ger. Version* **2011**.

125. Elman, Z.; Boris, M. Acoustic Emission Apparatus and Data Acquisition Available

online: https://www.slideshare.net/mboria/acoustic-emission-sensors-equipment (accessed on 2 December 2020).

126. An, Y.-K.; Kim, M.; Sohn, H. Piezoelectric Transducers for Assessing and Monitoring Civil Infrastructures. In *Sensor Technologies for Civil Infrastructures*; Elsevier, 2014; pp. 86–120.

127. ASTM Inernational Standard Guide for Mounting Piezoelectric Acoustic Emission Sensors. *ASTM E650 / E650M-17* 2017.

128. Theobald, P.; Zeqiri, B.; Avison, J. Couplants and Their Influence on AE Sensor Sensitivity. *J. Acoust. Emiss.* **2008**, *26*, 91–97.

129. Ono, K. Through-Transmission Characteristics of AE Sensor Couplants. *J. Acoust. Emiss.* **2017**, *34*, 1–12.

130. Eaton, M. *Acoustic Emission (AE) Monitoring of Buckling and Failure in Carbon Fibre Composite Structures.*; Cardiff University, 2007; ISBN 1303209667.

131. Mccrory, J. Advanced Acoustic Emission (AE) Monitoring Techniques for Aerospace Structures. Cardiff School of Engineering, Cardiff University Cardiff UK 2015, 1–174.

132. Biondini, F.; Frangopol, D.M. Life-Cycle Performance of Deteriorating Structural Systems under Uncertainty. *J. Struct. Eng.* **2016**, *142*, F4016001.

133. Raj, B.; Jayakumar, T.; Rao, B.P.C. Non-Destructive Testing and Evaluation for Structural Integrity. *Sadhana* **1995**, *20*, 5–38.

134. Marks, R. Methodology Platform for Prediction of Damage Events for Self-Sensing Aerospace Panels Subjected to Real Loading Conditions, Cardiff University, 2016.

135. ASTM International. ASTM E976-15 Standard Guide for Determining the Reproducibility of Acoustic Emission Sensor Response. **2021**, 1–7.

136. ASTM International. ASTM E1106-12 Standard Test Method for Primary Calibration of Acoustic Emission Sensors. **2021**, 1–13.

137. Castaings, M.; Bacon, C.; Hosten, B.; Predoi, M. V Finite Element Predictions for the Dynamic Response of Thermo-Viscoelastic Material Structures. *J. Acoust. Soc. Am.* **2004**, *115*, 1125–1133.

138. Greve, D.W.; Neumann, J.J.; Nieuwenhuis, J.H.; Oppenheim, I.J.; Tyson, N.L. Use of Lamb Waves to Monitor Plates: Experiments and Simulations. In Proceedings of the Smart Structures and Materials 2005: Sensors and Smart Structures Technologies for Civil, Mechanical, and Aerospace Systems; International Society for Optics and Photonics, 2005; Vol. 5765, pp. 281–292.

139. Nienwenhui, J.H.; Neumann, J.J.; Greve, D.W.; Oppenheim, I.J. Generation and Detection of Guided Waves Using PZT Wafer Transducers. *IEEE Trans. Ultrason. Ferroelectr. Freq. Control* **2005**, *52*, 2103–2111.

140. Pimentel, J.V.; Klemm, R.; Dalgic, M.; Irretier, A.; Krieger, K.-L. 29-Damage Monitoring on a Steel Truck Trailer Using Parameter-Based Analysis of Acoustic Emissions. *J. Acoust. Emiss.* **2018**, *35*.

141. Piotrowski, L.; Sertucha, J. An Adaptive Approach to Non-Destructive Evaluation (NDE) of Cast Irons Containing Precipitated Graphite Particles with the Help of Magnetoacoustic Emission. *NDT E Int.* **2023**, *133*, 102739.

142. Engineering ToolBox. Solids and Metals - Speed of Sound. Available online: https://www.engineeringtoolbox.com/sound-speed-solids-d_713.html (accessed on 4 February 2022).

143. Moser, F.; Jacobs, L.J.; Qu, J. Modeling Elastic Wave Propagation in Waveguides with the Finite Element Method. *Ndt E Int.* **1999**, *32*, 225–234.

144. Mohd, S.; Holford, K.M.; Pullin, R. Continuous Wavelet Transform Analysis and Modal Location Analysis Acoustic Emission Source Location for Nuclear Piping Crack Growth Monitoring. In Proceedings of the AIP Conference Proceedings; American Institute of Physics, 2014; Vol. 1584, pp. 61–68.

145. Yamada, H.; Mizutani, Y.; Nishino, H.; Takemoto, M.; Ono, K. Lamb Wave Source

Location of Impact on Anisotropic Plates. *J. Acoust. Emiss.* **2000**, *18*, 51.

146. Jeong, H.; Jang, Y.-S. Wavelet Analysis of Plate Wave Propagation in Composite Laminates. *Compos. Struct.* **2000**, *49*, 443–450.

147. Hamam, Z.; Godin, N.; Fusco, C.; Doitrand, A.; Monnier, T. Acoustic Emission Signal Due to Fiber Break and Fiber Matrix Debonding in Model Composite: A Computational Study. *Appl. Sci.* **2021**, *11*, 8406.

148. Tsangouri, E.; Aggelis, D.G. The Influence of Sensor Size on Acoustic Emission Waveforms—a Numerical Study. *Appl. Sci.* **2018**, *8*, 168.

149. El-Meligi, A.A. Corrosion Preventive Strategies as a Crucial Need for Decreasing Environmental Pollution and Saving Economics. *Recent Patents Corros. Sci.* **2010**, *2*.

150. Craig, B.D.; Anderson, D.S. *Handbook of Corrosion Data*; ASM international, 1994; ISBN 0871705184.

151. Rasheeda, K.; Vijaya, D.P.; Krishnaprasad, P.A.; Samshuddin, S. Pyrimidine Derivatives as Potential Corrosion Inhibitors for Steel in Acid Medium-An Overview. *Int. J. Corros. Scale Inhib.* **2018**, *7*, 48–61.

152. Slepski, P.; Gerengi, H.; Jazdzewska, A.; Orlikowski, J.; Darowicki, K. Simultaneous Impedance and Volumetric Studies and Additionally Potentiodynamic Polarization Measurements of Molasses as a Carbon Steel Corrosion Inhibitor in 1M Hydrochloric Acid Solution. *Constr. Build. Mater.* **2014**, *52*, 482–487.

153. Cheong, Y.-M.; Kim, K.-M.; Kim, D.-J. High-Temperature Ultrasonic Thickness Monitoring for Pipe Thinning in a Flow-Accelerated Corrosion Proof Test Facility. *Nucl. Eng. Technol.* **2017**, *49*, 1463–1471.

154. Peng, X.; Anyaoha, U.; Liu, Z.; Tsukada, K. Analysis of Magnetic-Flux Leakage (MFL) Data for Pipeline Corrosion Assessment. *IEEE Trans. Magn.* **2020**, *56*, 1–15.

155. Kearns, J.R.; Scully, J.R.; Roberge, P.R.; Reichert, D.L.; Dawson, J.L. *Electrochemical Noise Measurement for Corrosion Applications*; ASTM International,

1996; Vol. 1277; ISBN 080312032X.

156. Hladky, K.; Dawson, J.L. The Measurement of Localized Corrosion Using Electrochemical Noise. *Corros. Sci.* **1981**, *21*, 317–322.

157. Sadowski, Ł. New Non-Destructive Method for Linear Polarisation Resistance Corrosion Rate Measurement. *Arch. Civ. Mech. Eng.* **2010**, *10*, 109–116.

158. Torres, C.E. de A.S.; Costa, C.G.F.; Pereira, A.P.; de Castro, M. das M.R.; Lins, V. de F.C. Corrosion Failure Analysis in a Biodiesel Plant Using Electrical Resistance Probes. *Eng. Fail. Anal.* **2016**, *66*, 365–372.

159. Legat, A. Monitoring of Steel Corrosion in Concrete by Electrode Arrays and Electrical Resistance Probes. *Electrochim. Acta* **2007**, *52*, 7590–7598.

160. Hass, F.; Abrantes, A.C.T.G.; Diógenes, A.N.; Ponte, H.A. Evaluation of Naphthenic Acidity Number and Temperature on the Corrosion Behavior of Stainless Steels by Using Electrochemical Noise Technique. *Electrochim. Acta* **2014**, *124*, 206–210.

161. Calixto, E. *Gas and Oil Reliability Engineering*; Gulf Professional Publishing, 2013; ISBN 9780123919144.

162. Prateepasen, A.; Jirarungsatian, C. Implementation of Acoustic Emission Source Recognition for Corrosion Severity Prediction. *Corrosion* **2011**, *67*, 56001.

163. Bai, Y.; Kim, Y.; Yan, H.; Song, X.; Jiang, H. Reassessment of the Jacket Structure Due to Uniform Corrosion Damage. *Ships Offshore Struct.* **2016**, *11*, 105–112.

164. Sayigh, A.A.M. *Comprehensive Renewable Energy*; Comprehensive Renewable Energy; Elsevier, 2013; Vol. 50; ISBN 9780080971612.

165. Andrade, C.; Alonso, C. Test Methods for On-Site Corrosion Rate Measurement of Steel Reinforcement in Concrete by Means of the Polarization Resistance Method. *Mater. Struct.* **2004**, *37*, 623–643.

166. Sause, M.G.R.; Gribov, A.; Unwin, A.R.; Horn, S. Pattern Recognition Approach to Identify Natural Clusters of Acoustic Emission Signals. *Pattern Recognit. Lett.* **2012**,

33, 17–23, doi:10.1016/j.patrec.2011.09.018.

167. Aljets, D.; Chong, A.; Wilcox, S.; Holford, K. Acoustic Emission Source Location on Large Plate-like Structures Using a Local Triangular Sensor Array. *Mech. Syst. Signal Process.* **2012**, *30*, 91–102.

168. Sedlak, P.; Hirose, Y.; Khan, S.A.; Enoki, M.; Sikula, J. New Automatic Localization Technique of Acoustic Emission Signals in Thin Metal Plates. *Ultrasonics* **2009**, *49*, 254–262.

169. Aljets, D. *Acoustic Emission Source Location in Composite Aircraft Structures Using Modal Analysis*; University of South Wales (United Kingdom), 2011; ISBN 1392610435.

170. Aljets, D.; Chong, A.; Wilcox, S.; Holford, K. ACOUSTIC EMISSION SOURCE LOCATION IN PLATE-LIKE STRUCTURES USING A CLOSELY ARRANGED TRIANGULAR SENSOR ARRAY. *J. Acoust. Emiss.* **2010**, *28*.

171. Mochizuki, M. Control of Welding Residual Stress for Ensuring Integrity against Fatigue and Stress–Corrosion Cracking. *Nucl. Eng. Des.* **2007**, *237*, 107–123.

172. Parkins, R.N. Stress Corrosion Spectrum. *Br. Corros. J.* **1972**, *7*, 15–28.

173. Parkins, R.N. The Application of Stress Corrosion Crack Growth Kinetics to Predicting Lifetimes of Structures. *Corros. Sci.* **1989**, *29*, 1019–1038.

174. Ford, F.P. Quantitative Prediction of Environmentally Assisted Cracking. *Corrosion* **1996**, *52*, 375–395.

175. Frankel, G.S. Electrochemical Techniques in Corrosion: Status, Limitations, and Needs. *J. Test. Eval.* **2014**, *42*, 517–538.

176. Turnbull, A. Modeling of the Chemistry and Electrochemistry in Cracksa Review. *Corrosion* **2001**, *57*.

177. Sheikh, M.F.; Kamal, K.; Rafique, F.; Sabir, S.; Zaheer, H.; Khan, K. Corrosion Detection and Severity Level Prediction Using Acoustic Emission and Machine

Learning Based Approach. *Ain Shams Eng. J.* **2021**, *12*, 3891–3903.

178. Zhang, Z.; Zhao, Z.; Bai, P.; Li, X.; Liu, B.; Tan, J.; Wu, X. In-Situ Monitoring of Pitting Corrosion of AZ31 Magnesium Alloy by Combining Electrochemical Noise and Acoustic Emission Techniques. *J. Alloys Compd.* **2021**, *878*, 160334.

179. Calabrese, L.; Galeano, M.; Proverbio, E.; Di Pietro, D.; Cappuccini, F.; Donato, A. Monitoring of 13% Cr Martensitic Stainless Steel Corrosion in Chloride Solution in Presence of Thiosulphate by Acoustic Emission Technique. *Corros. Sci.* **2016**, *111*, 151–161.

180. Calabrese, L.; Galeano, M.; Proverbio, E.; Pietro, D. Di; Donato, A.; Cappuccini, F. Advanced Signal Analysis of Acoustic Emission Data to Discrimination of Different Corrosion Forms. *Int. J. Microstruct. Mater. Prop.* **2017**, *12*, 147–164.

181. Li, D.; Yang, W.; Zhang, W. Cluster Analysis of Stress Corrosion Mechanisms for Steel Wires Used in Bridge Cables through Acoustic Emission Particle Swarm Optimization. *Ultrasonics* **2017**, *77*, 22–31.

182. Wu, K.; Ito, K.; Shinozaki, I.; Chivavibul, P.; Enoki, M. A Comparative Study of Localized Corrosion and Stress Corrosion Cracking of 13Cr Martensitic Stainless Steel Using Acoustic Emission and X-Ray Computed Tomography. *Materials (Basel).* **2019**, *12*, 2569.

183. Zhang, Z.; Zhang, Z.; Tan, J.; Wu, X. Quantitatively Related Acoustic Emission Signal with Stress Corrosion Crack Growth Rate of Sensitized 304 Stainless Steel in High-Temperature Water. *Corros. Sci.* **2019**, *157*, 79–86.

184. Zhang, Z.; Wu, X.; Tan, J. In-Situ Monitoring of Stress Corrosion Cracking of 304 Stainless Steel in High-Temperature Water by Analyzing Acoustic Emission Waveform. *Corros. Sci.* **2019**, *146*, 90–98.

185. ASTM G129-21 Standard Practice for Slow Strain Rate Testing to Evaluate the Susceptibility of Metallic Materials to Environmentally Assisted Cracking 2021.

186. ASTM G36-94 Standard Practice for Evaluating Stress-Corrosion-Cracking Resistance

of Metals and Alloys in a Boiling Magnesium Chloride Solution 2018.

187. NACE TM0177 Laboratory Testing of Metals for Resistance to Sulfide Stress Cracking and Stress Corrosion Cracking in H2S Environments 2005.

188. International Organization for Standardization (ISO) ISO 15324-Corrosion of Metals and Alloys - Evaluation of Stress Corrosion Cracking by the Drop Evaporation Test 2000, 14.

189. Armstrong, D.E.J.; Rogers, M.E.; Roberts, S.G. Micromechanical Testing of Stress Corrosion Cracking of Individual Grain Boundaries. *Scr. Mater.* **2009**, *61*, 741–743.

190. Ito, K.; Enoki, M. Acquisition and Analysis of Continuous Acoustic Emission Waveform for Classification of Damage Sources in Ceramic Fiber Mat. *Mater. Trans.* **2007**, *48*, 1221–1226.

191. Mohamad, I. Bin; Usman, D. Standardization and Its Effects on K-Means Clustering Algorithm. *Res. J. Appl. Sci. Eng. Technol.* **2013**, *6*, 3299–3303.

192. Jain, A.K.; Dubes, R.C. *Algorithms for Clustering Data*; Prentice-Hall, Inc., 1988; ISBN 013022278X.

193. Milligan, G.W.; Cooper, M.C. A Study of Standardization of Variables in Cluster Analysis. *J. Classif.* **1988**, *5*, 181–204.

194. Al-Jumaili, S.K.; Holford, K.M.; Eaton, M.J.; McCrory, J.P.; Pearson, M.R.; Pullin, R. Classification of Acoustic Emission Data from Buckling Test of Carbon Fibre Panel Using Unsupervised Clustering Techniques. *Struct. Heal. Monit.* **2015**, *14*, 241–251.

195. Wise, B.M.; Gallagher, N.B.; Butler, S.W.; White Jr, D.D.; Barna, G.G. A Comparison of Principal Component Analysis, Multiway Principal Component Analysis, Trilinear Decomposition and Parallel Factor Analysis for Fault Detection in a Semiconductor Etch Process. *J. Chemom. A J. Chemom. Soc.* **1999**, *13*, 379–396.

196. Eaton, M.J.; Pullin, R.; Hensman, J.J.; Holford, K.M.; Worden, K.; Evans, S.L. Principal Component Analysis of Acoustic Emission Signals from Landing Gear

Components: An Aid to Fatigue Fracture Detection. *Strain* **2011**, *47*, e588–e594.

197. Gutkin, R.; Green, C.J.; Vangrattanachai, S.; Pinho, S.T.; Robinson, P.; Curtis, P.T. On Acoustic Emission for Failure Investigation in CFRP: Pattern Recognition and Peak Frequency Analyses. *Mech. Syst. Signal Process.* **2011**, *25*, 1393–1407.

198. Godin, N.; Huguet, S.; Gaertner, R.; Salmon, L. Clustering of Acoustic Emission Signals Collected during Tensile Tests on Unidirectional Glass/Polyester Composite Using Supervised and Unsupervised Classifiers. *Ndt E Int.* **2004**, *37*, 253–264.

199. Pomponi, E.; Vinogradov, A. A Real-Time Approach to Acoustic Emission Clustering. *Mech. Syst. Signal Process.* **2013**, *40*, 791–804.

200. Nair, A.; Cai, C.S.; Kong, X. Acoustic Emission Pattern Recognition in CFRP Retrofitted RC Beams for Failure Mode Identification. *Compos. Part B Eng.* **2019**, *161*, 691–701.

201. Li, L.; Lomov, S. V; Yan, X.; Carvelli, V. Cluster Analysis of Acoustic Emission Signals for 2D and 3D Woven Glass/Epoxy Composites. *Compos. Struct.* **2014**, *116*, 286–299.

202. Godin, N.; Huguet, S.; Gaertner, R. Integration of the Kohonen's Self-Organising Map and k-Means Algorithm for the Segmentation of the AE Data Collected during Tensile Tests on Cross-Ply Composites. *Ndt E Int.* **2005**, *38*, 299–309.

203. De Oliveira, R.; Marques, A.T. Health Monitoring of FRP Using Acoustic Emission and Artificial Neural Networks. *Comput. Struct.* **2008**, *86*, 367–373.

204. Rousseeuw, P.J. Silhouettes: A Graphical Aid to the Interpretation and Validation of Cluster Analysis. *J. Comput. Appl. Math.* **1987**, *20*, 53–65.

205. Caliński, T.; Harabasz, J. A Dendrite Method for Cluster Analysis. *Commun. Stat. Methods* **1974**, *3*, 1–27.

206. Wu, K.; Byeon, J.-W. Morphological Estimation of Pitting Corrosion on Vertically Positioned 304 Stainless Steel Using Acoustic-Emission Duration Parameter. *Corros.*

Sci. **2019**, *148*, 331–337.

207. Wu, K.; Jung, W.-S.; Byeon, J.-W. Evaluation of Corrosion Critical Variables of 304 Stainless Steel by Delay Time of Acoustic Emission. *Mater. Trans.* **2015**, *56*, 398–403.

208. Wu, K.; Jung, W.-S.; Byeon, J.-W. Acoustic Emission of Hydrogen Bubbles on the Counter Electrode during Pitting Corrosion of 304 Stainless Steel. *Mater. Trans.* **2015**, *56*, 587–592.

209. Yonezu, A.; Cho, H.; Takemoto, M. Monitoring of Stress Corrosion Cracking in Stainless Steel Weldments by Acoustic and Electrochemical Measurements. *Meas. Sci. Technol.* **2006**, *17*, 2447.

210. Lou, X.; Yang, D.; Singh, P.M. Film Breakdown and Anodic Dissolution during Stress Corrosion Cracking of Carbon Steel in Bioethanol. *J. Electrochem. Soc.* **2009**, *157*, C86.